frontiers | Research Topics

Remote sensing advances in biodiversity and ecosystem functioning research

Edited by
Zhouyuan Li, Weiwei Sun, Yanjie Xu
and Jixi Gao

Coordinator by
Shijia Peng

Published in
Frontiers in Ecology and Evolution

ISSN 1664-8714
ISBN 978-2-8325-4425-9
DOI 10.3389/978-2-8325-4425-9

About Frontiers

Frontiers is more than just an open access publisher of scholarly articles: it is a pioneering approach to the world of academia, radically improving the way scholarly research is managed. The grand vision of Frontiers is a world where all people have an equal opportunity to seek, share and generate knowledge. Frontiers provides immediate and permanent online open access to all its publications, but this alone is not enough to realize our grand goals.

Frontiers journal series

The Frontiers journal series is a multi-tier and interdisciplinary set of open-access, online journals, promising a paradigm shift from the current review, selection and dissemination processes in academic publishing. All Frontiers journals are driven by researchers for researchers; therefore, they constitute a service to the scholarly community. At the same time, the *Frontiers journal series* operates on a revolutionary invention, the tiered publishing system, initially addressing specific communities of scholars, and gradually climbing up to broader public understanding, thus serving the interests of the lay society, too.

Dedication to quality

Each Frontiers article is a landmark of the highest quality, thanks to genuinely collaborative interactions between authors and review editors, who include some of the world's best academicians. Research must be certified by peers before entering a stream of knowledge that may eventually reach the public - and shape society; therefore, Frontiers only applies the most rigorous and unbiased reviews. Frontiers revolutionizes research publishing by freely delivering the most outstanding research, evaluated with no bias from both the academic and social point of view. By applying the most advanced information technologies, Frontiers is catapulting scholarly publishing into a new generation.

What are Frontiers Research Topics?

Frontiers Research Topics are very popular trademarks of the *Frontiers journals series*: they are collections of at least ten articles, all centered on a particular subject. With their unique mix of varied contributions from Original Research to Review Articles, Frontiers Research Topics unify the most influential researchers, the latest key findings and historical advances in a hot research area.

Find out more on how to host your own Frontiers Research Topic or contribute to one as an author by contacting the Frontiers editorial office: frontiersin.org/about/contact

Remote sensing advances in biodiversity and ecosystem functioning research

Topic editors
Zhouyuan Li — Beijing Forestry University, China
Weiwei Sun — Ningbo University, China
Yanjie Xu — Finnish Museum of Natural History, Finland
Jixi Gao — Center for Satellite Application on Ecology and Environment, Ministry of Ecology and Environment, China

Topic Coordinator
Shijia Peng — Harvard University, United States

Citation
Li, Z., Sun, W., Xu, Y., Gao, J., Peng, S., eds. (2024). *Remote sensing advances in biodiversity and ecosystem functioning research*. Lausanne: Frontiers Media SA.
doi: 10.3389/978-2-8325-4425-9

Table of contents

frontiers | Frontiers in Ecology and Evolution

TYPE Editorial
PUBLISHED 25 January 2024
DOI 10.3389/fevo.2024.1367840

OPEN ACCESS

EDITED AND REVIEWED BY
Alexander Kokhanovsky,
German Research Centre for Geosciences,
Germany

*CORRESPONDENCE
Zhouyuan Li
✉ lizhouyuan@bjfu.edu.cn

RECEIVED 09 January 2024
ACCEPTED 15 January 2024
PUBLISHED 25 January 2024

CITATION
Li Z, Wu J, Peng S, Xu Y, Sun W and Gao J (2024) Editorial: Remote sensing advances in biodiversity and ecosystem functioning research.
Front. Ecol. Evol. 12:1367840.
doi: 10.3389/fevo.2024.1367840

Editorial: Remote sensing advances in biodiversity and ecosystem functioning research

Zhouyuan Li[1]*, Jiaxin Wu[1], Shijia Peng[2], Yanjie Xu[3],
Weiwei Sun[4] and Jixi Gao[5]

[1]School of Grassland Science, Beijing Forestry University, Beijing, China, [2]Department of Organismic and Evolutionary Biology, Harvard University, Cambridge, MA, United States, [3]Finnish Museum of Natural History, University of Helsinki, Helsinki, Finland, [4]Department of Geography and Spatial Information Techniques, Ningbo University, Ningbo, China, [5]Satellite Application Center for Ecology and Environment, Ministry of Ecology and Environment, Beijing, China

KEYWORDS

remote sensing, environmental change, biodiversity, ecosystem functioning, geographic information system

Editorial on the Research Topic
Remote sensing advances in biodiversity and ecosystem functioning research

1 Introduction

Different dimensions of biodiversity are increasingly appreciated as critical for maintaining the functions of ecosystems and their services to humans. More recently, with the emergence of functional biogeography, functional diversity is of particular interest due to its strong links with ecosystem processes such as carbon, water and energy exchange, and climate mitigation. The multi-form diversity varies in space and time. Understanding this variation across scales is important for tracking the resilience of earth's ecosystem, and the information on the ecosystem structural features provides necessary foundations for monitoring, predicting the ecosystem functioning patterns and process of ecosystems from individual unit to its whole in a holistic manner.

In recent, the high-resolution, high-throughput, non-intrusive, and large-scale data on biodiversity monitoring and measurement are becoming a new trend toward enhancing the efficiency and coherency in ecological discovery. Remote sensing has proved to be a critical technology for addressing this research gap. Air- and satellite-borne spectrometers at different levels could develop novel diversity measurements and alternatives in various ecosystems and for different kinds of communities and taxa.

In this Research Topic, our goal is to bring together the latest research in a fast-growing direction that combines remote sensing techniques and their application in biodiversity and ecosystem functioning (BEF). We would like to know how the different levels of ecological theories, from species to ecosystems, are linked more coherently than ever via the multi-scale digitalized observational and computational method advances. Seen from the 11 published papers in this Research Topic, we generalized the three main directions in this field: (1) the novel observational techniques of biodiversity and their application, (2) the ecosystem functioning assessment at macroscopic scale with geoinformatics methods, and

(3) the linkage analysis of BEF under the geographical gradient of in a context of environmental change.

2 Novel observational techniques of biodiversity

In the realm of novel biodiversity observational techniques, Hagani et al. ‘s research delves into the historical invasion of Phragmites australis in a brackish coastal marsh, utilizing high-resolution remote sensing to meticulously map its expansion over two decades. Despite individual management efforts, Hagani et al. emphasizes the need for adaptive, collaborative strategies to eradicate this invasive species on a large scale.

Shifting focus to subtropical forests, Yan et al. introduces a groundbreaking forest measurement system using SLAM+AR technology through mobile phones. This system not only accurately measures tree parameters but also creates a virtual environment for precise spatial structural analysis, revolutionizing digitalized forest management practices.

Expanding the scope to forest ecosystems, Li et al. pioneers UAV-borne hyperspectral and LiDAR data for individual tree-based species diversity estimation. Li et al. ‘s classification method, relying on spectral information, proves superior in accurately predicting species richness and the Shannon-Wiener index. In contrast, Li et al. ‘s clustering method, while introducing uncertainties, rapidly captures forest diversity patterns without distinguishing specific tree species.

In conclusion, the studies showcase the frontier of biodiversity observation, leveraging remote sensing, mobile technology, and UAV-based approaches. They embody the innovative strides in understanding and managing diverse ecosystems.

3 Large-scale ecosystem functioning assessment

In the realm of large-scale ecosystem functioning assessment, Lu et al. utilizes geographic information systems (GIS) and spatial data to quantitatively study diversity patterns within Moraceae genera. Results reveal significant differences between monotypic and multiple-species genera, emphasizing the importance of spatial distribution analysis for effective conservation strategies.

Zhang et al. ‘s exploration of ecosystem services in Xinjiang Autonomous Region contributes to understanding driving factors and spatial heterogeneity. The study employs InVEST and RWEQ models, identifies precipitation, temperature, and fractional vegetation cover as dominant factors influencing essential ecosystem services. The study’s county-level analysis provides nuanced insights for tailored ecological protection policies.

On the analysis of city level, Wang et al. introduces the application of remote sensing ecological index (RSEI) to monitor ecological environment quality in Zhanjiang City. Utilizing Landsat satellite images and four indicators, the study quantitatively assesses changes in ecological quality over time. The study highlights the effectiveness of RSEI in evaluating and predicting ecological changes, essential for guiding conservation measures in urbanizing areas.

On a larger scale, Wei et al. ‘s study shifts the focus to synergies and trade-offs in ecosystem services within China’s arid regions. Using the northern sand-stabilization belt as a case study, Wei et al. explores how precipitation and fractional vegetation cover influence five simulated ecosystem services. The research uncovers increasing synergies with higher precipitation and vegetation cover, providing valuable insights for sustainable ecosystem management in arid environments.

These findings underscore the importance of spatial analysis, remote sensing technologies, and tailored conservation strategies for effective ecosystem management in diverse environments.

4 BEF under the environmental change

Peng et al. ‘s study on the impact of climate change on plant spectral diversity highlights significant shifts in spatial patterns across various forest types. The intricate relationships between species diversity, spatial interactions, and climate change are emphasized. This insight lays the foundation for understanding the broader implications of environmental changes on biodiversity.

From the forest to the grassland perspective, we delve into Yang et al. ‘s exploration of plant species diversity and aboveground biomass in alpine grasslands on the Qinghai–Tibet Plateau. Through advanced modeling, Yang et al. provides a comprehensive understanding of the spatial relationships and driving factors governing these crucial ecological parameters. This grassland-focused perspective contributes to our knowledge of ecosystem functioning in alpine regions.

Shifting our focus to urban environments, Ma et al. ‘s research investigates the projected effects of climate change and urban expansion on plant biodiversity in the city clusters of Northern China. Employing habitat suitability models, Ma et al.‘s findings underscore the urgency of addressing urban expansion as a primary driver of plant biodiversity loss in this region. The transition from natural to urban landscapes emphasizes the need for sustainable urban planning to mitigate the impact on local ecosystems.

Gao et al. ‘s study on vegetation water use efficiency (WUE) in the West Liao River Plain explores the temporal and spatial variations of WUE in response to climate change and human activities. By unraveling the intricate dynamics between carbon and water cycles, Gao et al.‘s research contributes to our understanding of ecosystem functioning in regions sensitive to environmental changes.

These studies collectively contribute to the understanding of biodiversity and ecosystem functioning under the complex interplay of environmental changes. From grasslands to forests and urban areas, each perspective offers unique insights into the challenges and opportunities for managing and conserving ecosystems in the face of increasing climate change and human activities.

Author contributions

ZL: Funding acquisition, Project administration, Supervision, Writing – original draft, Writing – review & editing. JW: Writing – original draft, Writing – review & editing. SP: Project administration, Writing – original draft, Writing – review & editing. YX: Project administration, Writing – review & editing, Resources. WS: Supervision, Writing – review & editing. JG: Supervision, Writing – review & editing.

Funding

The author(s) declare financial support was received for the research, authorship, and/or publication of this article. This work was financially supported by the National Natural Science Foundation of China (32101324, 42122009), the Second Tibetan Plateau Scientific Expedition and Research Program (2019QZKK0307), the National Key R&D Program of China (2023YFF1304305, 2021YFB3901102), Zhejiang Province "Pioneering Soldier" and "Leading Goose" R&D Project (2023C01027), Ningbo Science and Technology Innovation 2025 Major Special Project (2021Z107, 2022Z032), and the College Students Innovation and Entrepreneurship Training Program (202310022126).

Conflict of interest

The authors declare that the research was conducted in the absence of any commercial or financial relationships that could be construed as a potential conflict of interest.

Publisher's note

frontiers | Frontiers in Ecology and Evolution

TYPE Original Research
PUBLISHED 14 March 2023
DOI 10.3389/fevo.2023.1116484

OPEN ACCESS

EDITED BY
Yanjie Xu,
Finnish Museum of Natural History,
Finland

REVIEWED BY
Wang Jiping,
Chinese Academy of Forestry,
China
Siyuan Wang,
Research Center for Eco-environmental
Sciences (CAS),
China

*CORRESPONDENCE
Kai Su
✉ sukai_lxy@gxu.edu.cn

†These authors have contributed equally to this work

SPECIALTY SECTION
This article was submitted to
Environmental Informatics and Remote
Sensing,
a section of the journal
Frontiers in Ecology and Evolution

RECEIVED 05 December 2022
ACCEPTED 24 February 2023
PUBLISHED 14 March 2023

CITATION
Wei C, Su K, Jiang X, You Y, Zhou X, Yu Z,
Chen Z, Liao Z, Zhang Y and Wang L (2023)
Increase in precipitation and fractional
vegetation cover promote synergy of
ecosystem services in China's arid regions—
Northern sand-stabilization belt.
Front. Ecol. Evol. 11:1116484.
doi: 10.3389/fevo.2023.1116484

Increase in precipitation and fractional vegetation cover promote synergy of ecosystem services in China's arid regions—Northern sand-stabilization belt

Changwen Wei[1†], Kai Su[1*†], Xuebing Jiang[2], Yongfa You[3], Xiangbei Zhou[1], Zhu Yu[4], Zhongchao Chen[5], Zhihong Liao[1], Yiming Zhang[1] and Luying Wang[1]

[1]College of Forestry, Guangxi University, Nanning, China, [2]School of Mechanical Engineering, Guangxi University, Nanning, China, [3]International Center for Climate and Global Change Research, School of Forestry and Wildlife Sciences, Auburn University, Auburn, AL, United States, [4]Guangxi Forest Inventory and Planning Institute, Nanning, China, [5]Guizhou Linfa Survey and Design Co., Ltd., Guiyang, China

Research on synergies and trade-offs between ecosystem services (ES) contributes to a better understanding of the linkages between ecosystem functions. Relevant research mainly focuses on mountain areas, while research in arid areas is obviously insufficient. In this research, we use the northern sand-stabilization belt (NSB) as an example to explore how the synergies and trade-offs between different ES vary with the gradient of precipitation and fractional vegetation cover (FVC) over the period 2000-2020. Based on five simulated ecosystem services (habitat provision, sand-stabilization service, water conservation service, soil conservation service and carbon sequestration service), the Pearson correlation coefficient method was used to analyze the various characteristics of the trade-offs and synergies among the different ES pairs along the FVC and precipitation gradients. Results showed that: Synergies between most paired ES increased significantly with increasing precipitation and FVC. However, ES have different sensitivities to environmental change, FVC promotes bit more synergy of ES pairs than precipitation. The study also found that land use/land cover may be an important driving factor for trade-offs and synergies between paired ES. The findings demonstrate that increased precipitation and FVC promote synergy of ecosystem services in arid regions of China. In the future, it can be investigated whether anthropogenic increase in FVC in arid regions can significantly contribute to the synergy of ES. In the meantime, this study could improve our understanding of arid and semi-arid (or macro-regional) ecosystems and contribute to the development of ecosystem management and conservation measures in NSB.

KEYWORDS

northern sand-stabilization belt, ecosystem services, FVC, precipitation, trade-offs and synergies

1. Introduction

Ecosystem services (ES) are the products, services, and environmental conditions that people derive from ecosystems and are essential to human well-being and survival (Costanza et al., 1997). However, long-term human over-cultivation and grazing have destroyed the self-regulating capacity of the ecological environment (Dumanski and Pieri, 2000). The first to bear the brunt are the arid and semi-arid areas, which are more sensitive to changes. Desertification in arid and semi-arid regions is a serious problem in China (Zhang, 2017). According to the results of the National Desert, Gobi and Sandy Land Survey and Desertification Research, the decertified land area in China in 2011 was 262.2 million km^2, representing 27.4% of the land area, and nearly 400 million people were affected by desertification (Fu et al., 2017).

Ecosystem services in arid and semi-arid regions are as valuable as ecosystem services in other regions. Ouyang et al. (2016) evaluated several ES in China, such as windbreak and sand-stabilization service, habitat provision, soil conservation service, and carbon sequestration service and found that arid and semi-arid regions were high-value areas providing various services and the distribution of ecosystem services in arid areas has significant spatial heterogeneity. Although the amount of vegetation in arid and semi-arid regions is much less than that in other areas, the types of vegetation are rich and play an important role in regional ecosystems (Wang et al., 2020; Yixuan et al., 2022). Meanwhile, these ES can generate substantial potential economic benefits. The research results of Su et al. (2020) showed that the sand-stabilization amount of Ordos's ecosystem was approximately 7.28×10^8 tons. The amount of dust-fall in the beneficiary area was reduced by 2.87×10^8 tons, and an investment of 4318.51×10^8 CNY in dust removal would be avoided. In addition, trade-off and synergy of multiple ecosystem services are also hot research topics at present, but the research mainly focuses on farmland, wetlands, oceans, cities, and other ecosystems. Especially ecosystems that can generate economic benefits, such as farmland and forests (Johns et al., 2014; Loomis and Paterson, 2014; Song and Deng, 2015; Malekmohammadi and Jahanishakib, 2017; Richards and Friess, 2017; Liao et al., 2022). Furthermore, our literature review found that few scholars, such as Fensholt et al. (2012) and Wen et al. (2019), have focused on the assessment of ecosystem services in arid and semi-arid regions, especially studies in megaregions.

However, previous studies have proven that ecosystems are vulnerable to precipitation and climate change, especially grasslands are highly sensitive to changes in precipitation (Knapp and Smith, 2001; Huxman et al., 2004; Heisler-White et al., 2008; Sloat et al., 2018; Gherardi and Sala, 2019). For example, Felton's study in mesic grassland found that in dry years, increasing growing season precipitation variability reduced rain-use efficiency, thereby reducing ecosystem function by up to 42%, but this effect diminishes as the year gets wetter (Felton et al., 2020). The gradient effect of environmental impact (such as vegetation cover, precipitation, and temperature) has been widely studied in mountainous areas (Su et al., 2007; Deng et al., 2020; Liu et al., 2020). For example, findings of Yu et al. (2021) in the Qinling Mountains showed that net primary productivity, soil conservation, and habitat quality increased significantly with altitude and vegetation coverage gradients, but the effects on water yield and grain production weakened. Liu et al. (2019) found that the precipitation increased in Taihang mountains, the trade-offs between the soil conservation service and net primary production, the water yield and net primary production, habitat quality, and the soil conservation service, and water yield and habitat quality all decreased significantly. The arid and semi-arid regions span the north of China and have obvious horizontal spatial heterogeneity. In the lateral direction, there are horizontal differences in climate, upper soil, and vegetation distribution affected by precipitation, thus forming the horizontal spatial heterogeneity of land use and land cover (farmland, grassland, forest, etc.; Sun et al., 1998; Liu and Ren, 2012; Liu et al., 2014). The special geographical location makes arid and semi-arid regions have obvious gradient characteristics such as mountains, and this characteristic will have a certain impact on ecological processes and lead to changes in the regional ecosystem. The response mechanism of multiple mountain ecosystem services on environmental gradients is basically clear (Yang et al., 2018; Liu et al., 2019; Zhang et al., 2020; Zhou et al., 2021); however, the response of multiple ecosystem services on environmental gradients in arid and semi-arid regions is unclear and lacks in-depth research. An understanding of the impact of precipitation, vegetation cover, and other factors on ecosystem services would improve our knowledge of ecosystem services and develop effective ecological management measures in arid and semi-arid regions.

The northern sand-stabilization belt (NSB) is located mainly in northwest China, and as one of the ecological security barriers in China, the ecological environment in this area plays an important role in stabilizing the current ecological security pattern in northwest China and even the whole county (Su et al., 2020; Zhu et al., 2020; Wang J. et al., 2022). There are also many ecological projects in NSB, such as the Three-North Shelter Forest Program (Huang and Kong, 2016), the Grain for Green Project (Cao et al., 2009), and the Natural Forest Protection Project (Hu and Liu, 2006). These projects protect and improve the habitats of wild animals and play a positive role in water conservation and carbon sequestration (Li et al., 2015). Therefore, the study chooses five ES of sand-stabilization service, habitat provision, water conservation service, soil conservation service, and carbon sequestration service, which were selected as research objects.

Using meteorological, soil, remote sensing, and land use data, we aimed to quantify the ES in NSB, including soil conservation service, habitat provision, carbon sequestration service, water conservation service, and sand-stabilization service. Based on the image-by-image spatial correlation analysis method-Pearson product–moment correlation coefficient method, this study intends to address the following questions: (1) What are the synergies and trade-offs between different ES? (2) How does the synergy and trade-off between different ES change with the gradient of precipitation and FVC? (3) Which synergy or trade-off are more influenced by precipitation or FVC? Clarifying the trade-offs and synergy between ES on these environmental gradients can provide data and information to support scientific research and policy formulation in addressing climate change, implementing ecological and environmental protection, achieving sustainable development, and ensuring food security.

2. Materials

2.1. Study area

The NSB is a long and thin belt across northern China (Figure 1A), located in the transition zone between arid and semi-arid areas, divided into three sections from west to east, the Tarim Basin sand-stabilization belt (TB), the Hexi Corridor sand-stabilization belt (HC), and the Inner Mongolia sand-stabilization belt (IM). With a total area of 869,558.5 km^2. The slope of the study area ranges from 0 to 55 degrees, with the larger slopes

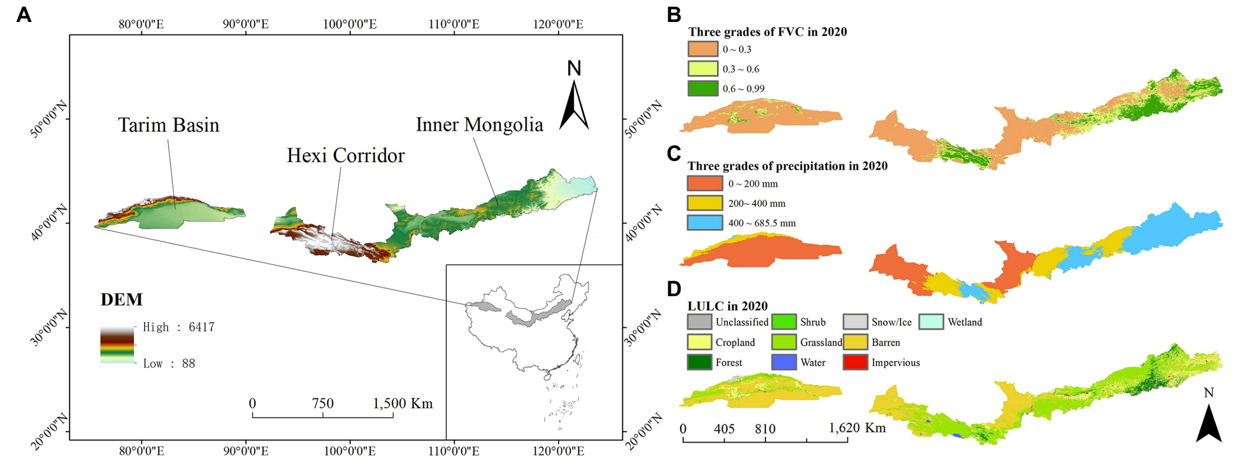

FIGURE 1
Location of the study area.

concentrated in the northern part of the TB, the HC, and the partial eastern part of the IM. The mean annual precipitation of around 300 mm, with a significant precipitation gradient (Zhang, 2017). The mean annual temperature ranges from −1.9 to 13.5°C. The average wind speed of sand-raising is about 6.5–8.0 m/s. The average wind speed of sand-raising is larger in the middle and smaller in the west and east. FVC increases gradually from west to east. The vegetation types are desert grassland, steppe, forest grassland, forest meadow grassland, scrub meadow, alpine meadow, coniferous forest, deciduous broadleaved forest, hyper-arid shrubs, semi-shrubs, small shrubs, and semi-trees. The distribution of precipitation is generally uneven and highly variable.

We refer to some conventions and classification standards to divide FVC and precipitation gradient. For example, the classification of FVC refers to the Standard for "Soil Erosion Classification and Grading Standards" (SL190-2007) by the Ministry of Water Resources of the People's Republic of China in 2008. And combined with the actual situation of the study area, the FVC was divided into three classes: FVC<30% (low vegetation cover), 30% ≤ FVC < 60% (medium vegetation cover), FVC ≥ 60% (high vegetation cover; Gao et al., 2015; Figure 1B). According to the convention of annual precipitation division, above 800 mm is the humid zone, 800–400 mm belongs to the semi-humid zone, 400–200 mm belongs to the semi-arid zone, and below 200 mm belongs to the arid zone (Zhang et al., 2011; Gao et al., 2015). The maximum annual precipitation was 685.5 mm in 2020, and most of the study area belongs to the arid zone. For convenience of analysis, this study divides the grades according to the gradient of 0–200, 200–400, and 400 mm<, which accounted for 46.31, 22.76, and 30.93%, respectively, (Figure 1C). The main land use and land cover (LULC) of NSB are grassland and desert (Figure 1D). Demonstrating the spatial distribution pattern of LULC in the belt-shaped study area helps to describe the distribution of ES related to LULC.

2.2. Data source

Loess plateau science data center, National Earth System Science Data Sharing Infrastructure, National Science & Technology Infrastructure of China,[1] including average annual precipitation and temperature (Peng et al., 2019), relative humidity, and hours of sunshine. DEM data with 90 m resolution came from the geospatial data cloud platform of the Computer Network Information Center of the Chinese Academy of Sciences.[2] Land cover and FVC data were obtained from MODIS-based land use product extraction.[3] The soil dataset is derived from the Harmony World Soil Database_China subset of the National Qinghai-Tibet Plateau/Third Pole Environmental Data Center, which includes soil texture, sandy soils, chalky soils, clays, and organic carbon. The above data came from different platforms, so this study resampled all the raster data to the same image size with Arcgis, and then computed the raster data in Python.

3. Methods

3.1. Sand-stabilization service

In this study, sand-stabilization service is represented by the sand stabilization amount, which is equal to the difference between the potential wind erosion amount and the actual wind erosion amount. This project uses the revised wind erosion equation (RWEQ) model (Fryrear et al., 2000) to estimate the sand-stabilization service in NSB. The calculation formula is shown below:

$$G = S_{L1} - S_{L2} \tag{1}$$

$$S_{L1} = \frac{2 \times x}{S_1^{\,2}} Q_{\max 1} \times e^{-\left(\frac{x}{S_1}\right)^2} \tag{2}$$

---

[1] http://loess.geodata.cn
[2] http://www.gscloud.cn
[3] https://ladsweb.nascom.nasa.gov/search

$$S_{L2} = \frac{2 \times x}{S^2} Q_{\max 2} \times e^{-\left(\frac{x}{S_2}\right)^2} \tag{3}$$

$$Q_{\max 1} = 109.8\left[WF \times EF \times SCF \times K'\right] \tag{4}$$

$$S_1 = 150.71\left(WF \times EF \times SCF \times K'\right)^{-0.3711} \tag{5}$$

$$Q_{\max 2} = 109.8\left[WF \times EF \times SCF \times K' \times COG\right] \tag{6}$$

$$S_2 = 150.71\left(WF \times EF \times SCF \times K' \times COG\right)^{-0.3711} \tag{7}$$

where, G is the amount of sand fixation, kg/m^2; S_{L1} and S_{L2} are the potential amount of wind erosion and the actual amount of wind erosion, kg/m^2; $Q_{\max 1}$, $Q_{\max 2}$ are the maximum transport capacity of potential soil erosion and actual soil erosion, respectively, kg/m^2; S_1, S_2 are the critical field lengths for potential and actual soil erosion, respectively, m; x is the distance of maximum wind erosion occurrence in the downwind direction, m; WF for meteorological factors; EF is soil erodibility factor; SCF as soil crust factor; K' is the surface roughness factor; and COG is the vegetation cover factor.

3.2. Soil conservation service

Soil conservation service is represented by the soil retention amount, which is equal to the difference between the potential soil retention and the actual soil retention. The Universal Soil Loss Equation (USLE) is the most widely used remote sensing quantitative model of soil loss with good practicality and has been applied and practiced in large regional soil conservation studies in China. Therefore, USLE (Pandey et al., 2007) was selected to assess soil conservation services in NSB ecosystems for this project. The calculation formula is shown below:

$$SC = SE_p - SE_a = R \times K \times LS \times (1 - COG) \tag{8}$$

where, SC for soil retention, $[\mathrm{t/(hm^2 \times a)}]$; SE_p and SE_a are the potential soil erosion and actual soil erosion, respectively, $[\mathrm{t/\ (hm^2 \times a)}]$; R is the rainfall erosion force factor, $MJ \times \mathrm{mm/(hm^2 \times h \times a)}$; K is the soil erodibility factor, $t \times \mathrm{hm^2 \times h/(hm^2 \times MJ \times mm)}$; LS and COG are topography factor and vegetation cover factor, respectively, and are dimensionless. The calculation process for the different factors is shown below:

3.2.1. Rainfall erosion force factor (R)

$$R = \sum_{k=1}^{24} \bar{R}_k \tag{9}$$

$$\bar{R}_k = \frac{1}{n} \sum_{i=1}^{n} \sum_{j=0}^{m} \left(\alpha \times P_{i,j,k}^{1.7265}\right) \tag{10}$$

$$\bar{R}_k = \sum_{k=1}^{24} \sum_{i=1}^{n} \sum_{j=0}^{m} \left(\alpha \times P_{i,j,k}^{1.7265}\right) \tag{11}$$

where, R is the multi-year average annual rainfall erosion force, $MJ \cdot \mathrm{mm/(hm^2 \cdot h \cdot a)}$; $\bar{R}_k$ semimonthly k is the rainfall erosion force of the kth semimonthly, $MJ \times \mathrm{mm/(hm^2 \times h \times a)}$; k for 24 and a half months of the year, i.e., $k = 1,2,\ldots,24$; i is the year of the used rainfall information, i.e., $i = 1,2,\ldots,n$; j is the number of days of erosive rainfall days in the kth half month of the i-th year, i.e., $j = 1,2,\ldots,m$; $P_{i,j,k}$ is the j-th erosive daily rainfall in the k-th half month of year i(mm); α is a parameter with $\alpha = 0.3937$ in the warm season and $\alpha = 0.3101$ in the cold season.

3.2.2. Soil erodibility factor (K)

$$K = \left(-0.01383 + 0.51575 \times K_{EPIC}\right) \tag{12}$$

$$\begin{aligned} K_{EPIC} = & \left\{0.2 + 0.3 \cdot e^{\left[-0.0256 \cdot m_s \left(1 - m_{silt}/100\right)\right]}\right\} \times \left[m_{silt} / \left(m_c + m_{silt}\right)\right]^{0.3} \\ & \times \left\{1 - 0.25 \cdot orgC \Big/ \left[orgC + e^{\left(3.72 - 2.995 \cdot orgC\right)}\right]\right\} \\ & \times \left\{1 - 0.7\left(1 - \frac{m_s}{100}\right) \Big/ \left\{\left(1 - \frac{m_s}{100}\right) + e^{\left[-5.51 + 22.9\left(1 - \frac{m_s}{100}\right)\right]}\right\}\right\} \end{aligned} \tag{13}$$

where, m_c, m_{silt}, m_s, and $orgC$ are the clay grain (<0.002 mm), powder grain (0.002–0.05 mm), sand grain (0.05–2 mm), and organic carbon, %, respectively.

3.2.3. Topographic factors (LS)

$$L = \left(\lambda / 2.13\right)^m \tag{14}$$

$$S = \begin{cases} 10.8\sin\theta + 0.03 & \theta < 5.14° \\ 16.8\sin\theta - 0.5 & 5.14° \le \theta < 10.20° \\ 21.91\sin\theta + 0.96 & 10.20° \le \theta < 28.81° \\ 9.5988 & \theta > 28.81° \end{cases} \tag{15}$$

where, L is the slope length factor; S is the slope factor; m is the slope length index, θ is the slope,°; and λ is the slope length, m.

3.2.4. Vegetation coverage factor (COG)

The vegetation cover factor can have a positive effect on controlling soil erosion, between 0 and 1. The larger vegetation coverage factor (COG) value, the poorer the vegetation cover and the weaker the soil retaining effect; the smaller the COG value, the better the vegetation cover and the stronger the soil retaining effect. The magnitude of the vegetation cover factor depends on the combined effect of ecosystem type and vegetation cover, and should theoretically be obtained through experimental observation calculations. However, the existing assessment practice has basically formed two camps of considering only the ecosystem type and considering only the vegetation cover, and it is unscientific to ignore either the influence of vegetation cover or the influence of ecosystem type. Therefore, the vegetation cover factors were assigned according to the difference of ecosystem types and the level of vegetation cover by combining remote sensing parameter inversion and field positioning observation. As the ecosystem types involved in this project are grassland, forest and shrub, the values were assigned according to the different levels of vegetation cover, taking into account expert knowledge and previous research experience (Wang and Jiao, 1996; Zhang et al., 2017; Table 1).

$$\mathrm{COG} = 0.221 - 0.595 \log c \tag{16}$$

where, c is the vegetation cover in fractional form.

3.3. Water conservation service

The water conservation service was calculated using the balance equation of water quantity (Zhang et al., 2001), which treats the water service as precipitation minus evapotranspiration and storm runoff. The calculation index includes annual precipitation, annual evapotranspiration, and annual stormwater production volume. The water balance equation is calculated as follows:

$$WR = PET - ET - QF \tag{17}$$

where, WR is the water-bearing capacity, mm; PET is the annual precipitation, mm; QF is the storm water runoff, mm. ET is the actual evapotranspiration, mm.

The calculation of the main indicator factors required for the calculation of the water conservation services is shown below:

3.3.1. Rainfall

Spatial distribution data pre-processing: using weather station data as the basis, the daily weather data are accumulated to the annual scale and then interpolated to the space using ArcGIS spatial interpolation method.

3.3.2. Evaporation

Here, the actual evapotranspiration is calculated using the Zhang model based on the Budyko hydrothermal equilibrium assumption, the main formula of which is shown below:

$$ET = \frac{1 + w \times \frac{PET}{P}}{1 + w \times \frac{PET}{P} + \frac{P}{PET}} \times P \tag{18}$$

where, ET is actual evapotranspiration; P is rainfall; w is the water use coefficient for a particular land use type; PET is potential evapotranspiration, mm. The calculation equation is as follows:

$$PET = 0.162 \frac{SR}{58.5} \left(DT + 17.8 \right) \tag{19}$$

where, SR is the monthly average total solar radiation of each month, $\mathrm{cal} / \mathrm{cm}^2$; DT is the monthly average temperature of each month, °C.

3.3.3. Stormwater runoff

Stormwater runoff is calculated using precipitation multiplied by runoff coefficients, where the extent to which different land use types respond to precipitation varies.

$$QF = P \times \alpha \tag{20}$$

where, P is rainfall, mm; α is the surface runoff coefficient for different land use/cover types (Table 2).

3.4. Carbon sequestration service

Carbon sequestration service is calculated using aboveground biomass multiplied by the biomass-carbon conversion coefficient (Fang et al., 2001; Piao et al., 2009). The main calculation formula is as follows:

$$COS = \sum_{i=1}^{j} AGB_i \times C_i \tag{21}$$

where COS is the above-ground carbon stock of terrestrial ecosystems. i is the i-th type of ecosystem; j is the total number of ecosystem types; $AGBi$ is the aboveground biomass of the ith ecosystem type; and C_i is the biomass-carbon conversion coefficient for ecosystem type i.

TABLE 1 C values of different land cover types.

Land cover type	Vegetation cover (%)					
	<10	10–30	30–50	50–70	70–90	>90
Grassland	0.45	0.24	0.15	0.09	0.043	0.011
Forest	0.10	0.08	0.06	0.02	0.004	0.001
Shrub	0.40	0.22	0.14	0.085	0.040	0.011

TABLE 2 Surface runoff coefficients for different grassland types.

Grassland ecosystem type	α
Meadow	8.2
Grassland	4.78
Grass	9.37

3.5. Habitat provision

Reflected by the biological habitat quality index, the regional biodiversity was evaluated in this project mainly in terms of regional habitat quality and habitat scarcity, which were obtained using the INVEST model calculation (Aneseyee et al., 2020; Wu et al., 2021). The calculation formula is as follows:

3.5.1. Site quality

$$D_{xj} = \sum_{r=1}^{R}\sum_{y=1}^{Y_r}\left(\frac{w_r}{\sum_{r=1}^{R} w_r}\right) r_y i_{rxy} \beta_x S_{jr} \tag{22}$$

$$i_{rxy} = 1 - \left(\frac{d_{xy}}{d_{r\max}}\right) \tag{23}$$

$$i_{rxy} = \exp\left(-\left(\frac{2.99}{d_{r\max}}\right) d_{xy}\right) \tag{24}$$

where, D_{xj} is the total stress level of raster x in LULC or habitat type j; w_r is the weight of the stressor, indicating the relative destructive power of a given stressor on all habitats; β_x is the reachability level of the raster x; S_{jr} is the sensitivity of habitat type j to stress factor r. If $S_{jr} = 0$, then D_{xj} is not a function of threat r; r_y is the stress factor in raster y; i_{rxy} is the stress effect of the stress factor r in raster x on raster y. The stress effect is divided into linear decay and exponential decay. d_{xy} is the linear distance between the raster x and y. $d_{r\max}$ is the maximum action distance of the threat r.

3.5.2. Habitat scarcity

$$R_x = \sum_{x=1}^{X} \sigma_{xy}\left(1 - \frac{N_j}{N_{jbaseline}}\right) \tag{25}$$

where R_x is the scarcity of the raster x; N_j is the number of grids of current land use and land cover j. $N_{jbaseline}$ is the number of LULC type j grids in the baseline landscape pattern. σ_{xy} is a binary number, $\sigma_{xy} = 1$ when the raster x is of LULC type j, otherwise σ_{xy} is 0.

3.6. Quantification of ES trade-offs and synergies

Synergies between two ES occur when an enhancement of one ES leads to an increase in another ES (Bennett et al., 2009). While, Trade-offs between two ES occur when one ES is promoted at the expense of the other (Rodriguez et al., 2006). In addition to trade-offs and synergies, there is also a neutral category, which means that an increase in one ES does not result in an increase or decrease in the other. A negative correlation coefficient for two ES that passes the significance test is considered a trade-off, while a positive correlation coefficient that passes the significance test is considered a synergy relationship (Jopke et al., 2015). NSB is composed of three sub-barriers. A certain ES has spatial heterogeneity in each sub-barrier, and this spatial distribution pattern may produce trade-offs and synergies in the whole area. Therefore, this paper used pixel-by-pixel (resampling to align the raster) spatial correlation analysis to calculate the correlation coefficients between ES pairs for five periods from 2000 to 2020 in the study area and conducts significance tests (Figure 2).

Based on the pixel-by-pixel spatial correlation analysis is method-Pearson product–moment correlation coefficient method (Mukaka, 2012). The correlation coefficients between the two groups of ES were calculated separately, and the trade-offs and synergies between the ES were measured based on the positive and negative correlation coefficients and the absolute magnitude of the relationship. The formula is as follows:

$$R = \frac{\sum(x_i - \bar{x})\sum(y_i - \bar{y})}{\sqrt{\sum(x_i - \bar{x})^2 \sum(y_i - \bar{y})^2}} \tag{26}$$

where, R is the correlation coefficient, if R is positive, the relationship between two services is synergistic, and vice versa is a trade-off. If R is zero, there is no relationship, and a larger absolute value indicates a stronger correlation, i.e., a greater degree of synergy or trade-off. x and y are the two ES variables; i is the i-th year.

Significance of trade-offs and synergies between ES determined by t-test (Niu et al., 2022). The formula is as follows:

$$T = \frac{R}{\sqrt{\frac{1 - R^2}{n - 2}}} \tag{27}$$

The significance of the interrelationships between ES was judged based on the null hypothesis test t-test of the correlation coefficient. When $|T| < T_{0.05,\,3}$, i.e., $p > 0.05$, the original hypothesis is valid and the correlation result is not significant. When $T_{0.05,\,3} \leq |T| < T_{0.01,\,3}$, i.e., $0.01 < p \leq 0.05$, rejection of the original hypothesis and more significant correlation results. When $|T| \geq T_{0.01,\,3}$, i.e., $p \leq 0.01$, the original hypothesis was rejected and the correlation result was highly significant.

4. Results

4.1. Spatial variations in ecosystem services

Figure 3 shows the spatial distribution of ES. High values of soil conservation service are clustered in the southern part of IM, while low values of soil conservation service are mainly distributed in the west and the plains between HC and IM. Not only the forests and grasslands in eastern IM and eastern HC, but also parts of the cropland in TB show a high carbon sequestration supply. The lower carbon sequestration service supply is mainly found in the TB and desert areas at both ends of the HC. The high sand-stabilization service is distributed in the northern part of IM and the grassland between IM and HC, and the rest of the area had low

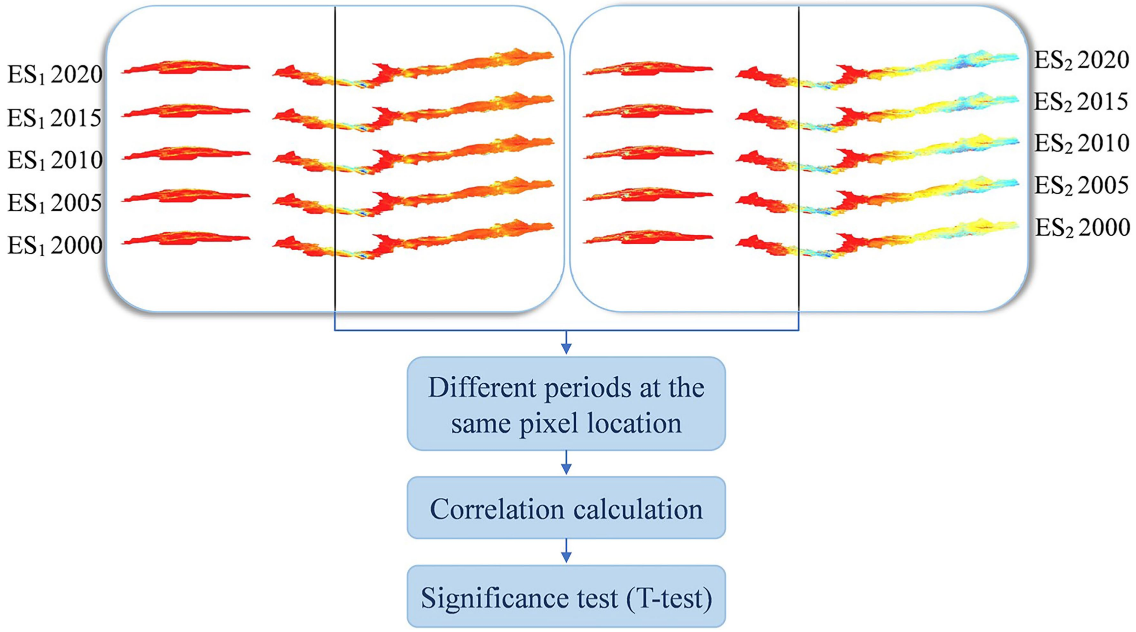

FIGURE 2
Technical processes of the correlation calculation.

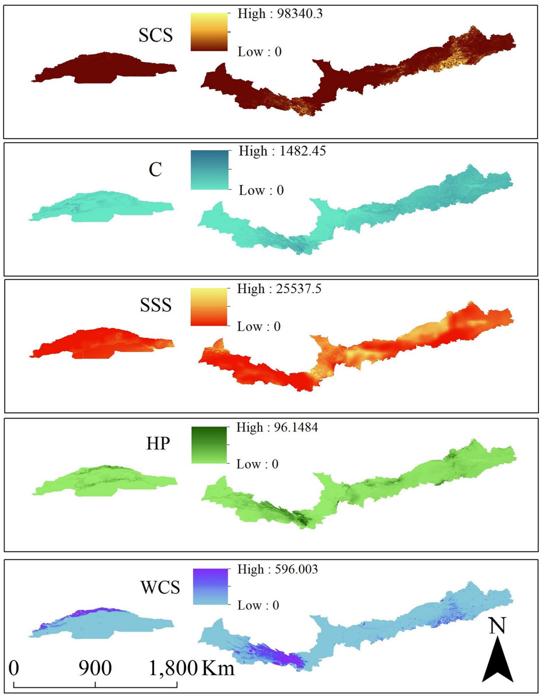

FIGURE 3
Spatial distribution of the carbon sequestration service (C, t/km^2·a), sand-stabilization service (SSS, t/km^2·a), water conservation service (WCS, t/km^2·a), soil conservation service (SCS, t/km^2·a), and habitat provision (HP, the value is scaled by a factor of 100) in the NSB.

sand-stabilization service values. The high habitat provision values are mainly distributed in the eastern part of HC where the elevation changes are dramatic, and low habitat provision is generally distributed in grassland and desert areas. The water conservation service in the study area is generally small, but the values of the water conservation service are high in lakes and high-altitude mountain areas.

4.2. Distribution of ecosystem services along different gradients of precipitation and fractional vegetation cover

The distribution of five ES in the study area is inhomogeneous, showing obvious differences in the precipitation gradient and the FVC gradient. We made statistics on the distribution of precipitation gradient, as shown in Figure 4. 33.80–78.10% of the total amount of the five ES are mainly distributed in areas with precipitation greater than 400 mm, followed by areas with precipitation of 200–400 mm. The areas with precipitation in the range of 0–200 mm are the least, accounting for 4.43–33.80% of the total amount of ES. It shows that ES increases with increased precipitation. Figure 5 shows the distribution of five ES across the FVC gradient, which is not obvious compared to the distribution characteristics of the precipitation gradient. The total distribution of habitat provision and carbon sequestration service in the three gradients is basically the same. The soil conservation service is mainly distributed in areas of FVC greater than 0.6. On the contrary, sand-stabilization service and water conservation service are mainly distributed in areas with FVC less than 0.3. From the perspective of ES per unit area, except soil conservation service and water conservation service, other ES increases with the increase of FVC. When the FVC range is 0.3–0.6, the soil conservation service and water conservation service per unit area reach the maximum.

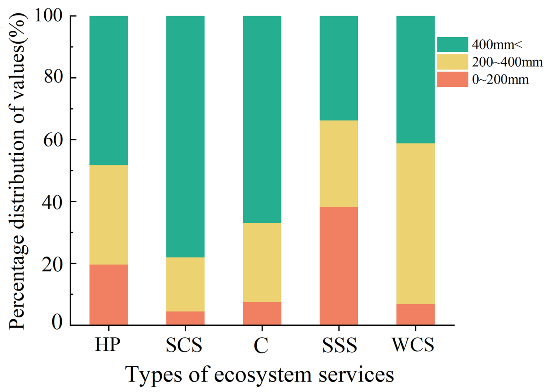

FIGURE 4
Spatial distribution pattern of the precipitation gradient.

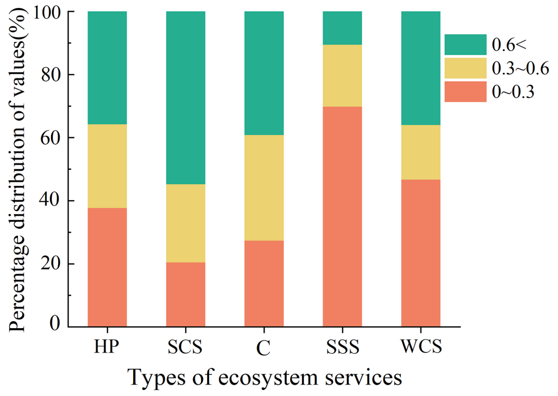

FIGURE 5
Spatial distribution pattern of fractional vegetation cover (FVC).

4.3. Ecosystem service trade-offs and synergies

Figure 6 shows the areas where synergies and trade-offs occur between the five ecosystem services. As shown in Table 3. The synergy between sand-stabilization service and habitat provision accounts for 86.67% of the study area, and the significant synergy accounts for 49.08% of the study area. Synergy, especially significant synergy, is widely distributed in the study area, but the trade-off area only accounts for 2.73%. The significant synergy/trade-off between sand-stabilization service and soil conservation service is staggered in the east of IM, and the significant synergy area (13.54%) is larger than the significant trade-off area (3.91%). The area of trade-off between soil conservation service and habitat provision is the largest among the 10 relationships (34.52%), mainly distributed in HC and TB areas with weak trade-off relationship. The synergy between sand-stabilization service and carbon sequestration service accounts for 43.52% of the study area, and the remarkable synergy is clustered and distributed in the east of the study area. The distribution of habitat provision and carbon sequestration service is similar to that of sand-stabilization service and carbon sequestration service. The unconnected relationship with carbon sequestration service and soil conservation service (43.97%) is distributed in the southern part of TB, the western part of HC, the plain between HC and IM, and the land use type is desert. The significant synergy/trade-off relationship are staggered in the eastern part of the study area. The four relationships between sand-stabilization service and water conservation service, carbon sequestration service and water conservation service, soil conservation service and water conservation service, habitat provision, and water conservation service are the relationships between water conservation service and other four ES. Obviously, the relationships including water conservation service services, unrelated relationships all account for more than 75% of the study area. Apart from the forests and grasslands in the middle of HC, the forests and grasslands in the southeast of IM, and the forests and grasslands in the north of TB, unrelated relationships are widely distributed in grasslands and deserts in the study area.

Since the unrelated area accounts for most of the total study area, the relationship between the two ES is better captured in terms of the area ratio of synergies to trade-offs when exploring the trade-offs between ES. The ratio of synergy to trade-off between sand-stabilization service and habitat provision was 31.74: 1, and the area of significant synergy represented 49.08% of the total area of the study area. The ratio of synergy to trade-off between carbon sequestration service and water conservation service was 21.53: 1. The area of significant synergy accounted for 9.45% of the total area of the study area, while the area of significant trade-off accounted for only 0.01% of the total area of the study area. In terms of the area ratio of synergy to trade-off, the synergy area was greater than the trade-off area in all 10 ES pairs, with an average ratio of 8.85:1.

4.4. Response of ecosystem services trade-offs and synergies on precipitation gradient

See Figures 7, 8. As precipitation increased, trade-offs and synergies between 10 paired ES increased, while their trade-offs decreased. Specifically, the synergies between soil conservation service and habitat provision, sand-stabilization service and habitat provision, and sand-stabilization service and soil conservation service all exceeded 80% of the study area. And their distribution pattern was consistent with the precipitation gradient. Trade-offs and synergies between pairs of ES, including water conservation service (habitat provision and water conservation service, soil conservation service and water conservation service, carbon sequestration service and water conservation service, and sand-stabilization service and water conservation service) were mainly distributed in the northern end of TB, central HC, and central and eastern IM, accounting for only 16.21–24.10% of the study area. However, note that the uncorrelated relationships between these paired ES were widely distributed throughout the study area. Nonetheless, the synergies still account for the vast majority in different precipitation gradients, and the synergies between paired ES also increase with the increase of precipitation. For sand-stabilization service and carbon sequestration service, carbon sequestration service and soil conservation service, and carbon sequestration service and habitat provision, the trade-offs and synergies between these ES pairs accounted for about 50–60% of the study area, and again, synergy effects dominate. Similarly, synergies accounted for the majority, which were mainly distributed in IM and scattered in TB and HC. Trade-offs and synergies did not exist in

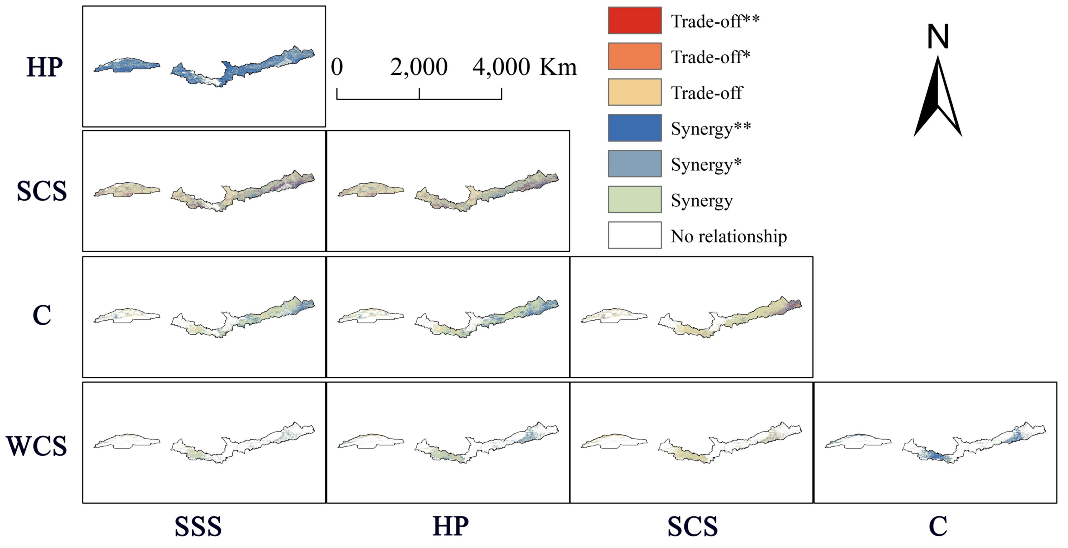

FIGURE 6
Trade-offs and synergistic salience of ecosystem services. *At a level of 0.05 (two-tailed), the correlation is significant; **At a level of 0.01 (two-tailed), the correlation is very significant.

TABLE 3 Significance of trade-offs and synergies of ecosystem service (%).

	No relationship	Synergy	Synergy*	Synergy**	Trade-off	Trade-off*	Trade-off**
SSS_WCS	83.80	9.76	3.24	1.16	1.85	0.11	0.07
SSS_C	50.44	29.19	10.25	4.07	5.70	0.29	0.05
SSS_SCS	19.21	26.06	9.58	13.54	22.72	4.98	3.91
SSS_HP	10.60	15.37	22.22	49.08	2.41	0.23	0.09
C_WCS	80.21	5.00	4.45	9.45	0.81	0.05	0.01
C_SCS	43.97	26.25	6.26	2.59	17.94	2.23	0.77
C_HP	42.74	32.09	13.71	5.03	6.09	0.28	0.06
SCS_WCS	75.92	11.29	2.23	0.81	8.67	0.86	0.23
SCS_HP	10.60	29.74	10.77	14.38	26.54	5.64	2.34
HP_WCS	76.09	11.96	5.71	3.20	2.87	0.14	0.04

C, carbon sequestration service; SSS, sand-stabilization service; WCS, water conservation service; SCS, soil conservation service; and HP, habitat provision.

about 40–50% of the areas, which were mainly desert areas. Among the 10 paired ES, sand-stabilization service and water conservation service changed most obviously with the gradient of precipitation. In the annual precipitation range of 0–200 mm, the area ratio of trade-offs and synergies was 4.23, while in the annual precipitation range of 400 mm <, it reached 24.59. Compared with other paired ES, the synergies of sand-stabilization service and habitat provision accounted for the largest proportion of each gradient area, indicating that in arid and semi-arid regions, increasing biodiversity can promote more sand-stabilization service in ecosystems. In addition, the ES pairs containing soil conservation service had the smallest synergies than other paired ES, indicating that it was more difficult to play the synergy between ES pairs containing soil conservation service than other paired ES, but with the increase of precipitation, this gap will be reduced. Although less than 20% of the regions have trade-offs and synergies between carbon sequestration service and water conservation service, the ratio of synergy and trade-off is close to sand-stabilization service and habitat provision in each precipitation gradient. The study showed that the synergy between ES was greater in areas with more precipitation, and this ratio increased with increasing precipitation.

4.5. Response of ecosystem services trade-offs and synergies on fractional vegetation cover gradients

We compared the trade-offs and synergies of ES along the FVC, See Figures 8, 9. Similarly to the change in trade-offs and synergies between paired ES with precipitation gradients, as the FVC increased, the synergies between other paired ES increased except sand-stabilization service and habitat provision. Furthermore, the distribution law of soil conservation service and habitat provision, sand-stabilization service and habitat provision, and sand-stabilization

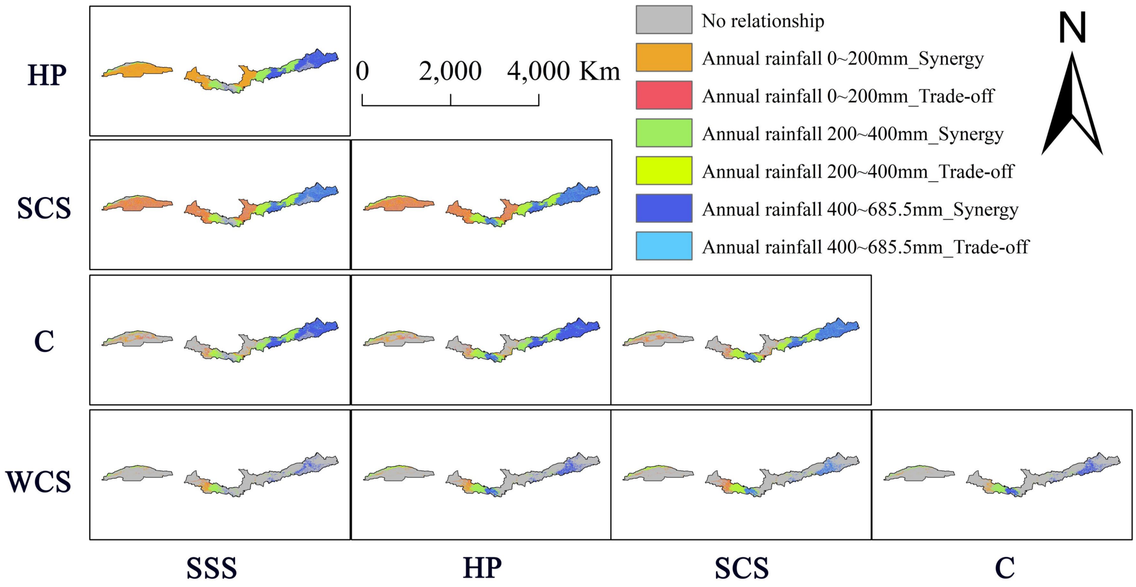

FIGURE 7
Ecosystem service synergies and trade-offs with precipitation gradients.

service and soil conservation service, as well as the various characteristics of the trade-offs and synergies with FVC of paired ES containing water conservation service and carbon sequestration service, respectively, were also similar to those between pairs of ES and precipitation gradient. Nonetheless, along the FVC, there were some different regularities in the trade-offs and synergies relationship between paired ES. Compared with other paired ES, the synergy of sand-stabilization service and habitat provision accounted for the largest proportion of each gradient area, indicating that in arid and semi-arid regions, increasing biodiversity can promote more sand-stabilization service in ecosystems. However, FVC had little effect on this synergy, and the synergy of sand-stabilization service and habitat provision did not increase with the increase of FVC. Although less than 20% of the regions had trade-off and synergy between carbon sequestration service and water conservation service, the ratio of synergy and trade-off is close to sand-stabilization service and habitat provision in each FVC gradient. It showed that in areas with low FVC, the synergy between ES was less, with the increase of FVC, its proportion was increasing. However, with the change of FVC, paired ES has a different trend. As FVC increases, the synergy of carbon sequestration service and water conservation service increases. This shows that increasing FVC in arid and semi-arid regions can first increase carbon sequestration, and in some regions can increase water conservation service through synergy effects.

5. Discussion

5.1. Trade-offs and synergies of paired ecosystem services in different land use and land cover

Previous studies suggest that land use/land cover affect trade-offs and synergies between paired ecosystems (Hasan et al., 2020; Liu et al., 2022). We also investigated the characteristics of the trade-offs and synergies of paired ES across different land uses and land covers (Figure 10). Among the eight land use/land cover, except that the trade-off values of sand-stabilization service and water conservation service and soil conservation service and water conservation service in the impervious is larger, paired ES has been synergy dominant in other land use types. However, the same paired ES differed among different land use types. Contrary to Shao et al. (2020), research that different spaces in the same LULC will have different effects on ES there are also differences in the performance of different ES in the same land use/land cover. The research of Vigl et al. (2017) also shows that land management types and biophysical conditions make the provision of ES unstable. In forests, grasslands, and barrens, sand-stabilization service and habitat provision have greater synergies than other paired ES. This finding has practical implications, suggesting that through anthropogenically increased vegetation cover (i.e., afforestation), similar benefits may be expected for other paired ES, while the synergy of sand-stabilization service and habitat provision may increase more in multiple paired ES. And this result also shows that with the emphasis on biodiversity, sand-stabilization service gains the most synergy from it. This is of great significance to protect wildlife and reduce soil wind erosion. In shrub areas, water conservation service and carbon sequestration service have greater synergy than other paired ES. In semi-arid and arid regions, these types of land use have better hydrothermal conditions, and increasing carbon sequestration service can promote the synergy growth of other ES. The finding is unexpected, but has practical implications, as low shrubs produce more ecological benefits than tall trees in semi-arid and arid regions. Adding low shrubs can first increase carbon sequestration service, and it is beneficial to reduce surface wind speed, reduce wind erosion, and can also increase habitat provision growth through synergy. However, it is more significant that in

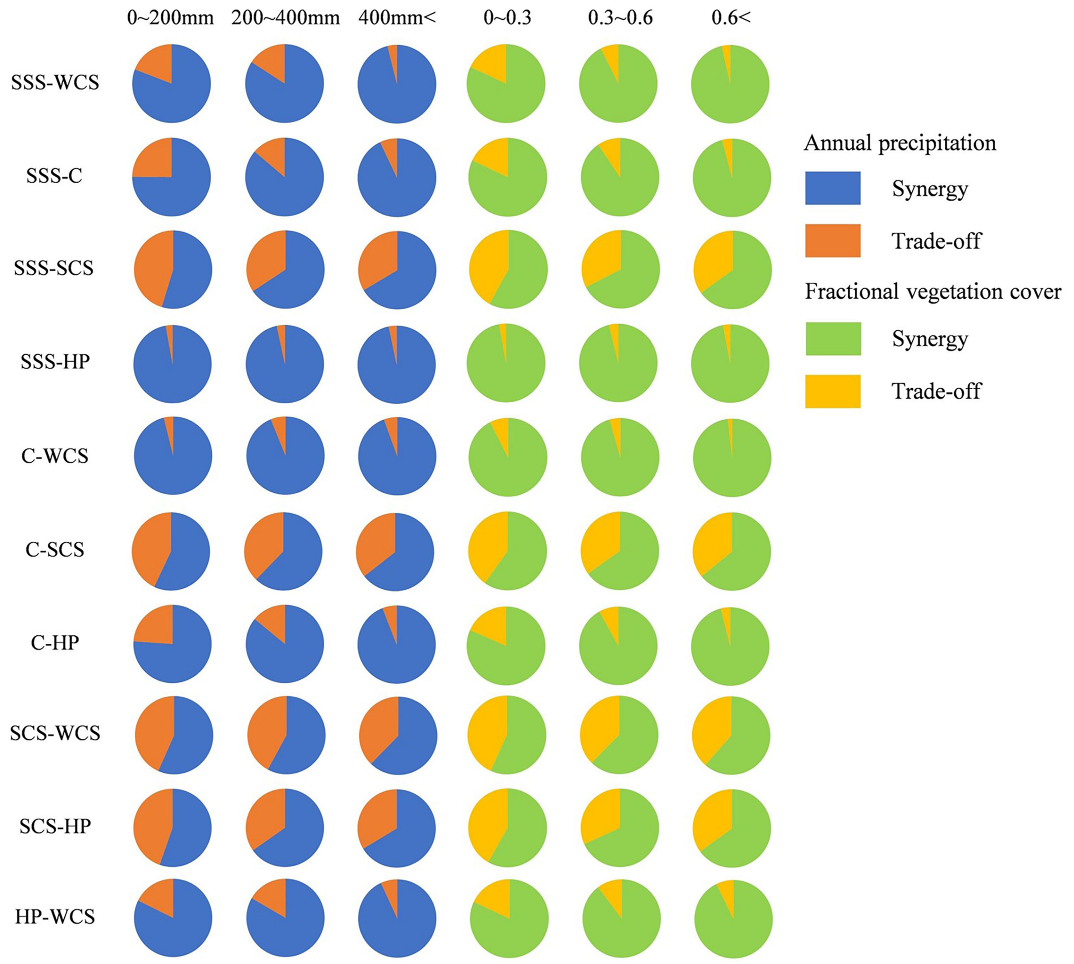

FIGURE 8
The ratio of synergies to trade-offs at different gradients. SSS-WCS indicates the relationship between sand-stabilization service and water conservation service.

precipitation-limited arid and semi-arid regions, the transpiration and actual evapotranspiration of low shrubs are lower than those of tall trees (Zhang and Huang, 2013), and low shrubs can produce more water conservation service. Therefore, in arid and semi-arid regions, in an attempt to improve the ecological environment through artificially increased vegetation coverage, appropriate vegetation types should be selected according to the target (the type of ES expected to be improved). For example, in desert-dominated NSB, by improving the sand-stabilization service of the ecosystem to control desert expansion, the choice of planting trees and grasses may reap more benefits. In smaller areas, such as cities, adding shrubs may be more appropriate. Therefore, in order to make better use of the synergistic effect of paired ES and improve the ecological environment, the trade-off between trees/grass and shrubs is very important.

Through the above analysis of LULC, increasing the greenness of land is the most effective way to increase the synergy relationship among ecosystem services. For managers, it is the most effective and scientific management measure to continuously promote desertification control and increase vegetation cover in the Northern Sand-stabilization Belt area.

5.2. Variations in trade-offs and synergies for paired ecosystem services in northern sand-stabilization belt

From the precipitation distribution, 46.31% of the study area in 2020 has less than 200 mm of annual precipitation, which is an arid region. The precipitation distribution is similar to FVC, which gradually decreases from east to west. However, there are higher precipitation and FVC values in the middle of the HC. In TB region, precipitation increases with increasing altitude. Paired ES have different sensitivities to vegetation cover and precipitation due to differences in distribution patterns. Compared with precipitation, there are more pairwise synergistic changes in the effect of FVC. For example, among the 10 ES pairs, the synergy between sand-stabilization service and water conservation service, sand-stabilization service and carbon sequestration service, carbon sequestration service and water conservation service, carbon sequestration service and habitat provision increased significantly with increasing FVC. Because in arid and semi-arid regions, high evaporation and low precipitation are the norms (Yin et al., 2005). Vegetation can increase surface roughness and shade and reduce surface evaporation, wind erosion,

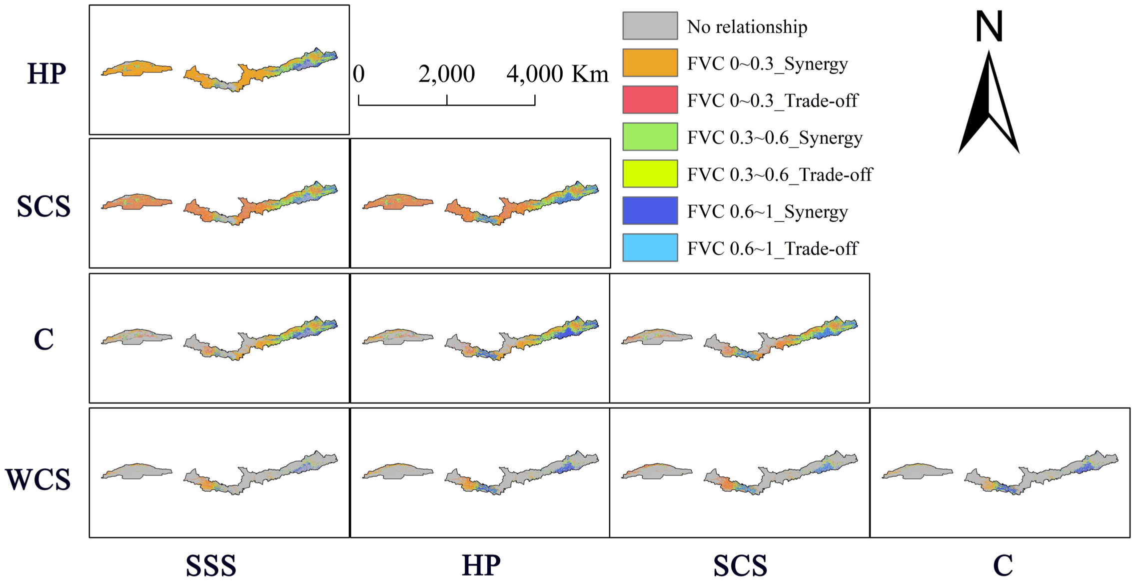

FIGURE 9
Ecosystem service synergies and trade-offs with changes in fractional vegetation cover gradients.

and water erosion. Synergy of ES pairs that increase with precipitation is only sand-stabilization service and soil conservation service. The study by Zhang et al. (2022) shows the high contribution of climatic factors to vegetation recovery in northern China. Wang X. et al. (2022) showed that a 30% increase in precipitation in desert areas stimulated the growth of *sophora alopecuroides*, *stipa breviflora*, *pennisetum centrasiaticum*, and other species. Thus, increased precipitation indirectly contributes to the synergy of sand-stabilization service and soil conservation service through increase vegetation. Due to the high overlap between the distribution of precipitation and FVC, the other four ES pairs were not differently affected by precipitation and FVC.

5.3. Limitations and implications

There are some limitations to this study. Uncorrelated relationships between pairs of ES account for a large proportion, especially for ES pairs containing water conservation service. We analyze the reasons, and the study area is located in northwest China, dominated by deserts and grasslands. While most of the water conservation service values in these areas are 0. When exploring the trade-offs and synergies between water conservation service and other ES, the correlation coefficient will be 0, resulting in a large area of irrelevant relationships. When the value of a certain ES of a grid is zero in five periods, then the relationship between this ES and other ES is irrelevant. There is also a situation that when the value of a certain ES does not change for five periods, it will also get an irrelevant result with other ES calculations. In addition, the interpolation method and resolution of the underlying data are also important influencing factors. For example, the uncorrelated relationships of sand-stabilization service and soil conservation service, carbon sequestration service and soil conservation service, soil conservation service and water conservation service, and soil conservation service and habitat provision are distributed in the eastern part of the study area in a grid-like form. The reason for this phenomenon may be that the grid meteorological data obtained by spatial interpolation is used in estimating soil conservation service. As far as the research content is concerned, this study only evaluated 5 ES, and did not evaluate other important ES (such as crop production and climate control). The estimation model involves a limited number of factors, and the model itself has some inaccuracies. In future studies, in addition to further investigating and addressing these limitations, we will also explore the driving mechanism of ES trade-off and synergy and the model of the relationship between its sustainability, so as to better provide information for ecosystem management measures, so as to achieve the goal of harmonious development between man and nature.

6. Conclusion

This paper selected the northern sand-stabilization belt, which is located in northwest China, as the study area. The results of this study provide us with a new understanding of arid and semi-arid (or macro-regional) ecosystems and formulate more reasonable ecosystem management and protection measures in NSB.

In this study, we used multi-source data and multiple indicators to evaluate the changes of ES in the NSB, the results show that there was a clear heterogeneity in the distribution of ES, with soil conservation service mainly distributed in the eastern part of HC and the southeastern part of IM; the distribution of sand-stabilization service had a high overlap with areas where the land cover type was desert and grassland; carbon sequestration service distribution is closely related to FVC; habitat provision showed higher values in places with drastic elevation changes; the values of water conservation service were related to the distribution of lakes and snow-capped mountains.

However, this article mainly focused on assessing the trade-offs and synergies of five ESs, especially across the precipitation and vegetation cover fraction gradient. The trade-offs and synergies among multiple ES were widespread in NSB, but synergies account for

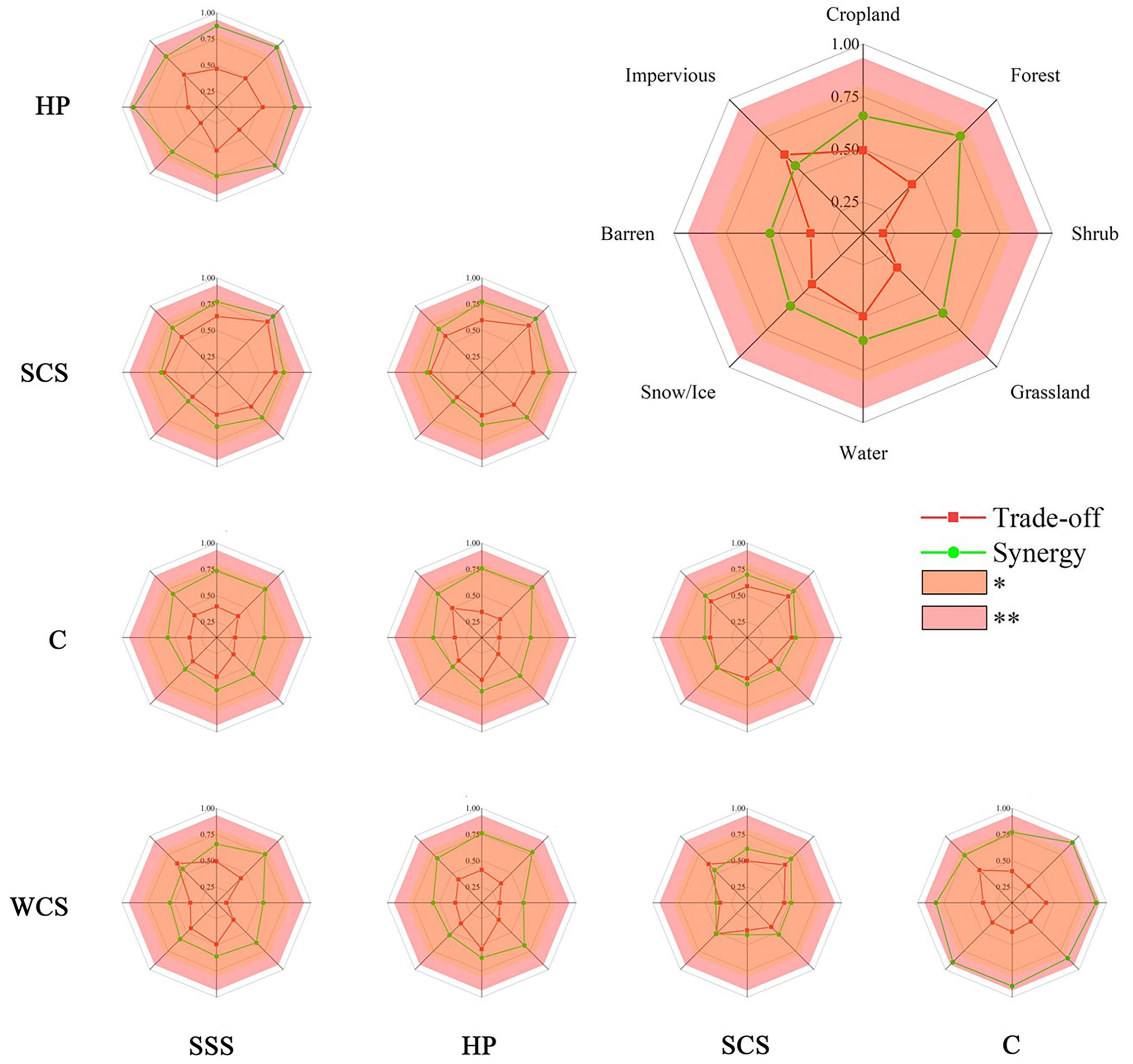

FIGURE 10
Synergies and trade-offs of ecosystem services in different land use/land cover. *At a level of 0.05 (two-tailed), the correlation is significant; **At a level of 0.01 (two-tailed), the correlation is very significant. The upper right corner is the legend. This result eliminates land use/land cover that are too small in area, and retains only eight land use/land cover.

a larger proportion. Changes in FVC and precipitation gradients could strongly enhance and weaken the trade-offs and synergies of some paired ES. The synergy between most paired ES increased significantly with increasing precipitation and FVC. However, pairwise ES have different sensitivities to FVC and precipitation, and there are more synergistic changes in paired ES for FVC effects than for the effects of precipitation. For example, the synergy and trade-off area ratio between sand-stabilization service and water conservation service in areas with less than 200 mm annual precipitation compared to those with more than 400 mm annual precipitation changed from 4.23 to 24.59, the synergy and trade-off area ratio changed from 4.53 to 27.46 for areas with FVC less than 0.3 compared to greater than 0.6. The study found that type of land use may be an important driving factor for trade-offs and synergies between paired ES. In arid and semi-arid areas, some measures such as planting trees and grass, are often taken to improve the ecological environment. To fully exploit the synergistic effect of paired ES, our research suggests that in improving the ecological environment through artificially increased vegetation coverage, appropriate vegetation types should be selected according to the target (the type of ES expected to be improved).

Data availability statement

The raw data supporting the conclusions of this article will be made available by the authors, without undue reservation.

Author contributions

CW and KS: conceptualization, methodology, formal analysis, and writing-original draft preparation. CW: software. XZ, ZY, and ZC: validation. KS: resources, supervision, project administration, and funding acquisition. LW, CW, ZL, and YZ: data curation and visualization. KS, XJ, and YY: writing-review and editing. All authors contributed to the article and approved the submitted version.

Funding

This research is supported by the National Natural Science Foundation of Guangxi (2022GXNSFBA035570) and High-level Talents Project of Guangxi University (A3360051018).

Acknowledgments

Acknowledgement for the data support from "Loess plateau science data center, National Earth System Science Data Sharing Infrastructure, National Science & Technology Infrastructure of China (http://loess.geodata.cn)."

Conflict of interest

ZC is employed by Guizhou Linfa Survey and Design Co., Ltd.

The remaining authors declare that the research was conducted in the absence of any commercial or financial relationships that could be construed as a potential conflict of interest.

Publisher's note

References

Aneseyee, A. B., Noszczyk, T., Soromessa, T., and Elias, E. (2020). The InVEST habitat quality model associated with land use/cover changes: a qualitative case study of the Winike watershed in the Omo-Gibe Basin, Southwest Ethiopia. *Remote Sens.* 12. doi: 10.3390/rs12071103

Bennett, E. M., Peterson, G. D., and Gordon, L. J. (2009). Understanding relationships among multiple ecosystem services. *Ecol. Lett.* 12, 1394–1404. doi: 10.1111/j.1461-0248.2009.01387.x

Cao, S. X., Chen, L., and Yu, X. X. (2009). Impact of China's grain for green project on the landscape of vulnerable arid and semi-arid agricultural regions: a case study in northern Shaanxi Province. *J. Appl. Ecol.* 46, 536–543. doi: 10.1111/j.1365-2664.2008.01605.x

Costanza, R., Darge, R., Degroot, R., Farber, S., Grasso, M., Hannon, B., et al. (1997). The value of the world's ecosystem services and natural capital. *Nature* 387, 253–260. doi: 10.1038/387253a0

Deng, H., Dan, L., Wang, Q., Yang, X., and Yang, F. (2020). Simulations of the impact of climate and vegetation cover changes on carbon and water cycles of a Subalpine Basin in the mountain region of southwestern China. *Climat. Environ. Res.* 25, 19–31. doi: 10.3878/j.issn.1006-9585.2019.18068

Dumanski, J., and Pieri, C. (2000). Land quality indicators: research plan. *Agric. Ecosyst. Environ.* 81, 93–102. doi: 10.1016/s0167-8809(00)00183-3

Fang, J. Y., Chen, A. P., Peng, C. H., Zhao, S. Q., and Ci, L. (2001). Changes in forest biomass carbon storage in China between 1949 and 1998. *Science* 292, 2320–2322. doi: 10.1126/science.1058629

Felton, A. J., Slette, I. J., Smith, M. D., and Knapp, A. K. (2020). Precipitation amount and event size interact to reduce ecosystem functioning during dry years in a Mesic grassland. *Glob. Chang. Biol.* 26, 658–668. doi: 10.1111/gcb.14789

Fensholt, R., Langanke, T., Rasmussen, K., Reenberg, A., Prince, S. D., Tucker, C., et al. (2012). Greenness in semi-arid areas across the globe 1981-2007—an earth observing satellite based analysis of trends and drivers. *Remote Sens. Environ.* 121, 144–158. doi: 10.1016/j.rse.2012.01.017

Fryrear, D. W., Bilbro, J. D., Saleh, A., Schomberg, H., Stout, J. E., and Zobeck, T. M. (2000). RWEQ: improved wind erosion technology. *J. Soil Water Conserv.* 49, 485–505. doi: 10.1006/jare.2001.0807

Fu, B., Wang, X., and Feng, X. (2017). *National Ecological Barrier Area Ecosystem Assessment*. Beijing: Science Press

Gao, Y., Xie, Y., Qian, D., Zhang, L., and Gong, J. (2015). Dynamic variations of vegetation coverage and landscape pattern in Bailongjiang Basin of southern Gansu. *Res. Soil Water Conserv.* 22, 181–187. doi: 10.13869/j.cnki.rswc.2015.01.035

Gao, J., Yang, X., Dong, C., and Li, K. (2015). Precipitation resource changed characteristics in arid and humid regions in northern China with climate changes. *Trans. Chin. Soc. Agric. Eng.* 31, 99–110. doi: 10.11975/j.issn.1002-6819.2015.12.014

Gherardi, L. A., and Sala, O. E. (2019). Effect of interannual precipitation variability on dryland productivity: a global synthesis. *Glob. Chang. Biol.* 25, 269–276. doi: 10.1111/gcb.14480

Hasan, S. S., Zhen, L., Miah, M. G., Ahamed, T., and Samie, A. (2020). Impact of land use change on ecosystem services: a review. *Environ. Dev.* 34:100527. doi: 10.1016/j.envdev.2020.100527

Heisler-White, J. L., Knapp, A. K., and Kelly, E. F. (2008). Increasing precipitation event size increases aboveground net primary productivity in a semi-arid grassland. *Oecologia* 158, 129–140. doi: 10.1007/s00442-008-1116-9

Hu, H., and Liu, G. (2006). Carbon sequestration of China's National Natural Forest Protection Project. *Acta Ecol. Sin.* 26, 291–296.

Huang, S. W., and Kong, J. M. (2016). Assessing land degradation dynamics and distinguishing human-induced changes from climate factors in the three-north shelter Forest region of China. *ISPRS Int. J. Geo Inf.* 5. doi: 10.3390/ijgi5090158

Huxman, T. E., Cable, J. M., Ignace, D. D., Eilts, J. A., English, N. B., Weltzin, J., et al. (2004). Response of net ecosystem gas exchange to a simulated precipitation pulse in a semi-arid grassland: the role of native versus non-native grasses and soil texture. *Oecologia* 141, 295–305. doi: 10.1007/s00442-003-1389-y

Johns, G., Lee, D. J., Leeworthy, V., Boyer, J., and Nuttle, W. (2014). Developing economic indices to assess the human dimensions of the South Florida coastal marine ecosystem services. *Ecol. Indic.* 44, 69–80. doi: 10.1016/j.ecolind.2014.04.014

Jopke, C., Kreyling, J., Maes, J., and Koellner, T. (2015). Interactions among ecosystem services across Europe: Bagplots and cumulative correlation coefficients reveal synergies, trade-offs, and regional patterns. *Ecol. Indic.* 49, 46–52. doi: 10.1016/j.ecolind.2014.09.037

Knapp, A. K., and Smith, M. D. (2001). Variation among biomes in temporal dynamics of aboveground primary production. *Science* 291, 481–484. doi: 10.1126/science.291.5503.481

Liao, Z. H., Su, K., Jiang, X. B., Zhou, X. B., Yu, Z., Chen, Z. C., et al. (2022). Ecosystem and Driving Force Evaluation of Northeast Forest Belt. *Land* 11. doi: 10.3390/land11081306

Li, G., Zhao, W., Zhao, Y., Fang, X., Gao, B., and Dai, L. (2015). Evaluation on the influence of natural forest protection program on forest ecosystem service function in changbai mountain. *Acta Ecol. Sin.* 35, 984–992. doi: 10.5846/stxb201304240799

Liu, M. X., Dong, X. B., Wang, X. C., Zhao, B. Y., Wei, H. J., Fan, W. G., et al. (2022). The trade-offs/synergies and their spatial-temporal characteristics between ecosystem services and human well-being linked to land-use change in the capital region of China. *Landscape* 11. doi: 10.3390/land11050749

Liu, X., Liu, C., Chen, L., Pei, S., and Qiao, Q. (2020). Gradient effects and ecological zoning of ecosystem services in transition zone of Beijing Bay. *Trans. Chin. Soc. Agric. Eng.* 36, 276–285. doi: 10.11975/j.issn.1002-6819.2020.12.033

Liu, X., and Ren, Z. (2012). Vegetation coverage change and its relationship with climate factors in Northwest China. *Sci. Agric. Sin.* 45, 1954–1963. doi: 10.3864/j.issn.0578-1752.2012.10.008

Liu, L., Wang, Z., Wang, Y., Zhang, Y., Shen, J., Qin, D., et al. (2019). Trade-off analyses of multiple mountain ecosystem services along elevation, vegetation cover and precipitation gradients: a case study in the Taihang Mountains. *Ecol. Indic.* 103, 94–104. doi: 10.1016/j.ecolind.2019.03.034

Liu, S., Yan, D., Shi, X., and Yuan, Z. (2014). Inter-annual variability of vegetation NDVI，accumulated temperature and precipitation and their correlations in China. *Arid Land Geogr.* 37, 480–489. doi: 10.13826/j.cnki.cn65-1103/x.2014.03.008

Loomis, D. K., and Paterson, S. K. (2014). Human dimensions indicators of coastal ecosystem services: a hierarchical perspective. *Ecol. Indic.* 44, 63–68. doi: 10.1016/j.ecolind.2013.12.022

Malekmohammadi, B., and Jahanishakib, F. (2017). Vulnerability assessment of wetland landscape ecosystem services using driver-pressure-state-impact-response (DPSIR) model. *Ecol. Indic.* 82, 293–303. doi: 10.1016/j.ecolind.2017.06.060

Mukaka, M. M. (2012). Statistics corner: a guide to appropriate use of correlation coefficient in medical research. *Malawi Med. J.* 24, 69–71. PMID: 23638278

Niu, L., Shao, Q., Ning, J., and Huang, H. (2022). Changing ecological conditions and ecosystem service trade-offs and synergies in the Western region. *Acta Geograph. Sin.* 77, 182–195. doi: 10.11821/dlxb202201013

Ouyang, Z., Zheng, H., Xiao, Y., Polasky, S., Liu, J., Xu, W., et al. (2016). Improvements in ecosystem services from investments in natural capital. *Science* 352, 1455–1459. doi: 10.1126/science.aaf2295

Pandey, A., Chowdary, V. M., and Mal, B. C. (2007). Identification of critical erosion prone areas in the small agricultural watershed using USLE, GIS and remote sensing. *Water Resour. Manag.* 21, 729–746. doi: 10.1007/s11269-006-9061-z

Peng, S. Z., Ding, Y. X., Liu, W. Z., and Li, Z. (2019). 1 km monthly temperature and precipitation dataset for China from 1901 to 2017. *Earth Syst. Sci. Data* 11, 1931–1946. doi: 10.5194/essd-11-1931-2019

Piao, S. L., Fang, J. Y., Ciais, P., Peylin, P., Huang, Y., Sitch, S., et al. (2009). The carbon balance of terrestrial ecosystems in China. *Nature* 458, 1009–1013. doi: 10.1038/nature07944

Richards, D. R., and Friess, D. A. (2017). Characterizing coastal ecosystem service trade-offs with future urban development in a Tropical City. *Environ. Manag.* 60, 961–973. doi: 10.1007/s00267-017-0924-2

Rodriguez, J. P., Beard, T. D., Bennett, E. M., Cumming, G. S., Cork, S. J., Agard, J., et al. (2006). Trade-offs across space, time, and ecosystem services. *Ecol. Soc.* 11. doi: 10.5751/ES-01667-110128

Shao, Y. J., Yuan, X. F., Ma, C. Q., Ma, R. F., and Ren, Z. X. (2020). Quantifying the spatial association between land use change and ecosystem services value: a case study in Xi'an, China. *Sustain. For.* 12. doi: 10.3390/su12114449

Sloat, L. L., Gerber, J. S., Samberg, L. H., Smith, W. K., Herrero, M., Ferreira, L. G., et al. (2018). Increasing importance of precipitation variability on global livestock grazing lands. Nature. *Climate Change* 8:214. doi: 10.1038/s41558-018-0081-5

Song, W., and Deng, X. Z. (2015). Effects of urbanization-induced cultivated land loss on ecosystem Services in the North China Plain. *Energies* 8, 5678–5693. doi: 10.3390/en8065678

Su, H., Shen, Y., Han, P., Li, J., and Lan, Y. (2007). Precipitation and its impact on water resources and ecological environment in Xinjiang region. *J. Glaciol. Geocryol.* 29, 343–350. doi: 10.3969/j.issn.1000-0240.2007.03.002

Su, K., Sun, X. T., Guo, H. Q., Long, Q. Q., Li, S., Mao, X. Q., et al. (2020). The establishment of a cross-regional differentiated ecological compensation scheme based on the benefit areas and benefit levels of sand-stabilization ecosystem service. *J. Clean. Prod.* 270:122490. doi: 10.1016/j.jclepro.2020.122490

Sun, H., Wang, C., Niu, Z., Bukhosor, and Li, B. (1998). Analysis of the vegetation cover change and the relationship between NDVI and environmental factors by using NOAA time series data. *J. Remote Sens.* 2, 204–210.

Vigl, L. E., Tasser, E., Schirpke, U., and Tappeiner, U. (2017). Using land use/land cover trajectories to uncover ecosystem service patterns across the Alps. *Reg. Environ. Chang.* 17, 2237–2250. doi: 10.1007/s10113-017-1132-6

Wang, W., and Jiao, J. (1996). Qutantitative evaluation on factors influencing soil erosion in China. *Bull. Soil Water Conserv.* 16, 1–20.

Wang, J., Liu, C., and Zhang, S. (2022). Ecological security pattern of typical counties in northern sand prevention belts. *Acta Ecol. Sin.* 42, 3989–3997. doi: 10.5846/stxb202103280813

Wang, L., Ma, A., Zhang, H., Zhang, J., Dong, Q., and Fu, G. (2020). Effects of Long-Term Vegetation Restoration on Distribution of Deep Soil Moisture in Semi-arid Northwest of China. *J. Soil Sci. Plant Nut.* 20. doi: 10.1007/s42729-020-00280-4

Wang, X., Xu, Y., Li, C., Yu, H., and Huang, J. (2022). Plant biomass, species diversity, and influencing factors in a desert steppe of northwestern China under long-term changing precipitation. *Chin. J. Plant Ecol.*, 1–12. doi: 10.17521/cjpe.2022.0211

Wen, X., Deng, X. Z., and Zhang, F. (2019). Scale effects of vegetation restoration on soil and water conservation in a semi-arid region in China: resources conservation and sustainable for management. *Resour. Conserv. Recycl.* 151:104474. doi: 10.1016/j.resconrec.2019.104474

Wu, L. L., Sun, C. G., and Fan, F. L. (2021). Estimating the characteristic spatiotemporal variation in habitat quality using the InVEST model: A case study from Guangdong-Hong Kong-Macao Greater Bay Area. *Remote Sens.* 13:1008. doi: 10.3390/rs13051008

Yang, S., Hu, S., and Qu, S. (2018). Terrain gradient effect of ecosystem service value in middle reach of Yangtze River. *Chin. J. Appl. Ecol.* 29, 976–986. doi: 10.13287/j.1001-9332.201803.016

Yin, Z., Zhu, Q., Bi, H., and Zhang, J. (2005). Research progress on water consumption characteristics of vegetation in loess plateau. *Yellow River* 27, 35–37.

Yixuan, Z., Yangjian, Z., Zhoutao, Z, Yaojie, L., Zhipeng, W., Nan, C., et al. (2022). Converted vegetation type regulates the vegetation greening effects on land surface albedo in arid regions of China. *Agri. Forest Meteorol.* 324. doi: 10.1016/j.agrformet.2022.109119

Yu, Y. Y., Li, J., Zhou, Z. X., Ma, X. P., and Zhang, X. F. (2021). Response of multiple mountain ecosystem services on environmental gradients: how to respond, and where should be priority conservation? *J. Clean. Prod.* 278:123264. doi: 10.1016/j.jclepro.2020.123264

Zhang, Z. (2017). Study on evaluation of service function change of windbreak and sand-fixing ecosystem in northern sand Prevention Belt. Chang'an University, Available at Cnki

Zhang, L., Dawes, W. R., and Walker, G. R. (2001). Response of mean annual evapotranspiration to vegetation changes at catchment scale. *Water Resour. Res.* 37, 701–708. doi: 10.1029/2000wr900325

Zhang, Y., and Huang, M. (2013). Evapotranspiration characteristics and their influencing factors for arbors and shrubs with different precipitation patterns in loess plateau. *Bull. Soil Water Conserv.* 33, 207–212. doi: 10.13961/j.cnki.stbctb.2013.06.058

Zhang, K., Lyu, Y., Fu, B., Yin, L., and Yu, D. (2020). The effects of vegetation coverage changes on ecosystem service and their threshold in the loess plateau. *Acta Geograph. Sin.* 75, 949–960. doi: 10.11821/dlxb202005005

Zhang, X., Shao, Q., Ning, J., Yang, X., Gong, G., and Liu, G. (2022). Effect of vegetation restoration on soil wind erosion and vegetation restoration potential in the three-north afforestation program. *J. Geo-info. Sci.* 24, 2153–2170. doi: 10.12082/dqxxkx.2022.220060

Zhang, Q., Zhang, L., Cui, X., and Zeng, J. (2011). Progresses and challenges in drought assessment and monitoring. *Adv. Earth Science* 26, 763–778.

Zhang, X., Zhao, W., and Liu, Y. (2017). Application of remote sensing Technology in Research of soil erosion: a review. *Bull. Soil Water Conserv.* 37, 228–238. doi: 10.13961/j.cnki.stbctb.2017.02.035

Zhou, H., Wang, Z., Wang, Z., and Bao, Y. (2021). Response of ecosystem service value of karst Mountainous City to terrain Gradient—A case study of downtown of Guiyang City. *Res. Soil Water Conserv.* 28, 337–347. doi: 10.13869/j.cnki.rswc.2021.06.027

Zhu, P., Liu, X., Zheng, Y., Wang, S., and Huang, L. (2020). Tradeoffs and synergies of ecosystem services in key ecological function zones in northern China. *Acta Ecol. Sin.* 40, 8694–8706. doi: 10.5846/stxb201912172717

Frontiers in Ecology and Evolution

TYPE Original Research
PUBLISHED 27 March 2023
DOI 10.3389/fevo.2023.1139458

OPEN ACCESS

EDITED BY
Zhouyuan Li,
Beijing Forestry University,
China

REVIEWED BY
Shihua Li,
University of Electronic Science and Technology of China,
China
Zhihui Wang,
Guangzhou Institute of Geography Guangdong Academy of Sciences,
China

*CORRESPONDENCE
Yuan Zeng
✉ zengyuan@aircas.ac.cn

SPECIALTY SECTION
This article was submitted to Environmental Informatics and Remote Sensing, a section of the journal Frontiers in Ecology and Evolution

RECEIVED 07 January 2023
ACCEPTED 10 March 2023
PUBLISHED 27 March 2023

CITATION
Li X, Zheng Z, Xu C, Zhao P, Chen J, Wu J, Zhao X, Mu X, Zhao D and Zeng Y (2023) Individual tree-based forest species diversity estimation by classification and clustering methods using UAV data.
Front. Ecol. Evol. 11:1139458.
doi: 10.3389/fevo.2023.1139458

Individual tree-based forest species diversity estimation by classification and clustering methods using UAV data

Xiuwen Li[1,2], Zhaoju Zheng[1], Cong Xu[1,2], Ping Zhao[1,2], Junhua Chen[1,2], Jinchen Wu[1,2], Xueming Zhao[1,2], Xuan Mu[1,2], Dan Zhao[1,2] and Yuan Zeng[1,2]*

[1]State Key Laboratory of Remote Sensing Science, Aerospace Information Research Institute, Chinese Academy of Sciences, Beijing, China, [2]University of Chinese Academy of Sciences, Beijing, China

Monitoring forest species diversity is essential for biodiversity conservation and ecological management. Currently, unmanned aerial vehicle (UAV) remote sensing technology has been increasingly used in biodiversity monitoring due to its flexibility and low cost. In this study, we compared two methods for estimating forest species diversity indices, namely the spectral angle mapper (SAM) classification approach based on the established species-spectral library, and the self-adaptive Fuzzy C-Means (FCM) clustering algorithm by selected biochemical and structural features. We conducted this study in two complex subtropical forest areas, Mazongling (MZL) and Gonggashan (GGS) National Nature Forest Reserves using UAV-borne hyperspectral and LiDAR data. The results showed that the classification method performed better with higher values of R^2 than the clustering algorithm for predicting both species richness (0.62>0.46 for MZL and 0.55>0.46 for GGS) and Shannon-Wiener index (0.64>0.58 for MZL, 0.52>0.47 for GGS). However, the Simpson index estimated by the classification method correlated less with the field measurements than the clustering algorithm (R^2=0.44 and 0.83 for MZL and R^2=0.44 and 0.62 for GGS). Our study demonstrated that the classification method could provide more accurate monitoring of forest diversity indices but requires spectral information of all dominant tree species at individual canopy scale. By comparison, the clustering method might introduce uncertainties due to the amounts of biochemical and structural inputs derived from the hyperspectral and LiDAR data, but it could acquire forest diversity patterns rapidly without distinguishing the specific tree species. Our findings underlined the advantages of UAV remote sensing for monitoring the species diversity in complex forest ecosystems and discussed the applicability of classification and clustering methods for estimating different individual tree-based species diversity indices.

KEYWORDS

forest species diversity, classification, clustering, UAV, individual tree-based

1. Introduction

Forest biodiversity is essential in maintaining ecosystem patterns, functions and services (Balvanera et al., 2006; Thompson et al., 2009; Brockerhoff et al., 2013). Forest species diversity is a fundamental component of biodiversity, which refers to the uniformity of the number and distribution of tree species in forest ecosystems (Magurran, 1988; Vellend, 2004). However, with the increasing pressure of human activities and climate change, it has faced severe threats, such as accelerated species extinction and increased endangered species (Iida and Nakashizuka, 1995; Haas et al., 2011). Therefore, accurate and repeated forest species diversity monitoring is important for biodiversity conservation and ecological management.

Currently, the assessment of species diversity in a certain region is mainly based on species diversity indices, among which species richness (Gaston, 2000) emphasizes the number of various species, while Shannon-Wiener index (Shannon, 1948) and Simpson index (Simpson, 1949) take into account both the amount and evenness of species. Traditional forest species diversity monitoring relies on field surveys to investigate these diversity indices (Kerr and Ostrovsky, 2003), which are labor- and material-intensive and focus on forest species distribution at the sample scale (Myers et al., 2000; Duro et al., 2007). Remote sensing has the advantages of an extensive detection range and a short data acquisition period, extending the possibilities of forest species diversity monitoring at both temporal and spatial scales (Turner et al., 2003; Skidmore et al., 2015). Near-surface remote sensing platform equipped with hyperspectral sensors and laser scanners has been a promising tool for forest species diversity monitoring in the past decade (Turner, 2014; Guo et al., 2017; Wang and Gamon, 2019; Pu, 2021). In particular, UAV (unmanned aerial vehicle) remote sensing technology, due to its advantages of flexibility and low cost, has shown great potential in species identification and biodiversity monitoring (Anderson and Gaston, 2013; Lin et al., 2019; De Almeida et al., 2021).

Hyperspectral data can obtain continuous spectral information of vegetation and has been increasingly used for monitoring forest species diversity (Féret and Asner, 2014; Ferreira et al., 2016; Laurin et al., 2016). The monitoring methods are mainly divided into two categories: supervised classification methods that directly identify forest species based on their spectroscopic characteristics (Féret and Asner, 2013; Fassnacht et al., 2016; Cao et al., 2018; Franklin and Ahmed, 2018), and spectral diversity metrics that indirectly link the variation of leaf or canopy spectra to species diversity (Palmer et al., 2002; Gholizadeh et al., 2018). Light Detection and Ranging (LiDAR) data can directly penetrate the vegetation canopy by actively emitting high-frequency pulses, so it is widely used for high-precision estimation of forest structural features, including tree height and crown diameter (Popescu, 2007; Morsdorf et al., 2009; Sankey et al., 2013; Wallace et al., 2014). Furthermore, advances in lidar remote sensing have enabled the accurate extraction of information from individual tree crowns (ITCs) (Ene et al., 2012; Zhao et al., 2014). Compared to the pixel-based approach, the ITC-based approach is more directly analogous to the field-based individual sampling method, which can better extract structural features of the canopy and minimize the signal confusion brought by non-tree pixels (Zheng et al., 2022). Based on LiDAR data, forest species diversity at the regional scale can be monitored by establishing relationships between structural features and field-measured species diversity indices (Lopatin et al., 2016; Torresani et al., 2020; Hu et al., 2021). However, the capability of forest species diversity monitoring using only hyperspectral data or LiDAR data might be limited by species complexity, image spectral mixing and canopy morphological variation (Koch, 2010; Guo et al., 2017). The fusion of hyperspectral and LiDAR data provides a synergistic ability, which can use vertical and horizontal information from each data source to acquire more robust diversity monitoring results.

Previous studies have integrated structural features extracted by LiDAR data and spectral characteristics from hyperspectral images for directly discriminating tree species by using classification techniques, including linear discrimination analysis (Alonzo et al., 2014), support vector machine (Dalponte et al., 2012), random forest (Liu et al., 2017) and spectral angle mapper (Zhao et al., 2020). Mayra et al. (2021) compared the performance of different classification methods for identifying the major tree species in a boreal forest based on airborne hyperspectral and LiDAR data. Assessing forest species diversity using remote sensing classification methods has the advantage of providing spatially explicit species distribution information for each ITC or pixel. However, it remains challenging to directly discriminate the species of all individuals accurately in complex subtropical or tropical forests due to the potential spectral or structural similarity among different species or differences existing for the same species (Price, 1994; Wang and Gamon, 2019). The confusion in classification usually increases with increasing biodiversity levels and more training data for species-rich forests is usually needed to improve the classification accuracy. Moreover, collecting sufficient training and validation data for each tree species in species-rich and topographically complex forests can be a challenging task. Although some methods are relatively capable of classifying trees with limited training samples (Christian et al., 2013; Awad, 2018), the classification results are achieved using specific images and algorithms with relatively lower transferability.

Many indirect approaches using spectral and structural information have shown great potential for monitoring forest species diversity, such as regression analysis and clustering. Regression analysis is to model the spectral and structural information directly with the measured species diversity indices, which is a mature and straightforward algorithm, but the applicability in different regions is poor (Ceballos et al., 2015). The clustering algorithm can evaluate species diversity by grouping trees with similar characteristics based on the biochemical and structural variation of different tree species (Asner et al., 2015; Padilla-Martinez et al., 2020; Pakgohar et al., 2021). Clustering can be used to identify patterns or trends in the distribution and abundance of different species within a forest ecosystem. Among them, the self-adaptive Fuzzy C-Means (FCM) clustering algorithm overcomes the disadvantage of traditional clustering methods, which require a pre-indication of the initial classes, and can determine the optimal number of clusters automatically (Bezdek et al., 1987; Li and Yu, 2009). Zhao et al. (2018) estimated the forest species richness and Shannon-Wiener index in a subtropical forest based on airborne LiDAR and hyperspectral data using seven biochemical components and tree height by the adaptive FCM clustering algorithm. The biochemical and structural parameters selected in each study area for clustering methods may be dependent, and their applicability to species diversity monitoring in other areas still needs to be determined, especially for forests with diverse species and complex compositions.

Several studies have used either classification or clustering methods to estimate forest species diversity by combining various features from remote sensing data, but it remains unclear which method is more effective for monitoring different aspects of diversity in different forest conditions. Although some studies have used spaceborne or airborne data to assess species diversity (Shen and Cao, 2017; Wan et al., 2021), they are often limited by spatial resolution or expensive costs. UAV-borne hyperspectral and LiDAR data could provide spatially explicit information on individual trees, so it is more advantageous to explore the applicability of advanced methods in different species-rich forests by UAV data.

Therefore, the major objectives of our study are to explore the performance of individual tree-based classification and clustering methods in estimating three commonly used forest species diversity indices (species richness, Shannon-Wiener index and Simpson index) in two typical subtropical forests in China using UAV-borne hyperspectral and LiDAR data. We aim to: (1) classify tree species using the SAM classification method based on hyperspectral image and the individual tree crown segmentation results from LiDAR data, (2) estimate forest species diversity using the self-adaptive FCM clustering algorithm based on optimal biochemical vegetation indices and structural features, and (3) further compare the performance of classification and clustering methods in these two subtropical forest sites.

2. Materials and methods

2.1. Study area

Subtropical forest in China is a hotspot of tree species richness and a priority area for forest species diversity monitoring (Li et al., 2009; Liu et al., 2018). We conducted research in two study areas, both of which are typical subtropical forests of China, but their forest species compositions and environmental conditions are different. The first study area is located in the Mazongling National Nature Reserve (MZL, 115°41′37′–115°42′5′E, 31°15′25′–31°15′44′N) in Jinzhai county, Anhui province of China (Figure 1). The study area covers about 23.8 ha with an elevation varying from 1,000 m to 1,184 m above sea level. This region is characterized by a subtropical monsoon climate. The average annual temperature is about 13 ~ 15°C, and the average annual precipitation is 1,510 mm (Fan et al., 2022). Mazongling National Nature Reserve has abundant forest resources, and the study area contains more than 10 dominant tree species, including *Quercus glandulifera*, *Platycarya strobilacea*, *Castanea mollissima* and *Lindera glauca*.

The second study area is situated in the Minya Konka National Park (also known as Gonggashan, GGS, 102°3′50′–102°4′28′E, 29°36′2′–29°36′15′N) in Ganzi (Garzê) Tibetan Autonomous Prefecture, Sichuan province of China with an elevation varying from 1959 m to 2,247 m above sea level (Figure 1). This study area is located in the transitional zone from the subtropical belt to the temperate belt of the eastern Tibetan Plateau, covering an area of approximately 20.5 ha. The average annual temperature is about 4.2°C, and the average annual precipitation is 1947 mm (Zhou et al., 2013). The forest canopy across this study area comprises more than 15 dominant tree species, including *Fagus longipetiolata*, *Jasminum nudiflorum*, *Ailanthus altissima*, *Cercidiphyllum japonicum* and *Bothrocaryum controversum*.

2.2. Data acquisition and preprocessing

2.2.1. UAV-borne hyperspectral and LiDAR data

The UAV-borne hyperspectral data were collected on September 18 and October 15, 2020, using the Cuber UHD185 Firefly imaging spectrometer (Cubert GmbH, Ulm, Baden-Württemberg, Germany) onboard a DJI Matrice 300 aircraft (Da Jiang innovate technology Ltd., Shenzhen, China) under cloudless conditions. The sensor comprises 125 visible and near-infrared spectral channels ranging from 450 nm to 946 nm with an 8 nm spectral resolution. The sensor was equipped on the UAV platform and flew at an altitude of 80 m, resulting in a 7 cm spatial resolution. The preprocessing of the images consisted of four preliminary steps. First, the Agisoft PhotoScan software (Agisoft LCC Co. St. Petersburg, Russia) was used for image mosaic. Spectral radiation calibration was the second step to convert the spectral response into the true spectral radiance. Then, the reflectance spectrum was calculated from the reference spectra of calibration plates and the spectral radiance. Finally, the geometric correction was performed in the Image Registration Workflow tool of ENVI5.3 software (Gai, 2019).

The UAV-borne LiDAR data were obtained simultaneously with the hyperspectral dataset acquisition using the LiAir VH Pro scanner (Green Valley Inc., Beijing, China) operating at a wavelength of 905 nm. The scanner provided a 70.4° horizontal (cross-track) and 77.2° vertical (along-track) angle of view. The height accuracy of the laser scanner was 5 cm and had an 80% flight strip overlap. The average point density in MZL is more than 117 points/m^2, and the average point density in MZL is more than 168 points/m^2. The point cloud data were noise filtered and classified into ground and vegetation returns using the software TerraSolid (Terrasolid, Helsinki, Finland). We generated the digital elevation model (DEM) based on the classified ground points and constructed the digital surface model (DSM) from the first pulse reflections of the LiDAR point clouds, and subtracted a canopy height model (CHM) with a resolution of 0.1 m (Zhao et al., 2013). The UAV-LiDAR data were normalized based on the ground points to remove the influence of terrain undulations on the height values. Besides, the vegetation point clouds with a normalized height below 2 m were removed to reduce the effect of background factors such as shrubs and grasses.

2.2.2. Field measurements

Field measurements were collected simultaneously with the UAV data acquisition in September–October 2020, and a supplemental survey was conducted in July 2022. A total of 26 square sample plots (30 × 30 m) within these two study areas were acquired. Differentially-corrected GPS determined the coordinates of the four corners of each sample plot. Tree parameters were measured in each sample plot, including tree species name, diameters at breast height (DBH), crown base height, tree height, crown classes (dominant, co-dominant, intermediate and suppressed trees) and crown diameters in two directions (south–north and east–west) for all individual trees with DBH ≥ 5 cm. The plot-level forest canopy closure and leaf area index (LAI) were also obtained by hemispherical photographs taken by a fish-eye camera along two diagonals. In addition, to validate individual tree segmentation and carry out classification research, we measured the location of each tree in two of the sample plots in MZL and four of the sample plots in GGS by integrating the Real Time Kinematic (RTK) GPS/GLONASS System with the total station.

We selected 10 dominant tree species in MZL and 15 dominant tree species in GGS and collected top-of-canopy leaves for these dominant tree species to measure their biochemical components and spectral properties. We measured 10 major biochemical components, including chlorophyll a and b (Chl-a, Chl-b), total carotenoids (Car),

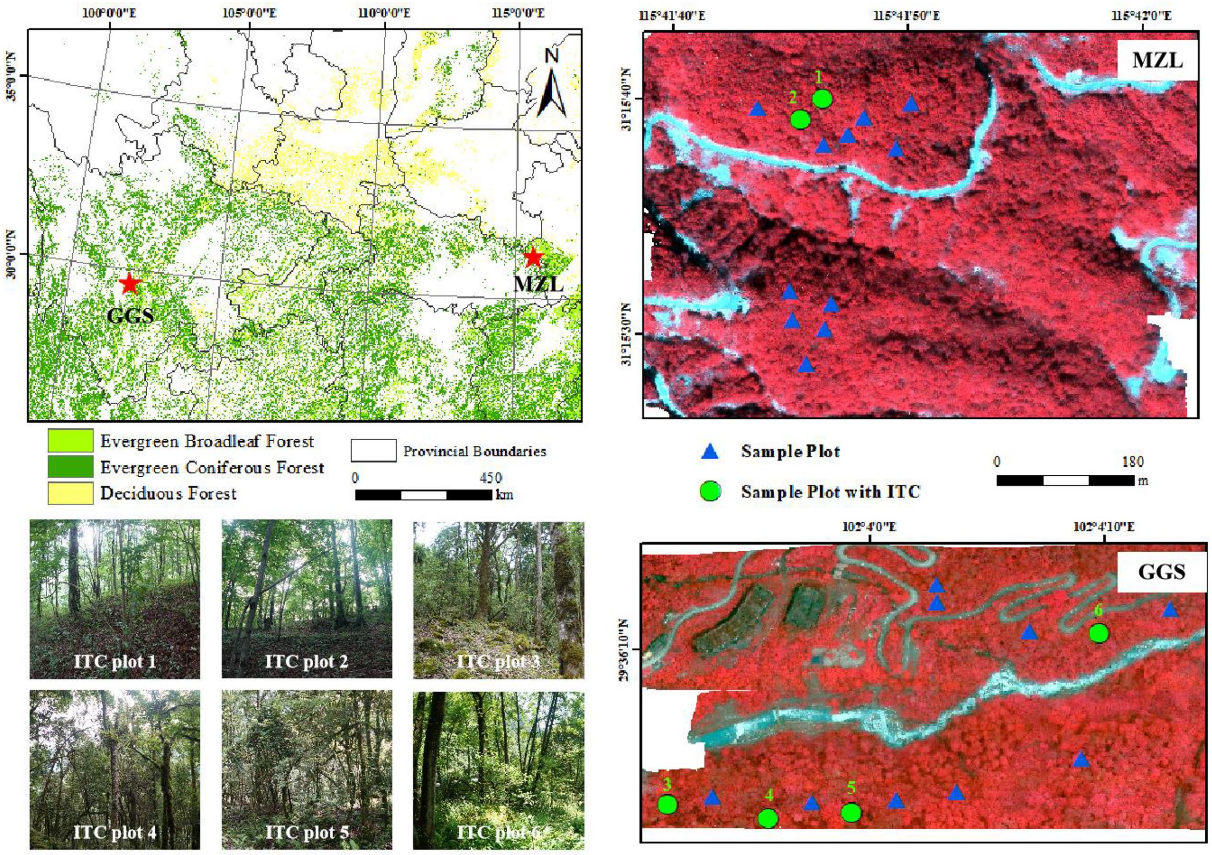

FIGURE 1
The location of two study areas (top left) with 10m spatial resolution from ChinaCover2020 (Wu et al., 2017), and MZL study area (top right) and GGS study area (bottom right) with imaging spectroscopy data acquired from Cuber UHD185 Firefly imaging spectrometer (Red: 866nm, Green: 654nm, Blue: 566nm). The blue triangles indicate the locations of field-measured sample plots. The green circles indicate the locations of individual tree crown (ITC) validation plots. Six photographs of these ITC plots are shown on the bottom left.

total carbon (C), nitrogen (N), phosphorus (P), cellulose (Cel), lignin (Lig), specific leaf area (SLA) and equivalent water thickness (EWT) similar as the previous study (Zheng et al., 2021). Leaves of each species with a mass of more than 150 g were selected and stored in plastic bags on ice and immediately transported to the laboratory for component analysis and spectroscopic measurement. Hemispherical reflectance spectra with 350–2,500 nm wavelengths were measured on 10 fresh leaves of each dominant tree species using a leaf clip coupled with the ASD FieldSpec 4 portable spectroradiometer (ASD Inc., Boulder, CO, United States). The bands with a wavelength of less than 400 nm and more than 2,400 nm were removed to eliminate the influence of instrument noise, and the spectra between 400 to 2,400 nm were smoothed by the Savitzky–Golay filter (Savitzky and Golay, 1964).

2.2.3. Species diversity indices

We used species richness, Shannon-Wiener index, and Simpson index to represent forest species diversity and calculated them within each sample plot based on the field measurements. Species richness refers to the total number of species in the sample plot. Shannon-Wiener index (Shannon, 1948) and Simpson index (Simpson, 1949) can reflect species richness and evenness of species distribution. They are comprehensive indicators reflecting the degree of species diversity. The Shannon-Wiener index is more sensitive to the number of species, and the Simpson index is more sensitive to the evenness of enriched species (Nagendra, 2002). The calculation formula of the Shannon-Wiener index (H) and Simpson index (D) were as follows:

$$H = \sum_{i=1}^{n} - p_i \ln p_i \tag{1}$$

$$D = 1 - \sum_{i=1}^{n} p_i^2 \tag{2}$$

where n is the total number of species in the sample plot, and p_i is the proportional abundance of the species i.

2.3. Methods

2.3.1. Individual tree crown segmentation

Based on the 0.1 m CHM data, we used a watershed algorithm combined with morphological crown control to separate the individual tree crowns (ITCs) (Wang et al., 2004; Chen et al., 2006; Zhao et al., 2014). Firstly, a morphological crown closing operator was used to determine the crown area and obtain the binary image of the canopy. Next, a local extremum algorithm was used to detect the positions of the potential individual treetop. The actual individual treetop positions and potential crown shapes were calibrated through two watershed transformations and image reconstruction operations. Finally, the crown shapes were determined using an adaptive optimized morphological crown opening operator.

2.3.2. Spectral angle mapper (SAM) classification

Among many supervised classification methods, the SAM classification was used for its better performance in the hyperspectral data (Park et al., 2004; Yang et al., 2008; Zhang and Li, 2014). The SAM algorithm is a physically based spectral classification that uses an n-dimensional angle to match the extracted endmember spectra (Kruse et al., 1993; Park et al., 2007; Mohajane et al., 2017). The SAM algorithm determines the spectral similarity though calculating the angle between the spectrum vectors. Smaller angles correspond to closer matches to the endmember spectrum.

We calculated the average spectrum of each canopy based on the ITC segmentation results in the sample plots. Firstly, pixels with NDVI <0.2 and canopy height < 2 m were removed from the hyperspectral images to reduce the effect of background factors such as canopy gaps. A total of 2 ITC plots with 14 tree species in MZL (covering more than 90% of local tree species) and a total of 4 ITC plots with 22 tree species in GGS (covering more than 75% of local tree species) were used to establish the endmember spectral library. Then we determined the average spectrum of each species in the two study areas and used the SAM algorithm to classify them according to the established spectral library. With the classification results, we acquired the species diversity indices of each sample plot and used for validation.

TABLE 1 Vegetation indices corresponding to the biochemical components.

Biochemical component	Vegetation index	Formula	Reference
Chl	TCARI/ OSAVI	TCARI / OSAVI = $3[(R_{750.6}-R_{704.6})-0.2(R_{750.6}-R_{550.6})(R_{750.66}/R_{704.6})] / (1+0.16)(R_{750.66}-R_{704.6})/(R_{750.66}+R_{704}+0.16)$	Daughtry et al. (2000) and Wu et al. (2008)
	VOG1	VOG1 = $R_{979.95}/R_{720.88}$	Vogelmann et al. (1993)
EWT	WBI	WBI = R_{895}/R_{972}	Penuelas et al. (1993)
Car	CRI	CRI = $1/R_{510}-1/R_{550}$	Gitelson et al. (2002)
Cel	PRI	PRI = $(R_{531} - R_{570})/(R_{531}+R_{570})$	Gamon et al. (1992)
N	CCCI	CCCI = $(0.7415R_{790}-0.6965R_{720})/(0.0319R_{790}-0.281R_{720})$	El-Shikha et al. (2007)
P	NDSI	NDSI = $(R_{553}-R_{518})/(R_{553}+R_{518})$	Patil et al. (2007)
SLA	RVI	RVI = R_{750}/R_{705}	Jordan (1969)
C	PSRI	PSRI = $(R_{680}-R_{500})R_{750}$	Merzlyak et al. (1999)

2.3.3. Self-adaptive fuzzy C-means (FCM) clustering algorithm

The optimal biochemical components selection followed two principles (Zhao et al., 2016): (1) biochemical components can be well inverted by the spectrum. (2) these biochemical components are sufficient to distinguish different tree species. The partial least squares regression (PLSR) was used to determine the relationships between the *in-situ* leaf spectral and the biochemical measurements and explore whether the biochemical components of tree species can be quantitatively estimated by their spectral signals. The PLSR method combines the advantage of principal component analysis, canonical correlation analysis, and multiple linear regression analysis. It was performed using JMP14.0 statistical software.

After the optimal biochemical components were determined, the corresponding vegetation indices (VIs) from the hyperspectral data could be selected through the existing vegetation index models to estimate the biochemical components. Due to the lack of influential lignin invention bands, we finally identified nine canopy-scale VIs to indicate Chl (Chl-a and Chl-b), Car, C, N, P, Cel, SLA and EWT based on the literature (Table 1). Many studies have confirmed that the standard deviation of VIs in an area can reflect the species diversity in this region (Cayuela et al., 2006; Stickler and Southworth, 2008; Costanza et al., 2011), so we calculated the standard deviation of VIs for all ITCs at the plot scale, and performed Spearman correlation analysis with the species diversity indices (corrplot, R-package) to select the optimal VIs. The VI for each ITC was calculated by extracting the VI of the central pixel of each ITC. These canopy-level biochemical VIs were then converted into leaf-scale biochemical VIs by dividing the canopy-level biochemical VIs by the ITC's LAI to eliminate the effects caused by the canopy structure (Zarco-Tejada et al., 2001; Zhao et al., 2018). ITC's LAI was calculated by establishing the relationship between forest gap fraction (GF) and LAI according to Beer–Lambert Law (Richardson et al., 2009), as shown in Formula (3):

$$\begin{cases} GF = \dfrac{n_{ground}}{n_{ground} + n_{vegetation}} \\ LAI = -\cos(\theta) * \dfrac{\ln(GF)}{k} \end{cases} \tag{3}$$

where n_{ground} is the number of extracted ground points, $n_{vegetation}$ is the number of vegetation points, k is the extinction coefficient and takes a value of 0.5 if the vegetation is considered to follow the spherical leaf angle distribution, θ is zenith angle (LiDAR scanning angle) and GF is gap fraction.

We extracted 58 structural features for each ITC, including canopy cover, leaf area index, and height variables (statistical parameters related to point cloud height value) based on UAV-LiDAR data and the ITC-segmented ITC boundaries using LiDAR 360 software (Supplementary Table S1). Then we calculated the standard deviation of these structural variables in each sample plot. Finally, the Spearman correlation coefficient test with species diversity indices was performed to obtain the optimal structural features.

Self-adaptive Fuzzy C-Means (FCM) clustering algorithm was applied to calculate the species richness (the number of clusters) based on the optimal biochemical VIs derived from the hyperspectral image and optimal structural features obtained from LiDAR data for each ITC. Each cluster was considered to be a specific but unidentified species. Then the Shannon-Wiener index and the Simpson index can be derived from the cluster amount and the ITC number of each cluster in the sample plot [Formula (1) and (2)]. The field-measured values of species diversity indices of 26 sample plots in two study areas were then compared with the forest biodiversity prediction results to verify the estimation accuracy of the clustering algorithms.

The standard Fuzzy C-Means algorithm transforms the cluster into a nonlinear optimization problem and achieves the number of categories through iteration (Bezdek et al., 1987). Self-adaptive Fuzzy C-Means (FCM) clustering algorithm was developed from the standard Fuzzy C-Means algorithm (Li and Yu, 2009). Self-adaptive FCM automatically determines the optimal number of clusters by using a new validity function without relying on the number of pre-set categories and prior knowledge, solving the acute problem of the clustering algorithm to the initial value. The validity function is defined as:

$$\left\{\begin{aligned} L(c) &= \frac{\sum_{i=1}^{c}\sum_{j=1}^{n}\dfrac{u_{ij}^{m} v_i - \bar{x}^{2}}{c-1}}{\sum_{i=1}^{c}\sum_{j=1}^{n}\dfrac{u_{ij}^{m} x_j - v_i^{-2}}{n-c}} \\ \bar{x} &= \frac{1}{n}\sum_{i=1}^{c}\sum_{j=1}^{n} u_{ij}^{m} x_j \end{aligned}\right. \tag{4}$$

where c is the number of clusters, m is the fuzzy weighting exponent, $X = \{x_1, x_2, \ldots, x_n\}$ is a sample data set, $V = \{v_1, v_2, \ldots, v_n\}$ is the cluster center dataset, u_{ij} represents the membership if the j-th sample point belongs to the i-th class, $\bar{x}$ is the central vector of all data, and $d_{ij} = x_j - v_i$ is the Euclidean distance between the j-th sample point and j-th cluster center.

3. Results

3.1. Individual tree crown segmentation

The ITC segmentation results of all 26 sample plots show that the amounts of segmented ITCs are quantitatively close to the ground-measured tree number (MZL: $R^2 = 0.76$, RMSE = 5.41; GGS: $R^2 = 0.82$, RMSE = 7.17; Figure 2). Due to the effects of crown overlap, point cloud density, small crowns, multi-stemmed trees and other reasons, some extra trees (over-segmentation) and missed trees (under-segmentation) can be found in the ITC segmentation results. The segmented and measured position of ITCs in sample plot 2 of MZL (71 segmented vs. 74 field-measured ITCs) and sample plot 4 of GGS (55 segmented vs. 54 field-measured ITCs) are shown in Figure 2 as an example. The over-segmentation phenomenon occurs in broad-leaved trees with large crowns and non-prominent treetops. In contrast, the under-segmentation phenomenon is caused by the overlapping crowns owing to the high forest canopy density. Multiple overlapping crowns are considered as one crown and are not isolated.

3.2. Forest species diversity prediction based on classification method

The SAM classification algorithm was applied to obtain the tree species of each ITC based on hyperspectral image and ITC boundaries from LiDAR data. As illustrated in Figure 3, a total of 14 endmembers in MZL and a total of 22 endmembers in GGS were extracted directly from the hyperspectral image. These tree species' endmembers were significantly different from each other and thus could be used for classification. Figure 4 shows the tree species classification results of two typical sample plots using the SAM algorithm.

The performance of the relationships between the predicted values and the three field-measured species diversity indices (species richness, Shannon-Wiener index, and Simpson index) is shown in Figure 5 (Blue colors). In MZL, the SAM classification algorithm demonstrated positive and significant predictive validity for species richness ($R^2 = 0.62$, RMSE = 1.44), Shannon-Wiener index ($R^2 = 0.64$, RMSE = 0.16) and Simpson index ($R^2 = 0.44$, RMSE = 0.05). In GGS, the estimated values and the measured species diversity indices were positively and significantly correlated only for species richness ($R^2 = 0.55$, RMSE = 2.87) and Shannon-Wiener index ($R^2 = 0.52$, RMSE = 0.24). The classification-based prediction of the Simpson index was positively correlated with the field measurements, but the correlation was not significant ($R^2 = 0.44$, $p = 0.01$).

3.3. Forest species diversity validation of clustering algorithm

The estimation accuracies of biochemical components based on leaf spectra of tree species are shown in Table 2. It demonstrates that: (1) In MZL, Chl-a, Chl-b, EWT, Car, SLA and C could be strongly predicted by leaf spectra based on PLSR models ($R^2 = 0.78$–0.82). Cel, N, Lig and P are also relatively quantified by spectral reflectance ($R^2 = 0.44$–0.74). (2) In GGS, Chl-a, Chl-b, EWT and SLA could be well estimated by spectral signatures ($R^2 = 0.62$–0.73). Car, N and C also perform a relatively positive relationship with spectral properties ($R^2 = 0.30$–0.46). Cel, Lig and P have no obvious correlation with spectral reflectance ($R^2 < 0.30$).

Based on the optimal biochemical components that are spectrally obtainable (Table 2), we determined 9 biochemical VIs (TCARI/OSAVI, VOG1, CRI, WBI, CCCI, RVI, PRI, NDSI and PSRI) in MZL to indicate Chl (Chl-a and Chl-b), Car, EWT, N, SLA, Cer, P and C, respectively. As for GGS, we selected 7 biochemical VIs (TCARI/OSAVI, VOG1, WBI, RVI, CRI, CCCI and PSRI) to express Chl (Chl-a and Chl-b), EWT, SLA, Car, N and C, respectively. Supplementary Figures S1, S2 show the relationships between the standard deviation of ITC's biochemical VIs of sample plots and the species diversity indices in the two study areas. In MZL, there was a positive correlation between the standard deviation of 7 ITC-based VIs (WBI, TCARI/OSAVI, PRI, RVI, CCCI, VOG1 and PSRI) and species richness at the sample plot scale. These 7 VIs were selected as the optimal biochemical VIs. In

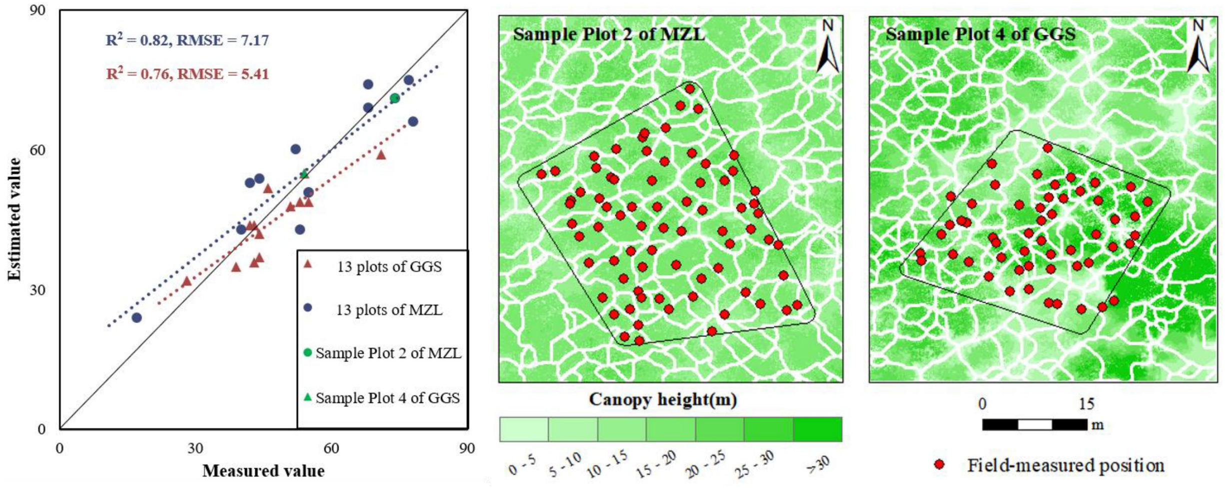

FIGURE 2
Scatter diagram for verification of ITCs (left) and results of individual tree separation in sample plot 2 of MZL (middle) and sample plot 4 of GGS (right) (black boxes represent the boundaries of plots, white polygons refer to the segmented tree crowns, and red points represent the field-measured positions at the base of tree stems).

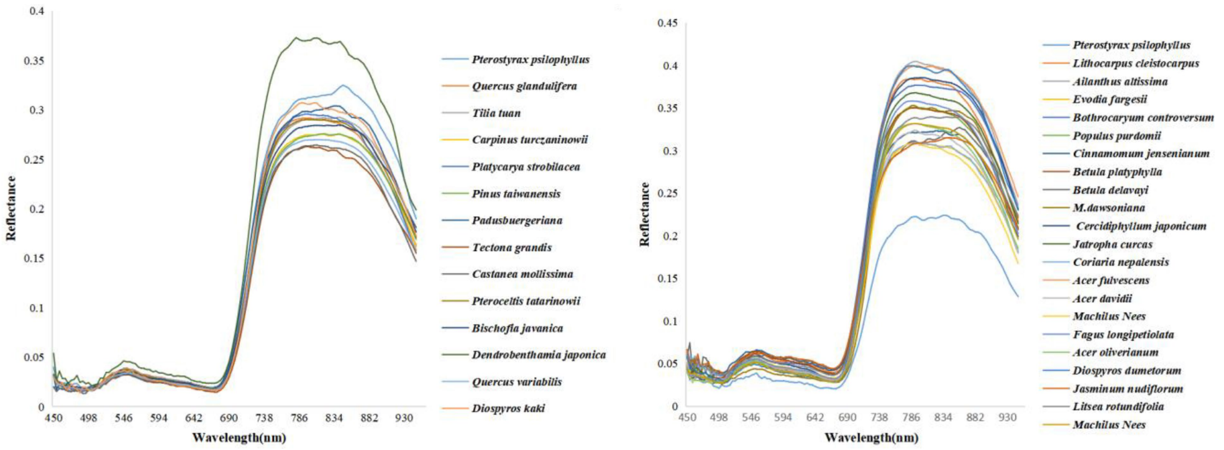

FIGURE 3
Endmember spectral library of dominant tree species in two study areas (left: MZL, right: GGS).

GGS, only 3 ITC's VIs (TCARI/OSAVI, RVI and PSRI) partially correlated with the species diversity indices. We regarded them as the optimal biochemical VIs.

The standard deviation of ITC-based structural features was weakly correlated with the species diversity indices in MZL. We finally conducted the two most relevant characteristics, namely canopy cover (CC) and density metric 30% (DM 30%) as the optimal structural features. In GGS, many structural features were positively and significantly correlated with species diversity indices. We finally determined five optimal structural features, including the interquartile range of accumulated elevation (Elev AIQ), coefficient of variance of elevation (Elev CV), the variance of elevation (Elev Var), density metric 20% (DM 20%) and density metric 30% (DM 30%), which showed high correlation with species diversity indices (Spearman correlation was above 0.5). Supplementary Figures S3, S4 show the relationships between the standard deviation of ITC's structural features of sample plots and the species diversity indices for MZL and GGS, respectively.

We applied the Self-adaptive FCM algorithm to estimate the three species diversity indices at 26 sample plots in two study areas based on the optimal biochemical VIs and optimal structural features for each ITC. The results are shown in Figure 5 (Red colors). In MZL, the clustering algorithm demonstrated positive and significant predictive validity for Shannon-Wiener index ($R^2 = 0.58$, RMSE = 0.22) and Simpson index ($R^2 = 0.83$, RMSE = 0.06). The estimated species richness was lower than the field-measured value (RMSE = 2.47) and performed relatively unsatisfactory inversion results ($R^2 = 0.46$, $p = 0.01$). In GGS, the estimated value and the measured species diversity indices were positively and significantly correlated only for Simpson index ($R^2 = 0.62$, RMSE = 0.07). The prediction results for

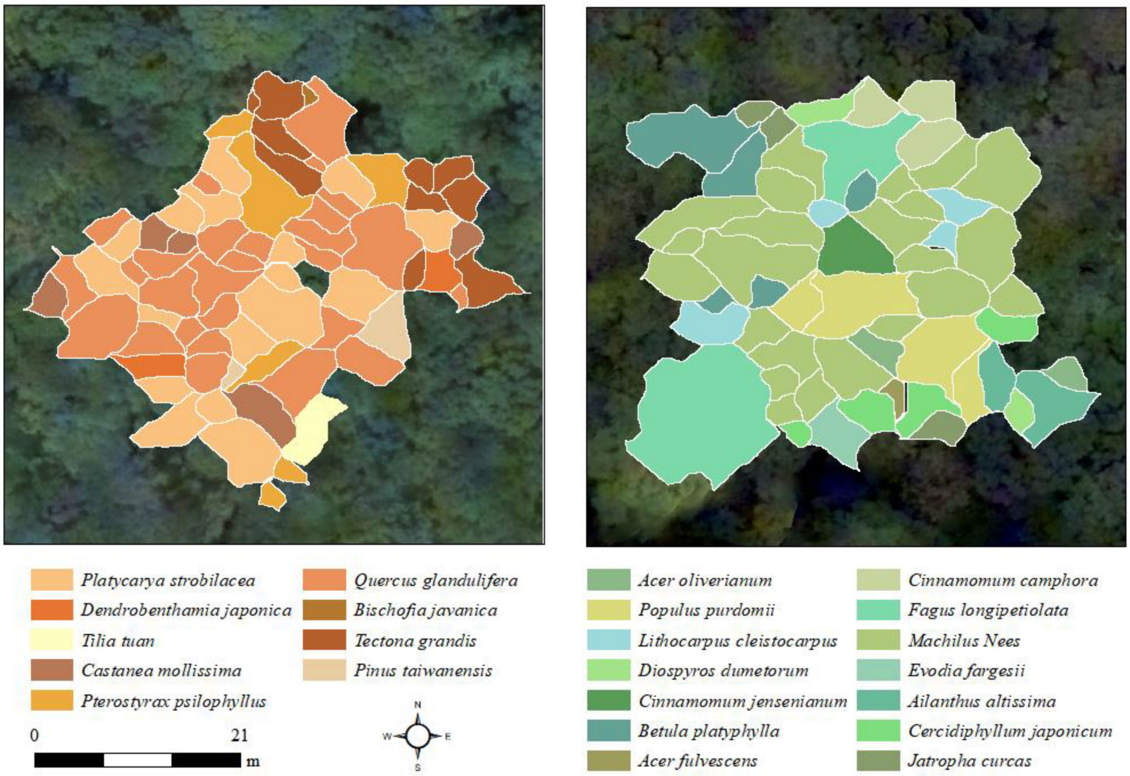

FIGURE 4
Tree species classification results of one sample plot in MZL (left) and one sample plot in GGS (right). Different geometric polygons represent identified ITCs, with white borders indicating the boundaries of the ITCs.

species richness ($R^2 = 0.46$, RMSE = 3.94) and Shannon-Wiener index ($R^2 = 0.47$, RMSE = 0.28) were positive but not significant enough ($p = 0.01$).

4. Discussion

Our results showed that the classification method performed better with higher values of R^2 than the clustering algorithm for predicting species richness (0.62 > 0.46 for MZL and 0.55 > 0.46 for GGS) and the Shannon-Wiener index (0.64 > 0.58 for MZL, 0.52 > 0.47 for GGS) in two study areas (Figure 5). However, the Simpson index estimated by the classification method correlated less with the field measurements than the clustering algorithm ($R^2 = 0.44$ and 0.83 for MZL and $R^2 = 0.44$ and 0.62 for GGS). This is probably due to the Simpson index weights rare species less and dominant species more than Shannon-Wiener index (Magurran, 1988; Daly et al., 2018), so the clustering algorithm taking dominant species/traits more into account are expected to predict the Simpson index accurately. Some previous studies have suggested that the Shannon-Wiener index is more closely related to species richness, while the Simpson index is more distantly correlated with richness (Nagendra, 2002; Costanza et al., 2011; Leinster and Cobbold, 2012). Our outcomes further indicated that the classification method is more advantageous in identifying rare species and estimating species richness, while the clustering method performs better in indicating the evenness of species. Constrained by the limited number of sample plots, it could be considered to use more independent validation plots to verify the advantages of classification and clustering methods in predicting species diversity indices in the future study.

We demonstrated that the individual tree-based SAM classification could be used to monitor the species diversity of complex forests and have the ability to distinguish the non-dominant species (Figure 4). This is mainly because SAM classification could distinguish similar spectra of tree species for classifying species based on hyperspectral data (e.g., *Platycarya strobilacea* and *Tilia tuan* in this experiment, Figure 3) when the endmember spectral library of dominant tree species is available (Awad, 2018; Zhao et al., 2020). However, when the spectra of non-dominant trees and dominant trees are very similar (such as *Carpinus turczaninowii* and *Castanea mollissima* in this study, Figure 3), SAM classification may also incorrectly classify them, which brings some challenges to the estimation of Shannon-Weiner and Simpson index. To better estimate species diversity using the SAM classification approach, it is necessary to extract their distinguishable bands to accurately classify these tree species. Moreover, forest structure has been identified as an essential indicator of forest species diversity (Ishii et al., 2004; Zeng et al., 2008; Guo et al., 2017; Torresani et al., 2020). We used the SAM classification to monitor species diversity based on the ITCs' spectral signal from UAV-hyperspectral data without considering the input of structural characteristics. The fusion of

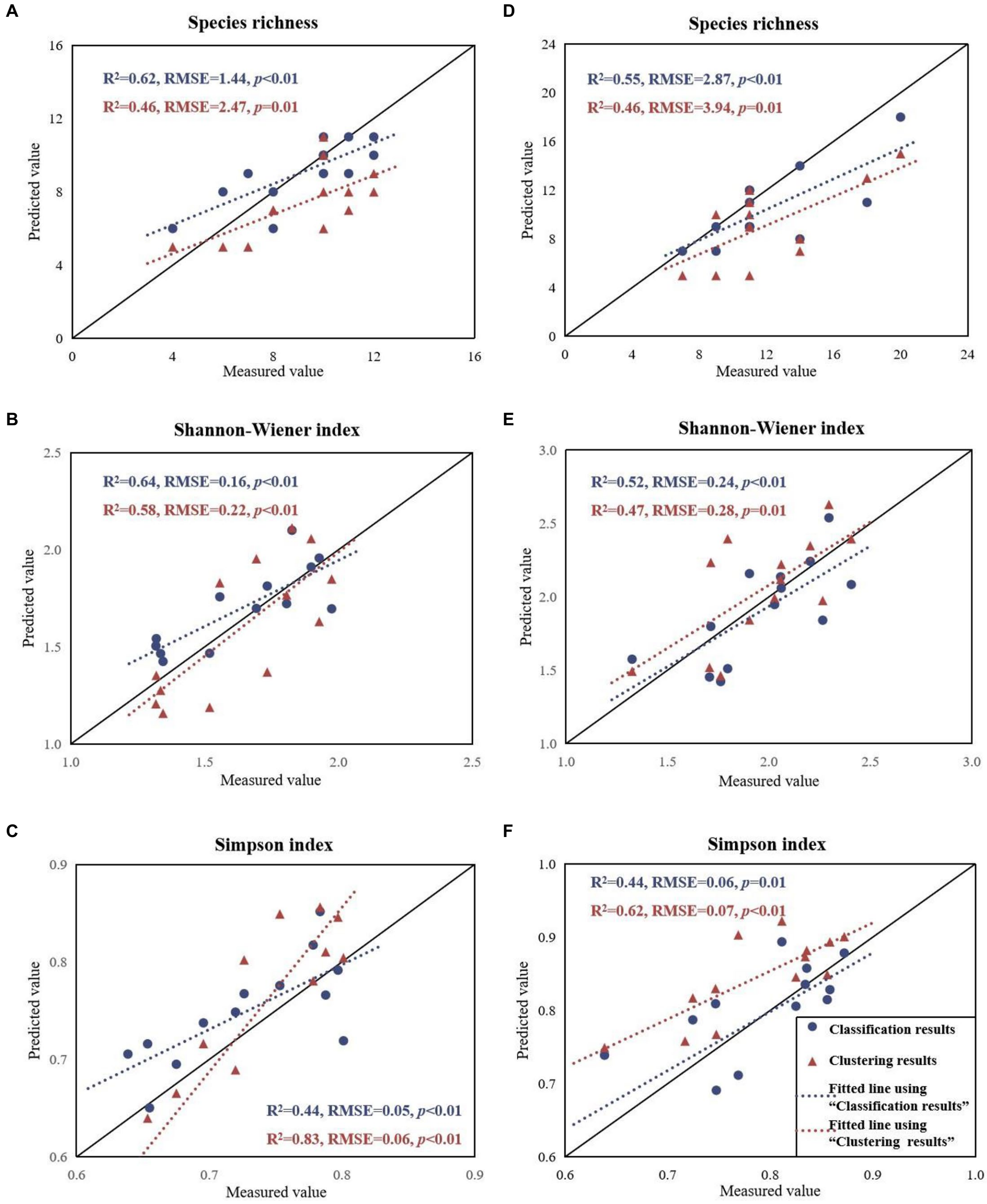

FIGURE 5
Field-measured species diversity indices compared with the predicted values based on classification and clustering approaches for MZL (left) and GGS (right).

TABLE 2 Estimation results of leaf biochemical components.

Biochemical component		Chl-a	Chl-b	EWT	Car	Cel	*N*	Lig	*P*	SLA	*C*
MZL	R^2	0.80	0.81	0.78	0.82	0.44	0.74	0.67	0.61	0.80	0.81
	RMSE	1.87	0.96	2.76	0.30	5.99	0.35	3.43	0.02	31.35	1.25
GGS	R^2	0.68	0.69	0.62	0.46	0.24	0.34	0.25	0.24	0.73	0.30
	RMSE	2.60	1.24	4.37	0.40	3.71	0.40	3.54	0.03	34.88	1.72

spectral and structural features could increase the dissimilarity among tree species and improve classification accuracy (Torabzadeh et al., 2019). Therefore, whether integrating LiDAR-derived tree structural parameters into the supervised classification of hyperspectral data can improve species diversity monitoring is worth to be further investigated.

Our results for both study areas demonstrated that forest diversity patterns could be rapidly acquired by the Self-adaptive FCM clustering algorithm based on individual tree-based variations in biochemical and structural features without distinguishing the tree species, which is similar to the previous clustering research (Féret and Asner, 2014; Schafer et al., 2016; Zhao et al., 2018). A maximum number of 11 and 15 tree species can be identified in the sample polt of MZL and GGS based on different optimal feature compositions using the clustering algorithm (7 optimal biochemical VIs and 2 optimal structural features for MZL, 3 optimal biochemical VIs and 6 optimal structural features for GGS, Figure 6). The outcomes of our feature selection further illustrated the spectral and structural heterogeneity of different regions and also emphasized the applicability of our clustering method in subtropical forests. Compared to the previous studies using Random Forest (RF) algorithm to select the optimal features, we underlined the strength of correlation analysis between the variation of biochemical VIs or structural features and species diversity indices at sample plot scale (Xie et al., 2019; Adhikari et al., 2020; de Almeida et al., 2021). The RF algorithm filters the optimal features according to the importance of the variables, while our feature selection method considers the basic biochemical and structural principles of forest (Hall, 2000; Strobl et al., 2008). However, the biochemical composition and structural characteristics of the same tree species vary considerably depending on individual development and landscape topography, introducing much uncertainty in selecting parameters for different forests.

Our results demonstrated better performance for forest species richness estimation in complex forests based on UAV-borne data (RMSE: 1.44 to 2.47 for MZL, 2.87 to 3.94 for GGS) than previous studies using airborne data (RMSE: 4.0 and 6.74) (Hernandez-Stefanoni et al., 2014; Zhao et al., 2018). Coarser image spatial resolution (typically between 1 to 10 m) and relatively lower point density (usually between 4 to 10 points/m^2) of airborne data can make it difficult to identify or segment trees with smaller canopies, and image spectral mixing may also be an issue (Medina et al., 2013; Sankey et al., 2017). This affects the accuracy of forest species diversity monitoring, as the spectral and structural differences between species may not be accurately captured (Ustin et al., 2004; Lesak et al., 2011; Naidoo et al., 2012). In contrast, UAV-borne LiDAR data with higher point cloud density (more than 100 points/m^2) could discriminate and detect individual trees with satisfactory accuracies (Figure 2). The spectral mixture problem would be solved with the ultra-high resolution UAV-borne imagery (Somers et al., 2011; Ronay et al., 2022), but how to better represent the spectral features of each ITC and avoid potential noise caused by intra-crown shade still need to be further studied (Rocchini et al., 2010). Given the lower flight altitude than conventional airborne platforms, the UAV-borne hyperspectral images are less affected by the atmosphere, leading to improved image quality and easier processing. UAV remote sensing has improved the timeliness of data acquisition, but it has limitations such as limited payload, short flight life, and more fabulous mosaic and geocode efforts (Nex and Remondino, 2014; Matese et al., 2015; Pu, 2021). In addition, due to the "top-down" operation method of UAV-borne platforms, the data for the understory in dense forest areas are often missing. Therefore, combining the advantages of different monitoring tools, such as ground-based LiDAR to complement and verify each other can provide more information for related forest diversity research.

5. Conclusion

In this study, we compared the performance of individual tree-based classification and clustering methods with UAV-borne data for estimating the forest species diversity indices in the Mazongling and Gonggashan National Nature Forest Reserves of China. We proved

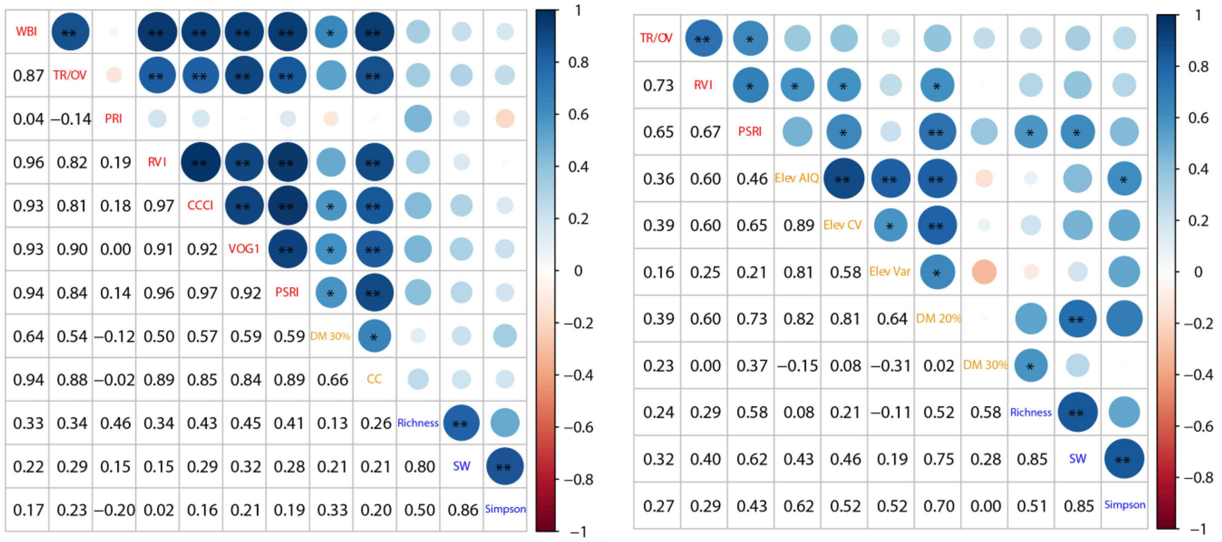

FIGURE 6
Selected features of two study areas (left: MZL, right: GGS; red labels: optimal biochemical VIs, orange labels: optimal structural features, blue labels: species diversity indices; TR/OV: TCARI/OSAVI, SW: Shannon-Wiener index).

that the SAM classification could provide more accurate predictions of species richness indices but requires spectral information of all dominant tree species. The Self-adaptive FCM clustering algorithm could achieve high-precision predictions for evenness indices (especially Simpson index), although information on specific tree species is unavailable.

The combination of UAV imaging spectroscopy and LiDAR make it possible to predict regional forest species diversity more accurately at individual canopy scale for complex forests. Future studies could improve the forest species-spectral library and explore forest species identification from multiple perspectives. Additionally, considering the variation in forest species characteristics over time, it would be valuable to further examine the accuracy of classification and clustering methods by incorporating phenological or multi-temporal features. Moreover, it would be beneficial to investigate the applicability of species diversity estimation models for forests in different ecological contexts and how high-resolution UAV data can be leveraged to bridge the scale gap between traditional field plot samplings and large-scale satellite observations.

Data availability statement

The raw data supporting the conclusions of this article will be made available by the authors, without undue reservation.

Author contributions

XL collected field data, calculated and analyzed the data, and wrote the manuscript. YZ and ZZ assisted in guiding the design of the experiment, discussing the results, and revising the manuscript. DZ and CX helped design the experiment and contributed to the manuscript. PZ, JC, JW, XZ, and XM supported the data investigation. All authors contributed to the article and approved the submitted version.

Funding

This work was supported by the National Key Research and Development Program of China (2020YFE0200800 and 2022YFF1302100) and the National Natural Science Foundation of China (No. 42071344).

Acknowledgments

We thank Ruiying Chang and Qiangxin Ou from the Gonggashan and Mazonglin National Nature Forest Reserves for their support with the fieldwork. We also thank Mingxing Zhang and Shaobo Yang for their assistance in the field sample collection.

Conflict of interest

The authors declare that the research was conducted in the absence of any commercial or financial relationships that could be construed as a potential conflict of interest.

Publisher's note

Supplementary material

The Supplementary material for this article can be found online at: https://www.frontiersin.org/articles/10.3389/fevo.2023.1139458/full#supplementary-material

References

Adhikari, H., Valbuena, R., Pellikka, P. K. E., and Heiskanen, J. (2020). Mapping forest structural heterogeneity of tropical montane forest remnants from airborne laser scanning and Landsat time series. *Ecol. Indic.* 108:105739. doi: 10.1016/j.ecolind.2019.105739

Alonzo, M., Bookhagen, B., and Roberts, D. A. (2014). Urban tree species mapping using hyperspectral and lidar data fusion. *Remote Sens. Environ.* 148, 70–83. doi: 10.1016/j.rse.2014.03.018

Anderson, K., and Gaston, K. J. (2013). Lightweight unmanned aerial vehicles will revolutionize spatial ecology. *Front. Ecol. Environ.* 11, 138–146. doi: 10.1890/120150

Asner, G. P., Martin, R. E., Anderson, C. B., and Knapp, D. E. (2015). Quantifying forest canopy traits: imaging spectroscopy versus field survey. *Remote Sens. Environ.* 158, 15–27. doi: 10.1016/j.rse.2014.11.011

Awad, M. M. (2018). Forest mapping: a comparison between hyperspectral and multispectral images and technologies. *J. For. Res.* 29, 1395–1405. doi: 10.1007/s11676-017-0528-y

Balvanera, P., Pfisterer, A. B., Buchmann, N., He, J. S., Nakashizuka, T., Raffaelli, D., et al. (2006). Quantifying the evidence for biodiversity effects on ecosystem functioning and services. *Ecol. Lett.* 9, 1146–1156. doi: 10.1111/j.1461-0248.2006.00963.x

Bezdek, J. C., Hathaway, R. J., Sabin, M. J., and Tucker, W. T. (1987). Convergence theory for fuzzy c-means: counterexamples and repairs. *IEEE Trans. Syst. Man Cybern.* 17, 873–877. doi: 10.1109/tsmc.1987.6499296

Brockerhoff, E. G., Jactel, H., Parrotta, J. A., and Ferraz, S. F. B. (2013). Role of eucalypt and other planted forests in biodiversity conservation and the provision of biodiversity-related ecosystem services. *For. Ecol. Manag.* 301, 43–50. doi: 10.1016/j.foreco.2012.09.018

Cao, J. J., Leng, W. C., Liu, K., Liu, L., He, Z., and Zhu, Y. H. (2018). Object-based mangrove species classification using unmanned aerial vehicle hyperspectral images and digital surface models. *Remote Sens.* 10:89. doi: 10.3390/rs10010089

Cayuela, L., Benayas, J. M., Justel, A., and Salas-Rey, J. (2006). Modelling tree diversity in a highly fragmented tropical montane landscape. *Glob. Ecol. Biogeogr.* 15, 602–613. doi: 10.1111/j.1466-8238.2006.00255.x

Ceballos, A., Hernandez, J., Corvalan, P., and Galleguillos, M. (2015). Comparison of airborne lidar and satellite hyperspectral remote sensing to estimate vascular plant richness in deciduous mediterranean forests of Central Chile. *Remote Sens.* 7, 2692–2714. doi: 10.3390/rs70302692

Chen, Q., Baldocchi, D., Gong, P., and Kelly, M. (2006). Isolating individual trees in a savanna woodland using small footprint LIDAR data. *Photogramm. Eng. Remote Sens.* 72, 923–932. doi: 10.14358/PERS.72.8.923

Christian, B., Saini, M., Joshi, N., and Krishnayya, N. (2013). *Endmember Extraction and Classification of Tropical Trees (India) Using SFF and SAM Algorithm.* In: 2013 5th Workshop on Hyperspectral Image and Signal Processing: Evolution in Remote Sensing (WHISPERS).

Costanza, J. K., Moody, A., and Peet, R. K. (2011). Multi-scale environmental heterogeneity as a predictor of plant species richness. *Landsc. Ecol.* 26, 851–864. doi: 10.1007/s10980-011-9613-3

Dalponte, M., Bruzzone, L., and Gianelle, D. (2012). Tree species classification in the southern Alps based on the fusion of very high geometrical resolution multispectral/hyperspectral images and LiDAR data. *Remote Sens. Environ.* 123, 258–270. doi: 10.1016/j.rse.2012.03.013

Daly, A. J., Baetens, J. M., and De Baets, B. (2018). Ecological diversity: measuring the unmeasurable. *Mathematics* 6:6070119. doi: 10.3390/math6070119

Daughtry, C. S. T., Walthall, C. L., Kim, M. S., De Colstoun, E. B., and Mcmurtrey, J. E. (2000). Estimating corn leaf chlorophyll concentration from leaf and canopy reflectance. *Remote Sens. Environ.* 74, 229–239. doi: 10.1016/s0034-4257(00)00113-9

De Almeida, D. R. A., Broadbent, E. N., Ferreira, M. P., Meli, P., Zambrano, A. M. A., Gorgens, E. B., et al. (2021). Monitoring restored tropical forest diversity and structure through UAV-borne hyperspectral and lidar fusion. *Remote Sens. Environ.* 264:112582. doi: 10.1016/j.rse.2021.112582

Duro, D., Coops, N. C., Wulder, M. A., and Han, T. (2007). Development of a large area biodiversity monitoring system driven by remote sensing. *Prog. Phys. Geogr. Earth Environ.* 31, 235–260. doi: 10.1177/0309133307079054

El-Shikha, D. M., Waller, P., Hunsaker, D., Clarke, T., and Barnes, E. (2007). Ground-based remote sensing for assessing water and nitrogen status of broccoli. *Agric. Water Manag.* 92, 183–193. doi: 10.1016/j.agwat.2007.05.020

Ene, L., Naesset, E., and Gobakken, T. (2012). Single tree detection in heterogeneous boreal forests using airborne laser scanning and area-based stem number estimates. *Int. J. Remote Sens.* 33, 5171–5193. doi: 10.1080/01431161.2012.657363

Fan, W., Wang, J. J., Wang, H. L., Deng, P. F., Li, A. Q., Zhang, S. S., et al. (2022). Fine-root chemical traits rather than morphological traits of Chinese fir (*Cunninghamia lanceolata* (lamb.) hook.) plantations vary along an altitudinal gradient in eastern China. *Forest Syst.* 31:e010. doi: 10.5424/fs/2022312-18793

Fassnacht, F. E., Latifi, H., Sterenczak, K., Modzelewska, A., Lefsky, M., Waser, L. T., et al. (2016). Review of studies on tree species classification from remotely sensed data. *Remote Sens. Environ.* 186, 64–87. doi: 10.1016/j.rse.2016.08.013

Féret, J. B., and Asner, G. P. (2013). Tree species discrimination in tropical forests using airborne imaging spectroscopy. *IEEE Trans. Geosci. Remote Sens.* 51, 73–84. doi: 10.1109/tgrs.2012.2199323

Féret, J. B., and Asner, G. P. (2014). Mapping tropical forest canopy diversity using high-fidelity imaging spectroscopy. *Ecol. Appl.* 24, 1289–1296. doi: 10.1890/13-1824.1

Ferreira, M. P., Zortea, M., Zanotta, D. C., Shimabukuro, Y. E., and De Souza, C. R. (2016). Mapping tree species in tropical seasonal semi-deciduous forests with hyperspectral and multispectral data. *Remote Sens. Environ.* 179, 66–78. doi: 10.1016/j.rse.2016.03.021

Franklin, S. E., and Ahmed, O. S. (2018). Deciduous tree species classification using object-based analysis and machine learning with unmanned aerial vehicle multispectral data. *Int. J. Remote Sens.* 39, 5236–5245. doi: 10.1080/01431161.2017.1363442

Gai, J. (2019). Establishment of plot-yield prediction models in soybean breeding programs using UAV-based hyperspectral remote sensing. *Remote Sens.* 11:2752. doi: 10.3390/rs11232752

Gamon, J. A., Penuelas, J., and Field, C. B. (1992). A narrow-waveband spectral index that tracks diurnal changes in photosynthetic efficiency. *Remote Sens. Environ.* 41, 35–44. doi: 10.1016/0034-4257(92)90059-s

Gaston, K. J. (2000). Global patterns in biodiversity. *Nature* 405, 220–227. doi: 10.1038/35012228

Gholizadeh, H., Gamon, J. A., Zygielbaum, A. I., Wang, R., Schweiger, A. K., and Cavender-Bares, J. (2018). Remote sensing of biodiversity: soil correction and data dimension reduction methods improve assessment of alpha-diversity (species richness) in prairie ecosystems. *Remote Sens. Environ.* 206, 240–253. doi: 10.1016/j.rse.2017.12.014

Gitelson, A. A., Zur, Y., Chivkunova, O. B., and Merzlyak, M. N. (2002). Assessing carotenoid content in plant leaves with reflectance spectroscopy. *Photochem. Photobiol.* 75, 272–281. doi: 10.1562/0031-8655(2002)075<0272:Accipl>2.0.Co;2

Guo, X., Coops, N. C., Tompalski, P., Nielsen, S. E., Bater, C. W., and Stadt, J. J. (2017). Regional mapping of vegetation structure for biodiversity monitoring using airborne lidar data. *Eco. Inform.* 38, 50–61. doi: 10.1016/j.ecoinf.2017.01.005

Haas, S. E., Hooten, M. B., Rizzo, D. M., and Meentemeyer, R. K. (2011). Forest species diversity reduces disease risk in a generalist plant pathogen invasion. *Ecol. Lett.* 14, 1108–1116. doi: 10.1111/j.1461-0248.2011.01679.x

Hall, M. A.. (2000). *Feature Selection for Discrete and Numeric Class Machine Learning.* Stanford, CA, USA: Proceedings of the Seventeenth International Conference on Machine Learning (ICML 2000), Stanford University.

Hernandez-Stefanoni, J. L., Dupuy, J. M., Johnson, K. D., Birdsey, R., Tun-Dzul, F., Peduzzi, A., et al. (2014). Improving species diversity and biomass estimates of tropical dry forests using airborne LiDAR. *Remote Sens.* 6, 4741–4763. doi: 10.3390/rs6064741

Hu, T. Y., Sun, X. L., Su, Y. J., Guan, H. C., Sun, Q. H., Kelly, M., et al. (2021). Development and performance evaluation of a very low-cost UAV-Lidar system for forestry applications. *Remote Sens.* 13:77. doi: 10.3390/rs13010077

Iida, S., and Nakashizuka, T. (1995). Forest fragmentation and its effect on species diversity in sub-urban coppice forests in Japan. *For. Ecol. Manag.* 73, 197–210. doi: 10.1016/0378-1127(94)03484-e

Ishii, H. T., Tanabe, S., and Hiura, T. (2004). Exploring the relationships among canopy structure, stand productivity, and biodiversity of temperature forest ecosystems. *For. Sci.* 50, 342–355. doi: 10.1093/forestscience/50.3.342

Jordan, C. F. (1969). Derivation of leaf-area index from quality of light on the Forest floor. *Ecology* 50, 663–666. doi: 10.2307/1936256

Kerr, J. T., and Ostrovsky, M. (2003). From space to species: ecological applications for remote sensing. *Trends Ecol. Evol.* 18, 299–305. doi: 10.1016/s0169-5347(03)00071-5

Koch, B. (2010). Status and future of laser scanning, synthetic aperture radar and hyperspectral remote sensing data for forest biomass assessment. *ISPRS J. Photogramm. Remote Sens.* 65, 581–590. doi: 10.1016/j.isprsjprs.2010.09.001

Kruse, F. A., Lefkoff, A. B., Boardman, J. W., Heidebrecht, K. B., Shapiro, A. T., Barloon, P. J., et al. (1993). The spectral image processing system (SIPS)-interactive visualization and analysis of imaging spectrometer data. *Remote Sens. Environ.* 44, 145–163. doi: 10.1016/0034-4257(93)90013-n

Laurin, G. V., Puletti, N., Hawthorne, W., Liesenberg, V., Corona, P., Papale, D., et al. (2016). Discrimination of tropical forest types, dominant species, and mapping of functional guilds by hyperspectral and simulated multispectral Sentinel-2 data. *Remote Sens. Environ.* 176, 163–176. doi: 10.1016/j.rse.2016.01.017

Leinster, T., and Cobbold, C. A. (2012). Measuring diversity: the importance of species similarity. *Ecology* 93, 477–489. doi: 10.1890/10-2402.1

Lesak, A. A., Radeloff, V. C., Hawbaker, T. J., Pidgeon, A. M., Gobakken, T., and Contrucci, K. (2011). Modeling forest songbird species richness using LiDAR-derived measures of forest structure. *Remote Sens. Environ.* 115, 2823–2835. doi: 10.1016/j.rse.2011.01.025

Li, L., Huang, Z. L., Ye, W. H., Cao, H. L., Wei, S. G., Wang, Z. G., et al. (2009). Spatial distributions of tree species in a subtropical forest of China. *Oikos* 118, 495–502. doi: 10.1111/j.1600-0706.2009.16753.x

Li, Y., and Yu, F. S.. (2009). *A New Validity Function for Fuzzy Clustering.* In: International Conference on Computational Intelligence and Natural Computing, pp. 462–465.

Lin, Q. N., Huang, H. G., Wang, J. X., Huang, K., and Liu, Y. Y. (2019). Detection of pine shoot beetle (PSB) stress on pine forests at individual tree level using UAV-based hyperspectral imagery and Lidar. *Remote Sens.* 11:2540. doi: 10.3390/rs11212540

Liu, L. X., Coops, N. C., Aven, N. W., and Pang, Y. (2017). Mapping urban tree species using integrated airborne hyperspectral and LiDAR remote sensing data. *Remote Sens. Environ.* 200, 170–182. doi: 10.1016/j.rse.2017.08.010

Liu, X. J., Trogisch, S., He, J. S., Niklaus, P. A., Bruelheide, H., Tang, Z. Y., et al. (2018). Tree species richness increases ecosystem carbon storage in subtropical forests. *Proc. R. Soc. B Biol. Sci.* 285:1888. doi: 10.1098/rspb.2018.1240

Lopatin, J., Dolos, K., Hernandez, H. J., Galleguillos, M., and Fassnacht, F. E. (2016). Comparing generalized linear models and random forest to model vascular plant species richness using LiDAR data in a natural forest in Central Chile. *Remote Sens. Environ.* 173, 200–210. doi: 10.1016/j.rse.2015.11.029

Magurran, A. E.. (1988). *Ecological Diversity and its Measurement*. Springer Netherlands.

Matese, A., Toscano, P., Di Gennaro, S. F., Genesio, L., Vaccari, F. P., Primicerio, J., et al. (2015). Intercomparison of UAV, aircraft and satellite remote sensing platforms for precision viticulture. *Remote Sens.* 7, 2971–2990. doi: 10.3390/rs70302971

Mayra, J., Keski-Saari, S., Kivinen, S., Tanhuanpaa, T., Hurskainen, P., Kullberg, P., et al. (2021). Tree species classification from airborne hyperspectral and LiDAR data using 3D convolutional neural networks. *Remote Sens. Environ.* 256:112322. doi: 10.1016/j.rse.2021.112322

Medina, O., Manian, V., and Chinea, J. D. (2013). Biodiversity assessment using hierarchical agglomerative clustering and spectral Unmixing over hyperspectral images. *Sensors* 13, 13949–13959. doi: 10.3390/s131013949

Merzlyak, M. N., Gitelson, A. A., Chivkunova, O. B., and Rakitin, V. Y. (1999). Non-destructive optical detection of pigment changes during leaf senescence and fruit ripening. *Physiol. Plant.* 106, 135–141. doi: 10.1034/j.1399-3054.1999.106119.x

Mohajane, M., Essahlaoui, A., Oudija, F., El Hafyani, M., and Teodoro, C. (2017). Mapping Forest species in the central middle atlas of Morocco (Azrou Forest) through remote sensing techniques. *ISPRS Int. J. Geo Inf.* 6:275. doi: 10.3390/ijgi6090275

Morsdorf, F., Nichol, C., Malthus, T., and Woodhouse, I. H. (2009). Assessing forest structural and physiological information content of multi-spectral LiDAR waveforms by radiative transfer modelling. *Remote Sens. Environ.* 113, 2152–2163. doi: 10.1016/j.rse.2009.05.019

Myers, N., Mittermeier, R. A., Mittermeier, C. G., Da Fonseca, G. A. B., and Kent, J. (2000). Biodiversity hotspots for conservation priorities. *Nature* 403, 853–858. doi: 10.1038/35002501

Nagendra, H. (2002). Opposite trends in response for the Shannon and Simpson indices of landscape diversity. *Appl. Geogr.* 22, 175–186. doi: 10.1016/s0143-6228(02)00002-4

Naidoo, L., Cho, M. A., Mathieu, R., and Asner, G. (2012). Classification of savanna tree species, in the greater Kruger National Park region, by integrating hyperspectral and LiDAR data in a random Forest data mining environment. *ISPRS J. Photogramm. Remote Sens.* 69, 167–179. doi: 10.1016/j.isprsjprs.2012.03.005

Nex, F., and Remondino, F. (2014). UAV for 3D mapping applications: a review. *Appl. Geomat.* 6, 1–15. doi: 10.1007/s12518-013-0120-x

Padilla-Martinez, J. R., Corral-Rivas, J. J., Briseno-Reyes, J., Paul, C., Lopez-Serrano, P. M., and Von Gadow, K. (2020). Patterns of density and production in the community forests of the Sierra Madre occidental, Mexico. *Forests* 11:307. doi: 10.3390/f11030307

Pakgohar, N., Rad, J. E., Gholami, G., Alijanpour, A., and Roberts, D. W. (2021). A comparative study of hard clustering algorithms for vegetation data. *J. Veg. Sci.* 32:e13042. doi: 10.1111/jvs.13042

Palmer, M. W., Earls, P. G., Hoagland, B. W., White, P. S., and Wohlgemuth, T. (2002). Quantitative tools for perfecting species lists. *Environmetrics* 13, 121–137. doi: 10.1002/env.516

Park, B., Windham, W. R., Lawrence, K. C., and Smith, D. P.. (2004). *Classification of Hyperspectral Imagery for Identifying Fecal and Ingesta Contaminants*. In: Monitoring Food Safety, Agriculture, and Plant Health).

Park, B., Windham, W. R., Lawrence, K. C., and Smith, D. P. (2007). Contaminant classification of poultry hyperspectral imagery using a spectral angle mapper algorithm. *Biosyst. Eng.* 96, 323–333. doi: 10.1016/j.biosystemseng.2006.11.012

Patil, V. D., Adsul, P. B., and Deshmukh, L. S. (2007). Studies on spectral reflectance under normal and nitrogen, phosphorus and pest and disease stress condition in soybean (*Glycine max* L.). *J. Indian Soc. Remote Sens.* 35, 351–359. doi: 10.1007/bf02990790

Penuelas, J., Filella, I., Biel, C., Serrano, L., and Save, R. (1993). The reflectance at the 950–970 nm region as an indicator of plant water status. *Int. J. Remote Sens.* 14, 1887–1905. doi: 10.1080/01431169308954010

Popescu, S. C. (2007). Estimating biomass of individual pine trees using airborne lidar. *Biomass Bioenergy* 31, 646–655. doi: 10.1016/j.biombioe.2007.06.022

Price, J. C. (1994). How unique are spectral signatures? *Remote Sens. Environ.* 49, 181–186. doi: 10.1016/0034-4257(94)90013-2

Pu, R. (2021). Mapping tree species using advanced remote sensing technologies: a state-of-the-art review and perspective. *J. Remote Sens.* 2021:9812624. doi: 10.34133/2021/9812624

Richardson, J. J., Moskal, L. M., and Kim, S. H. (2009). Modeling approaches to estimate effective leaf area index from aerial discrete-return LIDAR. *Agric. For. Meteorol.* 149, 1152–1160. doi: 10.1016/j.agrformet.2009.02.007

Rocchini, D., Balkenhol, N., Carter, G. A., Foody, G. M., Gillespie, T. W., He, K. S., et al. (2010). Remotely sensed spectral heterogeneity as a proxy of species diversity: recent advances and open challenges. *Eco. Inform.* 5, 318–329. doi: 10.1016/j.ecoinf.2010.06.001

Ronay, I., Kizel, F., and Lati, R.. (2022). *The Effect of Spectral Mixtures on WEED Species Classification*. 24th ISPRS Congress on Imaging Today, Foreseeing Tomorrow, pp. 477–484.

Sankey, T., Donager, J., Mcvay, J., and Sankey, J. B. (2017). UAV lidar and hyperspectral fusion for forest monitoring in the southwestern USA. *Remote Sens. Environ.* 195, 30–43. doi: 10.1016/j.rse.2017.04.007

Sankey, T., Shrestha, R., Sankey, J. B., Hardegree, S., and Strand, E. (2013). Lidar-derived estimate and uncertainty of carbon sink in successional phases of woody encroachment. *J. Geophys. Res. Biogeosci.* 118, 1144–1155. doi: 10.1002/jgrg.20088

Savitzky, A., and Golay, M. J. E. (1964). Smoothing and differentiation of data by simplified least squares procedures. *Anal. Chem.* 36, 1627–1639. doi: 10.1021/ac60214a047

Schafer, E., Heiskanen, J., Heikinheimo, V., and Pellikka, P. (2016). Mapping tree species diversity of a tropical montane forest by unsupervised clustering of airborne imaging spectroscopy data. *Ecol. Indic.* 64, 49–58. doi: 10.1016/j.ecolind.2015.12.026

Shannon, C. E. (1948). A mathematical theory of communication. *Bell Syst. Tech. J.* 27, 379–423. doi: 10.1002/j.1538-7305.1948.tb01338.x

Shen, X., and Cao, L. (2017). Tree-species classification in subtropical forests using airborne hyperspectral and LiDAR data. *Remote Sens.* 9:1180. doi: 10.3390/rs9111180

Simpson, E. H. (1949). Measurement of diversity. *Nature* 163:688. doi: 10.1038/163688a0

Skidmore, A. K., Pettorelli, N., Coops, N. C., Geller, G. N., Hansen, M., Lucas, R., et al. (2015). Agree on biodiversity metrics to track from space. *Nature* 523, 403–405. doi: 10.1038/523403a

Somers, B., Asner, G. P., Tits, L., and Coppin, P. (2011). Endmember variability in spectral mixture analysis: a review. *Remote Sens. Environ.* 115, 1603–1616. doi: 10.1016/j.rse.2011.03.003

Stickler, C. M., and Southworth, J. (2008). Application of multi-scale spatial and spectral analysis for predicting primate occurrence and habitat associations in Kibale National Park, Uganda. *Remote Sens. Environ.* 112, 2170–2186. doi: 10.1016/j.rse.2007.10.013

Strobl, C., Boulesteix, A. L., Kneib, T., Augustin, T., and Zeileis, A. (2008). Conditional variable importance for random forests. *BMC Bioinformatics* 9:307. doi: 10.1186/1471-2105-9-307

Thompson, I. D., Mackey, B. G., Mcnulty, S., and Mosseler, A.. (2009). *Forest Resilience, Biodiversity, and Climate Change: A Synthesis of the Biodiversity/Resilience/Stability Relationship in Forest Ecosystems*. Secretariat of the Convention on Biological Diversity, Montreal.

Torabzadeh, H., Leiterer, R., Hueni, A., Schaepman, M. E., and Morsdorf, F. (2019). Tree species classification in a temperate mixed forest using a combination of imaging spectroscopy and airborne laser scanning. *Agric. For. Meteorol.* 279:107744. doi: 10.1016/j.agrformet.2019.107744

Torresani, M., Rocchini, D., Sonnenschein, R., Zebisch, M., Hauffe, H. C., Heym, M., et al. (2020). Height variation hypothesis: a new approach for estimating forest species diversity with CHM LiDAR data. *Ecol. Indic.* 117:106520. doi: 10.1016/j.ecolind.2020.106520

Turner, W. (2014). Sensing biodiversity. *Science* 346, 301–302. doi: 10.1126/science.1256014

Turner, W., Spector, S., Gardiner, N., Fladeland, M., Sterling, E., and Steininger, M. (2003). Remote sensing for biodiversity science and conservation. *Trends Ecol. Evol.* 18, 306–314. doi: 10.1016/s0169-5347(03)00070-3

Ustin, S. L., Roberts, D. A., Gamon, J. A., Asner, G. P., and Green, R. O. (2004). Using imaging spectroscopy to study ecosystem processes and properties. *Bioscience* 54, 523–534. doi: 10.1641/0006-3568(2004)054[0523:Uistse]2.0.Co;2

Vellend, M. (2004). Parallel effects of land-use history on species diversity and genetic diversity of forest herbs. *Ecology* 85, 3043–3055. doi: 10.1890/04-0435

Vogelmann, J. E., Rock, B. N., and Moss, D. M. (1993). Red edge spectral measurements from sugar maple leaves. *Int. J. Remote Sens.* 14, 1563–1575. doi: 10.1080/01431169308953986

Wallace, L., Musk, R., and Lucieer, A. (2014). An assessment of the repeatability of automatic Forest inventory metrics derived from UAV-borne laser scanning data. *IEEE Trans. Geosci. Remote Sens.* 52, 7160–7169. doi: 10.1109/tgrs.2014.2308208

Wan, H. M., Tang, Y. W., Jing, L. H., Li, H., Qiu, F., and Wu, W. J. (2021). Tree species classification of Forest stands using multisource remote sensing data. *Remote Sens.* 13:144. doi: 10.3390/rs13010144

Wang, R., and Gamon, J. A. (2019). Remote sensing of terrestrial plant biodiversity. *Remote Sens. Environ.* 231:111218. doi: 10.1016/j.rse.2019.111218

Wang, L., Gong, P., and Biging, G. S. (2004). Individual tree-crown delineation and treetop detection in high-spatial-resolution aerial imagery. *Photogramm. Eng. Remote Sens.* 70, 351–357. doi: 10.14358/PERS.70.3.351

Wu, C. Y., Niu, Z., Tang, Q., and Huang, W. J. (2008). Estimating chlorophyll content from hyperspectral vegetation indices: modeling and validation. *Agric. For. Meteorol.* 148, 1230–1241. doi: 10.1016/j.agrformet.2008.03.005

Wu, B., Qian, J., and Zeng, Y.. (2017). *Land Cover Atlas of the People's Republic of China (1:1,000,000)*. Beijing: Sinomaps Press.

Xie, Z. L., Chen, Y. L., Lu, D. S., Li, G. Y., and Chen, E. X. (2019). Classification of land cover, Forest, and tree species classes with ZiYuan-3 multispectral and stereo data. *Remote Sens.* 11:164. doi: 10.3390/rs11020164

Yang, C., Everitt, J. H., and Bradford, J. M. (2008). Yield estimation from hyperspectral imagery using spectral angle mapper (SAM). *Trans. ASABE* 51, 729–737. doi: 10.13031/2013.20649

Zarco-Tejada, P. J., Miller, J. R., Noland, T. L., Mohammed, G. H., and Sampson, P. H. (2001). Scaling-up and model inversion methods with narrowband optical indices for chlorophyll content estimation in closed forest canopies with hyperspectral data. *IEEE Trans. Geosci. Remote Sens.* 39, 1491–1507. doi: 10.1109/36.934080

Zeng, Y., Schaepman, M. E., Wu, B., Clevers, J., and Bregt, A. K. (2008). Scaling-based forest structural change detection using an inverted geometric-optical model in the three gorges region of China. *Remote Sens. Environ.* 112, 4261–4271. doi: 10.1016/j.rse.2008.07.007

Zhang, X. Y., and Li, P. J. (2014). Litho logical mapping from hyperspectral data by improved use of spectral angle mapper. *Int. J. Appl. Earth Obs. Geoinf.* 31, 95–109. doi: 10.1016/j.jag.2014.03.007

Zhao, D., Pang, Y., Li, Z. Y., and Liu, L. J. (2014). Isolating individual trees in a closed coniferous forest using small footprint lidar data. *Int. J. Remote Sens.* 35, 7199–7218. doi: 10.1080/01431161.2014.967886

Zhao, D., Pang, Y., Li, Z. Y., and Sun, G. Q. (2013). Filling invalid values in a lidar-derived canopy height model with morphological crown control. *Int. J. Remote Sens.* 34, 4636–4654. doi: 10.1080/01431161.2013.779398

Zhao, D., Pang, Y., Liu, L. J., and Li, Z. Y. (2020). Individual tree classification using airborne LiDAR and hyperspectral data in a natural mixed Forest of Northeast China. *Forests* 11:303. doi: 10.3390/f11030303

Zhao, Y. J., Zeng, Y., Zhao, D., Wu, B. F., and Zhao, Q. J. (2016). The optimal leaf biochemical selection for mapping species diversity based on imaging spectroscopy. *Remote Sens.* 8:216. doi: 10.3390/rs8030216

Zhao, Y. J., Zeng, Y., Zheng, Z. J., Dong, W. X., Zhao, D., Wu, B. F., et al. (2018). Forest species diversity mapping using airborne LiDAR and hyperspectral data in a subtropical forest in China. *Remote Sens. Environ.* 213, 104–114. doi: 10.1016/j.rse.2018.05.014

Zheng, Z. J., Zeng, Y., Schneider, F. D., Zhao, Y. J., Zhao, D., Schmid, B., et al. (2021). Mapping functional diversity using individual tree-based morphological and physiological traits in a subtropical forest. *Remote Sens. Environ.* 252:112170. doi: 10.1016/j.rse.2020.112170

Zheng, Z. J., Zeng, Y., Schuman, M. C., Jiang, H. L., Schmid, B., Schaepman, M. E., et al. (2022). Individual tree-based vs pixel-based approaches to mapping forest functional traits and diversity by remote sensing. *Int. J. Appl. Earth Obs. Geoinform.* 114:103074. doi: 10.1016/j.jag.2022.103074

Zhou, J., Wu, Y. H., Jorg, P., Bing, H. J., Yu, D., Sun, S. Q., et al. (2013). Changes of soil phosphorus speciation along a 120-year soil chronosequence in the Hailuogou glacier retreat area (Gongga Mountain, SW China). *Geoderma* 195, 251–259. doi: 10.1016/j.geoderma2012.12.010

Frontiers in Ecology and Evolution

TYPE Original Research
PUBLISHED 28 March 2023
DOI 10.3389/fevo.2023.1168313

OPEN ACCESS

EDITED BY
Zhouyuan Li,
Beijing Forestry University, China

REVIEWED BY
Zhe Feng,
China University of Geosciences, China
Guanghui Jiang,
Beijing Normal University, China
Hua Zheng,
Research Center for Eco-Environmental Sciences (CAS), China

*CORRESPONDENCE
Huawei Wan
✉ wanhw@secmep.cn

SPECIALTY SECTION
This article was submitted to
Environmental Informatics and Remote Sensing,
a section of the journal
Frontiers in Ecology and Evolution

RECEIVED 17 February 2023
ACCEPTED 13 March 2023
PUBLISHED 28 March 2023

CITATION
Zhang Z, Wan H, Peng S and Huang L (2023) Differentiated factors drive the spatial heterogeneity of ecosystem services in Xinjiang Autonomous Region, China. *Front. Ecol. Evol.* 11:1168313.
doi: 10.3389/fevo.2023.1168313

Differentiated factors drive the spatial heterogeneity of ecosystem services in Xinjiang Autonomous Region, China

Zhiru Zhang[1,2], Huawei Wan[2]*, Shilei Peng[3] and Lin Huang[4]

[1]Chinese Research Academy of Environmental Sciences, Beijing, China, [2]Center for Satellite Application on Ecology and Environment, Ministry of Ecology and Environment, Beijing, China, [3]Institute of Subtropical Agriculture, Chinese Academy of Sciences, Beijing, Hunan, China, [4]Institute of Geographic Sciences and Natural Resources Research, Beijing, China

Exploring the driving factors of changing ecosystem services is critical for supply capacity maintaining and ecological management zoning. Xinjiang of Northwest China, is considered one of the most fragile ecological environment areas. However, studies on how ecosystem services' driving forces respond to the environmental conditions of Xinjiang are still insufficient, especially in sub−regions with considerable spatial heterogeneity. Based on 106 counties across Xinjiang, we employed models of the Integrated Valuation of Ecosystem Services and Tradeoffs (InVEST) and Revised Wind Erosion Equation (RWEQ) to quantify four essential ecosystem services (carbon storage, habitat quality, and sand fixation and water yield). Then, we investigated the spatial distribution of four ecosystem services and drivers at the county scale in 2020 by using multi−scale geographically weighted regression (MGWR). The results showed that the spatial distribution of ecosystem services is higher in the north and lower in the south, and hotspots and high−value ecosystem services areas were consistent. Precipitation, temperature, and fractional vegetation cover were the dominant factors influencing the four ecosystem services. Therefore, regulating climate and increasing vegetation will maximize the improvement of regional ecosystem services in Xinjiang. Significant differences exist in the counties of the type, intensity, and direction of ecosystem services drivers. The correlation between carbon storage, habitat quality and fractional vegetation cover was more robust stronger in the south. Water yield was more closely related to fractional vegetation cover in southern Xinjiang. Under different ecological and social conditions, the impact of driving forces on ecosystem services showed different changing trends. Three suggestions for improving ecosystem services management were proposed based on our results. The comparative analysis of the driving factors of county ecosystem services in this study will help to formulate differentiated ecological protection policies and promote a sustainable supply of ecosystem services in Xinjiang. In the future, it is necessary to strengthen the long-term monitoring and evaluation of ecosystem services and the research on the interaction of multiple drivers.

KEYWORDS

ecosystem services, spatial pattern, driving factors, remote sensing, InVEST model, multi−scale geographically weighted regression (MGWR), Xinjiang

1. Introduction

Ecosystem services are the benefits humans obtain directly or indirectly from an ecosystem. They serve as a link between humans and nature and have been the focus of considerable research (Costanza et al., 1997). However, the over–exploitation of land resources under climate warming and changing precipitation regimes has led to extensive global species extinctions. Ecosystems and sustainable human development are facing severe threats, and the supply capacity of ecosystem services is gradually declining (Jordan et al., 2005; Dobson et al., 2006). Therefore, it is urgent to support the sustainable use of ecological resources and determine how to use natural capital sustainably. The county scale plays a connecting role in China's ecological protection and restoration. Ecological and socio–economic driving factors affect ecological restoration policies and their implementation (Ding et al., 2022). Therefore, it is essential for guiding ecosystem services management decisions in the spatial distribution, hotspots, and driving factors of ecosystem services that have been examined at the county scale.

Quantifying ecosystem services, identifying ecosystem service hotspots, and investing limited resources in places with the greatest need for protection will help maximize the benefits of these resources. Ecosystem service "hotspots" ("coldspots") have gradually been more commonly used in works on ecosystem services mapping to determine priorities for regional protection (Zhang L. et al., 2015; Wu et al., 2016; Li et al., 2017; Gao et al., 2022). The Gi * statistical method is the most widely used. It can be used to identify spatial clustering of ecosystem services which show strong spatial correlations. This method identify hotspots of ecosystem services and determine which areas multiple ecosystem services are prioritized (Li and Zhang, 2021). The hotspots and coldspots for soil protection are also determined to support targeted ecosystem policy formulation (Li et al., 2017). Random areas are divided according to coldspots and hotspots of ecosystem services to mitigate the adverse impacts on ecosystem services (Han et al., 2020).

Ecosystem services are comprehensively affected by climatical and social factors. Several studies have explored the relationship between ecosystem services and driving factors at global and regional scales (Su et al., 2012; Yang et al., 2021; Rong et al., 2022). However, due to differences in geographical and socio–ecological factors, the response of ecosystem services to driving factors has spatial heterogeneity in direction and intensity. Therefore, the traditional global analysis (generalized linear model and ordinary least squares) cannot reasonably describe the nonstationary relationship in the ecosystem process. Multi–scale geographically weighted regression (MGWR) not only considers spatial non-stationarity, but also considers the scale differences of different variables (Fotheringham et al., 2019), which offers a new idea for the process analysis. For example, Hu et al. (2021) used the MGWR model to investigate the relationship between ecosystem services and drivers in Shanxi Province, which showed pronounced spatial heterogeneity in the nature and intensity of their correlation. Tang et al. (2016) and Luo et al. (2020) proposed differentiated ecological protection policies through quantitative measurement and comparative analysis of driving factors in different regions to promote the ecosystem service value. Therefore, we implement the MGWR model in this study to explore the spatial heterogeneity of ecosystem service drivers. Expected results could clarify the driving factors and mechanisms of ecosystem services and serve as a benchmark for how ecosystem service protection policies in various regions should be measured. The patterns and processes of ecosystem services show different characteristics at different scales, and the influence of scale is the focus of current research. The drivers of ecosystem services are usually related to specific scales, that is, the drivers of ecosystem services may change at different scales. Multiple driving factors of ecosystem services have been evaluated at different scales in macro–regions such as countries and urban belts, and micro–regions such as provinces and cities (Lyu et al., 2019; Chen et al., 2020; Qiu et al., 2020). The relationship between ecosystem services has also varied at different kilometer scales, and may even be the opposite (Liu et al., 2017; Sun et al., 2022). At the county level, the impact of driving forces on ecosystem services significantly differs in the east and west of Sichuan Province (Huang et al., 2022). Significant spatial heterogeneity affects a range of influencing factors in the Three Gorges Reservoir Area on the degree of coupling of ecosystem services and economic development (Li F. et al., 2022). Grid–scale can describe the spatial distribution of ecosystems in more detail, but the county scale is more conducive to ecological management zoning and regulation (Shen and Li, 2022). Therefore, this study studied the spatial distribution, hotspots and driving factors of ecosystem services at the county level.

Xinjiang Autonomous Region has a variety of ecosystems, which can provide various ecosystem services and species habitats. Xinjiang is also a typical arid and fragile ecosystem region, whereas vulnerable to human activities. It is enormously challenging to recover in a short time once it has been degraded. In recent years, population increase and infrastructure construction have accelerated land transformation and environmental degradation. This has resulted in declining in ecosystem services in the entire Xinjiang region. There has been an increase in soil erosion intensity, and a decline in the amount of sand fixation in the north (Zhang W. et al., 2015; Sun et al., 2021; Niu et al., 2022). Therefore, it is an ideal area to study the heterogeneity of ecosystem services and drivers. For example, research shows that the relationship between net primary productivity, soil and water conservation and water yield services in Xinjiang has changed in time and space on the grid scale, but the driving factors have not been analyzed (Wang et al., 2020). There is an essential interaction between urbanization and the continuous expansion of agricultural activities caused by population growth and ecosystem services (Zhang et al., 2020; Shi et al., 2021). Li et al. (2019) showed that the types and intensity of driving factors of ecosystem services in Xinjiang differed between southern and northern Xinjiang. Most studies on ecosystem services in Xinjiang have been undertaken at the grid scale (Wei et al., 2018; Yushanjiang et al., 2018; Lu et al., 2022). Therefore, given the high heterogeneity of Xinjiang's ecosystem, it is significant to study the ecosystem, and its driving factors at the county level for zoning management.

This study aimed to analyze the spatial distribution of ecosystem services, and the spatial heterogeneity of ecosystem services drivers at the county level in Xinjiang. Four typical ecosystem services, namely, carbon storage, habitat quality, sand fixation and water yield were quantified using InVEST and RWEQ model. Redundancy analysis (RDA) was then used to explore the relationship between ecosystem services and climate, vegetation, the proportion of urban area, and other multi–factors. A multi–scale geographically weighted regression (MGWR) model was used to express the spatial heterogeneity of driving factors to provide a reference for the sustainable development of ecosystem services and ecosystem management in Xinjiang.

2. Materials and methods

2.1. Study area

Xinjiang (34° 22′–49° 33′ N, 73° 32′–96° 21′ E) is located in the hinterland of Eurasia near the northwest border of China, with a total area of approximately 166 × 10^4 km^2, including 106 counties (cities and districts). This study's counties, cities and districts are all represented by counties. The land uses comprise grassland (30%), cultivated land, and the Gobi Desert (**Figure 1**). The landforms are relatively complex and are characterized by the distribution of "three mountains and two basins." The specific geographical location and the interaction of various complex geographical environments form various ecosystem types, supporting many rare animal and plant species, such as *Populus canescens*, *Ferula sinkiangensis*, and *Testudo horsfieldii*, etc., (Li et al., 2011). Xinjiang has an arid and semi–arid climate zone, with an annual precipitation of approximately 145 mm. The fractional vegetation cover is generally low, land desertification is severe, and the ecological environment is highly fragile (Liu et al., 2018; Bi et al., 2021).

2.2. Data sources

The research data included land use type data, meteorological data, landform data, and population spatial distribution network datasets (**Table 1**).

2.3. Data processing

The station data of wind speed, precipitation, temperature and sunshine hours are interpolated by the ANUSPLIN method based on thin slice spline theory, with a spatial resolution of 1 km. The vegetation coverage data is derived from MODIS image data (MOD13Q1). First, the NDVI annual data is calculated by resampling, filtering and maximum synthesis methods, and then the maximum annual vegetation coverage data in Xinjiang is calculated according to the pixel dichotomy model theory, with a spatial resolution of 1 km. The percentage of the urban area is calculated by extracting the construction land in each county's land use data and then calculating the percentage of construction land in the whole county.

2.4. Evaluation of ecosystem services

A series of ecological problems have emerged in Xinjiang, including water shortages, soil erosion, and desertification (Zhang W. et al., 2015; Chen et al., 2016). Therefore, according to the classification of ecosystem services proposed by the Millennium Ecosystem Assessment (Reid et al., 2005), four important ecosystem services were selected and combined with the current ecosystem and ecological pressure in the study area. This included carbon storage, habitat quality, sand fixation, and water yield. Carbon storage is vital in climate regulation (Xu et al., 2019). Diversified ecosystems provide habitats for organisms (Liu and Xu, 2020). Xinjiang has a large area of sand and bare land, and sand erosion by wind is severe (Gong et al., 2014). The lack of water resources and the uneven spatial and temporal distributions are the main influencing factors restricting economic development in Xinjiang (Li F. et al., 2022). The ecosystem services was quantified at a 1 km^2 scale in 2020, and then the mean values of ecosystem service indicators at the county scales was calculated. The county scale was chosen because it is more conducive to ecological management zoning and regulation.

2.4.1. Carbon storage (CS)

Carbon storage in ecosystem services plays a vital role in climate regulation and is an essential indicator for measuring the function of regional ecosystems. Strengthening the carbon fixation function of terrestrial ecosystems has become one of the primary needs in mitigating global climate change (Hu et al., 2018). The carbon pool (C_{total}) includes the aboveground biomass (C_{above}), underground biomass (C_{below}), dead organic carbon (C_{dead}), and soil carbon pool (C_{soil}). The four carbon reserve types were added to the InVEST model to determine the carbon reserves in the area. The calculation formula is as follows:

$$C_{total} = C_{above} + C_{below} + C_{soil} + C_{dead} \tag{1}$$

2.4.2. Habitat quality (HQ)

Habitat quality refers to the ability of ecosystems to provide living conditions suitable for individuals and populations based on the availability of living resources, biological reproduction, and existing quantity. It can reflect regional biodiversity and is closely related to regional land use types (Fellman et al., 2015; Sallustio et al., 2017). The habitat quality module of the InVEST model is based on the relationship between land use and stress factors. It considers the sensitivity of different habitat types to stress factors and the threat intensity from these stress factors. The degree of habitat degradation is calculated and then combined with the habitat adaptability of different land use types to score the habitat quality to generate a habitat quality grade map. The specific calculation process is as follows:

$$D_{xj} = \sum_{r=1}^{R} \sum_{y=1}^{Y_r} \left(\frac{W_r}{\sum_{r=1}^{R} W_r} \right) r_y i_{rxy} \beta_x S_{jr} \tag{2}$$

Where D_{xj} is the habitat degradation level of pixel x in habitat type j; r refers to a single stress factor; y is the pixel of stress factor r; W_r is the stress factor weight; r_y is the number of stress factors in each grid of the study area; β_x is the threat level of habitat pixel; S_{jr} is the sensitivity of habitat type j to stress factors and i_{rxy} is the threat level of stress factor in pixel y to habitat pixel x.

$$Q_{xj} = H_j \left(1 - \frac{D_{xj}^{x}}{D_{xj}^{z} + k^z} \right) \tag{3}$$

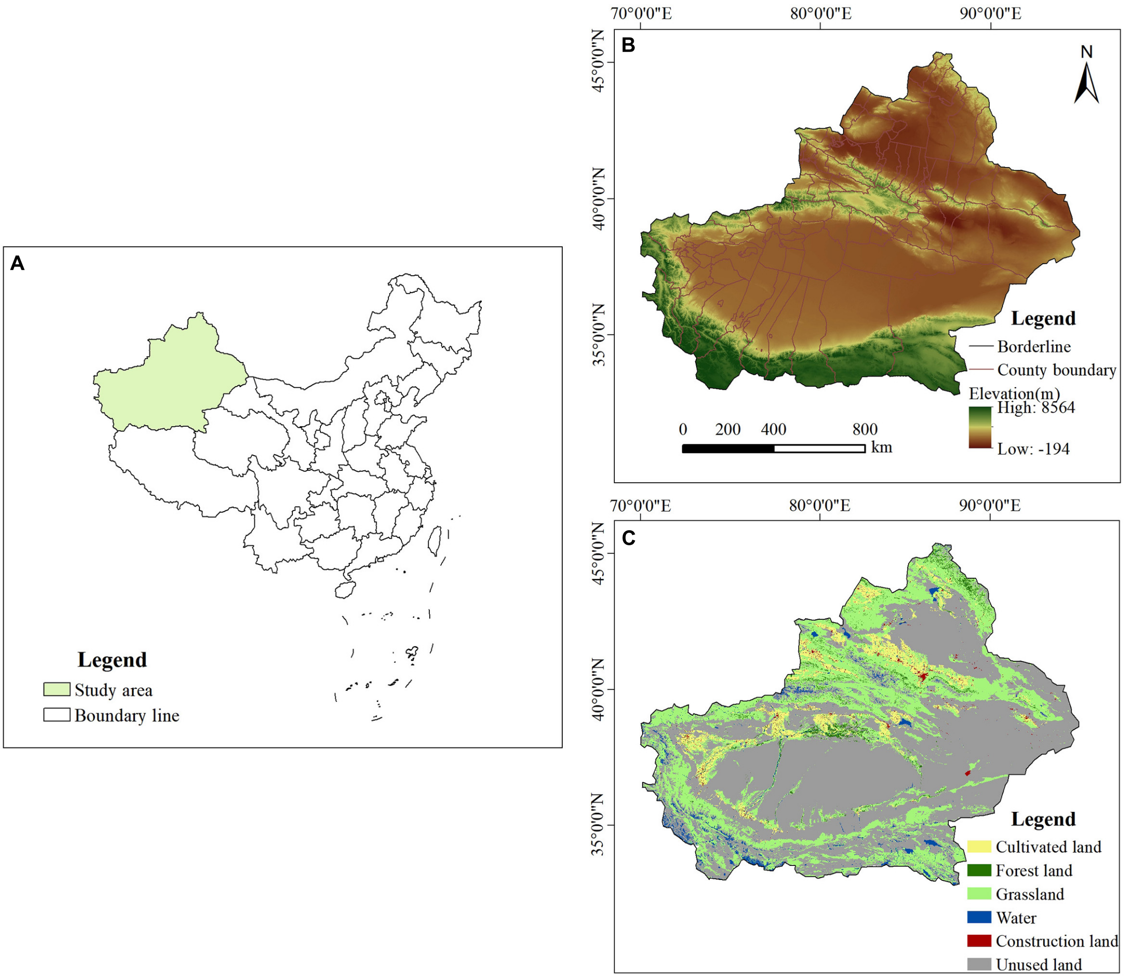

FIGURE 1
Location, elevation, and land use type of the study area. **(A)** Xinjiang location. **(B)** Elevation. **(C)** Land use type.

Where Q_{xj} is the habitat quality level of pixel x in habitat type j; H_j is the habitat adaptability of habitat type j; z is a constant, usually 2.5; k is the semi–saturation constant, and the default value is 0.5.

2.4.3. Sand fixation (SF)

Sand fixation is an important ecosystem function. Sand fixation can reduce soil erosion caused by wind erosion through its structure and processes. This soil conservation and wind erosion inhibition service is the sand fixation service. This is the most important protective service provided by the ecosystem in arid and semi–arid areas. The revised wind erosion equation (RWEQ) was used to estimate the sand fixation at the plot scale, taking into account the climate conditions, surface soil roughness, vegetation conditions, soil erodibility, and soil crust:

$$SR = SL_S - SL \tag{4}$$

$$Q_x = \frac{Q_{max}\left[1-e^{\left(\frac{x}{s}\right)^2}\right]}{x} \tag{5}$$

$$\mathrm{Q_{max}} = 109.8\left(\mathrm{WF} \times \mathrm{EF} \times \mathrm{SCF} \times \mathrm{K}' \times \mathrm{COG}\right) \tag{6}$$

Where SR is the sediment fixation amount ($\mathrm{t} \cdot \mathrm{hm}^{-2}$), SL_S is the potential soil wind erosion under the condition of potential bare soil, $\mathrm{t} \cdot \mathrm{hm}^{-2}$; SL is the actual soil wind erosion under fractional vegetation cover, $\mathrm{t} \cdot \mathrm{hm}^{-2}$; Q_x is the sand flux at x ($\mathrm{kg} \cdot \mathrm{m}^{-1}$); x is the length of the plot; Q_{max} is the maximum transfer amount, kg/m; s is the length of the key plot (m); WF is the climate factor, which is calculated from wind speed, soil moisture factor and snow cover factor; $K^{'}$' is the surface roughness factor; EF is the erodible soil factor, calculated according to Fryrear et al. (2000) equation; SCF is the soil crust factor, and COG is the fractional vegetation cover factor, which is calculated by vegetation coverage.

2.4.4. Water yield (WY)

The water yield service is one of the essential ecosystem services in arid and semi–arid areas. It is crucial to agriculture, industry, hydropower generation, and entertainment activities. It is also an important link in achieving sustainable development of ecosystem services. The water yield service was predominantly based on the water production module in the InVEST model, that is, the water yield per unit area at a specific time. According to the water balance principle, the regional water supply is the precipitation per unit

TABLE 1 Study data sources.

Data type	Data description	Data sources
Meteorological data	Daily average temperature, daily precipitation, daily average wind speed, sunshine duration (point data.)	The China Meteorological Data Service Center (http://data.cma.cn/)
	Monthly value of rainfall and potential evapotranspiration data (1 km)	National Earth System Science Data Center (http://www.geodata.cn/)
Land use data	Based on landsat TM image (1 km)	Research and Environment Science and Data Center (https://www.resdc.cn)
Fractional vegetation cover	Calculated by pixel dichotomy based on NDVI data (250 m)	https://ladsweb.modaps.eosdis.nasa.gov
Snow depth, Soil attribute data	Snow depth, soil attribute table and spatial distribution, soil calcium carbonate content distribution data	Environmental and Ecological Science Data Center for West China (http://westdc.westgis.ac.cn)
Digital elevation model (DEM) data	SRTMDEMUTM 90 m resolution digital elevation data product	Geospatial Data Cloud (http://www.gscloud.cn/)
Population density	Raster data (1 km)	WorldPop (http://www.worldpop.org/)

area minus evapotranspiration. The main formula for calculating the water yield under each grid pixel is:

$$Y_{x,j} = \left(1 - \frac{AET_{x,j}}{P_x}\right) \cdot P_x \tag{7}$$

$$\frac{AET_{xj}}{P_x} = \frac{1 + \omega_x R_{xj}}{1 + \omega_x R_{xj} + \left(\frac{1}{R_{xj}}\right)} \tag{8}$$

$$\omega_x = Z \frac{AWC_x}{P_x} \tag{9}$$

Where $Y_{x,j}$ is the water yield of pixel x of land use type j (mm); P_x is the annual precipitation on different pixels x (mm); $AET_{x,j}$ is the annual actual evapotranspiration of pixel x of land cover type j (mm); ω_x is the ratio of annual vegetation available water and precipitation; R_{xj} is the dry coefficient; and AWC_x is the effective moisture content of vegetation of pixel x (mm), and Z is Zhang's coefficient.

2.5. Analysis of ecosystem services hotspots

Spatial hotspot analysis can identify high–value spatial clusters of specific phenomena, limited direct resources to places with greater need, and achieve more effective and strategic resource allocation. This technique has been widely used in the field of ecological geography. In this study, the county was taken as the smallest unit, using the "Zone Statistics as Table" in ArcGIS 10.8 to calculate the average value of ecosystem services and drivers in each county. The Getis Ord Gi * method in the ArcGIS 10.8 hotspot analysis tool was used to identify the hotspot area with solid spatial correlation and the coldspot area with weak spatial correlation of ecosystem services. The Z score is statistically significant in Getis Ord Gi *. The larger the Z–score, the higher the cluster value (hotspots). The smaller the Z–score, the lower the cluster value (coldspots) (Benjamini and Yekutieli, 2001).

2.6. Drivers analysis

Factors affecting ecosystem services mainly include two types: ecological factors and socio–economic factors (Hu et al., 2022; Huang et al., 2022; Lu et al., 2022; Zhuang et al., 2022). The ecological factors selected in this study include precipitation (PRE), temperature (TEM), fractional vegetation cover (FVC), slope (SL), and digital elevation model (DEM). Social factors include a percentage of urban area (PU) and population density (PD) (Peng et al., 2017). RDA was used to detect the relationship between multiple response variables, such as ecosystem services and several explanatory variables such as drivers. This study used RDA to analyze the multicollinearity relationship between variables and perform a collinearity test in SPSS. When $0 < \text{VIF}$ (Variance inflation factor) < 10, it indicates that there is no collinearity for the driver (Sheng et al., 2017). Canoco software (version 5.0) was used to explore the correlation between ecosystem services and impact factors using RDA.

Geographically weighted regression (GWR) establishes the regression relationship between independent and dependent variables at the local scale, effectively avoiding errors caused by spatial differences of variables. The expression is as follows:

$$y_i = \beta_0 (u_i, v_i) + \sum_{j=1}^{p} \beta_j (u_i, v_i) x_{ij} + \varepsilon_i, i \in \{1, 2, \cdots, n\} \tag{10}$$

Where y is the dependent variable (including different types of ecosystem services); (u_i, v_i) is the position of the ith sample; $\beta_j (u_i, v_i)$ is the intercept; x_{ij} is the independent variable, including altitude, precipitation and other factors; $\beta_j(u_i, v_i)$ represents the regression coefficient of the ith sample for the jth driving factor, and ε_i is the error term.

Multi–scale geographically weighted regression (Oshan et al., 2019) is an improved version of GWR, which considers spatial multi–scale heterogeneity and reflects these differences in ecosystem services. The MGWR model expression is as follows:

$$y_i = \beta_0 (u_i, v_i) + \sum_{j=1}^{p} \beta_{bwj} (u_i, v_i) x_{ij} + \varepsilon_i, i \in \{1, 2, \cdots, n\} \tag{11}$$

Where β_{bwj} in bwj is the broadband used to calibrate the jth conditional relationship. MGWR allows local regression coefficients of dependent and independent variables to be estimated at different spatial scales.

In this study, the MGWR and GWR models used the Gaussian kernel function and golden section broadband selection routine for calibration. The OLS, GWR, and MGWR parameters were then compared. The higher R^2 indicates a better degree of the fitting. All the model calibrations were performed using MGWR2.2 software.

3. Results

3.1. Analysis of ecosystem services patterns

Four ecosystem services, namely, carbon storage, habitat quality, sand fixation and water yield were significantly different across the entire Xinjiang region (**Figure 2**), and they clustered in space (Moran's $I > 0.43$, $p < 0.001$). Due to Xinjiang's geographical location, the spatial heterogeneity of water and heat conditions was relatively high. As a result, the spatial distribution of various ecosystem services was quite different. Carbon storage, habitat quality, and water yield presented similar spatial patterns. High–value areas were predominantly distributed in the Tianshan Mountains and the eastern part of the Kunlun Mountains, as well as the Ili Kazakh Autonomous Prefecture, Altay City, Burqin County, and Habahe County near the Altay Mountains. Important areas of forest land and grassland were distributed in these areas. At the county scale, the maximum carbon storage, sand fixation and water yield per unit area are 116.4 t/hm^2, 385.2 t/hm^2, and 291.17 mm. The highest habitat quality in Xinyuan County of Ili Kazak Autonomous Prefecture is 0.78. Among them, there was a significant difference in water yield between the north and the south. High–value areas were mainly distributed in the north of Xinjiang. High–value water source protection areas were found in Altay and Tacheng. In the south of Xinjiang, the water yield of 30 counties is lower than 0. The high–value areas for sand fixation had a dispersed distribution and were predominantly in the east of the Taklimakan Desert, around the Altun Mountains, and near the Junggar Basin. The altitude was 500–1,000 m, the wind speed was relatively low, and the service level for sand fixation on the construction land was high, possibly due to buildings blocking some of the wind. In general, the spatial distribution of ecosystem services was higher in the north and lower in the south.

3.2. Analysis of ecosystem services hotspots

Regarding individual ecosystem services, the spatial pattern of hotspots and coldspots of ecosystem services showed pronounced spatial heterogeneity (**Figure 3**). The hotspots were predominantly concentrated in northern Xinjiang. Compared with the other three services, hotspots for water yield services were the largest, with 49 counties accounting for 46.23% of the total number in Xinjiang. They were mainly distributed in the Altay region, a national key ecological functional area for water conservation. The hotspots for carbon storage and habitat quality were highly coincident, with 35 and 31 counties, respectively, mainly distributed in Ili Kazakh Autonomous Prefecture, Bortala Mongolian Autonomous Prefecture, and Tacheng region in the west of the Tianshan Mountains. The hotspot area is mainly forest with strong carbon storage capacity, while the coldspot area is mainly unused land, cultivated land and other land use types with weak carbon storage capacity. As a whole, the level of habitat quality in Xinjiang is low. Due to urbanization construction, the surface vegetation is destroyed and the habitat quality is degraded. There are 39 counties serving as hotspots for sand fixation, and 48 counties serving as coldspots. Owing to the vast expanse of desert, sand fixation capacity in Xinjiang is weak, and the number of cold spots is larger than that of hotspots, mainly located in the northern part of Xinjiang.

Four counties, namely, Kuitun City, Huyanghe City, the Duzi Mountain Area and Karamay City provided four ecosystem service types. At the same time, there are 26 counties with three kinds of ecosystem service hotspots and 21 counties with two kinds of ecosystem service hotspots. These areas can be classified and managed according to the actual situation, prioritizing protecting cold spot services (**Figure 4**). In general, the supply capacity of ecosystem services in these areas is relatively low due to the ecological degradation in most of northern Xinjiang. In the future, we should not only maintain the ecosystem services of hotspots, but also take measures to improve the ecosystem services of coldspots.

3.3. Drivers analysis

3.3.1. Drivers of ecosystem services

We used the variance expansion factor for diagnosis. As shown in **Table 2**, VIF < 10 indicates no multicollinearity between the seven drives. **Figure 5** showed that ecosystem services were significantly correlated with the precipitation, fractional vegetation cover, the percentage of urban area, DEM, temperature ($p < 0.01$), and population density ($p < 0.05$). Ecological factors predominantly determined the first RDA axis explaining 49.01% of the variance. Social factors and altitude mainly determined the second axis explaining 14.87% of the variance. Precipitation and fractional vegetation cover contributed 61.7 and 17.0% to ecosystem services, respectively, which was considered decisive. This showed that precipitation and fractional vegetation cover were the main limiting factors for ecosystem services in Xinjiang. The percentage of urban area was also an important factor with an 8.7% contribution, indicating that urbanization considerably affected ecosystem service. Precipitation, fractional vegetation cover, and slope were positively correlated with water yield, carbon storage, and habitat quality, and were negatively correlated with sand fixation. Temperature, population density, and the percentage of urban area were positively correlated with sand fixation. However, these factors had little impact on ecosystem services. In general, the contribution of ecological factors was substantially higher than social factors, which indicated that precipitation, fractional vegetation cover, and terrain played an important role in the spatial distribution of ecosystem services in Xinjiang.

3.3.2. Spatial heterogeneity of ecosystem service drivers

The MGWR model was used to determine the spatial distribution of the influence of different driving factors on the change in ecosystem services. The Akaike information criterion (AIC) and calibration R^2 are widely used to describe the predictive power of models, whereby the lower the AIC, the closer the situation is to reality. The higher the adjusted R^2, the better the variance explanation. In general, the MGWR had strong explanatory power (**Table 3**).

The MGWR regression coefficient was positive, indicating that increasing influencing factors will increase the ecosystem service

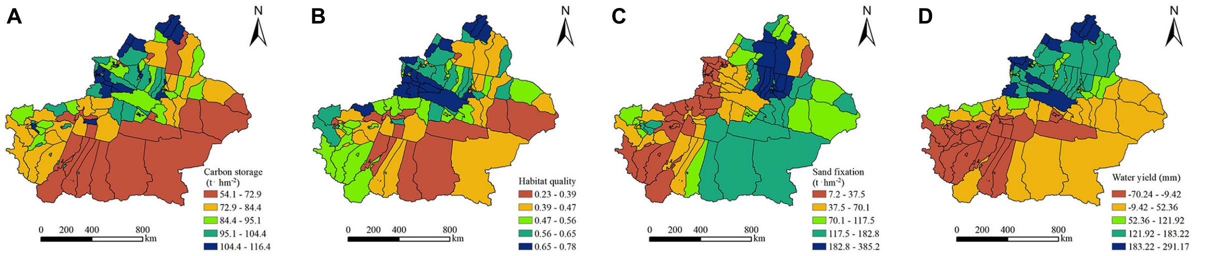

FIGURE 2
Spatial distribution of ecosystem services. **(A–D)** Carbon storage, Habitat quality, Sand fixation, and Water yield.

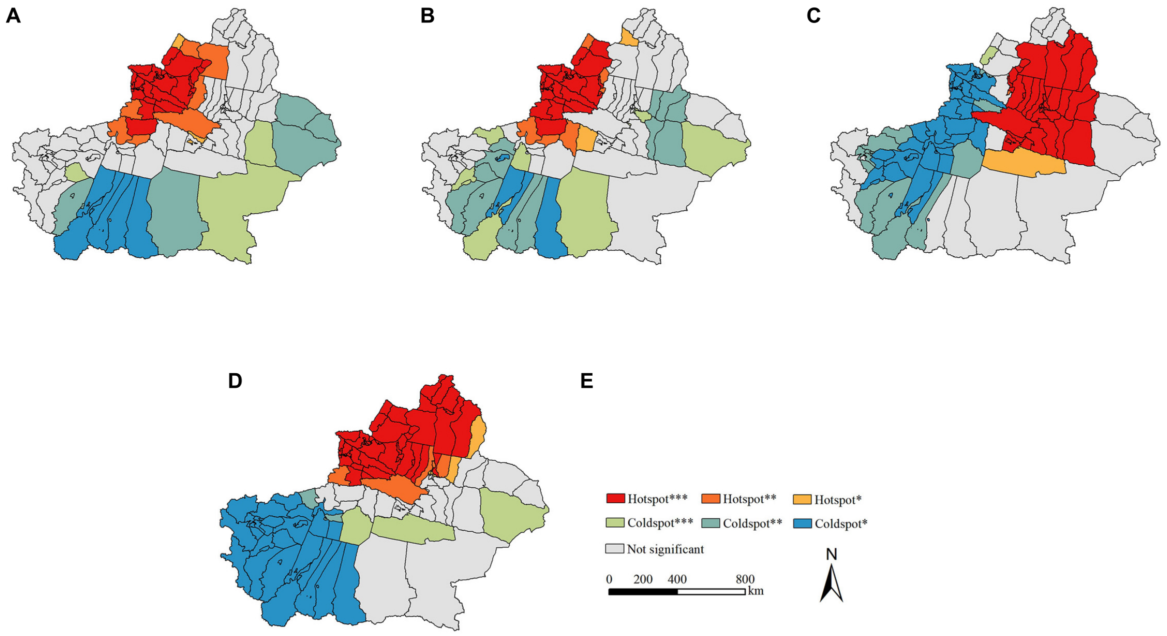

FIGURE 3
Spatial distribution of ecosystem service hotspots and coldspots. The statistical significance is shown as follows: (1) *** refers to the 99% confidence level; (2) ** refers to the 95% confidence level, and (3) * represents the 90% confidence level. **(A–D)** Carbon storage, Habitat quality, Sand fixation, and Water yield. **(E)** Legend.

level. Meanwhile, the negative regression coefficient indicated that increased in influencing factors would reduce the ecosystem service level. The results have shown that the regression coefficients in different regions had different values. In Xinjiang, the local coefficients for the seven drivers varied between counties, which reflected the non–stationary spatial response of ecosystem services to the influencing factors in Xinjiang. The seven influencing factors selected in this study could explain 73.0, 79.0, 77.1, and 97.8%, of carbon storage, habitat quality, sand fixation and water yield, respectively (Table 4).

Figure 6 and Table 4 show that carbon storage and habitat quality correlate strongly with fractional vegetation cover, with correlation coefficients of 0.737 and 0.440, and higher in the south. The correlation between carbon storage and precipitation, the percentage of urban area gradually increases from north to south (Figures 6C, D). The relationship between habitat quality and precipitation gradually increases from east to west (Figure 6F). The proportion of urban areas will lead to the reduction of habitats suitable for biological survival and the reduction of habitat quality (Figure 6G). There is a negative correlation between sand fixation and the percentage of urban area. The impact direction and intensity of precipitation on sand fixation in different regions of Xinjiang are also very different (Figure 6I). Temperature, DEM, and fractional vegetation cover negatively impacted water yield, with correlation coefficients of −0.730, −0.639 and −0.139, respectively. Precipitation has a direct positive impact on water yield, and the correlation coefficient is 0.693. The relationship between fractional vegetation cover and water yield is closer in the south of Xinjiang. In the north, the relationship between water yield and DEM, temperature and precipitation is closer. With the intensification of human activities and the increase in domestic water consumption, with the increase of cultivated land in the north, the expansion of irrigation area has increased evaporation to a certain extent, negatively impacting water yield (Liang et al., 2021). To sum up, ecological factors were the main driving factors for changes in regional ecosystem services. Therefore, regulating climate and increasing vegetation will maximize the improvement in regional ecosystem services.

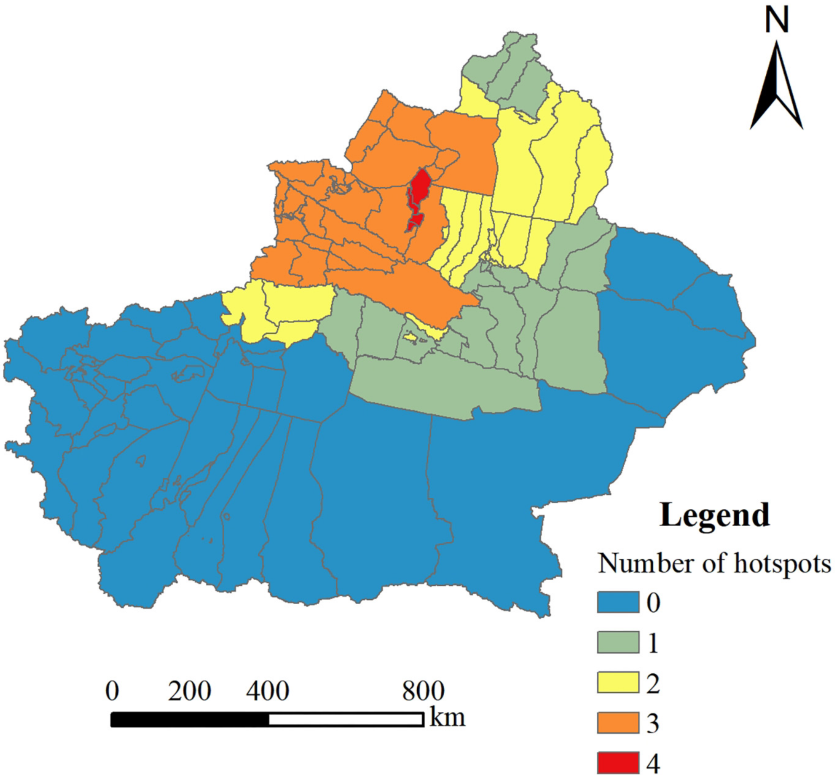

FIGURE 4
Concurrence of the four ecosystem service hotspots.

TABLE 2 Collinearity test.

Variable	Digital elevation model	Slope	Fractional vegetation cover	Precipitation	Temperature	Percentage of urban area	Population density
VIF	5.700	7.063	1.893	3.759	4.158	5.316	4.937

The spatial correlation and correlation intensity changes between the seven factors selected and the four ecosystem services were significantly different. This indicated that the ecosystem services in different regions were affected by different factors and that zoning management may be crucial to the sustainable supply of ecosystem services.

4. Discussion

In this study, our results show that high-value areas for carbon storage, habitat quality, sand fixation, and water yield, were predominantly distributed in the Tianshan Mountains, Altai Mountains, and oases around the southern Tarim Basin across Xinjiang. It is consistent with the finding of Wang et al. (2020). It was mainly attributed to the large area of forest land and grassland in the north, where is abundant rain, provides excellent habitat for species, and has a high capacity for carbon storage and sand fixation (Li et al., 2021). Altay, known as the "water tower" in northern Xinjiang, is a water conservation type mountain grassland ecological functional area that has significantly improved water supply. Therefore, conserving of mountain vegetation and water resources is a top priority for sustainable development in Xinjiang. Identifying the hotspots of ecosystem services helps to set priorities and take measures to maintain the level of ecosystem services. In the coldspots of ecosystem services, we should take targeted measures to improve the level of ecosystem services by analyzing the driving factors of ecosystem services.

According to the results of RDA and the regression coefficient of the MGWR model, we found that ecological and social factors significantly differ in the impact of ecosystem services in different regions. The comprehensive impact of precipitation and fractional vegetation cover on ecosystem services is significantly stronger than other factors (**Figure 5**). Precipitation is the main factor affecting the water yield in Xinjiang, and its coefficient value increases from south to north in turn (**Figure 6N**). Previous studies have shown that precipitation increase is the most important factor, because it significantly affects water volume and land hydrological process (Ziadat and Taimeh, 2013; Ma et al., 2021a,b). Temperature reduces water yield by affecting precipitation and evapotranspiration. Climate change can affect the distribution of water production by affecting hydrological processes and energy balance. Therefore, climate change can affect the water yield by changing the precipitation and temperature of Xinjiang. Sand fixation is affected by precipitation, vegetation and human activities, showing spatial heterogeneity, reflecting the comprehensiveness and complexity of

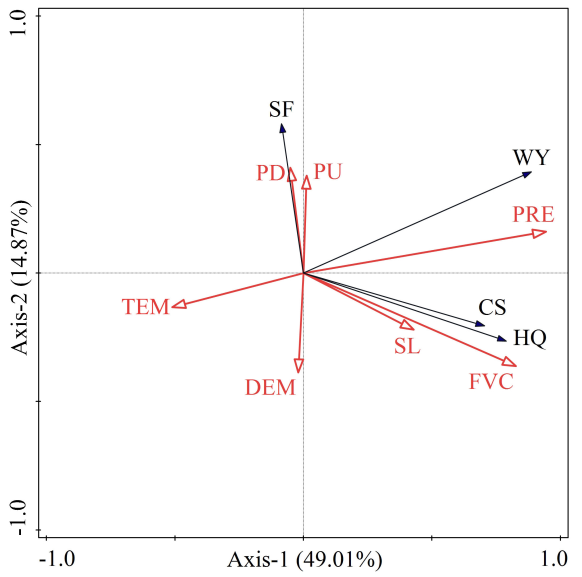

FIGURE 5
RDA showing the relationship between four ecosystem services and seven ecological, social drivers. The black arrow represents ecosystem services, and the red arrow represents ecological, and social driving factors. CS, carbon storage; HQ, habitat quality; SF, sand fixation; WY, water yield; DEM, digital elevation model; SL, slope; FVC, fractional vegetation cover; PRE, precipitation; TEM, temperature; PU, percentage of urban area; PD, population density.

the ecological process (Gong et al., 2022; Niu et al., 2022; Cui et al., 2023). From the perspective of the regression coefficient, fractional vegetation cover and precipitation strongly impact windbreak and sand fixation, and are the main driving factors for sand fixation. Higher precipitation can promote the growth of vegetation, which is conducive to soil surface crusting and thus enhance the resistance of the surface to wind erosion (Wu et al., 2021). The spatial distribution of precipitation in Xinjiang is extremely uneven, resulting in strong spatial heterogeneity of the impact of precipitation on sand fixation. Fractional vegetation cover can affect the wind erosion resistance of soil by affecting temperature, humidity and evapotranspiration (Řeháček et al., 2017). Fractional vegetation cover in eastern Xinjiang is low, and evaporation reduces the water content, which may be the reason for the spatial differentiation of the impact of fractional vegetation cover on sand fixation in eastern and western regions.

The carbon storage of terrestrial ecosystems is mainly distributed in vegetation and soil carbon pool, and the correlation between carbon storage and fractional vegetation cover is the strongest. There is a negative correlation between carbon storage and slope. When the slope is gentle, the soil erosion intensity is small, the conversion rate of microorganism to soil organic matter is low, and the soil carbon loss is low, conducive to carbon storage and fixation (Olson et al., 2012). Habitat quality is mainly affected by vegetation coverage, however, He et al. (2017) showed that habitat quality is mainly affected by land use types given that extensive construction land will occupy biological habitat. An important breakthrough required to improve the habitat quality in Xinjiang is to strategically determine the scope of construction land expansion from the perspective of land use, increase development of unused land, and reduce damage to forest land, grassland, and other natural landscapes (Deng et al., 2021). The study shows that the correlation between social factors and ecosystem services is weak, and there is spatial heterogeneity in direction and intensity, consistent with previous research results (Bennett et al., 2009; Guo et al., 2021). However, Zhang et al. (2020) showed a strong interaction between ecosystem services and human activities in Xinjiang, mainly due to differences in calculation methods and human activity indicators. In this study, the MGWR model was used to distinguish the spatial relationship strength between ecosystem services and driving factors, and the key factors affecting ecosystem services were identified from the perspective of spatial non–stationary, but the interaction between several variables could not be investigated.

This study reveals the impact of driving factors on ecosystem services in space, which is crucial to ecosystem service management. On this basis, three suggestions were put forward to improve the management of ecosystem services in

TABLE 3 Comparison of OLS, GWR, and MGWR model parameters.

Ecosystem services	AICc			Adjusted R^2			Moran's *I*	*p*
	AICc_{O}	AICc_{G}	AICc_{M}	R_{O}^{2}	R_{G}^{2}	R_{M}^{2}		
Carbon storage	192.647	194.985	183.599	0.680	0.679	0.730	0.430	0
Habitat quality	157.079	159.684	155.658	0.771	0.774	0.790	0.454	0
Sand fixation	270.976	228.461	182.647	0.330	0.656	0.771	0.725	0
Water yield	−17.932	−36.002	−73.216	0.956	0.968	0.978	0.833	0

TABLE 4 Mean of regression coefficient of ecosystem services and drivers in the MGWR model.

Mean value of correlation coefficient	Digital elevation model	Slope	Fractional vegetation cover	Precipitation	Temperature	Percentage of urban area	Population density
Carbon storage	0.275	−0.324	0.737	0.280	−0.019	0.259	−0.188
Habitat quality	0.080	0.137	0.440	0.271	−0.206	−0.335	0.073
Sand fixation	0.109	−0.178	−0.153	0.167	−0.032	−0.251	0.285
Water yield	−0.639	−0.064	−0.139	0.695	−0.730	0.026	−0.002

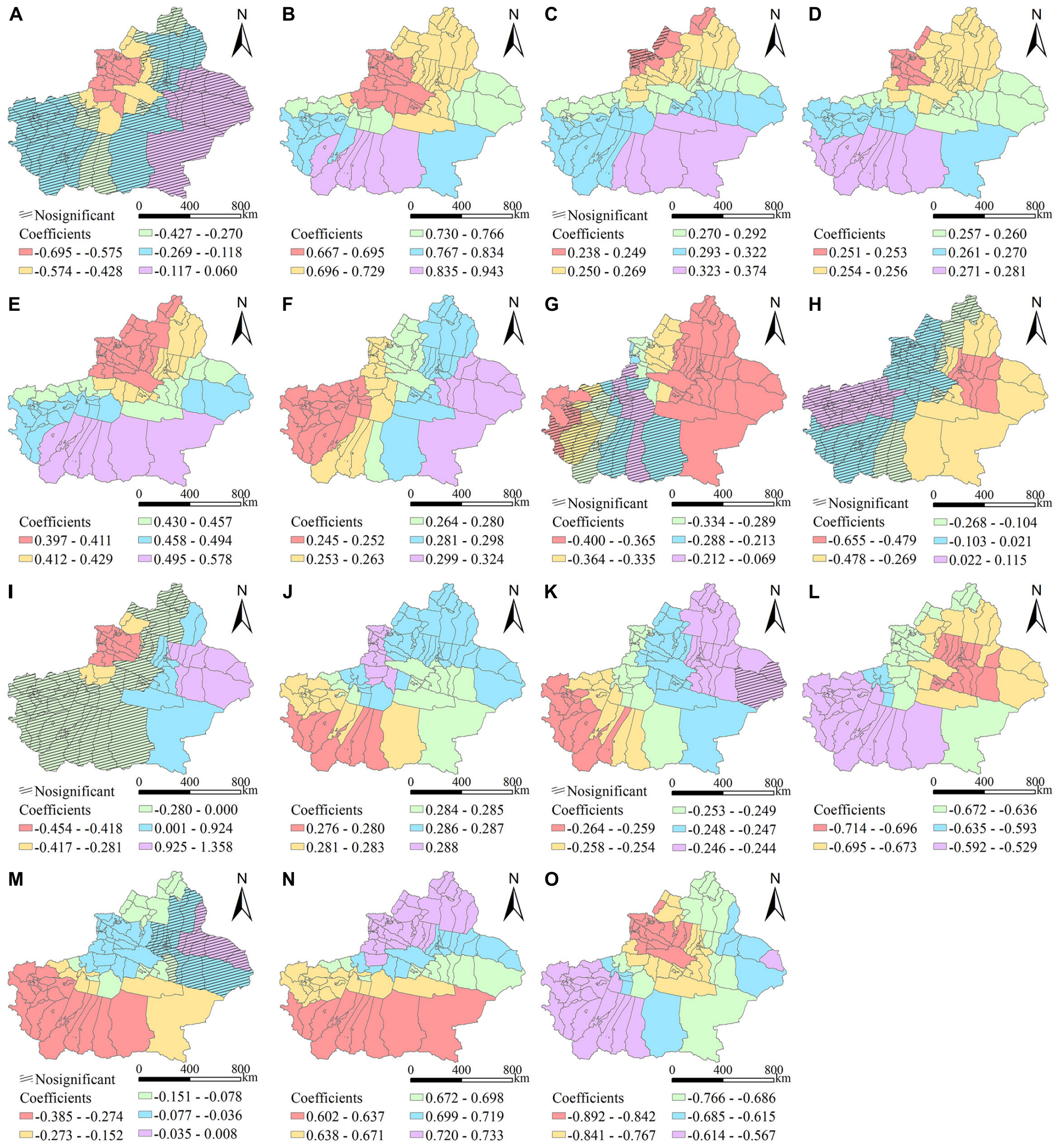

FIGURE 6

Expression of spatial heterogeneity of drivers. **(A–D)** CS–SL, CS–FVC, CS–PRE, and CS–PU. **(E–G)** HQ–FVC, HQ–PRE, and HQ–PU. **(H–K)** SF–FVC, SF–PRE, SF–PD, and SF–PU. **(L–O)** WY–DEM, WY–FVC, WY–PRE, and WY–TEM. (CS, carbon storage; HQ, habitat quality; SF, sand fixation; WY, water yield; DEM, digital elevation model; SL, slope; FVC, fractional vegetation cover; PRE, precipitation; TEM, temperature; PU, percentage of urban area; PD, population density).

Xinjiang. This study has shown that among the ecological factors, temperature had the largest negative correlation with ecosystem services (**Figures 5**, **6**). This indicated that policymakers should attempt to reduce temperature to improve ecosystem services. Crops can reflect sunlight to reduce temperature. According to the differences in climate, landform, and other conditions of counties, selecting suitable crops can effectively reduce the surface temperature (Ridgwell et al., 2009). Second, water is the lifeline of sustainable development in Xinjiang. The main potential of water–saving in Xinjiang lies in agriculture. On the one hand, we should strengthen the construction of farmland and water conservancy infrastructure, and on the other hand, we should implement sustainable farmland to restore rivers and lakes to reduce habitat fragmentation caused by human activities (Wang et al., 2017). Third, ecosystem service hotspots should be reserved to avoid being damaged. In this study, the hotspots of ecosystem services mainly appear in areas with high vegetation coverage, while the coldspots appear in areas with high unused land (**Figure 6**). Based on this, we suggest that the afforestation plan should be appropriately implemented in the coldspot area in combination with local conditions. However, farmers often destroy forests to increase their income. Appropriate commercial plants can be introduced into mixed agriculture to protect biodiversity and farmers' livelihoods (Njurumana et al., 2021).

This study focused on the spatial distribution, hotspots, and driving factors of ecosystem services, which can provide a reference for ecosystem management in Xinjiang. However, there were still some limitations in this study. Our method only captured the relationship between ecosystem services and their social drivers in 2020. However, the study lacked provision for long–term monitoring and assessment of changes in ecosystem services. Future research should focus on the "over time" approach. In addition, we only focused on four typical ecosystem services in Xinjiang, excluding other supply services such as food and cultural services such as tourism. There are many scenic spots in Xinjiang. The spatial area of cultivated land and grassland is relatively large, and the self–sufficiency rate for grain, oil, meat, eggs, and milk is relatively high. Therefore, the comprehensive assessment of ecosystem services should be the focus of future research (Castillo-Eguskitza et al., 2018). To date, most studies on the impact of ecosystem services have only focused on a single factor while excluding the impact of the effects on ecosystem services. However, the response of ecosystem services to climate factors is not a simple, isolated, linear response, but rather an in–depth response to multiple climate factors, vegetation conditions, and other conditions (Xue et al., 2023). Therefore, it is necessary to strengthen research on the compounding mechanisms of ecological and social factors on ecosystem services. Regional differences and the main driving factors should be considered when formulating policies.

5. Conclusion

Based on the InVEST and RWEQ models, this study evaluated ecosystem service hotspots and determined the priority for their protection by exploring the spatial distribution of carbon storage, habitat quality, water yield and sand fixation in Xinjiang. RDA and MGWR models analyzed the driving factors of ecosystem services and their spatial differentiation by integrating climate, vegetation, terrain, and social factors. The results showed that the ecosystem services (carbon storage, habitat quality, sand fixation and water yield) showed spatial heterogeneity at the county level. The high–value areas of ecosystem services were consistent with the hotspots, mainly distributed in the north of Xinjiang, e.g., Ili Kazak Autonomous Prefecture, Bortala Mongolian Autonomous Prefecture, Tacheng Prefecture and Altay Prefecture. The types, intensities, and directions of ecosystem services drivers were significantly different at counties scale. There was a stronger correlation between carbon storage, habitat quality and fractional vegetation cover in the southern regions. Water yield was affected by many drivers, and is more closely related to fractional vegetation cover in southern Xinjiang. This study contributes to determining the local characteristics that affect ecosystem services and formulating effective ecosystem management policies for different regions, intending to provide a reference for sustainable development and ecological security of ecosystems in Xinjiang.

Data availability statement

The raw data supporting by the conclusions of this article will be made available by the authors, without undue reservation.

Author contributions

HW and ZZ conceived the study. HW obtained funding for the study. LH and ZZ performed the statistical analysis. ZZ produced the figures and tables and wrote the first draft of the manuscript. SP modified and checked this manuscript. All authors contributed to the article and approved the submitted version.

Funding

This work was supported by the National Key R&D Program of China (Grant No. 2021YFB2600101), NSFC–RS exchange project between China and the UK (Grant No. 42011530175), and the National Natural Science Foundation of China (Grant No. 41801366).

Acknowledgments

We would like to acknowledge Editage (https://editage.com/) for English language editing.

Conflict of interest

The authors declare that the research was conducted in the absence of any commercial or financial relationships that could be construed as a potential conflict of interest.

Publisher's note

References

Benjamini, Y., and Yekutieli, D. (2001). The control of the false discovery rate in multiple testing under dependency. *Ann. Stat.* 29, 1165–1188. doi: 10.1214/aos/1013699998

Bennett, E. M., Peterson, G. D., and Gordon, L. J. (2009). Understanding relationships among multiple ecosystem services. *Ecol. Lett.* 12, 1394–1404. doi: 10.1111/j.1461-0248.2009.01387.x

Bi, X., Chang, B., Hou, F., Yang, Z., Fu, Q., and Li, B. (2021). Assessment of spatio-temporal variation and driving mechanism of ecological environment quality in the Arid regions of central asia, Xinjiang. *Int. J. Environ. Res. Public Health* 18:7111. doi: 10.3390/ijerph18137111

Castillo-Eguskitza, N., Martín-López, B., and Onaindia, M. (2018). A comprehensive assessment of ecosystem services: Integrating supply, demand

and interest in the Urdaibai Biosphere Reserve. *Ecol. Ind.* 93, 1176–1189. doi: 10.1016/j.ecolind.2018.06.004

Chen, T., Feng, Z., Zhao, H., and Wu, K. (2020). Identification of ecosystem service bundles and driving factors in Beijing and its surrounding areas. *Sci. Total Environ.* 711:134687. doi: 10.1016/j.scitotenv.2019.134687

Chen, Y., Li, W., Deng, H., Fang, G., and Li, Z. (2016). Changes in central asia's water tower: Past, present and future. *Sci. Rep.* 6:35458. doi: 10.1038/srep35458

Costanza, R., d'Arge, R., de Groot, R., Farber, S., Grasso, M., Hannon, B., et al. (1997). The value of the world's ecosystem services and natural capital. *Nature* 387, 253–260. doi: 10.1038/387253a0

Cui, L., Shen, Z., Liu, Y., Yu, C., Lu, Q., Zhang, Z., et al. (2023). Identification of driving forces for windbreak and sand fixation services in semiarid and arid areas: A case of Inner Mongolia, China. *Prog. Phys. Geogr. Earth Environ.* 47, 32–49. doi: 10.1177/03091333221105403

Deng, C., Guo, F., Huang, D., and Li, Z. (2021). Research on the impact of land use and lansacpe pattern on habitat quality in Dongting Lake area based on INVEST model. *Ecol. Sci.* 40, 99–109. doi: 10.14108/j.cnki.1008-8873.2021.02.013

Ding, Z., Zheng, H., Wang, J., O'Connor, P., Li, C., Chen, X., et al. (2022). Integrating top-down and bottom-up approaches improves practicality and efficiency of large-scale ecological restoration planning: Insights from a social-ecological system. *Engineering*. (in press) doi: 10.1016/j.eng.2022.08.008

Dobson, A., Lodge, D., Alder, J., Cumming, G. S., Keymer, J., McGlade, J., et al. (2006). Habitat loss, trophic collapse, and the decline of ecosystem services. *Ecology* 87, 1915–1924. doi: 10.1890/0012-9658(2006)87[1915:HLTCAT]2.0.CO;2

Fellman, J. B., Hood, E., Dryer, W., and Pyare, S. (2015). Stream physical characteristics impact habitat quality for Pacific salmon in two temperate coastal watersheds. *PLoS One* 10:e0132652. doi: 10.1371/journal.pone.0132652

Fotheringham, A. S., Yue, H., and Li, Z. (2019). Examining the influences of air quality in China's cities using multi-scale geographically weighted regression. *Transact. GIS* 23, 1444–1464.

Fryrear, D. W., Bilbro, J. D., Saleh, A., Schomberg, H., Stout, J. E., and Zobeck, T. M. (2000). RWEQ: Improved wind erosion technology. *J. Soil Water Conserv.* 55:183.

Gao, H., Fu, T., Liang, H., and Liu, J. (2022). Cold/hot spots identification and tradeodd/synergy analysis of ecosystem services in Taihang Mountain area. *Chin. J. Eco-Arric.* 30, 1045–1053.

Gong, G., Liu, J., Shao, Q., and Zhai, J. (2014). Sand-fixing function under the change of vegetation coverage in a wind erosion area in Northern China. *J. Resour. Ecol.* 5, 105–114.

Gong, J., Shi, J., Zhu, C., Li, X., Zhang, Z., Zhang, W., et al. (2022). Accounting for land use in an analysis of the spatial and temporal characteristics of ecosystem services supply and demand in a desert steppe of Inner Mongolia, China. *Ecol. Ind.* 144:109567. doi: 10.1016/j.ecolind.2022.109567

Guo, C., Gao, J., Zhou, B., and Yang, J. (2021). Factors of the ecosystem service value in water conservation areas considering the natural environment and human activities: A case study of funiu mountain, China. *Int. J. Environ. Res. Public Health* 18:11074. doi: 10.3390/ijerph182111074

Han, R., Feng, C.-C., Xu, N., and Guo, L. (2020). Spatial heterogeneous relationship between ecosystem services and human disturbances: A case study in Chuandong, China. *Sci. Total Environ.* 721:137818. doi: 10.1016/j.scitotenv.2020.137818

He, J., Huang, J., and Li, C. (2017). The evaluation for the impact of land use change on habitat quality: A joint contribution of cellular automata scenario simulation and habitat quality assessment model. *Ecol. Model.* 366, 58–67. doi: 10.1016/j.ecolmodel.2017.10.001

Hu, B., Kang, F., Han, H., Cheng, X., and Li, Z. (2021). Exploring drivers of ecosystem services variation from a geospatial perspective: Insights from China's Shanxi Province. *Ecol. Ind.* 131:108188. doi: 10.1016/j.ecolind.2021.108188

Hu, C., Wang, Z., Li, J., Liu, H., and Sun, D. (2022). Quantifying the temporal and spatial patterns of ecosystem services and exploring the spatial differentiation of driving factors: A case study of sichuan basin, China. *Front. Environ. Sci.* 10:927818. doi: 10.3389/fenvs.2022.927818

Hu, S., Zhang, R. X., and Guan, J. D. (2018). Analysis on carbon storage change of construction land expansion in chongqing based on InVEST Model. *Res. Soil Water Conserv.* 25, 323–331. doi: 10.13869/j.cnki.rswc.2018.03.046

Huang, Y., Wu, Y., Niu, S., and Gan, X. (2022). Estimating the effects of driving forces on ecosystem services and their responses to environmental conditions. *Environ. Sci. Pollut. Res.* 29, 71474–71486. doi: 10.1007/s11356-022-20867-x

Jordan, G., Rompaey, A. V., Szilassi, P., Csillag, G., Mannaerts, C., and Woldai, T. (2005). Historical land use changes and their impact on sediment fluxes in the Balaton basin (Hungary). *Agric. Ecosyst. Environ.* 108, 119–133. doi: 10.1016/j.agee.2005.01.013

Li, F., Li, Y., Zhou, X., Yin, Z., Liu, T., and Xin, Q. (2022). Modeling and analyzing supply-demand relationships of water resources in Xinjiang from a perspective of ecosystem services. *J. Arid Land* 14, 115–138. doi: 10.1007/s40333-022-0059-z

Li, J., and Zhang, C. (2021). Exploring the relationship between key ecosystem services and socioecological drivers in alpine basins: A case of Issyk-Kul Basin in Central Asia. *Glob. Ecol. Conserv.* 29:e01729. doi: 10.1016/j.gecco.2021.e01729

Li, J., Xu, E., and Zhang, H. (2019). Spatio-Temporal Pattern and hotspots migration under core driving force of ecosystem services of XinJiang. *Chin. J. Agric. Resour. Preg. Plann.* 40, 9–20.

Li, L., Yin, L., and Tang, Z. (2011). Distribution patterns of the species richness of plants and animals in Xinjiang, China. *Arid Zone Res.* 28, 1–9. doi: 10.13866/j.azr.2011.01.001

Li, S., Liu, Y., Yang, H., Yu, X., Zhang, Y., and Wang, C. (2021). Integrating ecosystem services modeling into effectiveness assessment of national protected areas in a typical arid region in China. *J. Environ. Manag.* 297:113408. doi: 10.1016/j.jenvman.2021.113408

Li, T., Li, D., Liang, D., and Huang, S. (2022). Coupling coordination degree of ecological-economic and its influencing factors in the counties of yangtze river economic belt. *Sustainability* 14:15467. doi: 10.3390/su142215467

Li, Y., Zhang, L., Yan, J., Wang, P., Hu, N., Cheng, W., et al. (2017). Mapping the hotspots and coldspots of ecosystem services in conservation priority setting. *J. Geograph. Sci.* 27, 681–696. doi: 10.1007/s11442-017-1400-x

Liang, J., Li, S., Li, X., Li, X., Liu, Q., Meng, Q., et al. (2021). Trade-off analyses and optimization of water-related ecosystem services (WRESs) based on land use change in a typical agricultural watershed, southern China. *J. Clean. Prod.* 279:123851. doi: 10.1016/j.jclepro.2020.123851

Liu, F., and Xu, E. (2020). Comparsion of spatial-temporal evolution of habitat quality between Xinjiang Corps and Non-corps Region based on land use. *Chin. J. Appl. Ecol.* 31, 2341–2351. doi: 10.13287/j.1001-9332.202007.014

Liu, Y., Bi, J., Lv, J., Ma, Z., and Wang, C. (2017). Spatial multi-scale relationships of ecosystem services: A case study using a geostatistical methodology. *Sci. Rep.* 7:9486. doi: 10.1038/s41598-017-09863-1

Liu, Y., Li, L., Chen, X., Zhang, R., and Yang, J. (2018). Temporal-spatial variations and influencing factors of vegetation cover in Xinjiang from 1982 to 2013 based on GIMMS-NDVI3g. *Glob. Planet. Chang.* 169, 145–155.

Lu, Y., Xu, X., Zhao, J., and Han, F. (2022). Spatiotemporal evolution of mountainous ecosystem services in an arid region and its influencing factors: A case study of the tianshan mountains in Xinjiang. *Land* 11:2164. doi: 10.3390/land11122164

Luo, Q., Zhou, J., Li, Z., and Yu, B. (2020). Spatial differences of ecosystem services and their driving factors: A comparation analysis among three urban agglomerations in China's Yangtze River Economic Belt. *Sci. Total Environ.* 725:138452. doi: 10.1016/j.scitotenv.2020.138452

Lyu, R., Clarke, K. C., Zhang, J., Feng, J., Jia, X., and Li, J. (2019). Spatial correlations among ecosystem services and their socio-ecological driving factors: A case study in the city belt along the Yellow River in Ningxia, China. *Appl. Geograph.* 108, 64–73. doi: 10.1016/j.apgeog.2019.05.003

Ma, S., Wang, L.-J., Jiang, J., Chu, L., and Zhang, J.-C. (2021a). Threshold effect of ecosystem services in response to climate change and vegetation coverage change in the Qinghai-Tibet Plateau ecological shelter. *J. Clean. Prod.* 318:128592. doi: 10.1016/j.jclepro.2021.128592

Ma, S., Wang, L.-J., Zhu, D., and Zhang, J. (2021b). Spatiotemporal changes in ecosystem services in the conservation priorities of the southern hill and mountain belt, China. *Ecol. Ind.* 122:107225. doi: 10.1016/j.ecolind.2020.107225

Niu, L., Shao, Q., Ning, J., and Huang, H. (2022). Ecological changes and the tradeoff and synergy of ecosystem services in western China. *J. Geograph. Sci.* 32, 1059–1075.

Njurumana, G. N., Sadono, R., Marsono, D., and Irham. (2021). Ecosystem services of indigenous kaliwu agroforestry system in sumba, Indonesia. *E3S Web Conf.* 305:04002.

Olson, K. R., Gennadiyev, A. N., Zhidkin, A. P., and Markelov, M. V. (2012). Impacts of land-use change, slope, and erosion on soil organic carbon retention and storage. *Soil Sci.* 177, 269–278. doi: 10.1097/SS.0b013e318244d8d2

Oshan, T. M., Li, Z., Kang, W., Wolf, L. J., and Fotheringham, A. S. (2019). mgwr: A python implementation of multiscale geographically weighted regression for investigating process spatial heterogeneity and scale. *ISPRS Int. J. Geo-Inform.* 8:269. doi: 10.3390/ijgi8060269

Peng, J., Tian, L., Liu, Y., Zhao, M., Hu, Y. N., and Wu, J. (2017). Ecosystem services response to urbanization in metropolitan areas: Thresholds identification. *Sci. Total Environ.* 607–608, 706–714. doi: 10.1016/j.scitotenv.2017.06.218

Qiu, S., Peng, J., Dong, J., Wang, X., Ding, Z., Zhang, H., et al. (2020). Understanding the relationships between ecosystem services and associated social-ecological drivers in a karst region: A case study of Guizhou Province, China. *Prog. Phys. Geograph. Earth Environ.* 45, 98–114. doi: 10.1177/0309133320933525

Řeháček, D., Khel, T., Kučera, J., Vopravil, J., and Petera, M. (2017). Effect of windbreaks on wind speed reduction and soil protection against wind erosion. *Soil Water Res.* 12, 128–135.

Reid, W. V., Mooney, H. A., Cropper, A., Capistrano, D., Carpenter, S. R., Chopra, K., et al. (2005). *Ecosystems and human well-being-synthesis: A report of the millennium ecosystem assessment*. Washington, DC: Island Press.

Ridgwell, A., Singarayer, J. S., Hetherington, A. M., and Valdes, P. J. (2009). Tackling regional climate change by leaf albedo bio-geoengineering. *Curr. Biol.* 19, 146–150. doi: 10.1016/j.cub.2008.12.025

Rong, Y., Li, K., Guo, J., Zheng, L., Luo, Y., Yan, Y., et al. (2022). Multi-scale spatio-temporal analysis of soil conservation service based on MGWR model: A case of Beijing-Tianjin-Hebei, China. *Ecol. Ind.* 139:108946. doi: 10.1016/j.ecolind.2022.108946

Sallustio, L., De Toni, A., Strollo, A., Di Febbraro, M., Gissi, E., Casella, L., et al. (2017). Assessing habitat quality in relation to the spatial distribution of protected areas in Italy. *J. Environ. Manag.* 201, 129–137. doi: 10.1016/j.jenvman.2017.06.031

Shen, W., and Li, Y. (2022). Multi-Scale assessment and spatio-temporal interaction characteristics of ecosystem health in the middle reaches of the yellow river of China. *Int. J. Environ. Res. Public Health* 19:16144. doi: 10.3390/ijerph192316144

Sheng, J., Han, X., and Zhou, H. (2017). Spatially varying patterns of afforestation/reforestation and socio-economic factors in China: A geographically weighted regression approach. *J. Clean. Prod.* 153, 362–371. doi: 10.1016/j.jclepro.2016.06.055

Shi, L., Halik, Ü, Mamat, Z., Aishan, T., Abliz, A., and Welp, M. (2021). Spatiotemporal investigation of the interactive coercing relationship between urbanization and ecosystem services in arid northwestern China. *Land Degrad. Dev.* 32, 4105–4120. doi: 10.1002/ldr.3946

Su, S., Xiao, R., Jiang, Z., and Zhang, Y. (2012). Characterizing landscape pattern and ecosystem service value changes for urbanization impacts at an eco-regional scale. *Appl. Geograph.* 34, 295–305. doi: 10.1016/j.apgeog.2011.12.001

Sun, C., Ma, Y., and Gong, L. (2021). Response of ecosystem service value to land use/cover change in the northern slope economic belt of the Tianshan Mountains, Xinjiang, China. *J. Arid Land* 13, 1026–1040. doi: 10.1007/s40333-021-0082-5

Sun, X., Wu, J., Tang, H., and Yang, P. (2022). An urban hierarchy-based approach integrating ecosystem services into multiscale sustainable land use planning: The case of China. *Resour. Conserv. Recycl.* 178:106097. doi: 10.1016/j.resconrec.2021.106097

Tang, X., Hao, X., Liu, Y., Pan, Y., and Li, H. (2016). Driving factors and spational heterogeneity analysis of ecosysten services value. *Trans. Chin. Soc. Agric. Mach.* 47, 336–342.

Wang, X., Cheng, C., Yin, L., Feng, X., and Wei, X. (2020). Spational-temporal changes and tradeoff/synergy relationship of ecosystem services in Xinjiang. *Chin. J. Ecosyst.* 39, 990–1000. doi: 10.13292/j.1000-4890.202003.028

Wang, X., Dong, X., Liu, H., Wei, H., Fan, W., Lu, N., et al. (2017). Linking land use change, ecosystem services and human well-being: A case study of the Manas River Basin of Xinjiang, China. *Ecosyst. Serv.* 27, 113–123. doi: 10.1016/j.ecoser.2017.08.013

Wei, H., Liu, H., Xu, Z., Ren, J., Lu, N., Fan, W., et al. (2018). Linking ecosystem services supply, social demand and human well-being in a typical mountain–oasis–desert area, Xinjiang, China. *Ecosyst. Serv.* 31, 44–57. doi: 10.1016/j.ecoser.2018.03.012

Wu, J., Xue, D., Wang, A., and Zhao, F. (2016). Case studies on the identification of key biodiversity areas(KBAs) in foreign countries and progress and prospects in China. *Acta Ecol. Sin.* 36, 3108–3114. doi: 10.5846/stxb201408261695

Wu, X., Fan, J., Sun, L., Zhang, H., Xu, Y., Yao, Y., et al. (2021). Wind erosion and its ecological effects on soil in the northern piedmont of the Yinshan Mountains. *Ecol. Ind.* 128:107825. doi: 10.1016/j.ecolind.2021.107825

Xu, Z., Fan, W., Wei, H., Zhang, P., Ren, J., Gao, Z., et al. (2019). Evaluation and simulation of the impact of land use change on ecosystem services based on a carbon flow model: A case study of the Manas River Basin of Xinjiang, China. *Sci. Total Environ.* 652, 117–133. doi: 10.1016/j.scitotenv.2018.10.206

Xue, C., Chen, X., Xue, L., Zhang, H., Chen, J., and Li, D. (2023). Modeling the spatially heterogeneous relationships between tradeoffs and synergies among ecosystem services and potential drivers considering geographic scale in Bairin Left Banner, China. *Sci. Total Environ.* 855:158834. doi: 10.1016/j.scitotenv.2022.158834

Yang, M., Gao, X., Zhao, X., and Wu, P. (2021). Scale effect and spatially explicit drivers of interactions between ecosystem services—A case study from the Loess Plateau. *Sci. Total Environ.* 785:147389. doi: 10.1016/j.scitotenv.2021.147389

Yushanjiang, A., Zhang, F., Yu, H., and Kung, H.-T. (2018). Quantifying the spatial correlations between landscape pattern and ecosystem service value: A case study in Ebinur Lake Basin, Xinjiang, China. *Ecol. Eng.* 113, 94–104. doi: 10.1016/j.ecoleng.2018.02.005

Zhang, L., Fu, B., Lü, Y., and Zeng, Y. (2015). Balancing multiple ecosystem services in conservation priority setting. *Landsc. Ecol.* 30, 535–546. doi: 10.1007/s10980-014-0106-z

Zhang, W., Zhou, J., Feng, G., Weindorf, D. C., Hu, G., and Sheng, J. (2015). Characteristics of water erosion and conservation practice in arid regions of Central Asia: Xinjiang, China as an example. *Int. Soil Water Conserv. Res.* 3, 97–111. doi: 10.1016/j.iswcr.2015.06.002

Zhang, Z., Xia, F., Yang, D., Huo, J., Wang, G., and Chen, H. (2020). Spatiotemporal characteristics in ecosystem service value and its interaction with human activities in Xinjiang, China. *Ecol. Ind.* 110:105826. doi: 10.1016/j.ecolind.2019.105826

Zhuang, Z., Li, C., Hsu, W.-L., Gu, S., Hou, X., and Zhang, C. (2022). Spatiotemporal changes in the supply and demand of ecosystem services in china’s huai river basin and their influencing factors. *Water* 14:2559. doi: 10.3390/w14162559

Ziadat, F. M., and Taimeh, A. Y. (2013). Effect of rainfall intensity, slope, land use and and antecedent soil moisture on soil erosion in an arid environment. *Land Degrad. Dev.* 24, 582–590. doi: 10.1002/ldr.2239

frontiers | Frontiers in Ecology and Evolution

TYPE Original Research
PUBLISHED 31 March 2023
DOI 10.3389/fevo.2023.1110018

Quantitative analysis of the spatial diversity of Moraceae in China

Dangui Lu[1], Lichuan Qiu[2], Meiqi Jiao[3]*, Zhongke Feng[1,4]* and Zhichao Wang[1]*

[1]Precision Forestry Key Laboratory of Beijing, Forestry College, Beijing Forestry University, Beijing, China, [2]School of Geographical Sciences, Taiyuan Normal University, Jinzhong, China, [3]Department of Hospitality Management, Shanghai Business School, Shanghai, China, [4]College of Forestry, Hainan University, Haikou, China

OPEN ACCESS

EDITED BY
Yonghao Xu,
Institute of Advanced Research in Artificial Intelligence (IARAI),
Austria

REVIEWED BY
Zhijie Wang,
Guizhou University,
China
Ion Catalin Petritan,
Transilvania University of Brașov,
Romania

*CORRESPONDENCE
Meiqi Jiao
✉ mqjiao@126.com
Zhongke Feng
✉ fengzhongke@bjfu.edu.cn
Zhichao Wang
✉ Zhichao@bjfu.edu.cn

SPECIALTY SECTION
This article was submitted to Environmental Informatics and Remote Sensing,
a section of the journal
Frontiers in Ecology and Evolution

RECEIVED 28 November 2022
ACCEPTED 28 February 2023
PUBLISHED 31 March 2023

CITATION
Lu D, Qiu L, Jiao M, Feng Z and Wang Z (2023) Quantitative analysis of the spatial diversity of Moraceae in China.
Front. Ecol. Evol. 11:1110018.
doi: 10.3389/fevo.2023.1110018

Changes in distribution patterns of economically essential forest species under global change are urgently needed in the scientific forecast, and large-scale spatial modeling is a crucial tool. Using diversity pattern indicators and other data obtained through geographic information systems (GIS) and spatial data on Moraceae species obtained from published data, we quantitatively studied the spatial diversity patterns of genera in the Moraceae in China. The results revealed that the patch richness, diversity index, and total shape index of the genera with multiple species were significantly higher than those of the monotypic genera. Monotypic genera had no spatial diversity and no distribution in patterns of spatial diversity. *Maclura* had the most concentrated spatial distribution and the lowest distribution area among the Moraceae in China. The number of patches and the total area were the smallest, while the most significant patch index was the highest. *Maclura* had no spatial diversity. *Streblus* had the highest patch abundance compared to other genera with fewer species. *Streblus* had the smallest number of patches and total area of distribution, the lowest spatial distribution, and a small total shape index, indicating its concentrated distribution. The values of the Shannon's Diversity Index (SHDI) and Simpson's Diversity Index (SIDI) were the highest, and the spatial distribution was the most diverse among the genera with fewer species. The patch type of *Streblus* had a more considerable value than other genera, but the number of patches was small, and the total shape index was low. *Streblus* was primarily distributed in the south of Yunnan, western Guangxi, the west and central parts of Hainan, and southern Guangdong. Most of these areas were mountainous. The temperature decreased with elevation, providing diverse environmental conditions for the narrow-stem genus. Among the Moraceae in China, the spatial distribution of *Ficus* was the most diverse, with the highest number of patches, patch types, total shape index, SHDI, and SIDI values. The spatial diversity of *Ficus* could be used as a protected area for Moraceae in China.

KEYWORDS

Moraceae, spatial diversity, China, geographic information systems, genus

1. Introduction

Large-scale patterns of species diversity are not only one of the central issues in macroecological and biogeographical studies (Colwell and Lees, 2000). In modern China, Moraceae includes 12 genera: *Antiaris*, *Artocarpus*, *Broussonetia*, *Cannabis*, *Cudrania*, *Fatoua*, *Ficus*, *Humulus*, *Maclura*, *Malaisia*, *Morus*, and *Streblus*. The diversity of Moraceae has been studied in terms of genetic diversity (Elhawary et al., 2018; Marcotuli et al., 2019; Martins et al., 2021), species diversity (Gardner et al., 2017; Machado et al., 2018; Shi et al., 2018; Pederneiras et al., 2020), and ecosystem diversity (Kong et al., 2020; Dong et al., 2022; Wang et al., 2022). Most studies on diversity in the Moraceae have been conducted for limited species of the genus *Morus* (Chen et al., 2016; Islam and Rahman, 2019; Hashemi and Khadivi, 2020) and *Ficus* species (Teixeira et al., 2018; Zhang et al., 2018; Chakraborty et al., 2022). On the contrary, in this work, all genera in the Chinese Moraceae were applied to investigate species diversity. Concerning research methodology for the study of the Moraceae in China, tabular statistics are frequently applied in studies to document plant species diversity (Chen et al., 2010), which has the disadvantage of requiring a great deal of work in discovering interprovincial relationships among species diversity. With the use of geographic information systems (GIS) technology, it is feasible to observe species diversity, i.e., spatial diversity, among regions. For now, the limited spatial distribution of some genera and species of Moraceae has been studied by researchers utilizing GIS (Berg, 1989). However, studies on the spatial distribution and diversity of all Moraceae across China are insufficient. Furthermore, studies on the species diversity of Moraceae are usually conducted using qualitative methods, and quantitative studies are insufficient (Zerega et al., 2005; Kumar et al., 2011). In this paper, we used GIS to study the species diversity of all Moraceae species in all of China. This was done because of these problems.

A quantitative study of species diversity in communities can utilize the Shannon-wiener index, which integrates species richness and evenness, combined with the Simpson index (Nagendra, 2002; Ganivet et al., 2020; Shukla et al., 2020), the Pielou evenness index (Pielou, 1966; Ricotta and Avena, 2003; He et al., 2019), and the Jaccard similarity index (Oluyinka Christopher, 2020). The index formula of spatial diversity patterns, such as the number of patches and total area, was applied to compute the index of spatial diversity patterns of the genus Moraceae in China. However, all of them lacked the ability to link with geoinformation to provide national-scale knowledge. In this research, GIS was applied to map the spatial distribution of 12 genera of Moraceae in China, with the county as the fundamental unit of spatial data and the Moraceae as the research object.

Large-scale vegetation distribution data can be obtained using remote sensing images, and landscape diversity indicators can analyze the spatial distribution pattern of vegetation. The Moraceae are primarily dominated by trees and shrubs, with a small number of vines. When the Moraceae building species are evident, the spatial pattern of the dominant species in the primary layer can be obtained using remote sensing technology. When the prevalent phenomenon of Moraceae is not evident, the spatial pattern does not contain species. However, species are the basis of plant community composition, and the workload of a species survey is immense. The published botanical histories of various places in China have the distribution sites of Moraceae, which lay the foundation for the study of the spatial distribution of Moraceae. Studying how species are spread out in space can help protect species and give a guide for figuring out what information about plants is in high-resolution remote sensing images.

In this study, GIS was used to create a map of the spatial diversity of 12 Moraceae genera in Chinese, using counties as the basic spatial data unit and Moraceae as the research object, from which not only the spatial distribution characteristics of the genera, but also further indicators of spatial diversity calculation, such as the number of patches and patch richness, can be obtained, providing a foundation for its quantitative study of spatial divergence. The quantitative study of the spatial diversity of Moraceae can provide a more accurate basis for species diversity, conservation, use, and restoration of Moraceae in China.

2. Materials and methods

2.1. Data collection and processing

In the first step, based on the contents of the Flora Reipublicae Popularis Sinicae [Vol. 23(1)], the species of Moraceae in China and their Latin names were collated and reviewed by plant taxonomy experts to determine a list of Moraceae species in China. Secondly, the database of Moraceae in China was established by compiling all kinds of data sources to record the geographical distribution of Moraceae. The primary data sources for geographical distribution were the full-text FRPS website[1], the National Plant Specimen Resource Center[2], and the National Specimen Information Infrastructure website[3]. Up to the end of 2021, they issued papers and journals on the geographical distribution of Moraceae in China (Wu Zhengyi, 1989; Arimoto et al., 2020), and regional flora was issued by some provinces and regions. Determine the particular distribution of each plant in the county. The data of provinces and regions and the range of distribution that the counties cannot determine will not be adopted. In the final step, we tested all species names for synonyms and merged all synonymized species records.

We also excluded cultivated species and hybrids, and all distribution data were natural species distributions. The attribute data in the database includes genus name, species name, Latin name, province of distribution, county of issuance, and data source, with a total of 28,537 county-level distribution records. The attribute data in the database contained genus name, species name, Latin name, distribution province, distribution county, and data source. It was eventually determined that there were 12 genera and 149 species of Moraceae in China, and a total of 28,537 county-level distribution records were compiled.

2.2. Methods

All of the species' spatial data, which includes both graphic and attribute data, was made in ArcGIS 10.2. The graphic data used a map of China with the county as the basic unit (a scale of 1:1,000,000). The attribute data was the distribution of species. Then, the number of genera was obtained, and the spatial diversity map was created. In the spatial distribution of the genus, an isolated county was a patch, and adjacent counties jointly formed a patch. The number of genera in the patch was different, forming different patch types. The spatial diversity and its pattern for the genus could be obtained by calculating the

---

[1] http://www.iplant.cn/frps2019/

[2] https://www.cvh.ac.cn/index.php

[3] http://www.nsii.org.cn/2017/home.php

index of spatial diversity pattern. The applicable data was obtained from the spatial data and studied according to the spatial diversity pattern indicators (Table 1). Complete all raster data calculations in Fragstats 3.3.

3. Results and analysis

3.1. Spatial diversity of monotypic genera

Monotypic genera are genera that comprise just one species. Moraceae includes *Maclura*, *Antiaris*, *Malaisia*, and *Cannabis*. Among Moraceae in China, these genera had the smallest patch richness, with a value of 1 (Table 2), indicating merely one patch type. However, the different genera had different numbers of patches. Shannon's diversity index (SHDI), Simpson's diversity index (SIDI), Shannon's evenness index (SHEI), and Simpson's evenness index (SIEI) of monotypic genera were all 0 (Table 2), implying that there was no diversity. The monotypic genus exhibited a high degree of aggregation. Additionally, it had a maximum plaque index but a low total shape index (Table 2).

The total number of all patches (NAP) on *Maclura* was six (Table 2), indicating six patches. Among the 12 genera of Moraceae, the spatial distribution of *Maclura* was the lowest, predominantly distributed in Medog County in Tibet and the eastern, central,

TABLE 1 Indices of spatial diversity patterns.

	Index	Formula	Meaning	Unit，Range
1	Patch richness	$PR = \mathrm{m}$	Number of patch types in the genus	$PR \geq 1$
2	Shannon's diversity index	$SIDI = -\sum_{i=1}^{m}\left(P_i \times \ln P_i\right)$	Diversity of spatial distribution in the genus	$0 \leq SIDI < 1$
3	Simpson's diversity index	$SHDI = 1 - \sum_{i=1}^{m} P_i^2$	Diversity of spatial distribution in the genus	$SHDI \geq 0$
4	Shannon's evenness index	$SHEI = \frac{-\sum_{i=1}^{m}\left(P_i \times \ln P_i\right)}{\ln m}$	Evenness of spatial distribution in the genus	$0 \leq SHEI \leq 1$
5	Simpson's evenness index	$SIEI = \frac{1 - \sum_{i=1}^{m} Pi^2}{1 - \left(\frac{1}{m}\right)}$	Evenness of spatial distribution in the genus	$0 \leq SIEI \leq 1$
6	Area of patch type	$APT = \sum_{j=1}^{m} a_{ij} \times \frac{1}{10000} \times \frac{1}{10000000}$	Area of patch type *i*	10^7hm^2 $APT>0$
7	Percentage of the genus	$PG = \frac{\sum_{j=1}^{n} a_{ij}}{A} \times 100$	Proportional abundance of patch type *i* in the genus	%，$0<PG \leq 100$
8	Number of patches	$NP = n_i$	Number of patches in patch type *i*	$NP \geq 1$
9	Largest patch index	$LPI = \frac{\max_{j=1}^{n}\left(a_{ij}\right)}{A} \times 100$	Percentage of the genus area comprwased by the largest patch in patch type *i*	%，$0<LPI \leq 100$
10	Shape index	$SI = \frac{e_i}{\min e_i}$	Measure of aggregation in patch type *i*	$SI \geq 1$
11	Total area	$TAP = \sum APT$	Area of genus	10^7hm^2
12	Number of all patches	$NAP = \sum NP$	Number of all patches in genus	$NAP \geq 1$
13	Total largest patch index	$TLPI = \sum LPI$	Sum of largest patch index of every patch type in genus	%，$0<TLPI \leq 100$
14	Total shape index	$TSI = \sum SI$	Sum of shape index of every patch type in genus	$TSI \geq 1$

m = number of patch types in the genus; P_i = proportion of the genus occupied by patch type i; a_{ij} = area of patch ij; ij = patch j in patch type i; A = area of genus; n_i = number of patches in patch type i; e_i = total length of patch type i.

TABLE 2 Spatial diversity of genera in the Moraceae in China.

Genera	Index								
	PR	SHDI	SIDI	SHEI	SIEI	TA	NAP	TLPI	TSI
Maclura	1	0	0	0	0	0.534	6	59.081	3.492
Antiaris	1	0	0	0	0	0.934	14	27.985	6.702
Malaisia	1	0	0	0	0	1.338	20	37.607	7.605
Cannabis	1	0	0	0	0	17.973	139	26.131	16.262
Fatoua	2	0.411	0.246	0.594	0.492	4.513	114	13.340	22.312
Humulus	3	0.034	0.01	0.031	0.015	11.661	158	12.488	20.836
Broussonetia	3	1.033	0.624	0.941	0.937	17.917	295	11.717	44.713
Cudrania	4	0.864	0.499	0.623	0.665	15.982	227	16.056	41.419
Streblus	5	1.302	0.683	0.809	0.854	1.964	42	32.517	23.884
Morus	7	1.184	0.628	0.609	0.733	31.357	428	18.856	61.714
Artocarpus	8	1.294	0.654	0.622	0.747	6.675	104	23.872	41.345
Ficus	41	3.017	0.931	0.813	0.954	23.664	742	15.975	200.219

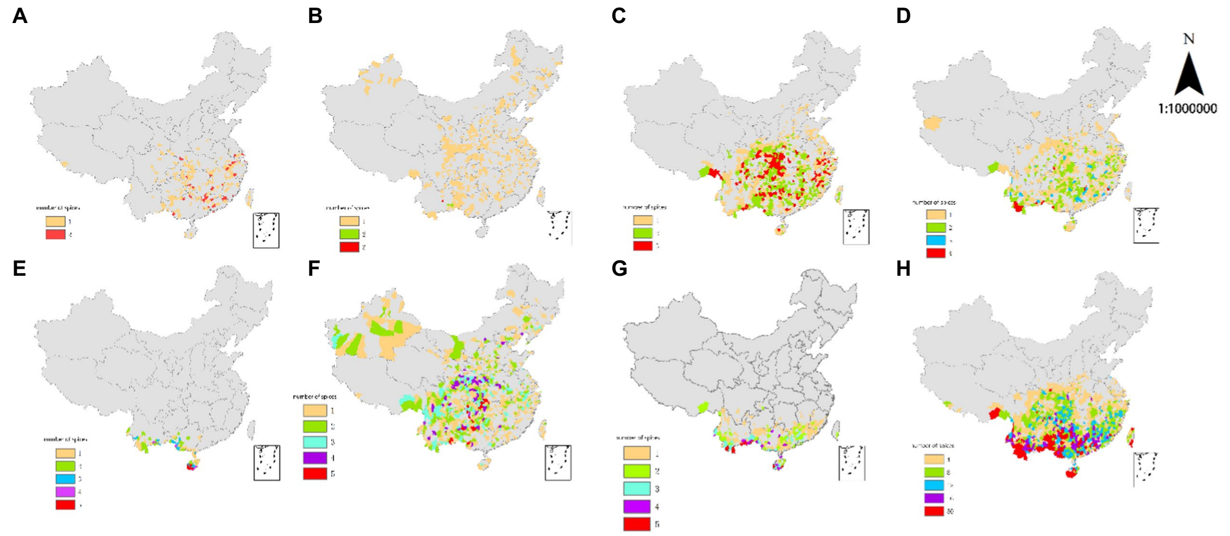

FIGURE 1
Spatial diversity distribution of every genus in the Moraceae in China. (A) Fatoua, (B) Humulus, (C) Broussonetia, (D) Cudrania (E) Streblus, (F) Morus, (G) Artocarpus, (H) Ficus.

northern, and southern parts of Yunnan. *Maclura* in the five counties had a significantly lower distribution range than the other genera. Consistent with the data shown in Figure 1A, the number of all patches (NAP) and total area (TA) of *Maclura* were the smallest (Table 2). Among monotypic genera, the *Maclura* spatial distribution was the most concentrated (Figure 1A), and the most extensive patch index (TLPI) was the highest among the 12 genera of Moraceae (Table 2).

The NAP value of *Antiaris* was 14 (Table 2), indicating that the number of patches was 14. The number of all patches (NAP) of Antiaris was slightly higher than that of Maclura, but Antiaris' distribution range was significantly larger. The numbers of all patches (NAP), total area (TA), and full shape index (TSI) of *Antiaris* in Table 2 were consistent with those of *Maclura*.

The number of all patches (NAP) of *Malaisia* was 20 (Table 2), which indicates that the number of patches in this genus was 20, and the number of patches was slightly larger than that of *Antiaris*. The distribution range was somewhat more extensive than that of *Antiaris*. The number of all patches (NAP) and total area (TA) of the three genera in Table 2 were the smallest among the Moraceae in China, and the total area (TA) of the three genera was comparable.

Among the monotypic genera, the number of all patches (NAP), total area (TA), and complete shape index (TSI) of *Cannabis* were extensive (Table 2). *Cannabis* was distributed in other parts of the county, though not in regions including Hainan, Taiwan, Hong Kong, and Macau. *Cannabis* had the most comprehensive distribution, and the sum of the most extensive patch index of every patch type in the genus (TLPI) was the lowest among the monotypic genera (Table 2).

3.2. Spatial diversity of lesser genera

The lesser genera (2–7 species) included *Fatoua*, *Humulus*, *Cudrania*, *Broussonetia*, and *Streblus*. Patch richness (PR) values of the five species were more significant than 1 (Table 2), and the patch richness increased as patch type gradually increased from 2 to 5. The species in these genera were diverse, and their SHDI, SIDI, SHEI, and SIEI index values were all greater than 0 (Table 2) and slightly higher than those of monotypic genera. Table 1 shows that the correlation index of the lesser genus species (except for *Cannabis*) was higher than monotypic genera for patch richness (PR), total area (TA), and the number of all patches (NAP). The species were more widely distributed and more dispersed than monotypic genera. The total shape index (TSI) was significantly higher than that of monotypic genera (Table 2).

The total area (TA) of *Fatoua* was close to that of *Artocarpus* (Table 2). The difference can be easily observed by comparing the plots of these two genera. The plaque richness (PR) value of *Fatoua* is 2 (Table 2). There are two types of patches with low patch richness. One plaque type had one species, and the other had two species, corresponding to 1 and 2 in the legend of Figure 1A, higher than *Fatoua*. In Figure 1G, the patch types are classified into five classes. *Fatoua* is more widely distributed, and it was concentrated in tropical and subtropical regions (Figure 1A). *Artocarpus* is concentrated in tropical and southern subtropical regions (Figure 1G). Although *Fatoua* had a slightly larger number of patches, *Artocarpus* had more patch types and a slightly higher total area (TA).

The spatial distribution of *Humulus* (Figure 1B) was analogous to that of monotypic *Cannabis*. The PR of *Humulus* was 3 (Table 2), indicating that its patch richness was higher than that of *Cannabis*. *Humulus* has three patches: patches with species, patches with two species, and patches with three species, which correspond to 1, 2, and 3 in the legend of Figure 1B, respectively. According to the total shape index (TSI), *Humulus* species had greater spatial dispersion and uniform spatial distribution than *Cannabis* (Table 2). However, the total most extensive patch index (TLPI) was less than that of *Cannabis*. Compared with *Cannabis*, *Humulus* had a slightly smaller number of patches, but the total area was slightly larger (Table 2). The SHDI, SIDI, SHEI, and SIEI index values of *Humulus* were more significant than 0, but the value was lower because the first patch type was more evenly distributed. In contrast, the second and third patches were distributed in the southwest in small quantities (Figure 1B).

Compared with the lesser genera in the previous section, the total area of *Broussonetia* was the largest, as was the number of patches. The PR of *Broussonetia* was 3 (Table 2), and patch richness was low. The spatial distribution of *Broussonetia* (Figure 1C) was similar to that of *Cudrania* (Figure 1D), and its total area (TA) and several patches (NP) were slightly higher than those of *Cudrania* (Table 2), with distribution in the south and north. The SHDI and SIDI diversity index values and the SHEI and SIEI meanness index values of *Broussonetia* were higher than the corresponding indicators for *Cudrania* (Table 2), so we determined that the spatial distribution of *Broussonetia* was diverse.

The total area of distribution of *Streblus* was similar to *Malaisia* (Table 2). The number of patches (NP) of *Streblus* was twice that of *Malaisia*, and the total shape index (TSI) was three times that of the latter. The spatial distribution of *Streblus* was western. The distribution was more dispersed (Figure 1E). The PR of *Streblus* was 5 (Table 2), indicating that its patch richness was the highest among the lesser genera. However, the total area (TA) and number of all patches (NAP) of *Streblus* were the smallest (Table 2). The smallest spatial distribution range was found (Figure 1E). Its total shape index (TSI) was moderately small and relatively concentrated. The SHDI and SIDI diversity indices of *Streblus* were the highest among the lesser genera, and the SHEI and SIEI values were higher than average. The spatial distribution was the most diverse among the more inferior generation. *Streblus* had the most considerable number of patch types, but the number of patches (NP) was small, and the total shape index (TSI) was weak. Because *Streblus* was predominantly distributed in the south of Yunnan, western Guangxi, the west and central parts of Hainan, and southern Guangdong (Figure 1E), most were in mountainous areas. The temperature decreases with height, providing different and challenging environmental conditions for *Streblus*, which grows in a limited range of suitable conditions.

3.3. Spatial diversity of multiple genera

The multiple genera (more than seven species) include *Morus*, *Artocarpus*, and *Ficus*. Among the 12 genera of Moraceae in China, the genera with more than 10 species had the most outstanding patch richness (PR). The number of patches (NP), total shape index (TSI), SHDI, SIDI, SHEI, and SIEI values of these genera were higher than those of smaller genera, but the most extensive patch index (LPI) values were lower (Table 2).

Morus had a PR of 7 (Table 2), with seven types of patches. Patch types 1, 2, 3, 4, 5, 6, and 7 represented patches comprising 1, 2, 3, 4, 5, 6, and 7 species, respectively. In Figure 1F, the patch types were divided into five levels. The number of patches (NP) and total shape index (TSI) values of *Morus* were high (Table 2), which was consistent with the number and distribution of patches in Figure 1F. Among genera with more than 10 species, *Morus* had the largest total area (TA) and was the most evenly distributed across the county. *Morus's* SHDI, SIDI, SHEI, and SIEI values were higher than those of other large genera, and the spatial distribution had higher diversity.

The PR of *Artocarpus* was 8 (Table 2), and patch richness (PR) was slightly higher than *Morus*'s. Patch types 1, 2, 3, and 4 represented patches containing 1, 2, 3, and 4 species, respectively, and patch type 5 represented patches containing 5–8 species. In Figure 1G, the patch types were divided into five levels. Among genera with more than 10 species, the patch richness of *Artocarpus* was relatively high. However, the number of patches (NP), total area (TA), and total shape index (TSI) values were the smallest (Table 2). The distribution range of *Artocarpus* was the smallest, and the spatial distribution was the most concentrated (Figure 1G). In Table 2, the SHDI, SIDI, SHEI, and SIEI values of *Artocarpus* were shown to be between the corresponding indicators for *Morus* and *Ficus*, with high spatial diversity.

The PR of *Ficus* was 41 (Table 2), the highest among the 12 genera of Moraceae in China. The patch types were species comprised of 1 to 37, 38, 40, 43, 49, and 50 (Figure 1H). The spatial distribution of *Ficus* was close to that of *Broussonetia*, though farther to the south (Figure 1H), and the spatial distribution was centered. However, the number of *Ficus* patches was 2.5 times that of *Broussonetia*, and the total shape index (TSI) was 4.5 times that of *Broussonetia*. The most extensive patch index (LPI), SHDI, and SIDI values of *Ficus* were higher than those of *Broussonetia* (Table 2). Among the Moraceae in China, the spatial distribution of *Ficus* was the most diverse and widely distributed, with the highest number of all patches (NAP), number of patch types, total shape index (TSI), SHDI, and SIDI values (Table 2). Therefore, areas with a substantial number of *Ficus* could be used as protected areas to protect the Moraceae resources in China.

4. Discussion

Our research applied spatial variety pattern indicators using spatial calculations based on the number of patches, genus and species types, and distribution areas. Spatial diversity patterns were calculated using spatial arrows based on the number of patches, genus or species types, and their distribution areas to create Moraceae's genus and species diversity in each county. Based on the patches, the analysis of the kinds of genera or species and their distribution areas in the study enables the species of mulberry genera and species in each county to be derived, and the spatial variety index can be computed. The computation of the spatial diversity index can quantify spatial diversity, which is unique to this research.

One of the most important features of species spatial distribution was the large-scale pattern of species diversity (Tittensor et al., 2010). The large-scale pattern of species diversity and its formation mechanism is one of the core issues in ecology and the basis of biodiversity conservation planning (Stuart-Smith et al., 2013). The most significant feature of this study was that the distribution was precise to the county level, quantitatively studying the spatial diversity of the Moraceae in China, and the diversity types were divided based on the number of species. Using GIS to draw distribution maps enabled us to carry out a spatially simple and intuitive observation of the species diversity of Moraceae in China and obtain spatial diversity computation indicators from patch maps. We obtained data on the spatial diversity, evenness index, and several patches using the spatial diversity model indicators. And then, we can quantitatively analyze the spatial diversity of Moraceae in China. Carrying out a study at this large scale not only enabled us to discover the spatial diversity center of Moraceae in China more accurately but could also aid in protecting and utilizing it.

The diversity analysis of genera can provide evidence and indications for investigating the evolution of flora (Yue, 2001). Among the Moraceae in China, the patch indicators of monotypic genera were consistent with the species, and spatial diversity did not differ between the species and genus. The number of all patches (NAP), total area (TA), and spatial distribution range of *Maclura* were the lowest among all 12 genera. *Maclura*'s most extensive patch index (LPI) was the highest among the 12 genera, and the spatial distribution was the most concentrated. Among monotypic genera, *Cannabis* had a moderately substantial total shape index (TSI), the most substantial number of patches (NP) and entire area (TA), and the most comprehensive distribution range. Among monotypic genera, the patch richness of *Streblus* was the highest, the total number of patches and total distribution area was the smallest, and the spatial distribution range was the smallest. The total shape index of *Streblus* was moderately small, and the distribution was relatively concentrated. We found that Streblus was mainly distributed in the south of Yunnan, the western part of Guangxi, the central and western parts of Hainan, and the southern part of Guangdong. This was because these areas are mostly mountainous, and the temperature decreases with elevation, providing different environmental conditions for Streblus, which can tolerate a narrow range of conditions.

The SHDI and SIDI diversity indices of *Streblus* were the highest, and the spatial distribution was the most diverse among the genera with few species. *Streblus* had more patch types, but the number of patches was small, and the total shape index (TSI) was low. *Streblus* was a non-monophyletic group, far from other genera. We found that *Streblus* was mainly distributed in the south of Yunnan, the western part of Guangxi, the central and western parts of Hainan, and the southern part of Guangdong. Because these areas were primarily mountainous, the temperature decreased with elevation, providing different environmental conditions for *Streblus*, which can tolerate a narrow range of conditions.

Among the genera with lesser species, the number of all patches (NAP), total area (TA), total shape index (TSI), SIDI, and SHEI values of *Broussonetia* were the highest. *Broussonetia* was widely distributed, and its distribution was the most diverse. The ecological adaptation of *Broussonetia papyrifera* was strong, and this species was widely distributed in China. The reason why is that the *B. papyrifera* population has high genetic diversity due to the fact that the tree was a cross-pollinated plant and geographical isolation due to features such as rivers, mountains, roads, and canals that block the flow of genes between *Broussonetia papyrifera* populations.

Among the Moraceae in China, the spatial distribution of *Ficus* was the most diverse, with the most significant number of all patches (NAP), number of patch types, total shape index (TSI), SHDI, and SIDI values. The diversified centers of *Ficus* were distributed in southeastern Gansu, northeastern Guizhou, southern Yunnan, southwestern Guangxi, southern Taiwan, and western Hainan. The spatial diversity of *Ficus* could be used when designating protected areas for the Moraceae in China. The spatial diversity center of the Moraceae in China was mainly distributed in tropical and subtropical regions. This conclusion was consistent with the view put forth by the Flora Reipublicae Popularis Sinicae that the Moraceae in China were prolific in tropical and subtropical areas, with a few distributed in the temperate zone.

Data availability statement

The datasets presented in this study can be found in online repositories. The names of the repository and accession number(s) can be found in the article.

Author contributions

DL: conceptualization, validation, formal analysis, data curation, and writing - original draft. LQ: conceptualization, resources, and acquisition of the financial support for the project leading to this publication. MJ: software, validation, formal analysis, data curation, and acquisition of the financial support for the project leading to this publication. ZF: conceptualization and resources. ZW: provided guidance on article format and acquisition of the financial support for the project leading to this publication. All authors contributed to manuscript revision, read and approved the submitted version.

Funding

This work was supported by grants from the National Natural Science Foundation of China (41071335, 41171423).

Conflict of interest

The authors declare that the research was conducted in the absence of any commercial or financial relationships that could be construed as a potential conflict of interest.

Publisher's note

References

Arimoto, K., MacGowan, I., and Su, Z.-H. (2020). New data on lance flies (Diptera, Lonchaeidae) associated with figs (Moraceae, *Ficus* spp.) in Japan and Taiwan, with descriptions of two new species of the genus Silba Macquart. *J. Asia Pac. Entomol.* 23, 364–370. doi: 10.1016/j.aspen.2019.11.007

Berg, C. (1989). Classification and distribution of *Ficus*. *Experientia* 45, 605–611. doi: 10.1007/BF01975677

Chakraborty, A., Mahajan, S., Bisht, M. S., and Sharma, V. K. (2022). Genome sequencing and comparative analysis of *Ficus bengalensis* and *Ficus religiosa* species reveal evolutionary mechanisms of longevity. *iScience* 25:105100. doi: 10.1016/j.isci.2022.105100

Chen, H., Chen, J., Yang, H., Chen, W., Gao, H., and Lu, W. (2016). Variation in total anthocyanin, phenolic contents, antioxidant enzyme and antioxidant capacity among different mulberry (*Morus* sp.) cultivars in China. *Sci. Hortic.* 213, 186–192. doi: 10.1016/j.scienta.2016.10.036

Chen, R.-F., Xu, L., Yu, M. D., Liu, X.-Q., and Chen, L.-Q. (2010). *Determination of the Origin and Evolution of Morus (Moraceae) by Analyzing the Internal Transcribed Spacer (ITS) Sequences*. In 2010 4th International Conference on Bioinformatics and Biomedical Engineering. IEEE.

Colwell, R. K., and Lees, D. C. (2000). The mid-domain effect: geometric constraints on the geography of species richness. *Trends Ecol. Evol.* 15, 70–76. doi: 10.1016/S0169-5347(99)01767-X

Dong, J.-L., Li, Z., Gao, J. X., Sun, B. N., and He, Y. L. (2022). Ficus leaves within the *Ficus* subgenus *Urostigma* (Moraceae) from the middle Miocene in South China and their biogeography implications. *Rev. Palaeobot. Palynol.* 302:104671. doi: 10.1016/j.revpalbo.2022.104671

Elhawary, S. S., Younis, I. Y., el Bishbishy, M. H., and Khattab, A. R. (2018). LC–MS/MS-based chemometric analysis of phytochemical diversity in 13 *Ficus* spp. (Moraceae): correlation to their *in vitro* antimicrobial and *in silico* quorum sensing inhibitory activities. *Ind. Crop. Prod.* 126, 261–271. doi: 10.1016/j.indcrop.2018.10.017

Ganivet, E., Unggang, J., Bodos, V., Demies, M., Ling, C. Y., Sang, J., et al. (2020). Assessing tree species diversity and structure of mixed dipterocarp forest remnants in a fragmented landscape of North-Western Borneo, Sarawak, Malaysia. *Ecol. Indic.* 112:106117. doi: 10.1016/j.ecolind.2020.106117

Gardner, E. M., Sarraf, P., Williams, E. W., and Zerega, N. J. C. (2017). Phylogeny and biogeography of *Maclura* (Moraceae) and the origin of an anachronisticfruit. *Mol. Phylogenet. Evol.* 117, 49–59. doi: 10.1016/j.ympev.2017.06.021

Hashemi, S., and Khadivi, A. (2020). Morphological and pomological characteristics of white mulberry (*Morus alba* L.) accessions. *Sci. Hortic.* 259:108827. doi: 10.1016/j.scienta.2019.108827

He, Y.-H., Gao, P.-L., and Qiang, S. (2019). An investigation of weed seed banks reveals similar potential weed community diversity among three different farmland types in Anhui Province, China. *J. Integr. Agric.* 18, 927–937. doi: 10.1016/S2095-3119(18)62073-8

Islam, S. M. S., and Rahman, M. S. (2019). Genetic diversity analysis based on morphological characters in mulberry (*Morus* spp.). *J. Biosci.* 28, 111–119. doi: 10.3329/jbs.v28i0.44717

Kong, W., Wu, S. H., Wu, X. Q., Zheng, X. R., Sun, X. R., Ye, J. N., et al. (2020). First report of leaf spot disease caused by Colletotrichum tropical on *Ficus binnendijkii* var. *variegata* in China. *Plant Dis.* 104:585. doi: 10.1094/PDIS-04-19-0834-PDN

Kumar, A., Bajpai, O., Mishra, A. K., Sahu, N., Behera, S. K., and Chaudhary, L. B. (2011). Assessment of diversity in the genus *Ficus* L. (Moraceae) of Katerniaghat wildlife sanctuary, Uttar Pradesh, India. American. *J. Plant Sci.* 2, 78–92. doi: 10.4236/ajps.2011.21011

Machado, A. F. P., Rønsted, N., Bruun-Lund, S., Pereira, R. A. S., and Paganucci de Queiroz, L. (2018). Atlantic forests to the all Americas: biogeographical history and divergence times of neotropical *Ficus* (Moraceae). *Mol. Phylogenet. Evol.* 122, 46–58. doi: 10.1016/j.ympev.2018.01.015

Marcotuli, I., Mazzeo, A., Nigro, D., Giove, S. L., Giancaspro, A., Colasuonno, P., et al. (2019). Analysis of genetic diversity of *Ficus carica* L. (Moraceae) collection using simple sequence repeat (SSR) markers. *Acta Sci. Polon. Hortorum Cultus* 18, 93–109. doi: 10.24326/asphc.2019.4.9

Martins, L. A. R., Lorenzoni, R. M., Pereira, R. M., de Miranda, F. D., Fontes, M. M., Carrijo, T. T., et al. (2021). Genetic diversity and structure of *Dorstenia elata* (Moraceae) in an Atlantic Forest remnant. *Rodriguésia*:72.

Nagendra, H. (2002). Opposite trends in response for the Shannon and *Simpson indices* of landscape diversity. *Appl. Geogr.* 22, 175–186. doi: 10.1016/S0143-6228(02)00002-4

Oluyinka Christopher, A. (2020). Comparative analyses of diversity and similarity indices of West Bank Forest and block a Forest of the International Institute of Tropical Agriculture (IITA) Ibadan, Oyo state, Nigeria. *Int. J. Forest. Res.* 2020, 1–8. doi: 10.1155/2020/4865845

Pederneiras, L. C., da Costa, A. F., Medeiros, H., Rivera, N. M., Forzza, R. C., Romaniuc-Neto, S., et al. (2020). Species diversity of *Ficus* L. sect. Americanae (Moraceae) in acre, Brazil. *Brittonia* 72, 215–231. doi: 10.1007/s12228-020-09620-1

Pielou, E. C. (1966). The measurement of diversity in different types of biological collections. *J. Theor. Biol.* 13, 131–144. doi: 10.1016/0022-5193(66)90013-0

Ricotta, C., and Avena, G. (2003). On the relationship between Pielou's evenness and landscape dominance within the context of Hill's diversity profiles. *Ecol. Indic.* 2, 361–365. doi: 10.1016/S1470-160X(03)00005-0

Shi, Y., Mon, A. M., Fu, Y., Zhang, Y., Wang, C., Yang, X., et al. (2018). The genus *Ficus* (Moraceae) used in diet: its plant diversity, distribution, traditional uses and ethnopharmacological importance. *J. Ethnopharmacol.* 226, 185–196. doi: 10.1016/j.jep.2018.07.027

Shukla, G., Rai, P., Abha Manohar, K., and Chakravarty, S. (2020). Quantification of diversity, biomass and carbon storage of climber and liana community in a foothill forest of Indian Eastern Himalayas. *Acta Ecol. Sin.* 40, 478–482. doi: 10.1016/j.chnaes.2020.09.009

Stuart-Smith, R. D., Bates, A. E., Lefcheck, J. S., Duffy, J. E., Baker, S. C., Thomson, R. J., et al. (2013). Integrating abundance and functional traits reveals new global hotspots offish diversity. *Nature* 501, 539–542. doi: 10.1038/nature12529

Teixeira, S. P., Costa, M. F. B., Basso-Alves, J. P., Kjellberg, F., and Pereira, R. A. S. (2018). Morphological diversity and function of the stigma in *Ficus* species (Moraceae). *Acta Oecol.* 90, 117–131. doi: 10.1016/j.actao.2018.02.008

Tittensor, D. P., Mora, C., Jetz, W., Lotze, H. K., Ricard, D., Berghe, E. V., et al. (2010). Global patterns and predictors of marine biodiversity across taxa. *Nature* 466, 1098–1101. doi: 10.1038/nature09329

Wang, H.-F., Xu, X., Cheng, X. L., Liu, Y., Luo, A., Lyu, T., et al. (2022). Spatial patterns and determinants of Moraceae richness in China. *J. Plant Ecol.* 15, 1142–1153. doi: 10.1093/jpe/rtac025

Wu Zhengyi, Z. X. (1989). Taxa nova nonnulla moracearum sinensium. *Plant Divers.* 11, 1–3.

Yue, T. (2001). Studies and questions of biological diversity. *Acta Ecol. Sin.* 21, 462–467.

Zerega, N. J., Clement, W. L., Datwyler, S. L., and Weiblen, G. D. (2005). Biogeography and divergence times in the mulberry family (Moraceae). *Mol. Phylogenet. Evol.* 37, 402–416. doi: 10.1016/j.ympev.2005.07.004

Zhang, J., Zhu, W. F., Xu, J., Kitdamrongtham, W., Manosroi, A., Manosroi, J., et al. (2018). Potential cancer chemo preventive and anticancer constituents from the fruits of *Ficus hispida* L.f. (Moraceae). *J. Ethnopharmacol.* 214, 37–46. doi: 10.1016/j.jep.2017.11.016

Frontiers in Ecology and Evolution

TYPE Original Research
PUBLISHED 14 April 2023
DOI 10.3389/fevo.2023.1138884

Relationship between plant species diversity and aboveground biomass in alpine grasslands on the Qinghai–Tibet Plateau: Spatial patterns and the factors driving them

Mingxin Yang[1,2], Ang Chen[2], Min Zhang[2], Qiang Gu[1], Yanhe Wang[1], Jian Guo[3,4], Dong Yang[2], Yun Zhao[1], Qingdongzhi Huang[1], Leichao Ma[2,5] and Xiuchun Yang[2]*

[1]Xining Natural Resources Comprehensive Survey Center, China Geological Survey, Xining, China, [2]School of Grassland Science, Beijing Forestry University, Beijing, China, [3]State Key Laboratory of Remote Sensing Science, Faculty of Geographical Science, Beijing Normal University, Beijing, China, [4]Beijing Key Laboratory for Remote Sensing of Environment and Digital Cities, Faculty of Geographical Science, Beijing Normal University, Beijing, China, [5]Natural Resources Comprehensive Survey Command Center, China Geological Survey, Beijing, China

OPEN ACCESS

EDITED BY
Yanjie Xu,
Finnish Museum of Natural History, Finland

REVIEWED BY
Xiao-Dong Yang,
Xinjiang University, China
Yan Ruirui,
Chinese Academy of Agricultural Sciences (CAAS), China
Yaoqi Li,
Xi'an Jiaotong-Liverpool University, China

*CORRESPONDENCE
Xiuchun Yang
✉ Yangxiuchun@bjfu.edu.cn

SPECIALTY SECTION
This article was submitted to Environmental Informatics and Remote Sensing,
a section of the journal
Frontiers in Ecology and Evolution

RECEIVED 06 January 2023
ACCEPTED 29 March 2023
PUBLISHED 14 April 2023

CITATION
Yang M, Chen A, Zhang M, Gu Q, Wang Y, Guo J, Yang D, Zhao Y, Huang Q, Ma L and Yang X (2023) Relationship between plant species diversity and aboveground biomass in alpine grasslands on the Qinghai–Tibet Plateau: Spatial patterns and the factors driving them. *Front. Ecol. Evol.* 11:1138884.
doi: 10.3389/fevo.2023.1138884

Alpine grasslands are important ecosystems on the Qinghai–Tibet Plateau and are extremely sensitive to climate change. However, the spatial responses of plant species diversity and biomass in alpine grasslands to environmental factors under the background of global climate change have not been thoroughly characterized. In this study, a random forest model was constructed using grassland ground monitoring data with satellite remote sensing data and environmental variables to characterize the plant species diversity and aboveground biomass of grasslands in the Three-River Headwaters Region within the Qinghai–Tibet Plateau and analyze spatial variation in the relationship between the plant species diversity and aboveground biomass and their driving factors. The results show that (1) the selection of characteristic variables can effectively improve the accuracy of random forest models. The stepwise regression variable selection method was the most effective approach, with an R^2 of 0.60 for the plant species diversity prediction model and 0.55 for the aboveground biomass prediction model, (2) The spatial distribution patterns of the plant species diversity and aboveground biomass in the study area were similar, they were both high in the southeast and low in the northwest and gradually decreased from east to west. The relationship between the plant species diversity and aboveground biomass varied spatially, they were mostly positively correlated (67.63%), but they were negatively correlated in areas with low and high values of plant species diversity and aboveground biomass, and (3) Analysis with geodetector revealed that longitude, average annual precipitation, and elevation were the main factors driving variation in the plant species diversity and aboveground biomass relationship. We characterized plant species diversity and aboveground biomass, as well as their spatial relationships, over a large spatial scale. Our data will aid biodiversity monitoring and grassland conservation management, as well as future studies aimed at clarifying the relationship between biodiversity and ecosystem functions.

KEYWORDS

remote sensing, plant species diversity, random forest model, plant species diversity and aboveground biomass relationships, driving factors, Qinghai–Tibet Plateau

1. Introduction

The relationship between species diversity and productivity has been the subject of much debate (Waide et al., 1999; Adler et al., 2011; Grace et al., 2016; Chen et al., 2018). Biodiversity is concerned with the stability and sustainability of ecosystem functions and affects the value of ecosystem services and regional quality development (Bai et al., 2004). In large-scale grassland ecosystems, there is great spatial heterogeneity in species composition and productivity due to variation in geography, climate, and other environmental conditions; consequently, the relationship between species diversity and productivity can vary. Single-peaked patterns, positive correlations, and negative correlations have been observed, and the lack of a correlation between species diversity and productivity has also been observed (Ma and Fang, 2006; Adler et al., 2011). At the regional scale, enhancing the monitoring and assessment of grassland biodiversity and ecosystem functions is essential for the development of grassland biodiversity conservation policies and grassland ecosystem management.

Remote sensing technology has a wide monitoring range and can be used to monitor vegetation over long periods unlike traditional ground survey approaches, it has thus been widely used to monitor variables such as grassland aboveground biomass (AGB) and plant species diversity (PSD) (Reddy et al., 2021; Ge et al., 2022; Sun et al., 2022). Indicators such as grassland biomass and plant species richness are well correlated with remotely sensed vegetation indices such as the normalized vegetation index (NDVI) and enhanced vegetation index (EVI), and they are often used to construct grassland models (Oindo and Skidmore, 2002; Chitale et al., 2019; Reddy, 2021; Yu et al., 2021). Due to the large area and diversity in grassland types, spatial heterogeneity in grasslands is pronounced, and multiple environmental variables need to be integrated to construct high-precision models. In previous studies in which biomass has been monitored *via* remote sensing, several variables including vegetation indices, climate, topography, soil, and other variables have been used to increase model accuracy (Liang et al., 2016). However, few studies have integrated variables such as effective vegetation index, climate, topography, soil, and other variables into models for large-scale grassland species diversity monitoring (Choe et al., 2021; Zhao et al., 2022). In addition, some studies (Fauvel et al., 2020; Ge et al., 2022) have compared the efficacy of multiple machine learning models for modeling grassland species diversity and biomass, previous studies have shown that the random forest (RF) model is particularly effective. However, the inclusion of various environmental variables can increase model complexity, multicollinearity of the model can also affect model accuracy. Consequently, the selection of key variables is critical for enhancing the computational efficiency and accuracy of models (Zeng et al., 2019; Yu et al., 2021). Screening for effective variables can improve the computational efficiency of models and reduce the workload of model spatial simulations.

Study of the spatial relationship between plant species diversity and aboveground biomass (PSD–AGB) in grasslands, as well as the mechanisms driving it is important for enhancing our understanding of grasslands and promoting their conservation. Some researchers have analyzed the PSD–AGB relationship in local areas using field data (Waide et al., 1999; Zhu et al., 2017; Sakowska et al., 2019), and some valuable insights have been obtained. But these studies have been limited to small spatial scales based on ground survey data. However, the PSD–AGB relationship varies with the spatial scale of the study (Chase and Leibold, 2002), Ni et al. (2007) showed that the PSD–AGB relationship varies at different ecological scales and geographic scales. Previous studies have been limited by the inability to achieve large scale PSD and AGB, so the PSD–AGB relationship at large scales is still inadequate, while the current remote sensing-based technology can provide high precision estimation of PSD and AGB at the large scales (Choe et al., 2021; Wang et al., 2022), which providing us with the possibility to study the spatial relationship between the two. In addition, the relationship between species diversity and biomass is not only influenced by multiple environmental factors but also by spatial factors (Spyros Tsiftsis, 2018; Li et al., 2020; Du et al., 2022; Ma et al., 2022). Qi et al. (2022) showed that the relationship between species diversity and biomass in the Qinghai–Tibetan Plateau was generally nonlinear and positive over space, and Omidipour et al. (2021) showed that the relationship between species diversity and biomass differed among grassland areas. But in study areas with large environmental differences, it is well worthwhile to deeply investigate how the PSD–AGB relationship in large scale grasslands, and what environmental factors drive spatial distribution patterns.

The Qinghai–Tibet Plateau features typical alpine grassland ecosystems, there is wide spatial variation in vegetation growth, and this region is highly sensitive to climate change (Ma et al., 2017; Piao et al., 2019). Therefore, several environmental variables need to be considered to efficiently monitor spatial patterns of and correlations between grassland species diversity and their productivity functions, as well as the response of grassland ecosystems to global climate change, this information can also aid ecological conservation efforts. In this study, grassland species richness and above-ground biomass data obtained from ground-based surveys, along with satellite remote sensing data, were used to analyze spatial relationships between species diversity and productivity and their drivers in alpine grasslands of the Qinghai–Tibet Plateau. The specific objectives were to (1) establish a reliable model to estimate the spatial distribution of species diversity and grassland productivity in the study area; (2) analyze spatial patterns in correlations between grassland species diversity and productivity in the study area; and (3) explore the main factors driving the spatial relationships between grassland species diversity and productivity in the study area.

2. Materials and methods

2.1. Study area

Our study was conducted in the Three-River Headwaters Region in the eastern part of the Qinghai–Tibet Plateau. The Three-River

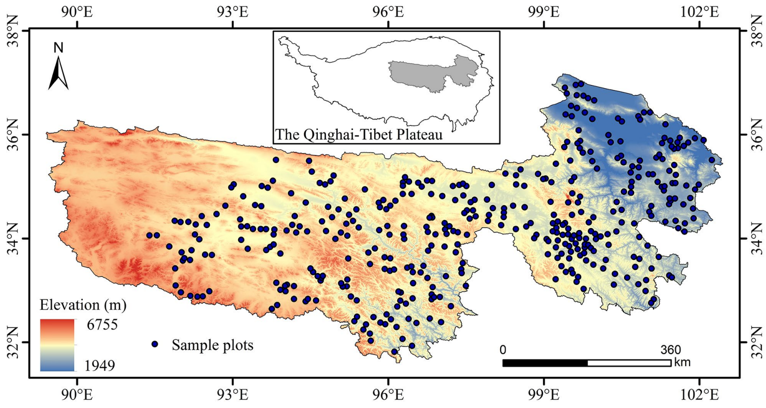

FIGURE 1
Location of the study area and spatial distribution of sample plots.

Headwaters Region is located in southern Qinghai Province, China from 31°39′N to 36°16′N and from 89°24′E to 102°41′E. The average elevation of the region is above 4,000 m, the average annual temperature ranges from −5.4 to 6.9°C, the average annual precipitation ranges from 392 to 764 nm, and the total area of the study area is 395,000 km^2. The sources of the Yangtze River, Yellow River, and Lancang River are located in the Three-River Headwaters Region, this region is also the world's highest and largest plateau wetland area and the most biodiversity high-altitude area, it is thus often referred to as the "Chinese Water Tower," "Plateau Species Gene Bank," and the "gene pool of plateau species" (Zhao, 2021). In addition, 71% of the region comprises typical alpine grassland ecosystems, the main types of grasslands are alpine meadows, alpine grasslands, and temperate grasslands. These grasslands provide several extremely important ecosystem services for the region, such as water containment, climate regulation, biodiversity maintenance, and a pasture supply.

2.2. PSD and AGB ground monitoring data

We collected field data during the peak of the grassland growing season from July to August 2021. In the field survey, 429 sample plots were set up to cover all grassland types in the study area as far as possible, with a relatively uniform spatial distribution and easy accessibility (Figure 1). In order to match with modis pixels, we set the sample plot size to 250 m × 250 m, and investigated the information of centroid coordinates, grassland vegetation types within the sample plot. Three to five replicate quadrats were set up in each sample plot, and the quadrat size was 1 m × 1 m. To collected information on the longitude (X), latitude (Y) and elevation of each quadrat, as well as the vegetation species richness, cover and height of the grassland community within the quadrat. The species richness was determined by counting the total number of species present within the quadrat. The vegetation cover was visually estimated by determining the percentage of the quadrat area covered by the vertical projection of the vegetation. The vegetation in the quadrats was mowed, bagged, taken to the laboratory, dried in an oven at 65°C for 48 h, and weighed to obtain the dry weight of grass biomass. To match quadrat-scale data to the sample plot scale, we took the average species richness and biomass dry weight of all quadrats in each sample plot to represent the PSD and AGB of that sample plot. A total of 417 valid sample plot data were obtained using the sample data set.

2.3. Remote sensing vegetation index

The satellite remote sensing data were called MOD09Q1 data and obtained using the Google Earth Engine (GEE) platform with a spatial resolution of 250 m and a temporal resolution of 8 d. The entire coverage of the study area required three scenes of images(h24v05, h25v05, and h26v05), and a total of 15 remote sensing images were obtained throughout the field survey (July 27 to August 24). A total of five vegetation indices, normalized vegetation index (NDVI), enhanced Vegetation Index 2 (EVI2), ratio vegetation index (RVI), soil adjustment vegetation index (SAVI), and optimization of soil-adjusted vegetation index (OSAVI), were calculated and downloaded through the GEE platform editor. The vegetation indices of each sample plot were extracted separately using ArcGIS software.

2.4. Data on other variables

Digital elevation model (DEM) data were obtained from Space Shuttle Radar Topography Mission (SRTM) images with a spatial resolution of 30 m and a spatial reference of GCS_WGS_1984. Slope gradient (SLOPE) and slope orientation (ASPECT) data with a resolution of 30 m were generated using ArcGIS software.

The National Geoscience Data Center[1] application was used to obtain month-by-month precipitation, temperature, and potential evapotranspiration data for 2021 with a spatial resolution of 1 km. The data were converted from nc format to tiff format in ArcGIS software, and the average values for the 12 months were used to calculate annual mean temperature (MAT), mean annual precipitation (MAP), and mean annual potential evapotranspiration (SPEI). The averages for May to October were used as the mean growing season temperature (MGT), mean precipitation (MGP), and mean potential evapotranspiration (GSPEI) in the study area.

Soil data were obtained from the National Geoscience Data Center (see text footnote 1) in nc format with a spatial fraction of 1 km. The data included soil bulk weight (BD), sand content (SA) chalk content (SI), clay content (CL), soil organic matter (SOM), total nitrogen content (TN), and total phosphorus content (TP) for eight

---

[1] http://www.geodata.cn/

soil layers at a depth of 0 to 3 m. Due to the relatively shallow root system of the grasslands, soil data from a depth of 0 to 0.3 m in the soil surface layer were used.

Grassland spatial distribution data were extracted from the secondary classification by downloading the LUCC2020 surface classification data. These grassland cover data in the study were extracted by masking the vector boundary of the Three-River Headwaters Region and these data were used to mask the grassland boundary in the study area.

We resampled the above data (DEM, SLOPE, ASPECT, MAT, MAP, SPEI, MGT, MGP, GSPEI, BD, SA, SI, CL, SOM, TN, and TP) at different resolutions to 250 m, the grassland boundary in the study area was then masked to extract the sample data for analysis.

2.5. PSD and AGB modeling inversion methods

2.5.1. Variable filtering methods

We prepared sample site latitude and longitude, five remotely sensed vegetation indices, and 16 environmental variables for a total of 23 variable factors to construct grassland PSD and AGB models. The complexity of the model increases with the number of variables included, variable screening can eliminate the problem of multicollinearity between multiple variables to improve model accuracy and computational efficiency. Thus, the selection of variables appropriate for machine learning modeling is key.

In this study, two methods, stepwise regression (STEP) and least absolute shrinkage and selection operator (LASSO), were used to determine the optimal set of variables and the optimal model. The STEP model works by introducing variables one by one into the model. STEP eliminates insignificant variables so that the multicollinearity between the retained variables is reduced, thus ensures that the final set of explanatory variables chosen by the model is optimal. LASSO (Wang et al., 2008) can deal with multicollinearity by automatically selecting the most important independent variables and setting the values of less important predictor variables to zero, thereby only retaining the most useful features. Both variable selection methods were implemented in RStudio, STEP was conducted through a stepwise fitting function, and LASSO was conducted through the "glmnet" package.

2.5.2. RF model construction and accuracy verification

In this study, PSD and AGB regression models for grasslands were established using the RF model. The models used the measured PSD and AGB data as dependent variables, and the variables obtained from the above 23 variables, as well as the variables identified from the STEP and LASSO variable selection methods, as independent variables. A total of six models were established, and the accuracy of the models was evaluated using the PSD and AGB data to identify the optimal variable screening results and models.

RF is a novel nonparametric machine learning algorithm that uses multiple decision trees to train samples and integrate predictions (Li, 2019). We incorporated all the independent and dependent variables into 417 datasets according to their spatial location, and randomly selected 293 sample plot data points (70% of valid samples) from the datasets as training datasets and 124 sample plot data points (30% of valid samples) as test datasets in the RF modeling process. In this study, the RF algorithm was implemented using the "randomForest" package in RStudio, and the optimal model was obtained by adjusting the number of decision classification trees (ntree) and the number of features of node segmentation (mtry) to find the optimal model. The model accuracy was evaluated using three metrics: root mean square error (RMSE), correlation coefficient (R^2), and mean absolute error (MAE). The formulas used to calculate these metrics are as follows:

$$RMSE = \sqrt{\frac{\sum_{i=1}^{n}\left(y_i - \hat{y}_i\right)^2}{n}} \tag{1}$$

$$R^2 = 1 - \frac{\sum_{i=1}^{n}\left(y_i - \hat{y}_i\right)^2}{\sum_{i=1}^{n}\left(y_i - \overline{y_i}\right)^2} \tag{2}$$

$$MAE = \frac{1}{n}\sum_{i=1}^{n}\left|y_i - \hat{y}_i\right| \tag{3}$$

where n is the number of sample plots, y_i is the model predicted value of the ith sample plot, $\overline{y_i}$ is the measured value of the ith sample plot, and $\hat{y}_i$ is the average of the measured values.

2.6. PSD and AGB correlation analysis method

Traditional raster data correlation analysis can only be used to calculate the correlation coefficients between two variables; however, this approach cannot be used to characterize the spatial distribution of correlations between raster data pixel-by-pixel. Consequently, we used a 3 × 3 moving window (nine pixels in each window) for the two raster data sets, the correlation coefficient of each spatially corresponding window was determined, and the spatial distribution of the correlations between the two raster data pixels was determined. The spatial distribution of the image-by-image correlations of raster data was finally obtained. The spatial distribution of the PSD–AGB relationship was obtained using the above method to analyze the pixel-by-pixel correlation of the PSD and AGB rasters.

2.7. Determination of the factors driving variation in the dependent variables

We used geodetector (Wang and Xu, 2017) to detect spatial heterogeneity, which mainly includes factor detectors, interaction detectors, risk detectors, and ecological detectors. Factor detectors are mainly used to detect the degree to which the independent variable X explains spatial heterogeneity in the dependent variable Y, and interaction detectors are used to detect the degree to which the interaction between two independent variables explains spatial heterogeneity in the dependent variable Y. The principle can be summarized as follows.

$$q = 1 - \frac{1}{N\sigma^2}\sum N_h \sigma_h^2 \qquad (4)$$

where q is an indicator of spatial heterogeneity; σ^2 is the variance of the variable; h is the stratification of the variable, and the value of q ranges from 0 to 1. Larger q values indicate stronger explanatory power of the variable.

In this study, a total of 16 geographic factors (LAT, LON, DEM, SLOPE, and ASPECT), climatic factors (MAT, MAP, and SPEI), and soil factors (BD, SA, SI, CL, SOM, TN, and TP) were used for single-factor detection and interaction detection of the spatial relationships of PSD–AGB to identify the factors driving variation in PSD–AGB. The GD package in R software was used for geodetector factor detection and interaction detection.

3. Results

3.1. Descriptive statistics of the PSD and AGB data

The descriptive statistics of PSD and AGB of the 417 measured samples used in the modeling are shown in Table 1. The maximum value of PSD was 26 n/m^2, the minimum value was 3 n/m^2, the mean value was 10.27 n/m^2, the standard deviation (SD) was 4.60 n/m^2, and the coefficient of variation (CV) was 0.45. The maximum value of AGB was 4365.70 kg/ha, the minimum value was 157.90 kg/ha, the mean value was 1465.43 kg/ha, the SD was 824.21 kg/ha, and the CV was 0.56.

3.2. Variable selection and model accuracy evaluation

In the PSD variable screening, STEP screening yielded eight variables: X, Y, EVI2, RVI, SAVI, MAT, SPEI, and SI. LASSO screening yielded nine variables: X, Y, EVI2, RVI, SPEI, SLOPE, BD, SI, and TN. Variables selected by both variable selection results included X, Y, EVI2, RVI, SPEI, and SI6. The model built with variables based on STEP screening had the highest accuracy (R^2, RMSE, and MAE of the test set were 0.60, 2.92, and 2.37, respectively), followed by the model built with all variables (R^2, RMSE, and MAE of the test set were 0.58, 3.00, and 2.45, respectively). The R^2, RMSE, and MAE of the test set from the LASSO-screened variables were 0.57, 3.03, and 2.46, respectively (Table 2). According to the accuracy indicators of the model training set and test set, the RF model established by the STEP screened variables was the optimal model for PSD estimation in the study area.

STEP screening of AGB variables yielded seven variables: X, Y, EVI2, RVI, MAT, DEM, and TN. LASSO screening yielded eight variables: X, Y, NDVI, EVI2, RVI, MAT, SLOPE, and CL. According to the RF model accuracy evaluation, variable screening can improve the estimation of AGB accuracy, and the R^2, RMSE, and MAE of the test set from the STEP-screened variables were 0.55, 578.93, and 434.10, respectively, followed by LASSO-screened variables (R^2, RMSE, and MAE of 0.52, 596.51, and 450.99, respectively, for the test set) (Table 2). The RF model established by STEP screened variables was finally used for AGB estimation in the study area based on the above results.

3.3. Comparison of measured and model predicted values of PSD and AGB

Based on the optimal models of PSD and AGB, we extracted the predicted and measured values of the models in the test set and established linear relationships and value domain distribution plots to evaluate the estimation ability of the models (Figure 2). In general, there were strong linear relationships of measured values with the PSD estimation model and the AGB estimation model, the PSD estimation model explained 60% of the variation in grassland PSD, and the AGB estimation model explained 55% of the variation in grassland AGB. However, both models underestimated high values and overestimated low values. In the PSD estimation model, the median model estimate was slightly higher than the measured value overall, and the model estimates were significantly higher than measured values between 8 and 12 n/m^2. In the AGB estimation model, the median model estimates were slightly lower than the measured values, the model overestimates AGB near values of 1,500 kg/ha and underestimates AGB when values exceed 2,200 kg/ha.

3.4. PSD and AGB spatial distribution characteristics

We inferred the spatial distribution of the maximum PSD and AGB in the study area in 2021 using the optimal model obtained by STEP screening variables (Figure 3). In general, the spatial distribution patterns of PSD and AGB are basically similar and mainly decrease from east to west and from southeast to northwest, some differences in their distribution were also observed in local areas. PSD and AGB were high in Nangqian and Yushu in the southern Three-River Headwaters Region and Henan, Zeku, Jiuzhi, and Banma in the southeast. PSD and AGB are medium in Xinghai, Maduo, Qumalai, Zaduo, and Eastern Zhiduo. The PSD and AGB are low in western Zhiduo and Geermu. Slight spatial differences were observed between PSD and AGB in some local areas, such as northwestern Republican

TABLE 1 Descriptive statistics of the PSD and AGB data of the measured grassland.

Category	Samples	Minimum	Maximum	Average	SD	CV
PSD	417	3	26	10.27	4.60	0.45
AGB	417	157.90	4365.70	1465.43	824.21	0.56

TABLE 2 Results of variable selection and evaluation of model accuracy.

Category	Variable selection	Variables	Training dataset			Test dataset		
			R^2	RMSE	MAE	R^2	RMSE	MAE
PSD	ALL	X, Y, NDVI, EVI2, RVI, SAVI, OSAVI, DEM, SLOPE, ASPECT, MAT, MGT, MAP, MGP, SPEI, GSPEI, BD, SA, SI, CL, SOM, TN, TP	0.92	1.66	1.31	0.58	3.00	2.45
	STEP	X, Y, EVI2, RVI, SAVI, MAT, SPEI, SI	0.90	1.65	1.24	0.60	2.92	2.37
	LASSO	X, Y, EVI2, RVI, SPEI, SLOPE, BD, SI, TN	0.91	1.63	1.27	0.57	3.03	2.46
AGB	ALL	X, Y, NDVI, EVI2, RVI, SAVI, OSAVI, DEM, SLOPE, ASPECT, MAT, MGT, MAP, MGP, SPEI, GSPEI, BD, SA, SI, CL, SOM, TN, TP	0.92	268.85	210.08	0.50	600.47	454.89
	STEP	X, Y, EVI2, RVI, MAT, DEM, TN	0.92	256.15	195.51	0.55	578.93	434.10
	LASSO	X, Y, NDVI, EVI2, RVI, MAT, SLOPE, CL	0.92	263.46	198.66	0.52	596.51	450.99

County where AGB is not high, but PSD is high, the same pattern was also observed in local areas in Xinghai and Zhiduo counties, as well as in local areas in Zeku, Henan, Maqin, Gande, and Jiuzhi counties where AGB is particularly high, but PSD is not particularly high. The minimum value of PSD of the inversion model in the study area was 4 n/m^2, the maximum value was 18 n/m^2, the mean value was 9.42 n/m^2, and the standard deviation was 2.37 n/m^2. The minimum value of AGB of the inversion model was 541.13 kg/ha, the maximum value was 2695.14 kg/ha, the mean value was 1392.34 kg/ha, and the standard deviation was 395.09 kg/ha.

3.5. Spatial pattern of PSD–AGB relationships

To analyze the spatial PSD–AGB relationships in different regions, we conducted pixel-by-pixel correlation analysis of PSD and AGB and obtained the spatial pattern shown in Figure 4. Large spatial variation was observed in the PSD–AGB relationship, mostly negative correlations were observed in the northwest and southeast, and mostly positive correlations were observed in the central region. Areas with negative correlations were mainly distributed in Geermu, Western Zhiduo, and Northern Qumalai in the northwestern part of the study area and local areas in Henan, Zeku, Maqin, and Jiuzhi counties in the southeastern part of the study area. In addition, negative correlations were also observed in the Jifushan mountain range (source of the Lancang River) at the junction of Zhiduo and Zaduo and in the valley of the Yellow River Basin (upstream of Longyangxia) in eastern Xinghai County. In addition, the PSD–AGB correlation coefficient was positive and strong in the central part of the study area in Qumalai, Eastern Zhiduo, Zaduo, and Chengduo and in the northeastern part of the study area in Xinghai, Guinan, and Guide. The correlations were positive and weak in the central part of the study area in Yushu, Maduo, Dari, Gande, and Banma. According to the PSD–AGB correlation coefficient significance statistics, a significant positive correlation was observed for 39.24% of the regions in the study area ($p < 0.05$), non-significant positive correlations were observed for 28.39% of the regions in the study area, significant negative correlations were observed for 9.36% of the regions in the study area ($p < 0.05$), non-significant negative correlations were observed for 20.58% of the regions in the study area, and non-significant relationships were observed for 2.43% of the study area.

3.6. Factors affecting spatial variation in the PSD–AGB relationship

Based on the q-statistic values of single factors detected *via* the geodetector (Figure 5A), the most important factors driving spatial variation in the PSD–AGB relationship in the study area were LON, followed by MAP, DEM, SI, TP, LAT, MAT, SLOPE, BD, SPEI, SOM, TN, SA, CL, and ASPECT. The q-value of LON was the largest (0.29), followed by MAP (0.21), DEM (0.18), and SI (0.15), indicating that spatial variation in the PSD–AGB relationship in the study area was mainly affected by LON, followed by MAP, DEM, and SI. The q-values of the other factors were lower, the q-value of ASPECT was the lowest (0.01).

Interaction effects (Figure 5B) on spatial variation in the PSD–AGB relationship were stronger than the effects of any single factor, and this same finding was obtained *via* two-factor enhancement and nonlinear enhancement. Factors with high performance include LON, MAP, and DEM, and the strongest interaction effect was that of LON–LAT (0.5 according to the nonlinear enhancement), followed by the interactions of LON–MAP (0.49 according to two-factor enhancement) and MAP–DEM (0.47 according to nonlinear enhancement).

4. Discussion

4.1. PSD and AGB inversion model accuracy

The results of this study show that variable selection effectively improved the accuracy of both the PSD and AGB models. The accuracy of the variable model was highest according to the STEP method, which is consistent with the results of Ge et al. (2022) showing that the accuracy of the variable model was highest when the STEP method was used. Wang et al. (2022) used three variable selection methods, although they did not use the STEP method, their results show that variable selection improves model accuracy. The STEP method used in this study introduces variables into the model

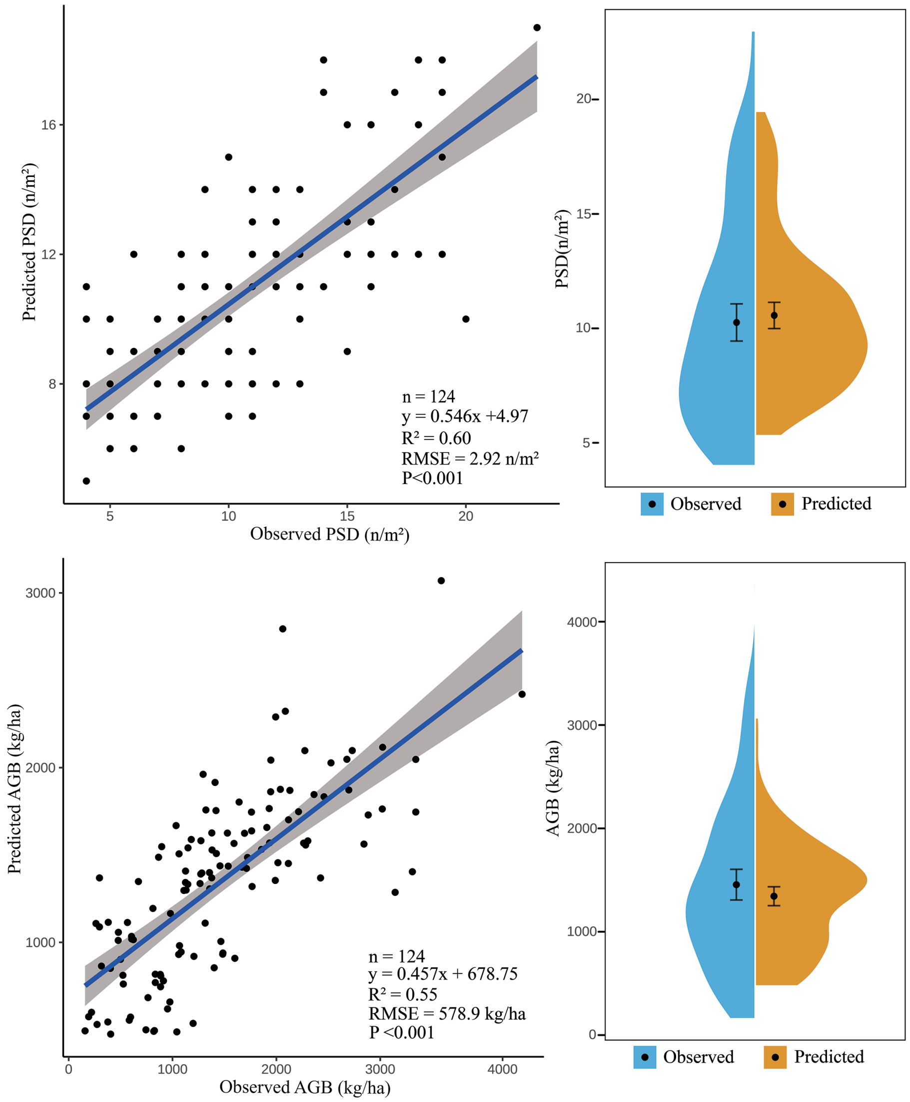

FIGURE 2
Comparison of the measured values of PSD and AGB with the predicted values of the optimal model.

one by one and eliminates insignificant variables, thus ensuring that the final set of explanatory variables obtained is optimal. In light of the widespread use of machine learning, an increasing number of environmental variables have been used as independent variables in models; thus, variable selection can greatly improve the computational efficiency of the model while also improving model accuracy. Overall, the specific variable selection method that enhances model accuracy likely varies with the study objective, data source, and comparison method.

The optimal AGB model of this study had an R^2 of 0.55, which is less accurate than previous simulations of the AGB of grasslands in the Three-River Headwaters Region according to the studies of Liang et al. (2016) (R^2 of 0.701) and Wang et al. (2022) (R^2 of 0.60) but more accurate than the study of Wang et al. (2018) (R^2 of 0.31). The optimal model of Liang et al. (2016) used grassland height, which has a direct relationship with productivity; consequently, their inverse AGB accuracy is higher. However, there is still much uncertainty in the inverse of grassland height. In contrast, Wang et al. (2022) used 1,620 samples obtained over 10 years, on the one hand the sample size was larger, and on the other hand the model was trained for environmental changes over a 10 year period, so the model accuracy was higher than this study. The R^2 of the optimal model in this study was 0.60, and the RMSE was 1.65 n/m^2 in the simulation of PSD; the RMSE of the RF model in Zhao et al. (2022) was 1.94 n/m^2, and the RMSE of the optimal HASM-XGBoot model reached 1.19 n/m^2. HASM can effectively solve ecological environmental surface modeling errors, thus improving the accuracy of conventional machine learning models, we aim to test combinations of HASM methods in the future. Generally, the sample size involved in the model, the variables involved in the modeling, and modeling methods vary, and this greatly affects the accuracy of the model.

Comparison of the measured and predicted values of the two models in this study revealed that the accuracy of both models was high; however, both models underestimated high values and overestimated low values, which is a common problem of many machine learning models (Ge et al., 2022; Sabatini et al., 2022; Zhao

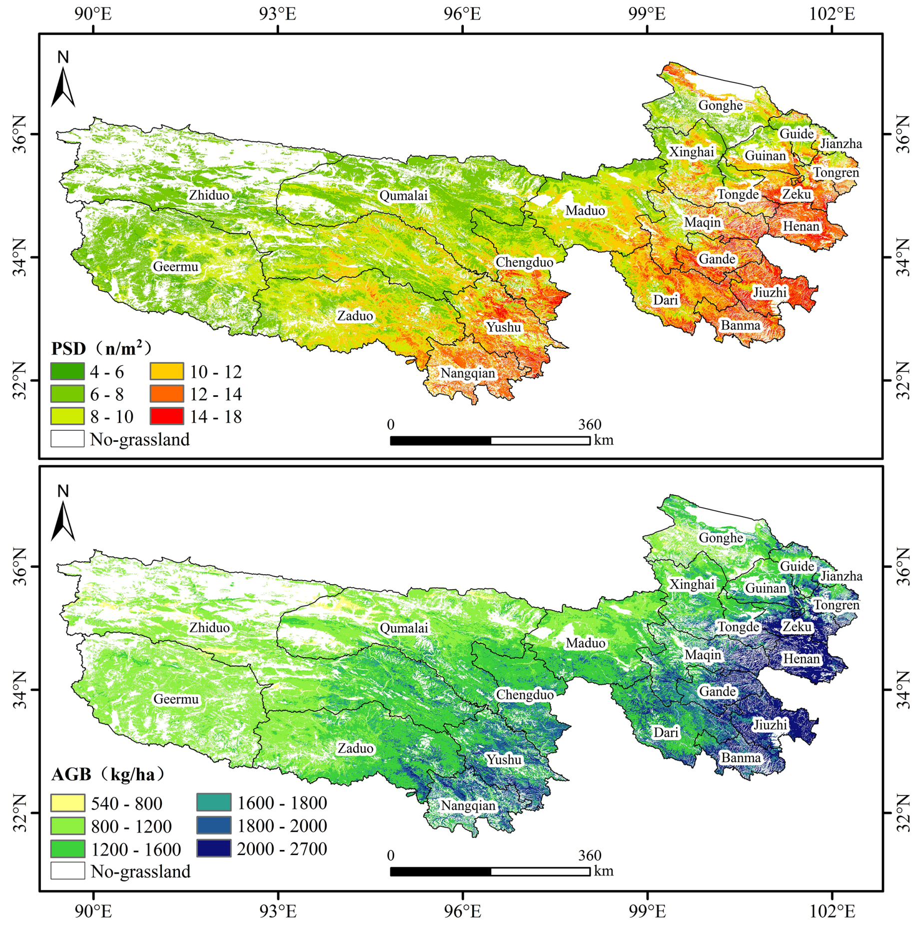

FIGURE 3
PSD and AGB spatial distribution map.

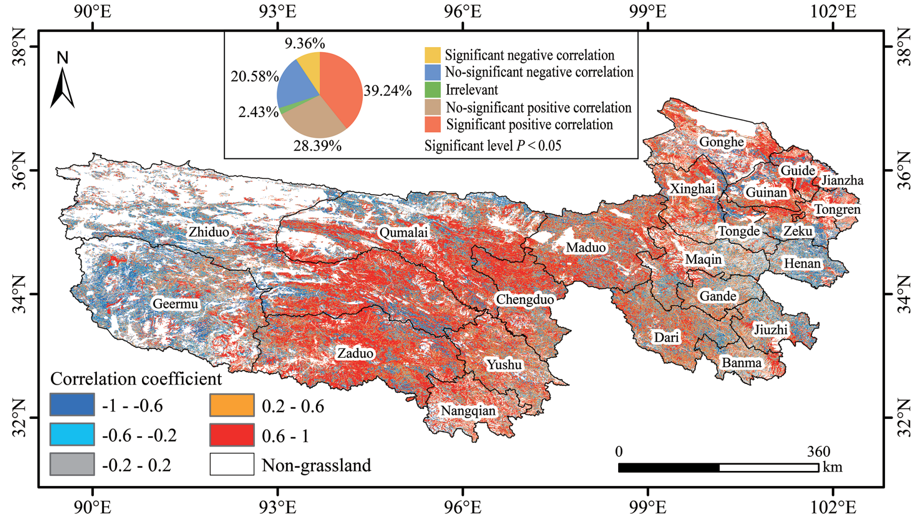

FIGURE 4
Spatial variation in the PSD–AGB relationship.

et al., 2022). In addition, the overall fit of the PSD model was better than that of the AGB model, the model overestimated PSD when values were near 9 n/m², and the model overestimated AGB when values were near 1,500 kg/ha. This might be explained by the uneven spatial distribution of our field sampling data, the large size of the study area, the large altitudinal gradient, and the fact that the western

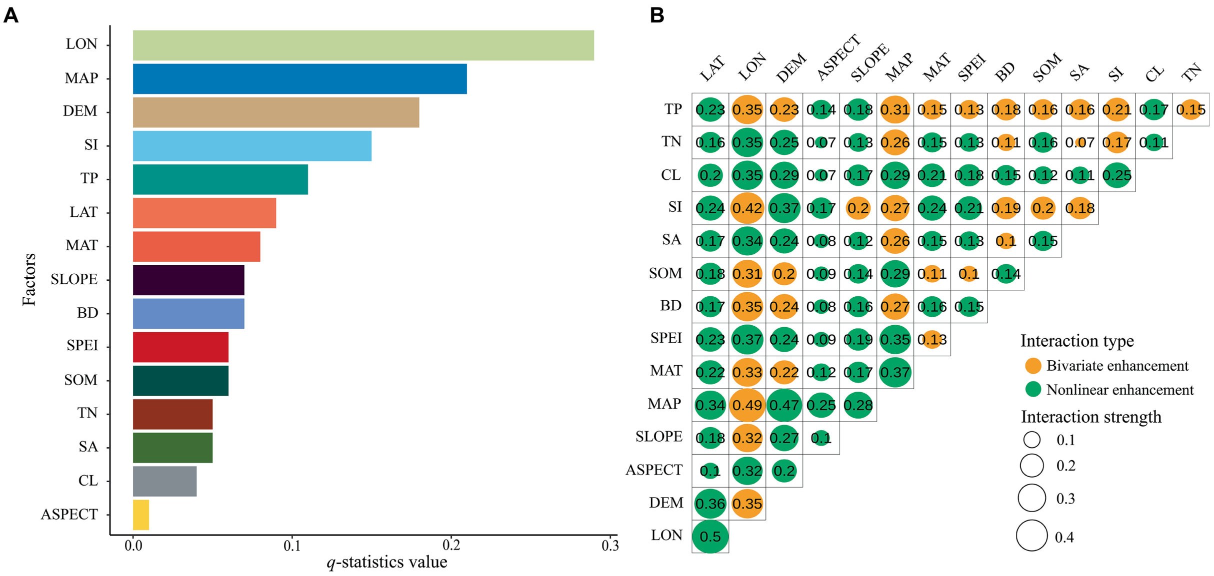

	LAT	LON	DEM	ASPECT	SLOPE	MAP	MAT	SPEI	BD	SOM	SA	SI	CL	TN
TP	0.23	0.35	0.23	0.14	0.18	0.31	0.15	0.13	0.18	0.16	0.16	0.21	0.17	0.15
TN	0.16	0.35	0.25	0.07	0.13	0.26	0.15	0.13	0.11	0.16	0.07	0.17	0.11	
CL	0.2	0.35	0.29	0.07	0.17	0.29	0.21	0.18	0.15	0.12	0.11	0.25		
SI	0.24	0.42	0.37	0.17	0.2	0.27	0.24	0.21	0.19	0.2	0.18			
SA	0.17	0.34	0.24	0.08	0.12	0.26	0.15	0.13	0.1	0.15				
SOM	0.18	0.31	0.2	0.09	0.14	0.29	0.11	0.1	0.14					
BD	0.17	0.35	0.24	0.08	0.16	0.27	0.16	0.15						
SPEI	0.23	0.37	0.24	0.09	0.19	0.35	0.13							
MAT	0.22	0.33	0.22	0.12	0.17	0.37								
MAP	0.34	0.49	0.47	0.25	0.28									
SLOPE	0.18	0.32	0.27	0.1										
ASPECT	0.1	0.32	0.2											
DEM	0.36	0.35												
LON	0.5													

FIGURE 5
Value of the *q*-Statistic for each variable. **(A)** shows the univariate probes for each variable and **(B)** shows the interaction probes for each variable.

region is mostly uninhabited because of its harsh climate. Thus, some areas with low values in the west were not considered, and areas with medium values were mainly concentrated in the center of the study area (Figure 1).

4.2. PSD and AGB spatial distribution characteristics

According to the spatial distributions of the inversion models of PSD and AGB, both PSD and AGB were high in the southeastern portion of the study region and low in the northwestern portion of the study region. The spatial distribution of AGB was similar to that observed in Zeng et al. (2019) using the RF model and Wang et al. (2018) using the ANN model; AGB values were high in southeastern portions of Henan, Zeku, Gander, and Jiuzhi and central and southern parts of Nangqian and Yushu; AGB values were lower in western regions. AGB ranged from 540 to 2,700 kg/ha in our study, which is similar to the range reported in Zeng et al. (300 to 2,500 kg/ha). The range of AGB values observed in Wang et al. (250 to 3,250 kg/ha) differed from that observed in our study, this difference might be related to differences in the variables included in the model and the methods used. The similar spatial distributions of PSD and AGB observed in our study are consistent with the hypothesis that biodiversity and productivity are positively correlated (Loreau et al., 2001); however, local differences in their distributions were observed. The PSD and AGB of species around Qinghai Lake are likely high because of the suitable water and heat conditions around the lake, but this area is traditionally used for grazing (Zhai et al., 2017), and the reason for the low AGB may be related to the high grazing intensity in the area. In addition, large-scale inverse mapping of grassland species diversity models has not been widely studied, the results of our study are superior in terms of model accuracy and spatial distribution. This method permits large-scale biodiversity remote sensing monitoring in grasslands with large heterogeneity, which fills gaps with no monitoring data in some unoccupied areas. Moreover the PSD spatial distribution map shows the spatial distribution pattern on a large scale, and these data can aid biodiversity assessment and conservation.

4.3. Spatial variation in PSD–AGB relationships and factors driving variation in PSD–AGB relationships

Recent studies that have examined PSD–AGB relationships have seldom considered the possible effects of spatial scale and spatial heterogeneity on PSD–AGB relationships. Most studies have focused exclusively on small spatial scales or regions with little spatial variation. In this study, we analyzed spatial variation in the PSD–AGB relationship on a large scale while accounting for geographical heterogeneity. Our findings indicate that the relationship between PSD and AGB in the western and southeastern parts of the study area was mostly negatively correlated, and the relationship between PSD and AGB in other regions was positively correlated. Significant positive correlations were observed over 39.24% of the study region, and significant negative correlations were observed over 9.36% of the study region. It is noteworthy that combining the spatial distribution of PSD and AGB (Figure 3), we found that PSD and AGB were negatively correlated in areas with low and high values; by contrast, PSD and AGB were positively correlated in areas with medium values. For this reason, we determined the relative contributions of various environmental factors driving spatial variation in the PSD–AGB relationship using geodetector. According to the single-factor analysis, longitude was the factor that had the largest effect on the PSD–AGB relationship (explaining 29% of the variation in the spatial pattern), followed by annual precipitation, altitude, and SI. And the factor interaction analysis revealed that longitude explained 50% of the variation in the PSD–AGB relationship; however, the interaction between precipitation, elevation, and SI had the greatest effect on spatial variation in the PSD–AGB relationship. Zhu et al. (2017) also showed that the PSD–AGB relationship varied with longitude in the Tibetan Plateau. Wang et al. (2007) and Xu et al. (2019) showed that spatial variation in the PSD–AGB relationship was correlated with longitude, latitude, and altitude. The study area spans several degrees of longitude but only a few degrees of latitude; consequently, there is large variation in longitude, as well as a significant elevational gradient and precipitation gradient in the east–west direction of the study area. Longitude, elevation, and precipitation in the east–west direction thus explain much spatial variation in the PSD–AGB relationship. Temperature varies more in the latitudinal direction, and the latitudinal variation in our study area was low, this might explain the weak effect of temperature on spatial variation in the PSD–AGB relationship. In addition, the spatial resolution of soil property data used in this study was 1 km, and spatial variation in several variables was low, this might contribute to explaining the weak effects of soil environmental variables on variation in the PSD–AGB relationship, with the exception of SI. Spatial variation in the environment of grassland plant communities can lead to differences in community characteristics and thus spatial variation in the PSD–AGB relationship. We speculate that the resource use complementarity hypothesis might explain variation in the PSD–AGB relationship across our study area (David Tilman, 1997; Loreau et al., 2001), the western part of the study area has a harsh climate, infertile soils, fewer available resources for plants, and strong interspecific competition, which results in a negative relationship between PSD and AGB. In the central part of the study area, the hydrothermal conditions are improved and the abundance of resources available to plants is greater. Increases in species diversity promote the complementary use of resources among species, which enhances the accumulation of biomass. However, PSD values plateaued in the southeastern part of the study area where biomass was highest. In addition, ecological niche space was lower, light, soil nutrients, and other resources were limited, interspecific competition was intense, and some dominant plants suppressed the growth of inferior plants in this region, such observations explain the negative relationship between PSD and AGB in areas with high AGB values (Schnitzer et al., 2011; Guo and Berry, 2013; Albert et al., 2022; Qi et al., 2022). Grassland productivity includes AGB and belowground biomass. In our study, we only monitored and analyzed the relationship between AGB and PSD. Additional monitoring of belowground biomass is needed in subsequent studies to characterize the spatial relationships between PSD and productivity.

5. Conclusion

In this study, an RF model was constructed using grassland ground monitoring data along with satellite remote sensing data and environmental variables to characterize spatial distribution patterns in PSD and AGB in the Three-River Headwaters Region. The accuracy of the model was compared using three variable selection methods, and the STEP variable selection method showed the highest performance, which indicates that variable selection could effectively improve the accuracy of the RF model. The R^2 of the PSD and AGB test sets based on the optimal STEP-RF model was 0.6 and 0.55, and the RMSE was 2.92 n/m^2 and 578.93 kg/ha, respectively. Spatial distribution patterns in PSD and AGB across the study area was similar, the PSD and AGB values were generally high in the southeast and low in the northwest. The modeling approach used in this study could be used to monitor grassland species diversity and productivity on a large scale, it could also aid biodiversity monitoring and grassland conservation management.

We also analyzed spatial variation in the PSD–AGB relationship, as well as the environmental variables driving variation in this relationship, including climate, topography, and soil. The PSD–AGB relationship tended to be mostly positively correlated. However, the PSD–AGB relationship was mostly negatively correlated in regions with low and high PSD and AGB values. Analysis using geodetector probes revealed that longitude, mean annual precipitation, and elevation were the main drivers of variation in the PSD–AGB relationship. The results of this study provide information that will aid future studies of the relationship between species diversity and ecosystem function in grasslands on the Qinghai–Tibet Plateau.

Data availability statement

The raw data supporting the conclusions of this article will be made available by the authors, without undue reservation.

Author contributions

MY: concepts, ideas, experimental design, data collection and analysis, and writing and editing. AC: ideas, experimental design, and writing-review. MZ: experimental design and data analysis. QG and YW: project administration and resources. JG, DY, and LM: experimental design and data analysis. YZ and QH: data collection and analysis. XY: ideas, project administration, writing-review, and editing. All authors contributed to the article and approved the submitted version.

Funding

This work was funded by the Natural Resources Comprehensive Survey Command Center Science and Technology Innovation Fund (no. KC20220018) and Natural Resources Comprehensive Survey Project in Key Areas of the Three-River Headwaters Region (no. ZD20220124) and the Special Program for the Institute of National Parks, Chinese Academy Sciences (no. KFJ-STS-ZDTP2021-003).

Conflict of interest

The authors declare that the research was conducted in the absence of any commercial or financial relationships that could be construed as a potential conflict of interest.

Publisher’s note

References

Albert, G., Gauzens, B., Loreau, M., Wang, S., and Brose, U. (2022). The hidden role of multi-trophic interactions in driving diversity-productivity relationships. *Ecol. Lett.* 25, 405–415. doi: 10.1111/ele.13935

Adler, P. B., Seabloom, E. W., Borer, E. T., Hillebrand, H., Hautier, Y., Hector, A., et al. (2011). Productivity is a poor predictor of plant species richness. *Science* 333, 1750–1753. doi: 10.1126/science.1204498

Bai, Y., Han, X., Wu, J., Chen, Z., and Li, L. (2004). Ecosystem stability and compensatory effects in the inner Mongolia grassland. *Nature* 431, 181–184. doi: 10.1038/nature02850

Chase, J. M., and Leibold, M. A. (2002). Spatial scale dictates the productivity-biodiversity relationship. *Nature* 416, 427–430. doi: 10.1038/416427a

Chen, S., Wang, W., Xu, W., Wang, Y., Wan, H., Chen, D., et al. (2018). Plant diversity enhances productivity and soil carbon storage. *Proc. Natl. Acad. Sci. U. S. A.* 115, 4027–4032. doi: 10.1073/pnas.1700298114

Chitale, V. S., Behera, M. D., and Roy, P. S. (2019). Deciphering plant richness using satellite remote sensing: a study from three biodiversity hotspots. *Biodivers. Conserv.* 28, 2183–2196. doi: 10.1007/s10531-019-01761-4

Choe, H., Chi, J., and Thorne, J. H. (2021). Mapping potential plant species richness over large areas with deep learning, MODIS, and species distribution models. *Remote Sens.* 13:2490. doi: 10.3390/rs13132490

David Tilman, C. L. L. A. (1997). Plant diversity and ecosystem productivity: theoretical considerations. *Proc. Natl. Acad. Sci. U. S. A.* 94, 1857–1861. doi: 10.1073/pnas.94.5.1857

Du, J., Wang, Y., Hao, Y., Eisenhauer, N., Liu, Y., Zhang, N., et al. (2022). Climatic resources mediate the shape and strength of grassland productivity-richness relationships from local to regional scales. *Agric. Ecosyst. Environ.* 330:107888. doi: 10.1016/j.agee.2022.107888

Fauvel, M., Lopes, M., Dubo, T., Rivers-Moore, J., Frison, P., Gross, N., et al. (2020). Prediction of plant diversity in grasslands using sentinel-1 and -2 satellite image time series. *Remote Sen. Environ.* 237:111536. doi: 10.1016/j.rse.2019.111536

Ge, J., Hou, M., Liang, T., Feng, Q., Meng, X., Liu, J., et al. (2022). Spatiotemporal dynamics of grassland aboveground biomass and its driving factors in North China over the past 20 years. *Sci. Total Environ.* 826:154226. doi: 10.1016/j.scitotenv.2022.154226

Grace, J. B., Anderson, T. M., Seabloom, E. W., Borer, E. T., Adler, P. B., Harpole, W. S., et al. (2016). Integrative modelling reveals mechanisms linking productivity and plant species richness. *Nature* 529, 390–393. doi: 10.1038/nature16524

Guo, Q., and Berry, W. L. (2013). Species richness and biomass: dissection of the hump-shaped relationships. *Ecology* 79, 2555–2559. doi: 10.1890/0012-9658(1998)079[2555:SRABDO]2.0.CO;2

Li, M., Zhang, X., Niu, B., He, Y., Wang, X., and Wu, J. (2020). Changes in plant species richness distribution in Tibetan alpine grasslands under different precipitation scenarios. *Glob. Ecol. Conserv.* 21:e848:e00848. doi: 10.1016/j.gecco.2019.e00848

Li, X. H. (2019). Random forest is a distinctive model, not a one-size-fits-all model. *J. Appl. Entomol.* 56, 170–179. (in Chinese).

Liang, T., Yang, S., Feng, Q., Liu, B., Zhang, R., Huang, X., et al. (2016). Multi-factor modeling of above-ground biomass in alpine grassland: a case study in the three-river headwaters region. *China. Remote Sens. Environ.* 186, 164–172. doi: 10.1016/j.rse.2016.08.014

Loreau, M., Naeem, S., Inchausti, P., Bengtsson, J., Grime, J. P., Hector, A., et al. (2001). Biodiversity and ecosystem functioning: current knowledge and future challenges. *Science* 294, 804–808. doi: 10.1126/science.1064088

Ma, L., Zhang, Z., Shi, G., Su, H., Qin, R., Chang, T., et al. (2022). Warming changed the relationship between species diversity and primary productivity of alpine meadow on the Tibetan plateau. *Ecol. Indic.* 145:109691. doi: 10.1016/j.ecolind.2022.109691

Ma, W. H., and Fang, J. Y. (2006). Relationship between species richness and productivity in typical grasslands of Northern China. *Biodiversitas* 14, 21–28. doi: 10.1360/biodiv.050146

Ma, Y., Ma, W., Zhong, L., Hu, Z., Li, M., Zhu, Z., et al. (2017). Monitoring and modeling the Tibetan Plateau's climate system and its impact on East Asia. *Sci. Rep.* 7:44574. doi: 10.1038/srep44574

Ni, J., Wang, G. H., Bai, Y. F., and Li, X. Z. (2007). Scale-dependent relationships between plant diversity and above-ground biomass in temperate grasslands, South-Eastern Mongolia. *J. Arid Environ.* 68, 132–142. doi: 10.1016/j.jaridenv.2006.05.003

Oindo, B. O., and Skidmore, A. K. (2002). Interannual variability of NDVI and species richness in Kenya. *Int. J. Remote Sens.* 23, 285–298. doi: 10.1080/01431160010014819

Omidipour, R., Tahmasebi, P., Faal Faizabadi, M., Faramarzi, M., and Ebrahimi, A. (2021). Does β diversity predict ecosystem productivity better than species diversity? *Ecol. Indic.* 122:107212. doi: 10.1016/j.ecolind.2020.107212

Piao, S. L., Zhang, X. Z., Wang, T., Liang, E. Y., Wang, S. P., Zhu, J. T., et al. (2019). Response of Qinghai–Tibet plateau ecosystems to climate change and its feedbacks. *Sci. Bull.* 64, 2842–2855 (in Chinese). doi: 10.1360/TB-2019-0074

Qi, W., Kang, X., Knops, J. M. H., Jiang, J., Abuman, A., and du, G. (2022). The complex biodiversity-ecosystem function relationships for the Qinghai–Tibetan grassland community. *Front. Plant Sci.* 12:772503. doi: 10.3389/fpls.2021.772503

Reddy, C. S. (2021). Remote sensing of biodiversity: what to measure and monitor from space to species? *Biodivers. Conserv.* 30, 2617–2631. doi: 10.1007/s10531-021-02216-5

Reddy, C. S., Kurian, A., Srivastava, G., Singhal, J., Varghese, A. O., Padalia, H., et al. (2021). Remote sensing enabled essential biodiversity variables for biodiversity assessment and monitoring: technological advancement and potentials. *Biodivers. Conserv.* 30, 1–14. doi: 10.1007/s10531-020-02073-8

Sabatini, F. M., Jiménez-Alfaro, B., Jandt, U., Chytrý, M., Field, R., Kessler, M., et al. (2022). Global patterns of vascular plant alpha diversity. *Nat. Commun.* 13:4683. doi: 10.1038/s41467-022-32063-z

Sakowska, K., MacArthur, A., Gianelle, D., Dalponte, M., Alberti, G., Gioli, B., et al. (2019). Assessing across-scale optical diversity and productivity relationships in grasslands of the italian alps. *Remote Sens.* 11:614. doi: 10.3390/rs11060614

Schnitzer, S. A., Klironomos, J. N., HilleRisLambers, J., Kinkel, L. L., Reich, P. B., Xiao, K., et al. (2011). Soil microbes drive the classic plant diversity-productivity pattern. *Ecology* 92, 296–303. doi: 10.1890/10-0773.1

Spyros Tsiftsis, Z. Š. P. K. (2018). Role of way of life, latitude, elevation and climate on the richness and distribution of orchid species. *Biodivers. Conserv.* 28, 75–96. doi: 10.1007/s1053

Sun, Y., Qin, Y., Wei, T. F., Chang, L., Zhang, R. P., Liu, Z. Y., et al. (2022). Methods and development trend for the measurement of plant species diversity in grasslands. *Appl. Ecol.* 33, 655–663. (in Chinese).

Waide, R. B., Willig, M. R., Steiner, C. F., Mittelbach, G., Gough, L., Dodson, S. I., et al. (1999). The relationship between productivity and species richness. *Annu. Rev. Ecol. Syst.* 30, 257–300. doi: 10.1146/annurev.ecolsys.30.1.257

Wang, C. T., Long, R. J., Wang, Q. J., Ding, L. M., and Wang, M. P. (2007). Effects of altitude on plant-species diversity and productivity in an alpine meadow. *Qinghai-Tibetan Plateau. Aust. J. Bot.* 55:110. doi: 10.1071/BT04070

Wang, H., Li, G., and Tsai, C. L. (2008). Regression coefficients and autoregressive order shrinkage and selection via the lasso. J. R. *Stat. Soc. Series B Stat. Methodol.* 69, 267–288. doi: 10.1111/j.1467-9868.2007.00577.x

Wang, J., Lu, G., Wei, C., Wang, S., and Fan, J. (2018). Prediction of aboveground biomass applied artificial neural network over three-rivers headwater regions, Qinghai, China. In: IGARSS 2018–2018 IEEE International Geoscience and Remote Sensing Symposium.

Wang, J. F., and Xu, C. D. (2017). Geodetectors: principles and perspectives. *J. Geogr.* 72, 116–134. (in Chinese).

Wang, Z., Ma, Y., Zhang, Y., and Shang, J. (2022). Review of remote sensing applications in grassland monitoring. *Remote Sens.* 14:2903. doi: 10.3390/rs14122903

Xu, M., Zhang, S., Wen, J., and Yang, X. (2019). Multiscale spatial patterns of species diversity and biomass together with their correlations along geographical gradients in subalpine meadows. *PLoS One* 14:e211560:e0211560. doi: 10.1371/journal.pone.0211560

Yu, H., Wu, Y., Niu, L., Chai, Y., Feng, Q., Wang, W., et al. (2021). A method to avoid spatial overfitting in estimation of grassland above-ground biomass on the Tibetan plateau. *Ecol. Indic.* 125:107450. doi: 10.1016/j.ecolind.2021.107450

Zeng, N., Ren, X., He, H., Zhang, L., Zhao, D., Ge, R., et al. (2019). Estimating grassland aboveground biomass on the Tibetan plateau using a random forest algorithm. *Ecol. Indic.* 102, 479–487. doi: 10.1016/j.ecolind.2019.02.023

Zhai, W. T., Chen, Z. W., Li, Q., Zhao, L., Liu, Z., Xu, S. X., et al. (2017). Effects of grazing intensity on carbon metabolism characteristics of soil microbial communities in alpine grasslands around Qinghai Lake. *J. Appl. Environ. Biol.* 23, 685–692. (in Chinese).

Zhao, X. Q. (2021). *Ecosystem Status, Changes and Management in the Three-River Headwaters National Park*. Beijing. Science Publishers (in Chinese).

Zhao, Y., Yin, X., Fu, Y., and Yue, T. (2022). A comparative mapping of plant species diversity using ensemble learning algorithms combined with high accuracy surface modeling. *Environ. Sci. Pollut. Res.* 29, 17878–17891. doi: 10.1007/s11356-021-16973-x

Zhu, G. L., Li, J., Wei, X. H., and He, N. P. (2017). Longitude patterns of vegetation productivity and biodiversity in Qinghai–Tibet alpine grasslands. *Nat. Resour.* 32, 210–222. (in Chinese).

frontiers | Frontiers in Ecology and Evolution

TYPE Methods
PUBLISHED 03 May 2023
DOI 10.3389/fevo.2023.1153342

OPEN ACCESS

EDITED BY
Weiwei Sun,
Ningbo University, China

REVIEWED BY
Chao Chen,
Zhejiang Ocean University, China
Bolin Fu,
Guilin University of Technology, China
Dehua Mao,
Northeast Institute of Geography and
Agroecology (CAS), China

*CORRESPONDENCE
Jia Wang
✉ wangjia2009@bjfu.edu.cn

RECEIVED 29 January 2023
ACCEPTED 12 April 2023
PUBLISHED 03 May 2023

CITATION
Wang J, Wang J and Xu J (2023) Spatio-temporal variation and prediction of ecological quality based on remote sensing ecological index – a case study of Zhanjiang City, China. *Front. Ecol. Evol.* 11:1153342.
doi: 10.3389/fevo.2023.1153342

Spatio-temporal variation and prediction of ecological quality based on remote sensing ecological index – a case study of Zhanjiang City, China

Jing Wang[1,2], Jia Wang[1,2]* and Jiangqi Xu[1,2]

[1]Beijing Key Laboratory of Precision Forestry, Beijing Forestry University, Beijing, China, [2]Institute of GIS, RS and GPS, Beijing Forestry University, Beijing, China

A significant portion of Zhanjiang City's ecological land areas have been reduced as a result of the city's growing urbanization, which has caused the city's ecological environment quality to decline. In order to monitor the quality of the ecological environment, the remote sensing ecological index (RSEI) is frequently utilized. In this study, the Landsat series satellite images from 2000, 2005, 2009, 2015, and 2020 were used. The Normalized Differential Vegetation Index (NDVI), Wetness (WET), Normalized Differential Build-up and bare Soil Index (NDBSI), and Land Surface Temperature (LST) were the four indicators utilized in the RSEI to quantitatively evaluate the changes in ecological environment quality in Zhanjiang City. The results are as follows. (1) The mean RSEI values for the years 2000, 2005, 2009, 2015, and 2020 are, respectively, 0.579, 0.597, 0.597, 0.607, and 0.601. In addition, the overall ecological environment of Zhanjiang is very good. In terms of spatial differences, the ecological environment quality in the central and southeastern parts of Zhanjiang is significantly higher than that in other areas, while the ecological environment quality in its coastal town areas is much worse. The lower RSEI index of developed land in coastal areas proves that the RSEI index can reflect the deterioration of the urban environment in coastal areas from 2000 to 2020. Therefore, the RSEI can be used to evaluate the ecological environment quality of Zhanjiang City. (2) The ecological environment changes in the study area are "substantially better," "better," "no change," "worse," and "much worse," respectively, according to the difference in RSEI processed between 2000 and 2020. These changes were 38.38, 6,047, 13.93, 6.65, and 34.58%. The percentage of ecological environmental quality in Zhanjiang City that has become better is higher than that has become worse. This indicates that the quality of ecological environment in Zhanjiang City has improved between 2000 and 2020. (3) The regression produced the following equation for the association, which was significant at the 0.053 level: 100*Rsei=154.69−1.18*IS(R=0.66). The remote sensing ecological index for Zhanjiang in 2035 is 0.488 when the city's planned population and area are added together.

KEYWORDS

ecological environment quality, remote sensing ecological index, Zhanjiang City, forecast, impervious area balance

1. Introduction

Ecosystem quality is closely related to human beings and is the material basis for human survival and social development, so it is of great practical significance to monitor and evaluate ecosystem quality. In recent years, remote sensing technology has been widely used for ecological environment monitoring with its advantages of multi-directional, large range, long time series and low cost (Rai, 2013; Matco-Caria et al., 2018), but most of the traditional remote sensing ecological evaluation methods are based on a single indicator for monitoring, which does not reveal the ecosystem changes comprehensively (Qin et al., 2023).

Therefore, Ministry of Environmental Protection (2005) proposed the Ecological Environment Index (EI) based on remote sensing technology in 2005. It was proposed to quantitatively analyze the quality of the ecological environment from six aspects, such as biology, vegetation, land and human activities. This method is difficult to obtain statistical data, and the assignment of ecological index weights is more subjective (2015). On this basis, Xu et al. (2013) proposed the Remote Sensing Environment Index (RSEI) to evaluate the ecological quality of Fuzhou City in 2013, using the Normalized Differential Vegetation Index (NDVI) to represent the greenness component, the tasseled cap transformation (TCT) to represent the Wetness (WET), Land Surface Temperature (LST) and Normalized Differential Build-up and bare Soil Index (NDBSI). And combined with Principal Component Analysis (PCA) to establish a remote sensing ecological index model for rapid quantitative analysis of the regional ecological environment. This algorithm is simpler to calculate, easier to obtain data sources, and can objectively reflect the quality of the regional ecological environment. Therefore, this method has been widely used in a variety of scenarios (Gao et al., 2020; Nong and Wang, 2020; Miao and Liang, 2021; Wu et al., 2021; Ji et al., 2022). In the subsequent research on remote sensing ecological index, scholars proposed MSRE, IRSEI and ERSEI, which are improved versions of remote sensing ecological index models adapted to different geographic environments, according to the changes of geographic environments in the study area, such as: cities, villages, forests, wetlands, islands, deserts, loess lands, mining areas, etc. (Jiang et al., 2019; Song et al., 2019; Wang et al., 2020; Cheng et al., 2021).

Zhanjiang is subject to the interaction of fresh and brackish water as well as land and sea, therefore, Zhanjiang is characterized by rich biodiversity as well as complex and diverse wetland types, such as mangrove wetlands, mudflat wetlands, etc. (Xu et al., 2006; Chen et al., 2018). However, along with the development of socio-economic and urbanization processes, the increasingly frequent reclamation projects have caused some damage to the ecological environment of coastal areas, resulting in some coastal areas becoming typical ecologically fragile and sensitive areas, causing habitat destruction, resource reduction and landscape degradation. At present, there is a lack of research on the long time series monitoring of the ecological environment in Zhanjiang City, and it is necessary to study the spatial and temporal changes in ecological environment quality in Zhanjiang City.

In this paper, the Google Earth Engine (GEE) cloud platform was used to acquire Landsat remote sensing images for the years 2000, 2005, 2009, 2015, and 2020. The ENVI 5.3 and ArcGIS 10.8 platforms were used to construct the Remote Sensing Ecological Index (RSEI) for the ecological pattern evaluation of Zhanjiang City, and the Spss platform was used to predict the ecological environment quality of Zhanjiang City, using the relationship between the change of impervious area and ecological environment quality, combined with the planned population and total planned area of Zhanjiang City in 2035. Ecological environment quality is predicted. It provides a scientific basis for the subsequent ecological development of Zhanjiang City, fills the gap of ecological environment quality evaluation in the coastal zone, and provides a scientific basis and sustainable development strategy to ensure the effective use of resources and avoid ecological risks.

2. Materials and methods

2.1. Study area

The region for the research is the city of Zhanjiang, which is situated between latitudes 20°13′N and 21°57′N and longitudes 109°40′E and 110°58′E. The majority of the territory is made up of peninsulas and islands, with Donghai Island being the sixth largest island in China. The region is long and width. The urban area is around 13,225 square kilometers in size, while the coastline is 1,556 kilometers long. It is surrounded by the South China Sea to the south, Maoming City to the east, and Beibu Gulf to the west. It is situated where the provinces of Guangxi, Guangdong, and Hainan converge. Its authority spans two counties, three county-level cities, and five districts. Its authority spans two counties, three county-level cities, and five districts (Figure 1). The area has a tropical northern monsoon climate that is mostly influenced by the ocean, with an average yearly temperature ranging from 22.7°C to 23.5°C. The wet season lasts from April to September, and the dry season lasts from October to March. Zhanjiang's geography is primarily flat, with terraced land only making up a small fraction of the coastline region. The landscape has a relatively low slope of 1–4° and is typically high from north to south and low from east to west.

Mudflat wetlands abound in Zhanjiang, which also has China's most concentrated, diverse, and sizable mangrove wetland natural reserve with a total size of roughly 20, 278.8 acres (Wang, 2008).

2.2. Data sources

The remote sensing images of Zhanjiang City are of poor quality due to the influence of clouds, so it is necessary to de-cloud/cloud shadow the multiview images before stitching them to obtain cloud-free images with complete coverage of the study area. Therefore, this paper acquires Landsat-5 surface reflectance dataset from May 2000 to September 2009 and the Landsat-8 surface reflectance dataset from May 2015 to September 2020 for the Zhanjiang city area based on GEE platform. And the minimum cloud image synthesis is performed to remove the cloudy image elements and synthesize the target year image with cloud-free image elements.

The land use data with a spatial resolution of 30 m in the fifth period were obtained from the product data (Earth System Science Data) of the study by Huang Xin's team at Wuhan University (Yang and Huang, 2021). The administrative boundary vector data of Zhanjiang city districts and counties were obtained from the geographic state monitoring platform (Table 1).[1]

---

[1] http://www.dsac.cn

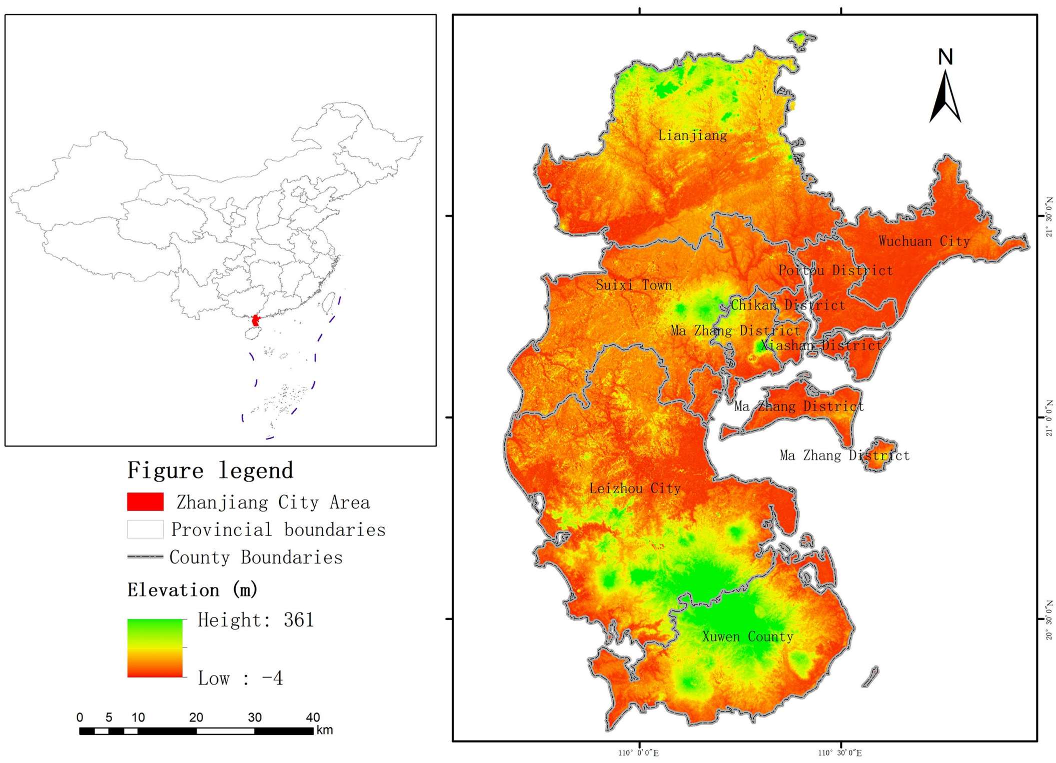

FIGURE 1
Location of Zhanjiang City.

TABLE 1 Data sources.

Data types	Resolution of data	Data source
Landsat5 SR	30 m	Google earth engine
Landsat8 SR	30 m	Google earth engine
Land use types	30 m	《30 m annual land cover and its dynamics in China from 1990 to 2019》
Administrative District Vector Boundaries	30 m	Geographical State Monitoring Platform

2.3. Remote sensing ecological index

2.3.1. Indicators used in RSEI

Vegetation Greenness, humidity, heat, and dryness all play significant roles in how humans perceive ecological conditions visually, and as a result, they are frequently used to evaluate ecosystems (Moran et al., 2004; Yuan and Bauer, 2007; Gupta et al., 2012; Wei et al., 2022). Based on this, Xu Hanqiu proposed RSEI, combining four crucial ecological factors—vegetation greenness, humidity, dryness, and heat, which can accurately describe the quality of the ecological environment (Xu et al., 2013). Thus, this essay makes reference to his work in developing RSEI to evaluate the ecological environment quality of the city of Zhanjiang. The following are the calculation formulas for each ecological index.

Vegetation greenness is used to quantitatively reflect the information of vegetation growth status, vegetation cover and biomass (Li et al., 2020). The normalized differential vegetation index (*NDVI*) is used to represent vegetation greenness. The calculation formula of *NDVI* is as follows.

$$NDVI = \left(\rho_{NIR} - \rho_{Red}\right) / \left(\rho_{NIR} + \rho_{Red}\right) \tag{1}$$

The wet indicator (*WET*) is intently connected to the ecologic environment, which indicates the humidity of water, soil, and vegetation (Nong et al., 2021). It acquired from the Tasseled Cap transformation (TCT). The calculation formula of *WET* is as follows and it is expressed differently by different satellite sensors (Wang et al., 2019).

$$\begin{aligned} WET_{(TM)} = {} & 0.0315\rho_{Blue} + 0.2021\rho_{Green} + 0.3102\rho_{Red} \\ & + 0.1594\rho_{NIR} - 0.6806\rho_{SWIR1} - 0.6109\rho_{SWIR2} \end{aligned} \tag{2}$$

$$\begin{aligned} WET_{(OLI)} = {} & 0.1511\rho_{Blue} + 0.1973\rho_{Green} + 0.3283\rho_{Red} \\ & + 0.3407\rho_{NIR} - 0.7117\rho_{SWIR1} - 0.4559\rho_{SWIR2} \end{aligned} \tag{3}$$

Heat reflects the surface temperature of an area and is closely related to the ecologic environment (Nichol, 2005). The land surface temperature (*LST*) is used to represent heat index.

The standard method for retrieving *LST* from raw Landsat datasets requires the conversion of the DN values of the thermal bands into at-satellite spectral radiance values (L_6). And then into the at-satellite brightness temperature (T; Chander et al., 2009). The calculation formula of *LST*, T, and L_6 is as follows:

$$LST = \mathrm{T} / \left[1 + \left(\mathrm{R} * \mathrm{T} / \mathrm{p}\right) \ln H\right] \quad (4)$$

$$\mathrm{T} = \mathrm{K2} / \ln\left(\mathrm{K1} / \mathrm{L6} + 1\right) \quad (5)$$

$$\mathrm{L}_6 = \mathrm{gain} \times \mathrm{DN} + \mathrm{bias} \quad (6)$$

The index-based built-up indicator (IBI) just reflects the situation of building land. Therefore, the dryness index can be declared by the average value of SI and IBI, called "*NDBSI*" (Rikimaru et al., 2002). The calculation formula of *NDBSI*, *IBI*, and *SI* are as follows:

$$NDBSI = \left(IBI + SI\right) / 2 \quad (7)$$

$$\begin{aligned} IBI = \{ & 2\rho_{SWIR1} / (\rho_{SWIR1} + \rho_{NIR}) \\ & -[\rho_{NIR} / (\rho_{NIR} + \rho_{Red})] + \rho_{Green} \\ & / (\rho_{Green} + \rho_{SWIR1})]\} / \{2\rho_{SWIR1} \\ & / (\rho_{SWIR1} + \rho_{NIR}) + [\rho_{NIR} / (\rho_{NIR} \\ & + \rho_{Red})] + \rho_{Green} / (\rho_{Green} + \rho_{SWIR1})]\} \end{aligned} \quad (8)$$

$$\begin{aligned} SI = & \left[\left(\rho_{SWIR1} + \rho_{Red}\right) - \left(\rho_{NIR} + \rho_{Blue}\right)\right] \\ & / \left[\left(\rho_{SWIR1} + \rho_{Red}\right) + \left(\rho_{NIR} + \rho_{Blue}\right)\right] \end{aligned} \quad (9)$$

2.3.2. Combination of the indicators

In this study, principal components analysis (PCA) was used to construct a remote sensing ecological index (RSEI). It couples four single indicators into one comprehensive index, concentrating the main information on the first principal component (PC1), which enables the RSEI to synthesize the information of the four indicators. The advantage of using the principal component analysis method is that the index weights are more objective and avoid the bias of results caused by weight settings that vary from person to person and from method to method.

Before creating the RSEI index, each index must be normalized such that its value is between 0 and 1, as the dimensions of the *NDVI*, *WET*, *NDBSI*, and *LST* are not uniform. The formula is defined as follows:

$$\mathrm{T_N} = \left(T - T_{\min}\right) / \left(T_{\max} - T_{\min}\right) \quad (10)$$

T represents the original index, T_{max} and T_{min} represent the maximal and minimal values, and T_N represents normalized value.

Due to the existence of a large range of water bodies and wetlands in the study area, the modified Normalized difference Water index (MNDWI) was used to mask the water bodies in Zhanjiang City before the principal component analysis of the indicators to avoid the influence of the water bodies on the weight of the WET components, which in turn affects the load value distribution of PCA.

The principal component analysis (PCA) was performed on the ecologic indicators of greenness, wetness, dryness, and heat obtained after normalization and water body masking, and ENVI software calculated the *RSEI*. The formula is showed as.

$$\mathrm{RSEI} = \mathrm{f}\left(NDVI, Wet, LST, NDBSI\right) \quad (11)$$

To facilitate comparison and metrics among indicators, RSEI can be normalized similarly.

$$RSEI = \left(RSE_0 - RSEI_{0\min}\right) / \left(RSEI_{0\max} - RSEI_{0\min}\right) \quad (12)$$

The higher the value of *RSEI* is, the better the quality of ecological environment, and vice versa, the worse the quality of ecological environment.

2.4. Estimation of total is area

Regional planning often takes into account population issues. Population growth will require more impervious developed space for work, living, and various social activities, which will result in the loss of natural landscapes such as vegetation and water, and affect the impact of regional planning on ecosystems and the environment. Xu (2013) related population density to potential IS growth area in order to predict the impact of the amount of population growth on the ecological environment. Therefore, this study combines population growth with potential IS area growth to predict the impact of future population growth on the ecological environment of Zhanjiang City.

Based on the predicted population expansion through 2035, the impervious equilibrium area is computed. After the expansion of IS, the area's general ecological quality will not be impacted. This amount is referred to as the imperviousness level metric. Current population, current IS area, current population density, planned future population, and planned future population density are among the factors used in the determination of the imperviousness level metric. The model is developed as follows:

$$\mathrm{A} = \mathrm{a} * \mathrm{p_p} * \mathrm{k} \quad (13)$$

$$\mathrm{a} = \mathrm{A_c} / \mathrm{P_C} \quad (14)$$

$$\mathrm{K} = \mathrm{D_c} / \mathrm{D_p} \quad (15)$$

where A is the estimated balance amount of total impervious surface area, where *Ac* is the current impervious surface area, *Pc* is the current population, *Dc* is the current population density, and *Dp* is the planned future population density.

2.5. Relevance of impervious surface and RSEI

Analyzing the functional relationship between the RSEI and impervious areas is an important prerequisite for predicting the ecological impact of urban development planning in Zhanjiang. In this paper, based on land use data and RSEI value in 2000, 2005, 2009, 2015, and 2020, we used a one-dimensional linear regression method to quantify the functional relationship between the percentage of impervious area and the RSEI through spss software to predict the possible impact of future construction activities on the environmental quality of the study area (Hanqiu et al., 2019).

3. Results and analysis

3.1. Factor attributes

According to Table 2, which shows the eigenvalue contribution rate for each year as well as the loadings of the four ecological indicators in various main components in 2000, 2005, 2009, 2015, and 2020, the Eigenvalue of the four indices is concentrated in PC1. 67.9, 71.1, 59.1, 75.6, and 75.2%, respectively, of the contributions to the PC1 eigenvalue in the years 2000, 2005, 2009, 2015, and 2020. The four indices' loadings are clearly symmetrical in PC1, with WET and NDVI having positive loadings and LST and NDBSI having negative loadings. This shows that ecosystem quality is positively impacted by humidity and greenness and negatively impacted by dryness and high heat indices. The outcome is essentially in accordance with the actual situation. As a result, the first principle component served as the foundation for this study's RSEI.

3.2. Ecological status

Table 3 shows that from 2000 to 2020, the RSEI went from 0.579 to 0.601, an increase of about 2.2%. One of them, the RSEI index, showed no change from 2005 to 2009, a 3.1% increase from 2000 to 2005, a 1.7% increase from 2009 to 2015, and a 0.1% decrease from 2015 to 2020. With a maximum value of 0.684 in 2015, the average correlation between NDVI and RSEI—which compares the four ecological indicators—is the greatest at 0.642. The average correlation between the four ecological indicators LST and RSEI is lower, at 0.435, with the minimum values occurring in 2015 at 0.395. The average correlation scores for the last two indicators are 0.575 and 0.596.

The spatial distribution of RSEI values in Zhanjiang city in 2000, 2005, 2009, 2015, and 2020 is shown in Figure 2. As can be seen, between 2000 and 2009, places with poor ecological conditions were primarily distributed in coastal urban areas and the north, while areas with better ecological conditions were primarily spread in the center and southern areas. The northern region's ecological environment quality has increased between 2000 and 2005. Nonetheless, the ecological condition of the northern region declined between 2005 and 2009. The RSEI values' spatial distribution is similar between 2015 and 2020. Urbanized coastal areas tend to have places with a worse natural environment. In general, Zhanjiang City's center and southeast regions have superior ecological conditions than its coastal metropolitan districts.

Table 4 displays the ecological environment quality in Zhanjiang City for the years 2000, 2005, 2009, 2015, and 2020. In general, the ecological conditions are good or exceptional in more than 60% of Zhanjiang City's areas. In terms of proportion, the distribution of grades in 2000, 2005, and 2009 is similar. Also, the percentages of each grade's natural environment are similar between 2015 and 2020. In Zhanjiang, the percentage of bad ecological quality declined by 5% from 2009 to 2015, while the percentage of good ecological quality

TABLE 2 Results of the principal component analysis of each index in each year.

Year	Principal component	NDVI	WET	NDBSI	LST	Percent correlation Eigen value (%)
2000	PC1	0.504	0.470	−0.400	−0.604	0.679
	PC2	−0.337	0.676	0.632	−0.174	0.207
	PC3	0.645	−0.342	0.663	−0.166	0.098
2005	PC1	0.514	0.420	−0.465	−0.586	0.711
	PC2	0.429	−0.728	−0.480	0.235	0.195
	PC3	0.575	−0.231	0.743	−0.251	0.079
2009	PC1	0.522	0.432	−0.372	−0.635	0.591
	PC2	−0.096	0.466	0.842	−0.255	0.214
	PC3	0.718	−0.575	0.391	−0.029	0.174
2015	PC1	0.532	0.427	−0.563	−0.466	0.756
	PC2	0.322	−0.643	0.325	−0.614	0.162
	PC3	0.690	−0.322	−0.119	0.637	0.075
2020	PC1	0.559	0.411	−0.593	−0.408	0.752
	PC2	0.277	−0.617	0.298	−0.674	0.171
	PC3	0.658	−0.423	−0.096	0.615	0.070

rose by 5%. As a result, Zhanjiang City's total ecological environment quality has improved since 2009, with the places with poor ecological quality seeing the most improvement.

According to the RSEI values and using equal intervals, the study region was categorized into five categories in Figure 3: excellent, good, medium, fairly poor, and poor. The majority of the regions with a pretty low grade are found in coastal towns, demonstrating that human activities have a negative impact on the ecological quality. The southeast and center regions of the country tend to have the best ecological conditions. Since this area contains forest land, it is clear that vegetation positively affects the ecological quality.

TABLE 3 The mean value of RSEI and mean correlation between RSEI and each index in different years.

Year	NDVI	WET	NDBSI	LST	RSEI_mean
2000	0.611	0.572	0.475	0.427	0.579
2005	0.628	0.564	0.450	0.400	0.597
2009	0.622	0.563	0.434	0.550	0.597
2015	0.684	0.592	0.499	0.395	0.607
2020	0.666	0.585	0.502	0.403	0.601
Mean value	0.642	0.575	0.472	0.435	0.596

3.3. Spatiotemporal ecological changes

The RSEI values of Zhanjiang City were differed for 5 periods in order to further study the temporal and spatial variations in ecological environmental quality in Zhanjiang City from 2000 to 2020. The differential results were graded. Table 5 shows the changes in Zhanjiang City's ecological environment quality and its percentage during a 20-year period. The percentage of Zhanjiang City's ecological environment that was significantly better and significantly worse over the course of the five periods

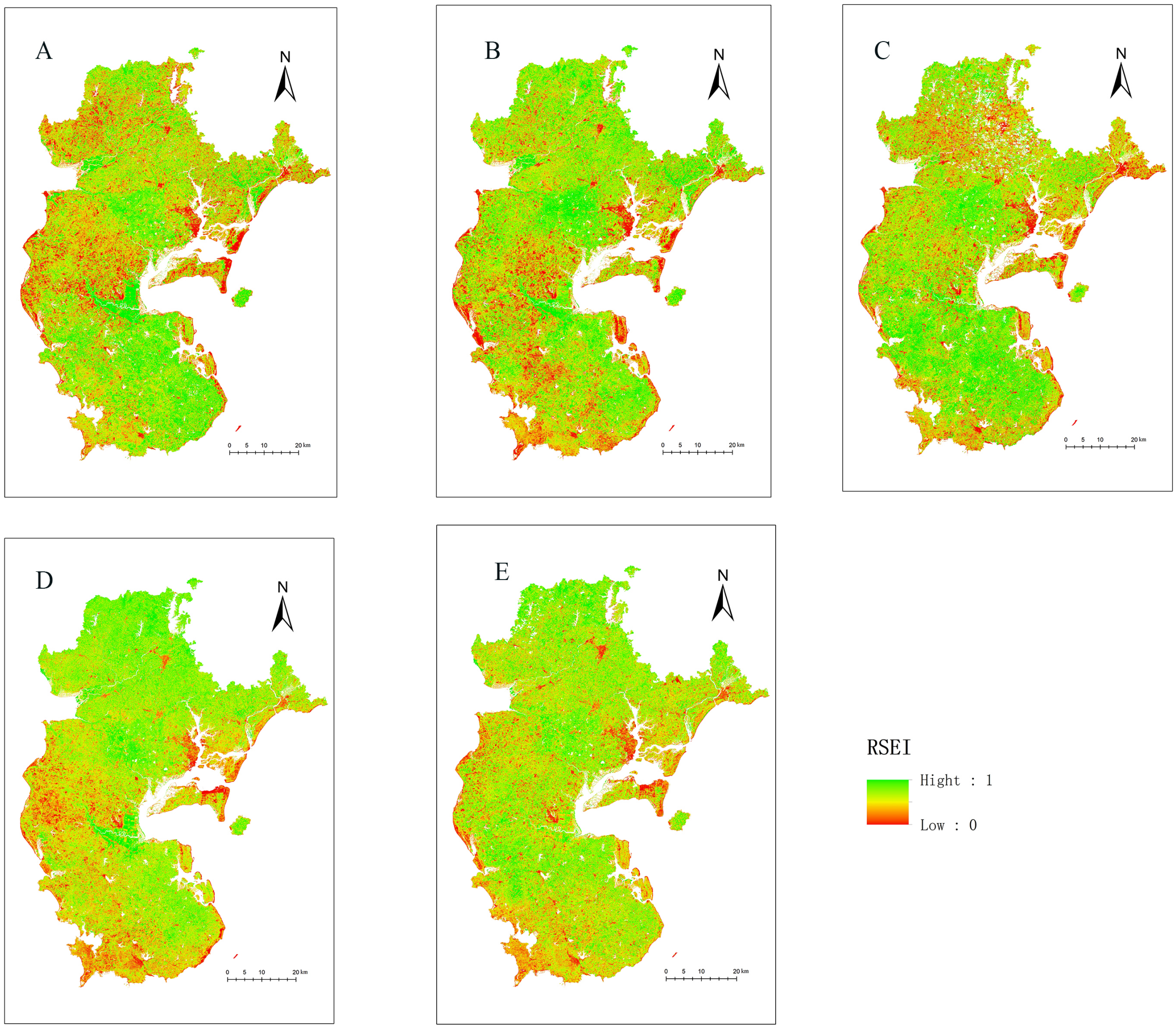

FIGURE 2
Remote sensing Ecological Index from 2000 to 2020; **(A)** Remote sensing Ecological Index in 2000, **(B)** Remote sensing Ecological Index in 2005, **(C)** Remote sensing Ecological Index in 2009, **(D)** Remote sensing Ecological Index in 2015, **(E)** Remote sensing Ecological Index in 2020.

TABLE 4 Area and proportion of RSEI of each grade in each year.

Grade	2000		2005		2009		2015		2020	
	Proportion/%	Area/km^2	Proportion/%	Area/km^2	Proportion/%	Area/km^2	Proportion/%	Area/km^2	Proportion/%	Area/km^2
Poor	13.27	1754.65	12.83	1696.37	12.52	1656.04	7.15	945.32	8.13	1075.78
Rather poor	10.12	1338.62	8.83	1167.95	8.77	1159.25	9.83	1299.48	9.70	1282.76
Medium	18.92	2502.23	16.73	2211.95	16.92	2237.73	19.50	2579.46	18.85	2492.80
Good	24.14	3192.95	24.28	3211.57	24.72	3268.61	29.11	3850.16	29.78	3937.80
Excellent	33.55	4436.55	37.33	4937.16	37.08	4903.38	34.41	4550.57	33.54	4435.87

is quite close to 30%. Around 7% of changes are for the better, whereas 7% are for the worse. Overall, the percentage of Zhanjiang City's ecological environment that is better than significantly worse is significantly higher, whereas this is not the case for the time periods 2005 to 2009 and 2015 to 2020, where the percentage of ecological environment that is better than significantly worse is lower. In Zhanjiang, the percentages of a better and substantially better ecological environment quality during the last 20 years are 6.47 and 38.38%, respectively. These percentages are somewhat higher than those of a poorer and significantly worse ecological environment quality. This suggests that in 2020, Zhanjiang City's ecological environment quality has increased compared to 2000.

According to Figure 4, there were similar regional variations in ecological quality between 2000 and 2005 and 2009 and 2015, with the northern portion of Zhanjiang experiencing significantly better ecological quality and the southern region experiencing significantly worse ecological quality. The areas with significantly worse ecological quality occur in the northern part of Zhanjiang, while the areas with significantly better ecological quality primarily occur in the southern part of the city, which is a similar pattern to the spatial changes in ecological quality from 2005 to 2009 and from 2015 to 2020. In the southern region and coastal urban area, the ecological environment's quality has declined.

3.4. Relation between impervious surface and RSEI

Using the RSEI index as the dependent variable and the percentage of impervious surface area in the study area as the independent variable, a multiple linear regression analysis was performed to obtain the following relationship equation.

$$100 * \mathrm{Rsei} = 54.69 - 1.18 * \mathrm{IS}\left(\mathrm{R} = 0.66\right) \qquad (16)$$

Equation (12) shows that R is greater than 0.6, indicating that the whole equation has a high agreement with the original data. The negative sign of the coefficient of IS indicates that impervious surfaces have a bad impact on environmental quality. The $p < 0.1$ significance test was passed in the regression equation, indicating that it is an important influence on regional environmental quality, influencing factors. According to model 16, as long as the percentage of impervious surfaces in the study area increases by 10% (e.g., from 20 to 30%), the RSEI value will decrease by 0.118.

3.5. Prediction of RSEI in 2035

According to the Zhanjiang City 2035 planning, the population growth and area expansion planned for 2035 are available at this stage. Therefore, this paper predicts the impact of population growth on ecological quality by linking population growth to IS increase based on the previous relationship between the two variables.

Zhanjiang City has a planned maximum population of 10 million in 2035 and a population density of 679 persons/km^2. According to the census data, the area has a population of 7.03 million in 2020 and a density of 576 persons/km^2. This study shows that the IS area and

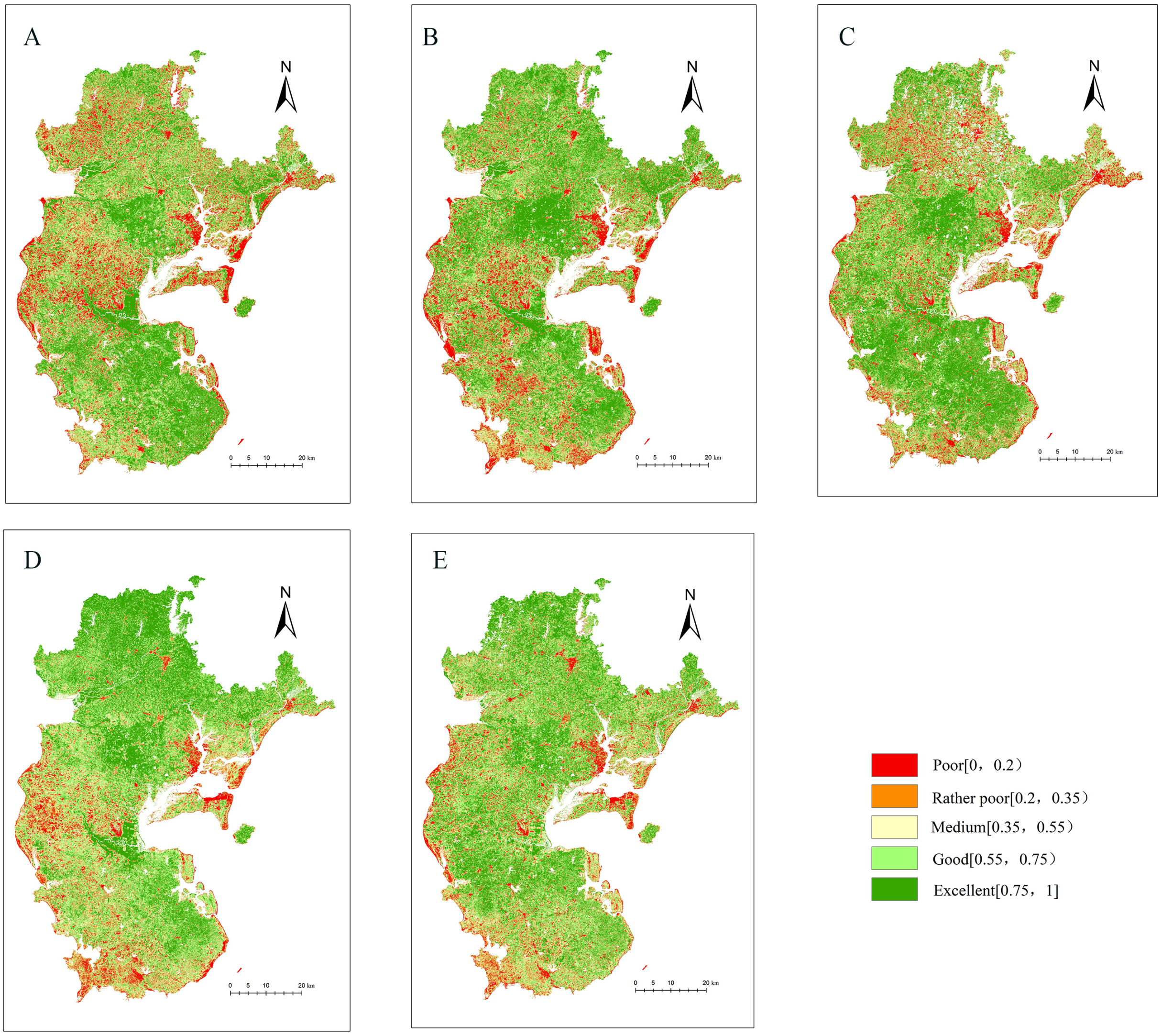

FIGURE 3
Remote sensing Ecological Index Grading from 2000 to 2020; **(A)** Remote sensing Ecological Index Grading in 2000, **(B)** Remote sensing Ecological Index Grading in 2005, **(C)** Remote sensing Ecological Index Grading in 2009, **(D)** Remote sensing Ecological Index Grading in 2015, **(E)** Remote sensing Ecological Index Grading in 2020.

the average RSEI of the area in 2020 are 470.53 km2 and 0.758 km2. These data are the inputs to the estimation model.

The expected value of the total IS area was first estimated using Eq. (13), and the results were subsequently used as input to Eq. (16) as a way to predict the RSEI in 2035.

The results show that the projected value of Eq. (16) for the total IS area of Zhanjiang City is 511 km^2. The mean value of RSEI in 2035 projected using this quantity is 0.488.

4. Discussion

Some academics analyze the relationship between population and ecological environment because they predict that increasing populations would result in resource shortages, exacerbate environmental contamination, and put more strain on ecosystems (Chen et al., 2009). According to some scholars, large-scale urban development not only modifies the original natural environment, causing significant ecological changes that make it easier to trigger geological disasters like landslides, debris flows, and soil erosion, but also causes cities to produce heat islands that have varying degrees of an impact on the natural environment around them (He et al., 2017; Zhao et al., 2017). The interaction of many components in the ecological environment is currently being given more attention in academic circles (Ping and Fang, 2014; Zhong et al., 2015; Yuan et al., 2016). Analysis reveals that the contribution level of a single factor is greatly outweighed by the interaction effect of numerous factors. Our research offers a

TABLE 5 Changes of ecological environment quality to different degrees.

	2000—2005		2005—2009		2009—2015		2015—2020		2000—2020	
	Proportion/%	Area/km^2	Proportion/%	Area/km^2	Proportion/%	Area/km^2	Proportion/%	Area/km^2	Proportion/%	Area/km^2
Significantly worse	29.35	3881.48	34.17	4519.05	33.47	4426.49	29.93	3957.82	34.58	4572.92
Worse	7.08	936.83	7.70	1018.18	7.02	927.97	10.14	1341.25	6.65	879.80
No change	19.64	2597.77	18.58	2457.67	15.83	2093.61	23.12	3058.15	13.93	1842.01
Better	7.9	1044.66	6.92	915.21	7.38	975.47	9.27	1225.54	6.47	855.12
Significantly better	36.02	4764.26	32.63	4314.89	36.31	4801.45	27.54	3642.24	38.38	5075.15

comparatively thorough identification approach for carefully taking into account numerous governance-related criteria. The RSEI integrates four factors, greenness, humidity, dryness and heat, which can more accurately represent the ecological environment quality of Zhanjiang City.

The findings of this study (Figure 2) are similar with those the study of Wang et al.'s (2022), arable land and impermeable surfaces tend to have a lower RSEI, wetlands and forests tend to correspond to higher RSEI values, and grasslands have RSEI values in the middle. In general, RSEI can more correctly describe the ecological environment quality of Zhanjiang. These show that the trend of ecological environmental quality is related to land-use types.

Table 3 shows the mean values of NDVI, WET, NDBSI and LST in 2000, 2005, 2009, 2015, and 2020. From the Table 3, it can be seen that the trend of NDVI change is similar to the trend of RSEI values in Zhanjiang City, which shows an increase in 2000–2015 and a decrease from 2015 to 2020. This indicates that, among these four indicators, the RSEI values are mainly influenced by NDVI. The other three indicators have less influence.

In this study, spass software was used to perform univariate linear regression between the impervious area and the RSEI value in the fifth period, and the Eq. (16), in which the impervious area showed a negative correlation with RSEI, and the RSEI value decreased with the increase of the impervious area. This is consistent with the results of Xu's (2013) study.

Although this study can relatively objectively analyze the changes in ecological environment quality in Zhanjiang City through RSEI, and objectively predict the RSEI values in 2035 based on the regression model of impervious planning area and RSEI values. However, there are shortcomings in the study.

The atmosphere, vegetation, water system, temperature, and population diversity are also causes of changes in ecological environment quality, and the driving mechanism of the above factors on ecological environment quality changes still needs to be studied. If future studies can consider other ecological indicators comprehensively, the ecological environment quality of Zhanjiang City can be evaluated more comprehensively.

Due to the cloud cover in some areas of the study area and the presence of a small amount of water bodies, the data were de-clouded and masked with water bodies. As a result, there are a few blank image elements in Figures 2–4.

There are large areas of mudflat wetlands in the study area, and there are certain differences in the area and extent of water bodies in different seasons, which have certain effects on the moisture factor and water body mask extraction. The time range of the image data selected in this study is summer, therefore, the RSEI of the study area has some seasonal differences. In the future development, the seasonality of ecological regions can be considered so that the RSEI can monitor the quality of ecological environment more comprehensively.

5. Conclusion

This study takes Zhanjiang City as the study area and constructs the Zhanjiang City Ecological Environment Evaluation System-RSEI model. The findings of the study are as follows.

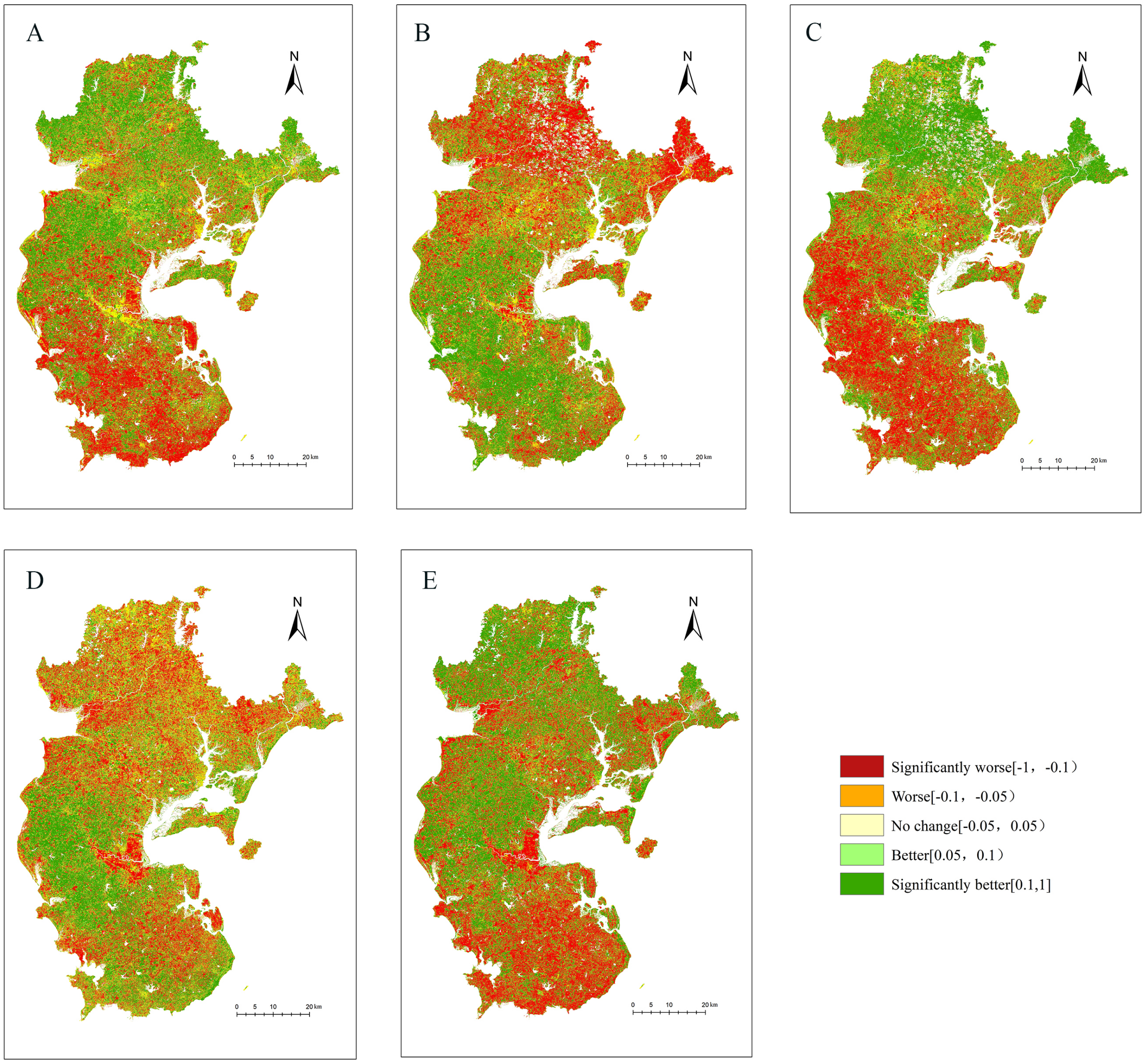

FIGURE 4
Space change of ecological environment in Zhanjiang city from 2000 to 2020, **(A)** Space change of ecological environment in Zhanjiang city in 2000, **(B)** Space change of ecological environment in Zhanjiang city in 2005, **(C)** Space change of ecological environment in Zhanjiang city in 2009, **(D)** Space change of ecological environment in Zhanjiang city in 2015, **(E)** Space change of ecological environment in Zhanjiang city in 2020.

(1) The contribution rates of the first principal components of the RSEI constructed in this paper are all over 59%, and in PC1, the eigenvalue signs of the greenness index and the humidity index are positive and play a positive role in ecological environment quality assessment, while the eigenvalue signs of the dryness index and the heat index are negative and play a negative role in ecological environment quality assessment. Spatially speaking, the areas with high RSEI values were distributed in the central and southeastern regions of Zhanjiang City, and the land use types in these areas were mainly forests. In contrast, the RSEI index is low in the eastern coastal area, which is the central urban area of Zhanjiang and is a type of building land. In summary, the effect of the four ecological indicators on the quality of the ecological environment is in line with the actual basic situation. The RSEI index can accurately and comprehensively assess the ecological environment quality of Zhanjiang city.

(2) From 2000 to 2020, the RSEI values were 0.579, 0.597, 0.597, 0.607, and 0.601, respectively, showing a trend of “rising-falling.” According to the analysis of the difference between the remote sensing ecological index in 2000 and 2020, the ecological environment quality of Zhanjiang City has improved in the last 20 years.

(3) According to the regression model of impervious area and RSEI obtained from the study area's population planning and total area planning in 2035, if the impervious planning area is 4.196% of the total planning area, obtain the 2035 Zhanjiang City RSEI forecast value of 0.488.

Data availability statement

The original contributions presented in the study are included in the article/supplementary material, further inquiries can be directed to the corresponding author.

Author contributions

JinW: methodology, writing—original draft, visualization, and supervision. JiaW: writing—review and editing, and funding acquisition. XJ: resources. All authors contributed to the article and approved the submitted version.

Acknowledgments

We are grateful to the undergraduate students and staff of the Laboratory of Forest Management and "3S" technology, Beijing Forestry University.

Conflict of interest

Publisher's note

References

Chander, G., Markham, B. L., and Helder, D. L. (2009). Summary of current radiometric calibration coefficients for Landsat MSS, TM, ETM+, and EO-1 ALI sensors. *Remote Sens. Environ.* 113, 893–903. doi: 10.1016/j.rse.2009.01.007

Chen, Y. Q., Li, Y. F., Qi, X. H., Chen, W. H., and Lin, J. H. (2018). Assessing ecosystem risk in coastal wetland of the South Fujian Golden Delta using a habitat risk assessment model based on the land-use effect on tidal flat wetland. *Acta Ecol. Sin.* 38, 4214–4225. doi: 10.5846/stxb201802120366

Chen, Q.-Q., Sun, X.-H., Wang, S.-L., and Yang, S. X. (2009). Impacts of social and economic factors on environment in Gannan Province. *Northwest Popul. J.* 30, 58–61. doi: 10.3969/j.issn.1007-0672.2009.06.024

Cheng, L. L., Wang, Z. W., Tian, S. F., Niu, Y. T., Sun, M. Y., and Yang, Y. M. (2021). Evaluation of eco-environmental quality in Mentougou District of Beijing based on improved remote sensing ecological index. *Chin. J. Ecol.* 40, 1177–1185. doi: 10.13292/j.1000-4890.202104.021

Gao, P., Kasimu, A., Zhao, Y., Chai, J., Rui, T., and Zhao, H. (2020). Evaluation of the temporal and spatial changes of ecological quality in the Hami oasis based on RSEI. *Sustainability* 12:7716. doi: 10.3390/su12187716

Gupta, K., Kumar, P., Pathan, S. K., and Sharma, K. P. (2012). Urban neighborhood green index – a measure of green spaces in urban areas. *Landsc. Urban Plan.* 105, 325–335. doi: 10.1016/j.landurbplan.2012.01.003

Hanqiu, X., Wang, M., Shi, T., Guan, H., Fang, C., and Lin, Z. (2019). Prediction of ecological effects of potential population and impervious surface increases using a remote sensing based ecological index (RSEI). *Ecol. Indic.* 93, 730–740. doi: 10.1016/j.ecolind.2018.05.055

He, J., Wang, S., Liu, Y., Ma, H., and Liu, Q. (2017). Examining the relationship between urbanization and the eco-environment using a coupling analysis: case study of Shanghai, China. *Ecol. Indic.* 77, 185–193. doi: 10.1016/j.ecolind.2017.01.017

Ji, J., Wang, S., Zhou, Y., and Wang, L. (2022). Spatiotemporal change and landscape pattern variation of eco-environmental quality in Jing-Jin-Ji urban agglomeration from 2001 to 2015. *IEEE Access* 8, 125534–125548. doi: 10.1109/ACCESS.2020.3007786

Jiang, C. L., Wu, L., Liu, D., and Xu, X. J. (2019). Dynamic monitoring of eco-environmental quality in arid desert area by remote sensing: taking the Gurbantunggut Desert China as an example. *Chin. J. Appl. Ecol.* 30, 877–883. doi: 10.13287/j.1001-9332.201903.008

Li, F. Y., Zhang, Y. Z., Zhao, Z. M., Cheng, M. Q., Cheng, M. Y., and Wang, Z. F. (2020). Evaluation of ecological pattern change of Nanhui Dongtan wetland in Shanghai based on remote sensing ecological index. *J. Shanghai Ocean Univ.* 29, 746–756. doi: 10.12024/jsou.20191002841

Matco-Caria, G., Comez-Chova, L., Amoros-Lopez, J., Muñoz-Marí, J., and Camps-Valls, G. (2018). Multitemporal eloud masking in the Google earth engine. *Remote Sens.* 10:1079. doi: 10.3390/rs10071079

Miao, X. H., and Liang, Q. O. (2021). Analysis of ecological environment changes in Yongjiang River basin based on remote sensing ecological index. *Resour. Environ. Yangtze River Basin* 30, 427–438. doi: 10.11870/cjlyzyyhj202102017

Ministry of Environmental Protection (2005). *Technical specifications for ecological environment assessment:HJ192—2015*. Beijing: China Environmental Science Press.

Moran, M. S., Peters-Lidard, C. D., Watts, J. M., and McElroy, S. (2004). Estimating soil moisture at the watershed scale with satellite-based radar and land surface models. *Can. J. Remote. Sens.* 30, 805–826. doi: 10.5589/m04-043

Nichol, J. (2005). Remote sensing of urban heat islands by day and night. *Photogramm. Eng. Remote Sens.* 71, 613–621. doi: 10.14358/PERS.71.5.613

Nong, L. P., and Wang, J. L. (2020). Dynamic monitoring of ecological environment quality in Kunming based on RSEI model. *Chin. J. Ecol.* 39, 2042–2050. doi: 10.13292/j.1000-4890.202006.025

Nong, L. P., Wang, J. L., and Yu, Y. H. (2021). Research on ecological environment quality in Central Yunnan based on MRSEI model. *J. Ecol. Rural Environ.* 37, 972–982. doi: 10.19741/j.issn.1673-4831.2020.0821

Ping, Y. I., and Fang, S. (2014). Coupling coordination between the socio-economic benefits and eco-environmental benefits of the songshan global geopark. *Resour. Sci.* 36:11. doi: 10.3969/jissn.1671-9646(X).2014.07.051

Qin, L., Chen, B. Q., Yu, Y., Yang, J. L., and Yang, Y. (2023). Study on Spatio-temporal variation of ecological environment before and after mine closure based on RSEI. *Metal Mine* 58, 1–12. doi: 10.19614/j.cnki.jsks.202303033

Rai, P. K. (2013). Forest and land use mapring using remote sensing and ceographical information system: a case study on model system. *Environ. Skep. Crit.* 2, 97–107.

Rikimaru, A., Roy, P. S., and Miyatake, S. (2002). Tropical forest cover density mapping. *Trop. Ecol.* 43, 39–47. doi: 10.20659/jfp.15.2_63

Song, M. J., Luo, Y. Y., and Duan, L. M. (2019). Evaluation of ecological environment in the Xilin Gol steppe based on modified remote sensing ecological index modell. *Arid Zone Res.* 36, 1521–1527. doi: 10.13866/j.azr.2019.06.22

Wang, Y. (2008). Guangdong Zhanjiang mangrove National Nature Reserve Management Status and conservation measures. *Wetl. Sci. Manag.* 4:2. doi: 10.3969/j.issn.1673-3290.2008.02.013

Wang, L. C., Jiao, L., Lai, F. B., and Zhang, N. M. (2019). Evaluation of ecological changes based on a remote sensing ecological index in a Manas Lake wetland, Xinjiang. *Acta Ecol. Sin.* 39, 2963–2972. doi: 10.5846/stxb201804030758

Wang, J., Ma, J. L., and Xie, F. F. (2020). Improvement of remote sensing ecological index in arid regions: taking Ulan Buh Desert as an example. *Chin. J. Appl. Ecol.* 31, 3795–3804. doi: 10.13287/j.1001-9332.202011.011

Wang, S., Zhang, M., and Xi, X. (2022). Ecological environment evaluation based on remote sensing ecological index: a case study in East China over the past 20 years. *Sustainability* 14:15771. doi: 10.3390/su142315771

Wei, X., Yang, J., Luo, P., Lin, L., Lin, K., and Guan, J. (2022). Assessment of the variation and influencing factors of vegetation NPP and carbon sink capacity under different natural conditions. *Ecol. Indic.* 138:108834. doi: 10.1016/j.ecolind.2022.108834

Wu, K. R., Gao, Q., Wang, R. H., Yang, P., Peng, Q., and Liu, C. W. (2021). Evaluation of ecological environment quality in Shijiazhuang based on RSEI model. *Prog. Geophys.* 36, 968–976. doi: 10.6038/pg2021EE0361

Xu, H. Q. (2013). A remote sensing urban ecological index and its application. *Acta Ecol. Sin.* 33, 7853–7862. doi: 10.5846/stxb201208301223

Xu, X. G., Peng, H. F., and Xu, Q. Z. (2006). Land resource conflicts and coordination in fast urbanized coastal zone: a case study of the Shandong peninsula. *J. Peking Univ. Nat. Sci. Ed.* 42, 527–5333. doi: 10.13209/j.0479-8023.2006.097

Xu, H. Q., Shi, T. T., Wang, M. Y., and Lin, Z. (2013). L.Land cover changes in the Xiong' an new area and a prediction of ecological response to forthcoming regional planning. *Acta Ecol. Sin.* 37, 6289–6301. doi: 10.5846/stxb201705210941

Yang, J., and Huang, X. (2021). The 30 m annual land cover dataset and its dynamics in China from 1990 to 2019. *Earth Syst. Sci. Data* 13, 3907–3925. doi: 10.5194/essd-13-3907-2021

Yuan, F., and Bauer, M. E. (2007). Comparison of impervious surface area and normalized difference vegetation index as indicators of surface urban heat island effects in Landsat imagery. *Remote Sens. Environ.* 106, 375–386. doi: 10.1016/j.rse.2006.09.003

Yuan, Y. Y., Wahap, H., Guan, J. Y., Lu, L. H., Zhang, Q. (2016). Spatial differentiation and impact factors of Yutian Oasis's soil surface salt based on GWR model. *Chin. J. Appl. Ecol.* 27, 3273–3282. doi: 10.13287/j.1001-9332.201610.022

Zhao, Y., Wang, S., Ge, Y., Liu, Q., and Liu, X. (2017). The spatial differentiation of the coupling relationship between urbanization and the eco-environment in countries globally: a comprehensive assessment. *Ecol. Model.* 360, 313–327. doi: 10.1016/j.ecolmodel.2017.07.009

Zhong, S., Peng, H. U., Xue, X., Yang, S., and Zhu, P. (2015). Multi-factor comprehensive evaluation model based on the selection of objective weight assignment method. *Acta Geograph. Sin.* 70, 2011–2031. doi: 10.11821/dlxb201512012

Frontiers in Ecology and Evolution

TYPE Original Research
PUBLISHED 05 June 2023
DOI 10.3389/fevo.2023.1152955

A precise forest spatial structure investigation using the SLAM+AR technology

Fei Yan[1,2], Tianshuo Guan[1], Mohammad Rahmat Ullah[3], Li Gao[1] and Yongxiang Fan[4]*

[1]Precision Forestry Key Laboratory of Beijing, Beijing Forestry University, Beijing, China, [2]Tibet Agricultural and Animal Husbandry University, Nyingchi, Tibet Autonomous Region, China, [3]The University of Sydney, Darlington, NSW, Australia, [4]Ji Hua Laboratory, Foshan, Guangdong, China

Check for updates

OPEN ACCESS

EDITED BY
Yanjie Xu,
Finnish Museum of Natural History, Finland

REVIEWED BY
Henn Korjus,
Estonian University of Life Sciences, Estonia
Huaiqing Zhang,
Chinese Academy of Forestry, China

*CORRESPONDENCE
Yongxiang Fan
✉ fanyx@jihualab.ac.cn

RECEIVED 28 January 2023
ACCEPTED 15 May 2023
PUBLISHED 05 June 2023

CITATION
Yan F, Guano T, Ullah MR, Gao L and Fan Y (2023) A precise forest spatial structure investigation using the SLAM+AR technology. *Front. Ecol. Evol.* 11:1152955.
doi: 10.3389/fevo.2023.1152955

Introduction: Forest spatial structures are the foundations of the structure and function of forest ecosystems. Quantitative descriptions and analyses of forest spatial structure have recently become common tools for digitalized forest management. Therefore, the accuracy and intelligence of acquiring forest spatial structure information are of great significance.

Methods: In this study, we developed a forest measurement system using a mobile phone. Through this system, the following tree measurements can be achieved: (1) point cloud of tree and chest diameter circle to measure tree diameter at breast height (DBH) and position coordinates of tree by using simultaneous localization and mapping (SLAM) technology, (2) virtual boundary creation of the sample plot, and the auxiliary measurement function of tree with the augmented reality (AR) interactive module, and (3) position coordinates and single-tree volume factor to calculate the spatial structural parameters of the forest (e.g., Mingling degree, Dominance index, Uniform angle index, and Crowdedness index).The system was tested in three 32 x 32 martificial forest plots.

Results: The average DBH estimations showed BIAS of -0.47 to 0.45 cm and RMSEs of 0.57 to 0.95 cm. Its accuracy level met the requirements of forestry sample surveys. The tree position estimates for the three plots had relatively small RMSEs with 0.17 to 0.22 m on the x-axis and 0.16 to 0.26 m on the y-axis. The spatial structural parameters were as follows: the mingling degree of plot 1 was 0.32, and the overall mixing degree of tree species was low. The trees in plots 2 and 3 were all single species, and the mixing degree of both plots was 0. The dominance index of the three plots was 0.56, 0.51, and 0.51, indicating that the competitive advantage of the whole orest species was not obvious. The uniform angle index of the three plots was 0.55, 0.59, and 0.61, indicating that the positions of trees in the three plots were randomly distributed. The crowdedness index of plot 1 was 1.03, indicating that the degree of aggregation of the trees was low and showed a random distribution trend. The crowdedness index of the other plots were 1.36 and 1.40, indicating that the trees in the plots show a trend of uniform distribution, and the uniformity of plot 3 is higher than that of plot 2, but the overall uniformity is relatively weak.

Discussion: The findings of this study provide support for the optimization of forest structures and improve our conceptual understanding of forest community succession and restoration, in addition to the informatization and precision of forest spatial structure surveys.

KEYWORDS

forest spatial structure, SLAM, AR, forest ecosystems, accuracy verification

Introduction

Forest structure describes the relationship between the distribution of individual trees and their attributes. Forests are ecosystems, and each tree is a structural element of the ecosystem, with species, size, and spatial distribution characteristics (Hui et al., 2019). Measuring and regulating forest structure is essential for achieving forest management objectives. Currently, various indices for quantitative analysis of forest structure have been proposed, which can be divided into two types: non-spatial and spatial structural parameters (Tang, 2010). Non-spatial structural parameters mainly include single-tree volume factor such as DBH, tree height, crown width, and tree species, which focus on the quality and quantity of trees in the forest. Spatial structural parameters (e.g., Mingling degree, Dominance index, Uniform angle index, and Crowdedness index) describe the spatial distribution characteristics of trees and their attributes, and require determining the position coordinates of trees and their relationships with neighboring trees (Hui and Gadow, 2003; Dong et al., 2022). Spatial grouping mainly refers to the positions of trees and their spatial associations (Pastorella and Paletto, 2013). Spatial distribution is fundamental to the study of the spatial behavior of populations (Hui et al., 2007). Any population is distributed in different positions in space, but due to the interaction between individuals within the population and the adaptation of the population to the environment, the same population presents different spatial distribution patterns under different environmental conditions. These spatial aspects determine not only the intensity of competition between adjacent trees but also the spatial niche between trees and the growth potential and stability of the surrounding forest (Gao et al., 2021). Therefore, the spatial aspect of the position of individual trees is often considered more important than the non-spatial aspect (Dong et al., 2022).

In traditional forestry inventory, the collection of forest structural parameters often relies on manual collection. Using traditional methods for forest inventory, variables such as tree height and DBH are obtained using tools such as the Blume-Leiss hypsometer, diameter tape, and measuring tape (Yan et al., 2012). However, the process of field measurements using these instruments is costly and inaccurate (Božić et al., 2005). Although ocular estimation is helpful for improving the efficiency of forest inventory, it hardly meets the accuracy requirements. A total station is a precise electronic surveying instrument that combines distance measurement, angle measurement, and automatic data processing with much higher accuracy. Total stations have been used for forest area measurements and tree height measurements since the 1990s in many developed countries (Feng et al., 2003).

The development of light detection and ranging (LiDAR) technology, coupled with improvements in computer performance, has provided new solutions for forest inventory (Lim et al., 2003). LiDAR technology involves scanning the sample plot to obtain a 3D sampling point cloud, from which the sample plot properties can be objectively extracted (Heidenreich and Seidel, 2022). Terrestrial laser scanning (TLS), a ground-based LiDAR technology, has been used by many scholars to sample plot inventory and extract and evaluate forest attributes using algorithms (Liang et al., 2016). TLS has been used to collect tree attributes in sample plots, such as DBH and tree position (Bienert et al., 2006; Maas et al., 2008; Vastaranta et al., 2009; Murphy et al., 2010). However, the scanning efficiency of general ground-based LiDAR is often limited due to the large size of the equipment, the limited scanning angle, and mutual occlusion by trees. The advent of mobile laser scanning (MLS) has solved some of these problems, allowing forest attribute inventory to be carried out in larger plots (Liang et al., 2014). MLS is characterized by easy installation, easy operation and portability, and adaptability to dense forests and complex terrain. MLS relies on the inertial measurement unit (IMU) and Global Navigation Satellite System (GNSS) to estimate the position and attitude information of LiDAR. However, MLS systems can be difficult to build globally consistent point clouds in areas under the forest that are not covered by GNSS. Hand-held mobile laser scanning (HMLS) has been used in forestry inventory in recent years (Bauwens et al., 2016). Simultaneous localization and mapping (SLAM) technology has enabled HMLS to locate under the forest without GNSS signaling. During the movement of the SLAM system, sensors such as LiDAR and cameras are used to observe the surrounding environment, thereby obtaining an observation sequence. This observation sequence is then used to map the surrounding environment and estimate the posture of the SLAM system (Fan et al., 2019). In forestry survey work, SLAM technology is used to construct point cloud maps of forest plots to quickly and accurately obtain the spatial location, shape, distribution, and other information of forest resources. Using mobile LiDAR scanners for SLAM technology measurements, information such as the three-dimensional structure of the forest, the height, diameter, and canopy coverage of trees can be obtained. Several studies have examined the use of SLAM techniques (James and Quinton, 2014; Ryding et al., 2015), and they found that HMLS could map complex environments about 40 times faster than TLS. However, LiDAR systems still have some limitations, such as high cost, cumbersome post-data processing, and inability to control measurement errors in real time. Additionally, current forest structure survey methods often focus on obtaining non-spatial structural parameters, and there is no complete solution for investigating and solving spatial structural parameters.

Forestry surveys using SLAM technology have primarily focused on LiDAR SLAM, with few studies exploring the use of visual SLAM. In this study, we designed a new measurement system that can be installed on a mobile phone, which uses real-time positioning technology to perceive the forest landscape environment and estimate the system's self-pose. By utilizing the camera as a sensor, the cost is significantly reduced compared to LiDAR. Our measurement system employs monocular SLAM algorithm to construct a point cloud map of the forest and fit the chest diameter circle according to the coordinates of the discrete point cloud. Additionally, the system calculates the position information of the tree based on the position and posture of the mobile phone and the fitting chest diameter circle. The augmented reality module of the system enables real-time interactive operation. It constructs a virtual sample boundary to assist surveyors in determining the measurement range, thus facilitating better measurement and error control. Based on the measured tree position information and non-spatial structural parameters, we aim to solve the forest's spatial structural parameters, such as mingling degree, dominance index, uniform angle index, and crowdedness index. Our goal is to provide a new measurement scheme for forest inventory and spatial structural parameter investigation.

Methods

Simultaneous localization and mapping

Simultaneous localization and mapping is a technology that allows sensors to build the consistent map of the unknown environment, and at the same time, use this map to deduce its position. That is, during SLAM, the position of the motion platform state and all road signs is estimated in real time without any prior information. From the point of view of probability distribution, the SLAM problem requires that the probability distribution *P* be computed for all times *k* (Bailey and Durrant-Whyte, 2006).

$$P(x_k, m|Z_{0:k}, U_{0:k}, x_0) \quad (1)$$

$Z_{0:k} = \{z_1, z_2, \cdots, z_k\} = \{Z_{0:k-1}, z_k\}$: the set of all landmark observations.

x_k: the state vector describing the position and orientation of the vehicle.

$U_{0:k} = \{u_1, u_2, \cdots, u_k\} = \{U_{0:k-1}, u_k\}$: the history of control inputs.

$m = \{m_1, m_2, \cdots, m_n\}$ the set of all landmarks.

In the SLAM algorithm, the motion model and the observation model can solve the posterior distribution of the current state through Bayes theorem. This computation requires a state transition model and an observation model those were described the effect of the control input and observation, respectively. Control input can be described as motion models.

$$P(x_k|x_{k-1}, u_k) \quad (2)$$

u_k: the control vector, applied at time $k-1$ to drive the vehicle to a state x_k at time k.

Observational inputs can be described as observational models.

$$P(z_k|x_k, m) \quad (3)$$

z_k: an observation taken from the vehicle of the position of the landmark at time k.

The SLAM algorithm is completed by estimating the prior state and solving the post-state by using the prior distribution and observation model. The estimation of prior state is described as time-update.

$$P(x_{k-1}, m|Z_{0:k-1}, U_{0:k}, x_0) = \int P(x_k|x_{k-1}, u_k) \times P(x_{k-1}, m|Z_{0:k-1}, U_{0:k-1}, x_0)dx_{k-1} \quad (4)$$

Post-check state estimation using prior distributions and observational models is described as measurement Update.

$$P(x_k, m|Z_{0:k}, U_{0:k}, x_0) = \frac{P(z_k|x_k, m)P(x_k, m|Z_{0:k-1}, U_{0:k}, x_0)}{P(z_k|Z_{0:k-1}, U_{0:k})} \quad (5)$$

Through the recursion of the above two steps, the joint posterior $P(x_k, m|Z_{0:k}, U_{0:k}, x_0)$ for the state x of the sensor and map m at a time k are calculated. Bayes theorem only solves the SLAM problem from the perspective of probability, and the specific form of the motion model and the observation model needs to be given in practical application.

Measurement system

In this paper, the system is divided into two parts: the front end and the back end. The front end is a visual-inertial odometer which estimates the pose of the device and the position of the landmark points using techniques such as those described in Gui et al. (2015) and Leutenegger et al. (2015). The back end uses loop closure detection to identify the areas that have been visited, and then employs graph optimization techniques, such as those described in Angeli et al. (2008) and Hu et al. (2013), to optimize the global pose. In this way, the system is able to achieve drift-free pose estimation and construct a globally consistent map.

Front end

The SLAM front-end fuses observation sensor data, such as cameras, with motion sensor data, such as IMU, to achieve pose estimation in complex application scenarios. The front-end used in this paper is a visual-inertial odometer, which uses the camera as the observation input sensor and the IMU as the motion input sensor. During the movement of the mobile platform, the two data are fused in real-time to estimate the current pose. This study employs an EKF to fuse IMU data and camera observation data for real-time pose estimation. Firstly, the IMU data is pre-integrated from the previous frame to the current frame to estimate the prior pose estimation of the current frame. After acquiring the camera image, feature extraction is performed on the image, and the descriptor is calculated. Based on the descriptor, it is matched with the features retained in the sliding window. Finally, the posterior pose estimation is performed based on the prior pose estimation and feature constraints (Li and Mourikis, 2012, 2013).

In this study, the Oriented-FAST and Rotated BRIEF algorithms are chosen for feature extraction and descriptor calculation, respectively. Specifically, Oriented-FAST is used for feature detection, and the BRIEF descriptor is calculated to describe the feature points for matching (Rublee et al., 2011). Based on tests, this feature detection algorithm and descriptors are 100 times faster than SIFT, SURF, and other methods, making them more suitable for real-time scenarios and devices with low computing power, such as mobile phones (Figure 1).

Back end

After completing front-end pose estimation, the system enters back-end loop detection work. The Bag of Words method (BoW) is a popular appearance-based loop detection method (Angeli et al., 2008). The system uses the feature point description sub-sample of the observed environment image to obtain a dictionary through k-means training. Then, it checks whether a loop is formed by calculating word frequency (TF), inverse document frequency (IDF), and similarity calculation. Generally, when a loop is detected in multiple consecutive frames, it is considered that a loop is detected, and the pose transformation relationship (loop constraint) between the frame and

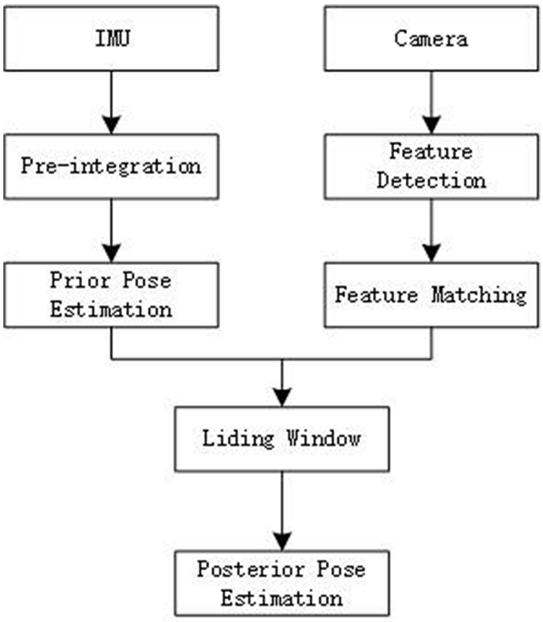

FIGURE 1
Front-end workflow.

the compared frame is calculated through feature matching, optimization, etc. Finally, new pose nodes and loop constraints are added to the keyframe pose graph, and the global pose can be corrected through graph optimization (Figure 2).

DBH and position calculation

The main difference between the DBH measurement function adopted in this study and the current forest survey using LiDAR SLAM lies in the real-time performance. With LiDAR SLAM, post-processing is required on the obtained point cloud data after scanning the plot, and additional work is needed to extract the DBH position. In contrast, this research is mainly based on the single-frame point cloud solution obtained by visual SLAM to calculate the diameter, position of the tree, and various forest parameters in real-time.

To obtain the DBH, the system first acquires more than three points at the height of the DBH of the tree and projects them onto the horizontal plane to obtain their plane coordinates. It then calculates the vertical bisector between two points and sets the corresponding weight coefficient according to the position. The center coordinates are calculated when the angle bisector intersects in pairs, and the weighted center plane coordinates, that is, the position coordinates, are determined according to the weight. Finally, the system uses the center coordinates and DBH height points to calculate the radius and its mean value to determine the cross-sectional area. Once the area is obtained, this value can be used to calculate the DBH.

System operation process

In this study, a mobile phone camera is used as the sensor in the SLAM system (Figure 3). The system acquires images and solved state data, and constructs a consistent point cloud map. Then, the single-tree volume factor is solved. The images and states are used to build 3D virtual scenes using OpenGL. By aligning the SLAM coordinate system with the OpenGL coordinate system, observers can view augmented reality (AR) scenes through the mobile phone screen (Figure 4). The AR scene can be interacted with through the screen in the following ways: (1) The plot boundary is constructed in the OpenGL coordinate system. When the observer approaches the plot boundary, the mobile phone screen displays the position of the plot boundary. (2) When measuring a tree, the observer clicks the position of the ground diameter and the position of the breast diameter on the mobile phone screen. This helps the system determine the point cloud at the diameter circle and fit the discrete point cloud in a circle. The measurement system consists of four parts: defining the sample coordinate system, constructing a globally consistent sparse map, measuring each tree, and calculating parameters. The operation flow is shown in Figure 5. The defined plot coordinate system describes the position of each tree in the plot. The construction of a globally consistent sparse map reduces the drift of the mobile phone pose obtained during measurement through loop detection, thereby reducing the estimation error of tree position. All trees in the sample plot are observed during the measurement of each tree. The parameter calculation process calculates the forest structural parameters of the area represented by the sample plot.

SLAM operates through a process that is divided into four modules: front-end odometer, back-end optimization, loop closure detection, and map building. The loop closure detection module is crucial for refining data and correcting pose drift caused by the front-end visual odometer. Its main function is to detect similar data collected by the sensor at the same place, and use this information to ensure data consistency. The accuracy of the globally consistent map is closely related to the scan trajectory, and proper loop closure detection during the scanning process is essential for obtaining an accurate map. In this study, a fixed sample scan path was designed, starting at the center of the sample plot and measuring the trees along the route of progress, as shown in the Figure 6. Traditional SLAM systems with image feature-based backends may not work well in poorly constructed forests. Therefore, an online trunk-based backend was designed in this study to estimate tree position accurately and correct pose drift in real time for large-scale forest inventories. Specifically, a trunk-based loop closure detection algorithm was developed to detect whether an earlier observed tree is re-observed, providing nodes and constraints for tree position graph optimization. This algorithm builds and optimizes the tree position graph using the provided nodes and constraints, and corrects the current pose based on the optimized globally consistent tree position graph.

Spatial parameter selection

The forest spatial structure index based on the relationship between adjacent trees has been widely used in the research of forest spatial structure analysis, competition and advantage calculation, species diversity measurement, forest structure reconstruction and management optimization. The spatial structural parameters are mainly a comprehensive expression of the single-tree volume factor and spatial position. The position of standing trees and the single-tree volume factor were measured by mobile phone measurement system to solve the spatial structural parameters, and the spatial structural

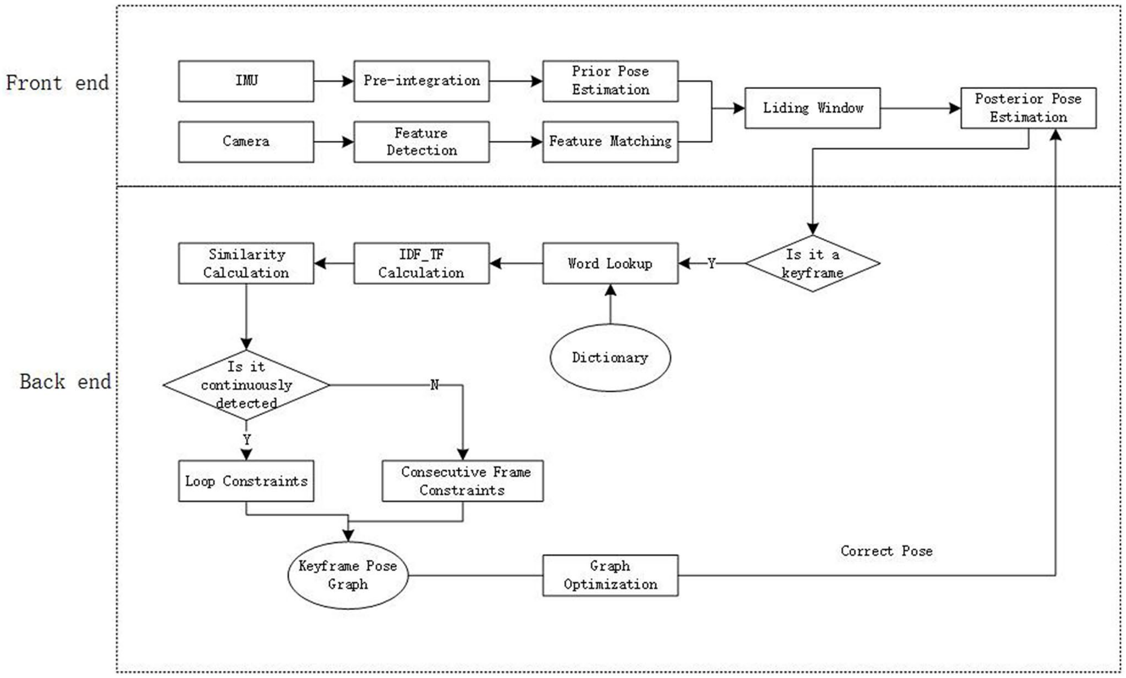

FIGURE 2
System workflow.

FIGURE 3
Measurement phone.

parameters considered in this study mainly included Mingling degree, Dominance index, Uniform angle index, and Crowdedness index.

Mingling degree mainly describes the species composition and spatial pattern in the forest. It is defined as the proportion of individuals in the four nearest neighboring trees of the target tree i who are not of the same species as the target tree.

$$Mi = \frac{1}{4}\sum_{j=1}^{4} vij$$

$$v_{ij} = \begin{cases} 1, \textit{If the } \text{neighboring tree } j \textit{ and the } \text{target } \textit{tree i} \\ \textit{are different species} \\ 0, \textit{If the } \text{neighboring tree } j \textit{ and the } \text{target } \textit{tree i} \\ \textit{are same species} \end{cases} \quad (6)$$

Uniform angle index describes the uniformity of adjacent trees around the reference tree *i*, and is defined as the proportion of the number of α angles less than the standard angle α_0 in the number of nearest neighboring trees. The standard angle α_0 is selected as 72° according to the research conducted by Hui et al. (2004).

$$Wi = \frac{1}{4}\sum_{j=1}^{4} zij$$

$$z_{ij} = \begin{cases} 1, \textit{If the} \pm \textit{is less than the} \pm_0 \\ 0, \textit{If the} \pm \textit{is greater than or equal to} \pm_0 \end{cases} \quad (7)$$

The Dominance index quantitatively describes tree competition and is defined as the proportion of the adjacent trees of the reference tree whose DBH is greater than the number of reference trees to the four nearest neighbors examined.

$$Di = \frac{1}{4}\sum_{j=1}^{4} \text{k}ij$$

$$\text{k}_{ij} = \begin{cases} 1, \textit{If the } \text{neighboring tree } j \textit{ is smaller than} \\ \textit{the } \text{target } \textit{tree i} \\ 0, \textit{If the } \text{neighboring tree } j \textit{ is greater than} \\ \textit{or equal to the } \text{target } \textit{tree i} \end{cases} \quad (8)$$

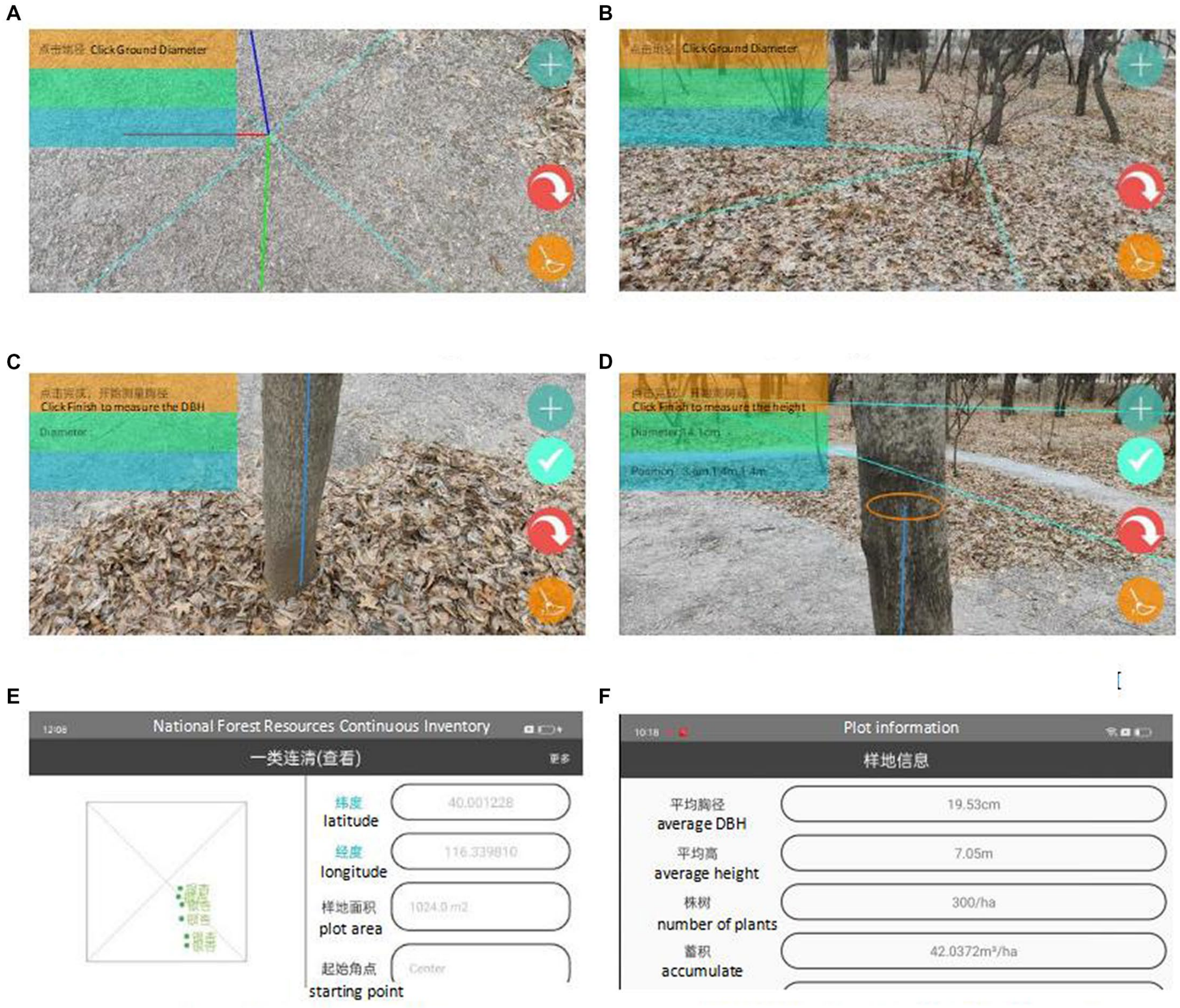

Diameter :

Diameter: 14.1cm

Position : 3.6m,1.4m,1.4m

National Forest Resources Continuous Inventory

一类连清(查看)

纬度 latitude	40.001228
经度 longitude	116.339810
样地面积 plot area	1024.0 m2
起始角点 starting point	Center

Plot information

样地信息

平均胸径 average DBH	19.53cm
平均高 average height	7.05m
株树 number of plants	300/ha
蓄积 accumulate	42.0372m³/ha

FIGURE 4
Different statuses of system during observation. **(A)** Determine the location of the plot center. **(B)** Sample boundaries. **(C)** Click on the position of the tree. **(D)** Click on the position of the DBH. **(E)** Overview of the sample. **(F)** Calculated forest structure parameters.

The Crowdedness index describes the horizontal distribution pattern of tree positions and is defined as the ratio of the average distance of the nearest neighbor to the expected average distance under random distribution.

$$R = \frac{\frac{1}{n}\sum_{i=1}^{n} ri}{\frac{1}{2}\sqrt{\frac{S}{n}}} \tag{9}$$

r_i is the distance from the tree i to its nearest neighbor; n is the total number of plants in the plot; S is the sample area.

Study area and sample plots information

In this study, three plots of 32 m × 32 m were selected for testing, located in the campus forest area of Beijing Forestry University, the Olympic Forest Park, and Dongsheng Bajia Park in Beijing, China. Plot 1 is a mixed forest with *Juniperus chinensis* L. as the dominant tree species, while the other two plots are artificial pure forests dominated by *Ginkgo biloba* L. and Populus L. The three plots contain trees of different diameters, and the number and distribution of trees in each plot are different, which comprehensively tests the function of the measurement system. The sample plots have few shrubs and are convenient for data collection. The mobile phone measurement system was used to conduct the sample plot survey, and the spatial structure of the forest area was analyzed using the calculated spatial structural parameters. Additionally, the chest diameter and position data of the trees were recorded as reference data using a total station and a chest diameter ruler to test the accuracy.

Results

DBH accuracy

The diameter at breast height (DBH) of trees in the sample plot was estimated using a mobile phone measurement system, and the

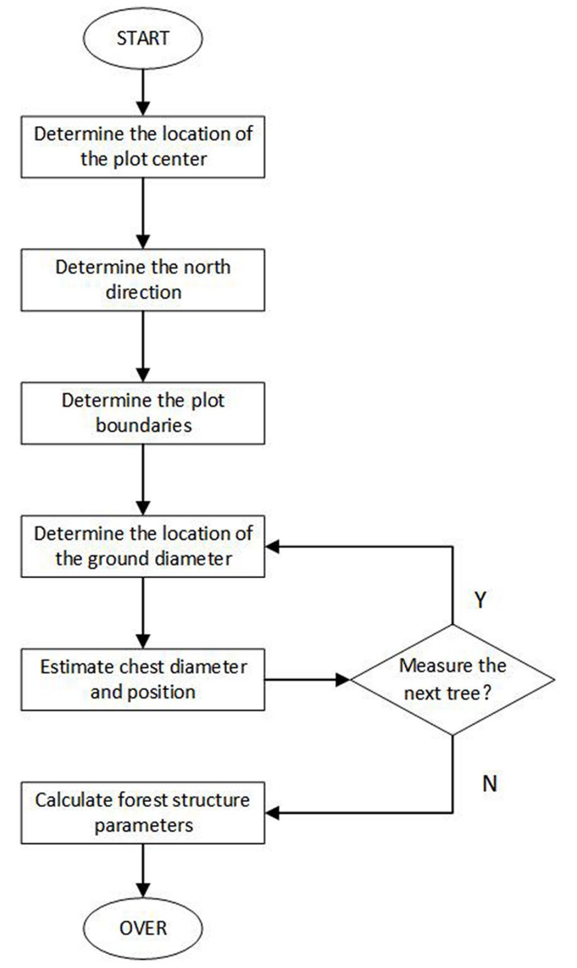

FIGURE 5
Workflow of forest inventory system.

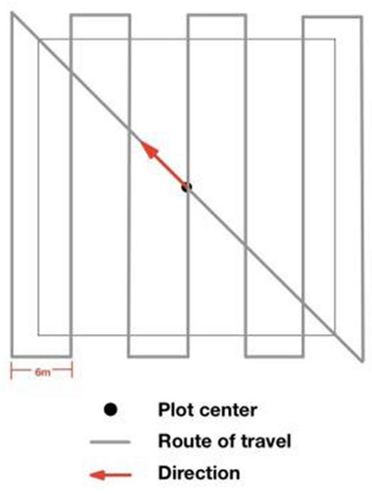

FIGURE 6
Scanning trajectory for building plot map.

estimated values were compared to the true DBH obtained by measuring the trees with a diameter tape as a reference. In this study, the accuracy of DBH estimation was evaluated using the BIAS, RMSE, relative BIAS (relBIAS), and relative RMSE (relRMSE) metrics, which were calculated using the following formulas:

$$B_{IAS} = \frac{\sum_{i=1}^{n}\left(x_i - x_{ir}\right)}{n} \tag{10}$$

$$\mathrm{rel}BIAS = \frac{\sum_{i=1}^{n}\left(xi / xir - 1\right)}{n} \times 100\% \tag{11}$$

$$R_{MSE} = \sqrt{\frac{\sum_{i=1}^{n}\left(x_i - x_{ir}\right)^2}{n}} \tag{12}$$

$$\mathrm{rel}RMSE = \sqrt{\frac{\sum_{i=1}^{n}\left(xi / xir - 1\right)^2}{n}} \times 100\% \tag{13}$$

where x_i is an estimate; x_{ir} is the reference value corresponding to x_i; n is the total number of trees.

The Figure 7A displays the overall distribution of DBH estimates for the three plots obtained using the mobile phone measurement system. The figure shows that all DBH estimates were close to the corresponding reference values, and there were no apparent abnormal estimates. This observation suggests that this method of estimating breast diameter is highly robust. Statistical analysis of all DBH estimates was performed, and the results are presented in Table 1.

The DBH obtained through the mobile phone measurement system had a BIAS value close to zero, indicating that it was nearly unbiased (−0.47 ~ 0.45 cm, −2.04% ~ 2.74%) compared to the reference value obtained using the diameter tape. Moreover, the DBH estimates had small RMSEs overall (0.57 ~ 0.95 cm, 2.95% ~ 4.5%), as shown in Table 1. Figure 7B is a box plot of the error of the DBH estimates in different diameter steps, which indicates that the average error of the DBH estimate in different DBH ranges was close to zero. These results demonstrate that the mobile phone measurement system can achieve high-precision DBH measurement, and the measurement accuracy meets the requirements for further determining forest structural parameters.

Position accuracy

The measured tree position data for the three plots are shown in Figure 8. The overall deviation was small, and the estimated position could accurately reflect the actual position of the sampled trees. As shown in Table 2, the BIAS of the x-axis was −0.04 to 0.22 m and the y-axis was 0.01 to 0.20 m. The tree position estimates for the three plots had relatively small RMSEs of 0.17 to 0.22 m on the x-axis and 0.16 to 0.26 m on the y-axis. The scatter distribution of errors in the two axes was relatively uniform. Since the spatial structural parameters only require the determination of neighboring trees based on their position, and the position data was not calculated as a parameter, the position accuracy of the system fitting could meet the requirements for further spatial structural parameter calculations.

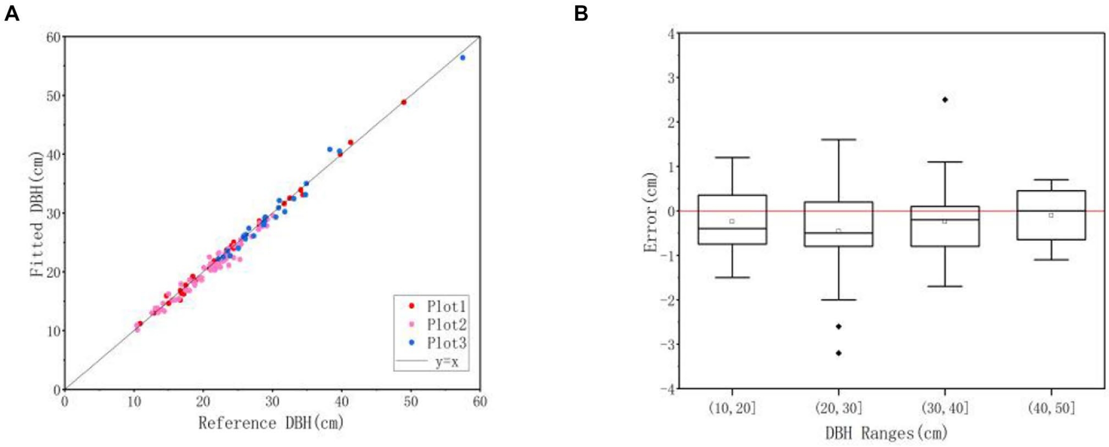

FIGURE 7
DBH estimates error statistics. **(A)** DBH estimates distribution. **(B)** The errors under different DBH ranges.

TABLE 1 Accuracies of the DBH estimates.

	BIAS (cm)	relBIAS (%)	RMSE (cm)	relRMSE (%)
Plot 1	0.45	2.74%	0.57	3.08%
Plot 2	−0.47	−2.04%	0.95	4.50%
Plot 3	−0.25	−0.9%	0.94	2.98%

Spatial structural parameter calculation

The horizontal distance between trees was calculated based on the position coordinates, and the four nearest neighboring trees of each reference tree were determined based on their distances. By comparing the non-spatial structural parameters (such as DBH, tree species, and position distribution) of the reference tree and its neighboring trees, and applying the relevant formula, the spatial structural parameters of the forest area in the sample plot were calculated, including Mingling degree, Dominance index, Uniform angle index, and Crowdedness index. The value range and index system of each spatial parameter are presented in Table 3.

The spatial distribution of each tree species in Plot 1 can be clearly seen in Figure 9, where it shows that *Juniperus chinensis* L. was the dominant tree species in the area. The parameter values of the forest stand are presented in Table 4, showing that the mixing degree of the whole forest stand was 0.32, which is considered weak. As both Plots 2 and 3 were single-species plots, their species distribution is not shown, and the mixing degree of both plots was 0. From Figure 10A, a relatively high percentage of 0 values can be observed, indicating that trees of the same species were clustered in Plot 1. This conclusion is also apparent from Figure 8, as trees of the same species in the sample plot had a higher degree of aggregation. The dominance index reflects the competition among forest trees, and the dominance index values for the three plots were 0.56, 0.51, and 0.51, suggesting that the competitive advantage of the whole forest species was not apparent, and tree growth was relatively balanced. The uniform angle index and crowdedness index describe the spatial distribution of trees in the forest area. The uniform angle index values for the three plots were 0.55, 0.59, and 0.61, indicating that the position of trees in the plots was randomly distributed. The crowdedness index is the ratio of the mean distance between the horizontal distance of the reference tree and the neighboring trees to the expected average distance. The crowdedness index for Plot 1 was 1.03, indicating that the degree of aggregation of the trees was low and showed a random distribution trend. The crowdedness index for Plots 2 and 3 were 1.36 and 1.40, respectively, suggesting that the trees in the plots showed a trend of uniform distribution, and the uniformity of Plot 3 was higher than that of Plot 2, but the overall uniformity was relatively weak.

Discussion

In recent years, the development of forestry inventory has been based on intelligence and precision. Obtaining point cloud data of forest plots is an essential method to construct a 3D forest model and invert forest structural parameters. At this stage, the construction of forest point clouds mainly uses LiDAR (TLS, MLS, HMLS, etc.) to register the point cloud with different algorithms and realize the construction of a complete point cloud map. Its core is to find the corresponding relationship between the initial point cloud and the target point cloud, transform the point cloud on the target object into the coordinate system, and convert the point cloud of the same target object scanned multiple times into the same coordinate system. The difference in the algorithm between LiDARs with different working methods lies in the use of different methods to obtain the corresponding relationship of point clouds at different times. The SLAM algorithm is an algorithm that obtains the position and attitude changes of the sensor during its movement and calculates the corresponding relationship of point clouds at different times according to the changes to realize the work of point cloud registration and map construction. Research on intelligent forestry survey tools is mainly concentrated on LiDAR, and they include (1) designing a multi-sensor fusion LiDAR system to improve the scanning range and improve the point cloud mapping effect, (2) designing and improving point cloud matching algorithms to obtain high-quality point cloud data, and (3) proposing a more efficient and accurate circle fitting method based on the original discrete point fitting DBH circle algorithm (e.g., least squares method, random sample consensus, and HoughCircles).

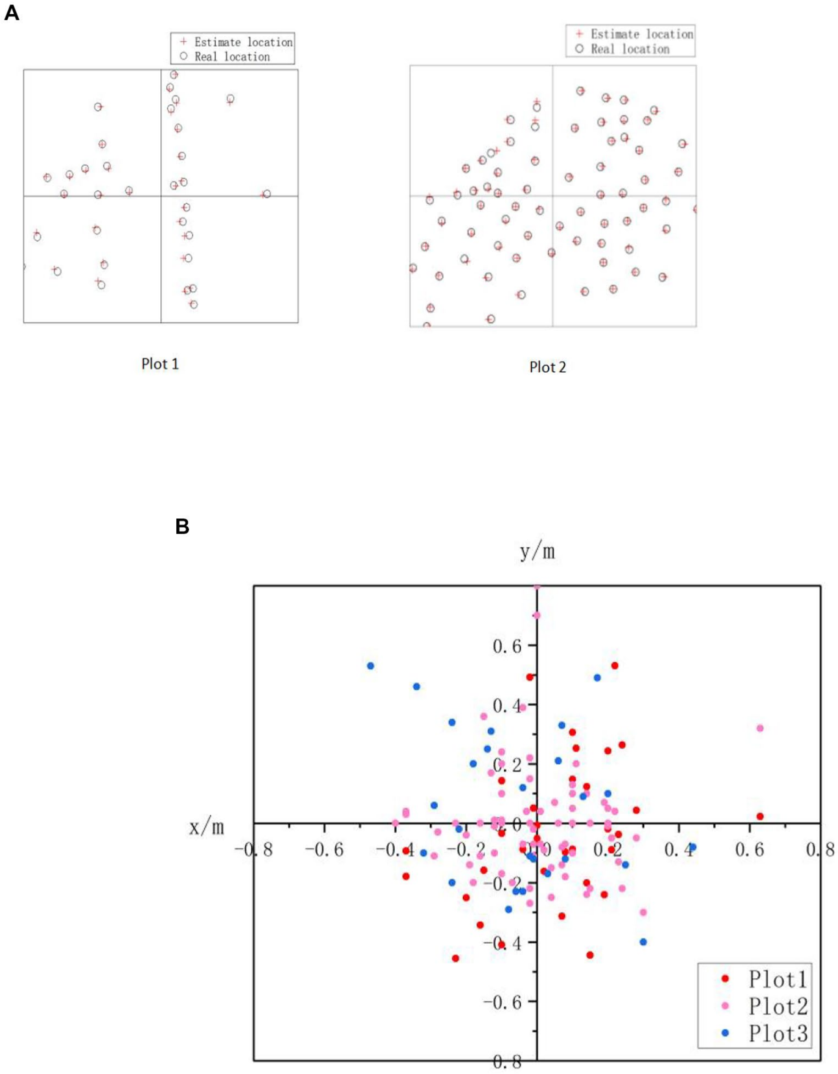

FIGURE 8
Position estimates error statistics. **(A)** Tree position distribution. **(B)** Position errors of all trees in plots.

TABLE 2 Accuracies of the position estimates.

	BIASx (m)	BIASy (m)	RMSEx (m)	RMSEy (m)
Plot 1	0.22	0.20	0.21	0.16
Plot 2	0.01	0.01	0.17	0.19
Plot 3	−0.04	0.05	0.22	0.26

These research efforts have greatly improved the efficiency and accuracy of forestry inventory.

However, lidar-based research still relies on computers for post-data processing and parameter extraction, which increases workload and reduces real-time performance. In this study, a measurement system was constructed on a mobile phone using visual SLAM+AR technology installed in the mobile phone camera to visually construct a sample site cloud map. This system got rid of the limitations of lidar for data collection, and real-time integrated measurement work was realized without requiring post-processing.

The results of the study show that the mobile phone measurement system can accurately solve the single-tree volume factor, meeting the needs of forestry inventory and providing high-quality data support for further solving other forest structural parameters. The system also allows for the investigation of forest spatial structure, which has become an increasingly important content of forestry investigation. The nearest neighbor method is an important means to calculate the parameters of the forest spatial structure. Using neighboring trees to investigate spatial structure parameters usually requires manual determination of neighboring trees to calculate parameters and assign values. This process is cumbersome and may cause errors due to subjective factors of the measurer. According to the position of the trees measured by this system, the four neighboring trees of the reference tree can be determined, and the spatial structural parameters of the forest can be preliminarily solved according to the relationship between the breast diameter and position of the reference tree and the neighboring tree. Therefore, by optimizing the forest inventory method, this study obtains the forest spatial structural parameters

TABLE 3 Forest spatial structure index system.

Spatial parameters	Variable	Values				
		0	0.25	0.5	0.75	1
Mingling degree (M)	Species	Non mixture	Low mixture	Intermediate mixture	High mixture	Complete mixture
Dominance index (D)	Diameter	Pre-dominant	Sub-dominant	Intermediate	Disadvantaged	Absolutely disadvantaged
Uniform angle index (U)	Angle	Very regular	Regular	Random	Clumped	Very clumped
Crowdedness index (C)	–	C > 1 is regular distribution; C = 1 is random distribution; and C < 1 is clustered distribution				

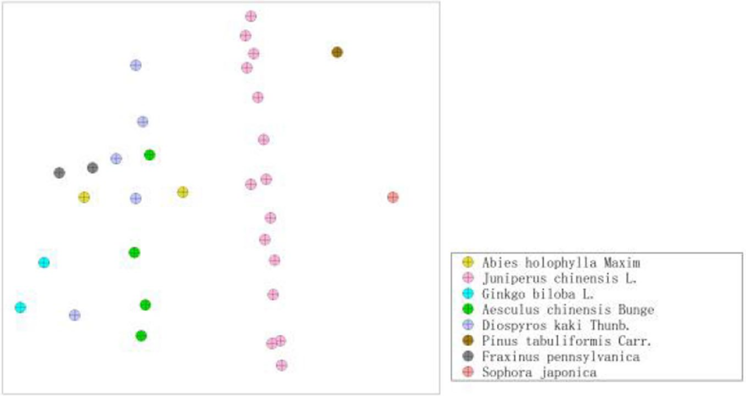

FIGURE 9
Spatial distribution of different tree species.

TABLE 4 Frequency values for different spatial structural parameters.

	Spatial parameters	Frequency distribution					Parameter value
		0	0.25	0.5	0.75	1	
Plot 1	Mingling degree	0.61	0	0.07	0.18	0.14	0.32
	Dominance index	0.21	0.14	0.14	0.11	0.4	0.56
	Uniform angle index	0.04	0.07	0.5	0.25	0.14	0.55
	Crowdedness index	–	–	–	–	–	1.03
Plot 2	Mingling degree	1	0	0	0	0	0
	Dominance index	0.21	0.21	0.18	0.30	0.14	0.51
	Uniform angle index	0.09	0.08	0.26	0.52	0.06	0.59
	Crowdedness index	–	–	–	–	–	1.36
Plot 3	Mingling degree	1	0	0	0	0	0
	Dominance index	0.16	0.21	0.26	0.16	0.21	0.51
	Uniform angle index	0.16	0.05	0.05	0.68	0.05	0.61
	Crowdedness index	–	–	–	–	–	1.40

more efficiently, moreover, provides good data support for the study of forest ecology, and ultimately realizes the promotion of forest ecological management, optimization, and promotion of ecological sustainable development.

However, due to the performance gap between the mobile phone camera and the lidar, the current system based on vision has issues with its stability. The problem of pose drift occurs in actual use, and the stability and robustness of the system need to be improved. In the future, more measurement and auxiliary functions can be developed on mobile phones, including tree species recognition based on the surface characteristics of trunks or leaves and using point clouds to realize 3D modeling of trees. Overall, this system has high application value and broad development space in forestry inventory, as it optimizes the forest inventory method, provides good data support for the study of forest ecology, and ultimately promotes ecological sustainable development.

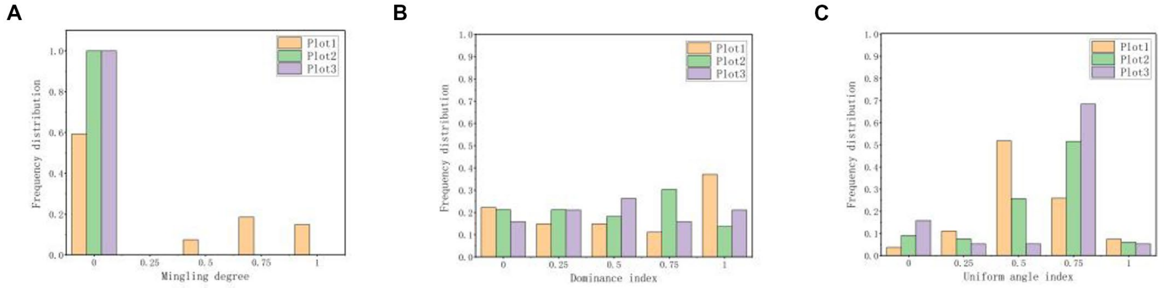

FIGURE 10
Frequency distribution of different spatial structural parameters. **(A)** Mingling degree. **(B)** Dominance index. **(C)** Uniform angle index.

Conclusion

In this study, the mobile phone is used as a sensor, and the visual SLAM technology is used to replace the HMLS based on LiDAR SLAM, which improves the efficiency and portability. At the same time, the embedding of augmented reality technology realizes real-time measurement and can control errors well with high measurement accuracy of DBH and position, which can be used to determine the neighboring trees and calculate the spatial structural parameters of the forest areas. The test results show that the system can meet the inventory needs well and can be used as a new direction for future forest resources investigation and solving spatial structure parameters.

At this stage, there are still some problems in this study. The positioning method based on vision sometimes has positioning drift, and the stability still needs to be further improved. In addition, the number of system calculation parameters is currently limited, and in some surveys it is still necessary to rely on other tools for assistance, and more measurement functions need to be embedded in the future.

Data availability statement

The raw data supporting the conclusions of this article will be made available by the authors, without undue reservation.

Author contributions

FY conceived and designed the project. TG and MU wrote the manuscript. YF and FY conceptualized the study, designed the methodology, and reviewed the manuscript. LG conducted field experiments. All authors contributed to the article and approved the submitted version.

Funding

This work was supported by Tibet Autonomous Region Science and Technology Plan Project, project number: XZ202301YD0043C.

Acknowledgments

The authors would like to extend our sincere gratitude to the undergraduate students and staff of the Laboratory of Forest Management and “3S” technology and Beijing Forestry University for various help in the experimentation.

Conflict of interest

The authors declare that the research was conducted in the absence of any commercial or financial relationships that could be construed as a potential conflict of interest.

Publisher’s note

References

Angeli, A., Doncieux, S., Meyer, J. A., and Filliat, D. Real-time visual loop-closure detection. In 2008 IEEE International Conference on Robotics and Automation. IEEE, (2008). 1842–1847.

Bailey, T., and Durrant-Whyte, H. (2006). Simultaneous localization and mapping (SLAM). Part II. IEEE Robotics and Automation Magazine, 13108–117. doi:10.1109/MRA.2006.1678144

Bauwens, S., Bartholomeus, H., Calders, K., and Lejeune, P. (2016). Forest inventory with terrestrial LiDAR: a comparison of static and hand-held Mobile laser scanning. *Forests* 7:127. doi: 10.3390/f7060127

Bienert, A., Scheller, S., Keane, E., Mullooly, G., and Mohan, F. (2006). Application of terrestrial laser scanners for the determination of forest inventory parameters. *Int. Arch. Photogram. Remote Sens. Spatial Inform. Sci.*:36, 1–5.

Božić, M., Čavlović, J., Lukić, N., Teslak, K., and Kos, D. (2005). Efficiency of ultrasonic vertex III hypsometer compared to the most commonly used hypsometers in Croatian forestry. *Croatian J. For. Eng. J. Theory Appl. Forest. Eng.* 26, 91–99.

Dong, L., Bettinger, P., and Liu, Z. (2022). Optimizing neighborhood-based stand spatial structure: four cases of boreal forests. *For. Ecol. Manag.* 506:119965. doi: 10.1016/j.foreco.2021.119965

Fan, Y., Feng, Z., Chen, P., Gao, X., and Shen, C. (2019). Research on Forest plot survey system based on RGB-D SLAM Mobile phone. *J. Agric. Mech.* 50, 226–234. doi: 10.6041/j.issn. 1000-1298.2019.08.024, in Chinese.

Feng, Z. K., Han, X. C., Zhou, K. L., Nan, Y. T., and Fu, X. (2003). The analysis of forestry mensuration principle and precision in fixed samples by total station. *Beijing Surv.* 2003, 28–30. in Chinese.

Gao, W., Lei, X., Liang, M., Larjavaara, M., Li, Y., Gao, D., et al. (2021). Biodiversity increased both productivity and its spatial stability in temperate forests in northeastern China. *Sci. Total Environ.* 780:146674. doi: 10.1016/j.scitotenv.2021.146674

Gui, J., Gu, D., Wang, S., and Hu, H. (2015). A review of visual inertial odometry from filtering and optimisation perspectives. *Adv. Robot.* 29, 1289–1301. doi: 10.1080/01691864.2015.1057616

Heidenreich, M. G., and Seidel, D., (2022). *Assessing Forest vitality and Forest structure using 3D data: A case study from the Hainich National Park*, Hainich: Frontiers in Forests and Global Change.

Hu, G., Khosoussi, K., and Huang, S.. Towards a reliable SLAM back-end. 2013 IEEE/RSJ International Conference on Intelligent Robots and Systems. IEEE, (2013). 37–43.

Hui, G., and Gadow, G. (2003). *Quantitative analysis of forest spatial structure*. Beijing: Science and Technology Press.

Hui, G., Gadow, K., and Hu, Y. (2004). Standard angle selection of angular scale of Forest stand spatial structure parameters. *For. Res.* 2004, 1001–1498. doi: 10.3321/j.issn:1001-1498.2004.06.001, (in Chinese).v

Hui, G., Li, L., Zhao, Z., and Dang, P. (2007). Comparison of methods in analysis of the tree spatial distribution pattern. *Acta Ecol. Sin.* 27, 4717–4728. doi: 10.1016/S1872-2032(08)60008-6

Hui, G., Zhang, G., Zhao, Z., and Yang, A. (2019). Methods of Forest structure research: a review. *Curr. Forest. Rep.* 5, 142–154. doi: 10.1007/s40725-019-00090-7

James, M. R., and Quinton, J. N. (2014). Ultra-rapid topographic surveying for complexenvironments: the hand-held mobile laser scanner (HMLS). *Earth Surf. Process. Landforms* 39, 138–142. doi: 10.1002/esp.3489

Leutenegger, S., Lynen, S., Bosse, M., Siegwart, R., and Furgale, P. (2015). Keyframe-based visual–inertial odometry using nonlinear optimization. *Int. J. Robot. Res.* 34, 314–334. doi: 10.1177/0278364914554813

Li, M., and Mourikis, A. I.. Improving the accuracy of EKF-based visual-inertial odometry. 2012 IEEE international conference on robotics and automation. IEEE, (2012). 828–835.

Li, M., and Mourikis, A. I. (2013). High-precision, consistent EKF-based visual-inertial odometry. *Int. J. Robot. Res.* 32, 690–711. doi: 10.1177/0278364913481251

Liang, X., Hyyppä, J., Kukko, A., Kaartinen, H., Jaakkola, A., and Yu, X. (2014). The use of a Mobile laser scanning system for mapping large Forest plots. *IEEE Geosci. Remote Sens. Lett.* 11, 1504–1508. doi: 10.1109/LGRS.2013.2297418

Liang, X., Kankare, V., Hyyppä, J., Wang, Y., Kukko, A., Haggrén, H., et al. (2016). Terrestrial laser scanning in forest inventories. *ISPRS J. Photogramm. Remote Sens.* 115, 63–77. doi: 10.1016/j.isprsjprs.2016.01.006

Lim, K., Treitz, P., Wulder, M., St-Onge, B., and Flood, M. (2003). LiDAR remote sensing of forest structure. *Progr. Phys. Geogr. Earth Environ.* 27, 88–106. doi: 10.1191/0309133303pp360ra

Maas, H. G., Bienert, A., Scheller, S., and Keane, E. (2008). Automatic forest inventory parameter determination from terrestrial laser scanner data. *Int. J. Remote Sens.* 29, 1579–1593. doi: 10.1080/01431160701736406

Murphy, G. E., Acuna, M. A., and Dumbrell, I. (2010). Tree value and log product yield determination in radiata pine (*Pinus radiata*) plantations in Australia: comparisons of terrestrial laser scanning with a forest inventory system and manual measurements. *Can. J. For. Res.* 40, 2223–2233. doi: 10.1139/X10-171

Pastorella, F., and Paletto, A. (2013). Stand structure indices as tools to support forest management: an application in Trentino forests (Italy). *J. Forest Sci.* 59, 159–168. doi: 10.17221/75/2012-JFS

Rublee, E., Rabaud, V., Konolige, K., and Bradski, G. (2011). ORB: an efficient alternative to SIFT or SURF. *Int. Conf. Comp. Vis.* 2011:107.

Ryding, J., Williams, E., Smith, M. J., and Eichhorn, M. P. (2015). Assessing handheld mobile laser scanners for forest surveys. *Remote Sens.* 7, 1095–1111. doi: 10.3390/rs70101095

Tang, M. (2010). Advances in study of Forest spatial structure. *Scientia Silvae Sinicae* 46, 117–122. (in Chinese).

Vastaranta, M., Melkas, T., Holopainen, M., Kaartinen, H., Hyyppä, J., and Hyyppä, H. (2009). Laser-based field measurements in tree-level forest data acquisition. *Photogram. J. Finland* 21, 51–61.

Yan, F., Mohammad, R. U., Gong, Y., Feng, Z., Chowdury, Y., and Wu, L. (2012). Use of a no prism total station for field measurements in *Pinus tabulaeformis* Carr. Stands in China. *Biosyst. Eng.* 113, 259–265. doi: 10.1016/j.biosystemseng.2012.08.007

frontiers | Frontiers in Ecology and Evolution

TYPE Original Research
PUBLISHED 14 June 2023
DOI 10.3389/fevo.2023.1171245

EDITED BY
Yanjie Xu,
Finnish Museum of Natural History, Finland

REVIEWED BY
Corrado Battisti,
Roma Tre University, Italy
Suresh Chandra Subedi,
Arkansas Tech University, United States

*CORRESPONDENCE
Jason S. Hagani
✉ jhagani@suisunrcd.org

RECEIVED 21 February 2023
ACCEPTED 24 May 2023
PUBLISHED 14 June 2023

CITATION
Hagani JS, Takekawa JY, Chappell SC, Tanner RL, Ernst AR and Kettenring KM (2023) A remote sensing approach to assess the historical invasion of *Phragmites australis* in a brackish coastal marsh.
Front. Ecol. Evol. 11:1171245.
doi: 10.3389/fevo.2023.1171245

A remote sensing approach to assess the historical invasion of *Phragmites australis* in a brackish coastal marsh

Jason S. Hagani[1]*, John Y. Takekawa[1], Steven C. Chappell[1], Richelle L. Tanner[2], Adrienne R. Ernst[3] and Karin M. Kettenring[3]

[1]Suisun Resource Conservation District, Suisun City, CA, United States, [2]Chapman University, Environmental Science and Policy Program, Orange, CA, United States, [3]Department of Watershed Sciences, Utah State University, Quinney College of Natural Resources, Logan, UT, United States

Introduction: Coastal estuarine wetlands provide important habitats for a variety of endemic flora and fauna but are particularly vulnerable to biological invasions. Regular monitoring of changes in these vulnerable wetlands has become increasingly important for effective management, especially considering threats from climate change effects and human disturbance. Historical analyzes of plant invasions may guide targeted management strategies to eradicate harmful species. Estimating the distribution of invasive species has never been more accessible with the improved availability of high-resolution data and innovations in remote sensing, estimating the distribution of invasive species has never been more accessible.

Methods: We assessed the spread of non-native *Phragmites australis* subsp. *australis* in Suisun Marsh on the upper San Francisco Estuary, one of the largest brackish coastal wetlands in North America. Suisun Marsh consists of managed and tidal wetlands, and efforts have been made to control invasive *P. australis* on the managed wetlands to support habitat values for wildlife. We used remote-sensing analyzes of publicly available, biennial color-infrared images taken by the National Agriculture Imagery Program (NAIP) to map the expansion of invasive *P. australis* across two decades. We generated random forest classifications of representative images to map the distribution of *P. australis*, then calculated a variety of metrics describing the rate and spatial extent of the *P. australis* spread. Additionally, we ran generalized linear models to examine factors related to the growth of *P. australis*.

Results: Our classifications yielded accuracies of over 90% and showed a 234% (1,084 ha) increase in *P. australis* between 2003 and 2018. The expansion rate of *P. australis* patches averaged 1.32 m/year (±0.53 SD) which is higher than most reported in the literature. We found that *P. australis* expansion in managed areas within levees was significantly correlated with invasion in tidal areas outside the levees on the same parcel and also related to its spread on adjacent parcels.

Discussion: Our findings suggest that despite individual landowner management efforts, *P. australis* has continued to expand substantially throughout Suisun Marsh. Future efforts to treat invasive *P. australis* may require emphasizing adaptive, collaborative management rather than individual management strategies to ensure the invasive species is eradicated on a large scale to preserve the valued ecosystem functions.

KEYWORDS

***Phragmites australis*, invasive species, marsh, estuary, random forest classification, wetland**

1. Introduction

The spread of non-native, invasive species poses a major threat to plant diversity, ecosystem function, and habitat quality (Vitousek et al., 1997; Mack et al., 2000; Quirion et al., 2018; Tadros et al., 2020). An estimated 5,000 invasive plant species have been introduced into the United States (Pimentel et al., 2000; Tallamy, 2004) and managing the spread of these non-native plants costs millions of dollars annually (Pimentel et al., 2000). The non-native common reed (*Phragmites australis* subsp. *australis*; hereafter *P. australis*) is one such plant–it is a broadly distributed grass species now found throughout the wetlands of North America. While there are some native *P. australis* lineages in different parts of North America (*Phragmites australis* subsp. *americanus*), the Eurasian lineage of *P. australis* was first introduced in the early 19th century and has since expanded throughout the continent (Saltonstall, 2002; Meyerson et al., 2010a). The Eurasian lineage has aggressively expanded into native wetlands and altered vegetation communities (Saltonstall, 2002; Meyerson et al., 2010a,b; Kettenring and Mock, 2012). It is now widely considered to be invasive in most wetland ecosystems across North America and especially in tidal marshes, brackish wetlands, salt marshes, and freshwater coastal wetlands (Meyerson et al., 2010a,b; Kettenring et al., 2012).

Invasive *P. australis* has been shown to cause detrimental impacts to native plant biodiversity, the quality of wildlife and fish habitat, and sedimentation rates (Lambert et al., 2010; Dibble et al., 2013; Wails et al., 2021). While in its native European range, *P. australis* reedbeds support a variety of specialized bird species (Poulin et al., 2002; Battisti et al., 2020), there is little evidence to suggest that invasive *P. australis* provides habitat for these species in North America (Benoit and Askins, 1999; Robichaud and Rooney, 2017; Tozer and Mackenzie, 2019). In addition, human development has exacerbated the spread of *P. australis*; its invasions are often associated with the soil denudation, nutrient enrichment, and hydrologic alteration caused by anthropogenic activities (Saltonstall, 2002; Kettenring et al., 2011; Mozdzer et al., 2013; Long et al., 2017b). For these reasons, the management of *P. australis* has become a priority for conservation practitioners in many wetlands (Hazelton et al., 2014; Long et al., 2017a).

Managing to control or eradicate *P. australis* is notoriously challenging (Hazelton et al., 2014; Long et al., 2017a). As a rhizomatous grass, *P. australis* can propagate both clonally as an underground network of rhizomes and via seeds resulting in rapid expansion from a local source (Kettenring et al., 2011; McCormick et al., 2016; Minchinton and Bertness, 2023). Early detection and rapid response (EDRR) efforts to control small patches (i.e., seed source patches) followed by efforts to slow expansion of increasingly larger patches is likely to lead to the most effective management across the landscape (Long et al., 2017a, Quirion et al., 2018; Rohal et al., 2019a). Numerous methods have been developed for treating *P. australis* with herbicides including hand-wiping, backpack spraying, and aerial spraying and with non-chemical approaches such as mowing, burning, and grazing (Hazelton et al., 2014; Samiappan et al., 2017; Volesky et al., 2017). However, while some methods may effectively control *P. australis* in the short term, a lack of monitoring and continuous follow-up treatments may result in reemergence of *P. australis* 2–3 years after the original control efforts (Lombard et al., 2012; Hazelton et al., 2014). Therefore, effectively managing *P. australis* to recover preferred wetland plant communities may be expensive to achieve over long time frames (Rohal et al., 2019a,b, 2023). A better understanding of the distribution of *P. australis* and the mechanisms that control its spread is necessary to improve management of this invasive species and to reduce its negative effects.

With advancements in the quality of aerial imagery and spatial analyzes, remote sensing has emerged as a valuable tool for studying and monitoring plant invasions (Samiappan et al., 2017; Abeysinghe et al., 2019; Paz-Kagan et al., 2019; Royimani et al., 2019). Recent images collected by satellites, aircraft, or unmanned aerial vehicles (UAVs) can be used to generate coverages for landscapes at a very high (<1-meter) resolution. Furthermore, remotely-sensed imagery provides a unique opportunity to examine historical landscapes and to detect changes, even where ground data are unavailable or costly (Andrew and Ustin, 2009). Covariates derived from remote-sensing imagery can be used to identify plant communities or particular species of interest with high accuracy (Andrew and Ustin, 2009; Samiappan et al., 2017; Abeysinghe et al., 2019; Paz-Kagan et al., 2019; Tadros et al., 2020). For example, Samiappan et al. (2017) used texture analysis to classify *P. australis* in the wetlands of Louisiana with an average accuracy of 85%, while in northern China invasive *Spartina alterniflora* was identified to a similarly high degree of accuracy (87–100%; Okoye et al., 2020). These classifications can then be used to target management efforts and reduce non-native plant invasions to improve overall ecosystem health (Abeysinghe et al., 2019; Tadros et al., 2020). Classifications of non-native plant species further provide the ability to follow EDRR principles and detect biological invasions early, providing managers with a better opportunity to eradicate or control the problem (Huang and Asner, 2009; Bradley, 2014).

While previous research has used aerial or satellite imagery to classify *P. australis* and other co-occurring vegetation in other regions of the United States (Rice et al., 2000; Philipp and Field, 2005; Samiappan et al., 2017; Long et al., 2017b; Abeysinghe et al., 2019), little effort has been directed at measuring the invasion of *P. australis* in Suisun Marsh in the upper reach of the San Francisco estuary, the largest contiguous brackish marsh on the Pacific coast of the continental U.S. Suisun Marsh is recognized as an important wetland for regional biodiversity supporting many endemic species of wildlife and plants and as an important migratory stopover for waterbirds along the Pacific Flyway (Moyle et al., 2014). A comprehensive understanding of the trajectory of the *P. australis* invasion in Suisun Marsh is especially crucial in light of the impending threats of sea-level rise that may further degrade natural resources in this region (Takekawa et al., 2006; Thorne et al., 2018). Native plants may struggle to tolerate increased inundation and salinity caused by sea-level rise, providing an opportunity for *P. australis* invasion and expansion (Patger et al., 2005; Touchette et al., 2007; Eller et al., 2017).

Our primary objective was to estimate the magnitude, distribution, and potential mechanisms of *P. australis* spread in Suisun Marsh. Thus, we used publicly available aerial imagery to conduct a historical analysis of the distribution and spread of *P. australis* in Suisun Marsh over two decades from 2003 to 2020. We used an iterative machine-learning approach (Breiman, 2001; Cutler et al., 2007) to compare patches of *P. australis* and non-*P. australis* and to generate an estimate of the changing extent of *P. australis*. We also compared the distributions generated with our method compared with those estimated with a manual classification approach to see if our models produced similar or higher accuracies.

2. Methods

2.1. Study area

We examined the historic spread of *P. australis* in the 46,950-ha brackish Suisun Marsh located on the upper reach of the San Francisco estuary in northern California, United States (38.1475 N, −122.0053 W). The region provides crucial habitat for over 200 bird species, 45 mammal species, and a wide variety of native plants (CDFW, 2023). These species include the endangered salt marsh harvest mouse (*Reithrodontomys raviventris*) and the endemic Suisun thistle (*Cirsium hydrophilum* var. *hydrophilum*). It also serves as an important nursery for several fishes in the San Francisco estuary, such as the critically endangered delta smelt (*Hypomesus transpacificus*) and endangered runs of Chinook salmon (*Oncorhynchus tshawytscha*). Ownership and management of wetlands involves a mix of public, private, and nonprofit landowners (CDFW, 2011).

There are two major types of wetlands in Suisun Marsh (Figure 1): *managed wetlands* that are surrounded by levees with water infrastructure controlling the timing and duration of applied water, and *tidal wetlands* that are open to the influence of the mixed diurnal tides resulting in twice-daily high and low tides differing in height by up to 2 m (CDFW, 2011). Most of the land parcels are managed wetlands with vegetated tidal berm areas on the exterior side of levees, although in the recent past, several parcels have been restored to tidal wetlands to benefit fish. Private landowners primarily oversee managed wetlands to support waterfowl habitat during the winter months, a traditional land use practice that was established in the late 1800s (Arnold, 1996). The area has been protected by state law since 1977, and recent goals for the region established in the Suisun Marsh Habitat Management, Preservation, and Restoration Plan EIR/EIS (CDFW, 2011) have included enhancing 16,000–20,000 ha of managed wetlands and restoring 2,000–3,000 ha of tidal wetlands.

While the exact timing of the invasion is unknown, it is believed that non-native *P. australis* was introduced to Suisun Marsh about 50–60 years ago. Historic reports and vegetation survey results do not mention *P. australis* until after the 1970s, but the species was not a dominant plant reported in the region at that time (Simpson and Baruth, 1966). The invasion was still not considered to be extensive as recently as 20 years ago when *P. australis* was found only occasionally in brackish marshes of the region (Chambers et al., 1999). The dramatic expansion of *P. australis* in the estuary is therefore a recent

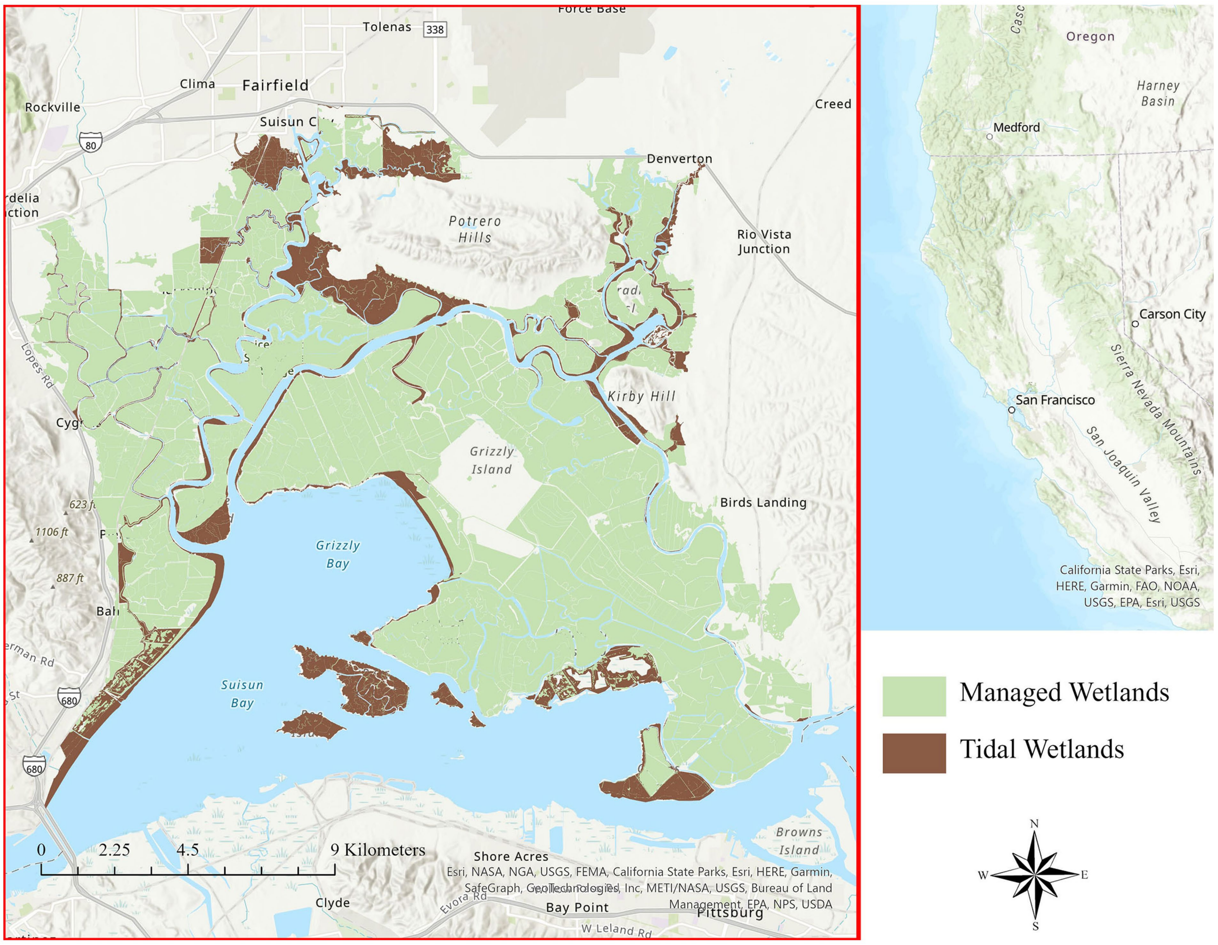

FIGURE 1
Suisun Marsh in the upper San Francisco estuary of northern California, United States. The location of Suisun Marsh in central California is indicated by the red square on the right inset map. Managed wetlands are shaded green, and tidal wetlands are brown. There are an estimated 20,562 hectares of managed and tidal wetlands in Suisun Marsh.

phenomenon. Thus, while it remains a possible that some native *Phragmites australis* subsp. *americanus* are found Suisun Marsh (B. Grewell, pers. comm.), the majority of the species in the region are considered to be the invasive Eurasian lineage (Saltonstall, 2002).

2.2. Random forest classifications

We obtained aerial imagery from 2003 to 2020 taken under the National Agriculture Imagery Program (NAIP) of the U. S. Department of Agriculture. In California, these images were collected every 3 years from 2003 to 2009 and every 2 years from 2010 to the present. NAIP flights are typically conducted from early April to mid-August with most images of Suisun Marsh collected in May (2012, 2016, 2020) or June (2003, 2006, 2009, 2014). The exception to this timing was in 2018 when images were taken in July. Aerial imagery obtained just before peak growth season (late-spring to early-summer in Suisun Marsh) may allow for early detection of *P. australis* (Abeysinghe et al., 2019) which would be helpful to promote a rapid response (Reaser et al., 2020); however, *P. australis* does not reach its peak growth until the late summer (Rice et al., 2000; Engloner, 2009), and new growth may not be detected until the subsequent year's images are taken. NAIP images from 2003 and 2006 had a 2-meter resolution and included three color bands: red, blue, and green. From 2009 onwards, NAIP images included an additional band of near infrared (NIR) and were processed at a 1-meter resolution. Therefore, our classifications were built on slightly different image characteristics pre-2009 versus post-2009; however, our preliminary analyzes indicated that these resolution differences were not substantially affecting our classifications.

We generated classifications from aerial imagery spanning eight different years over the past two decades: 2003, 2006, 2009, 2012, 2014, 2016, 2018, and 2020. For each year, representative *P. australis* patches were selected from the image and manually classified (Tadros et al., 2020) to use as a baseline to automate classification of the entire image. *Phragmites australis* often displays a unique, lime-green spectral signature and forms ovular patches (Kettenring et al., 2016; Figure 2). These patches were assumed to be homogeneous polygons of *P. australis*, since the species forms dense monocultures within 1–2 years of its initial invasion (Orson, 1999; Holdredge and Bertness, 2011). Separate polygons were manually selected to serve as "non-*P. australis*" data for the classifications; these polygons were much larger than the *P. australis* polygons and included a wide range of spectral values including those with signatures similar to *P. australis*.

For each classification, the *P. australis* and non-*P. australis* polygons were randomly subset into groups: 70% for training and 30% for validation (Paz-Kagan et al., 2019). Within the *P. australis* training polygons, 3,500 pixels were randomly selected for analysis, and within the validation polygons, 1,500 pixels were selected. Seven thousand pixels were randomly selected for analysis from the non-*P. australis* training polygons, and 3,000 pixels were randomly selected from the validation polygons. This process ensured that we maintained the 70:30 split between training and validation data while including substantially more non-*P. australis* than *P. australis* pixels in our models.

Classifications were built with three color bands for 2003 and 2006 and four bands (color and infrared) for 2009–2020. We also included an additional predictor variable for every year following 2003 which described the distance of every pixel from the nearest *P. australis* pixel classified on the previous image. *Phragmites australis* often spreads rapidly from a source patch (Lathrop et al., 2003; Kettenring et al., 2011, 2016); therefore, we expected that if *P. australis* was present in a given location in 1 year, there was a much greater probability of its presence nearby in the subsequent year. This additional predictor variable was created as a continuous raster in ArcGIS Pro (ESRI, 2019) with the "Euclidean Distance" tool from a shapefile of the previous year's classification (Eq. 1). Covariate values were extracted at each *P. australis* and non-*P. australis* point in R Studio Version 1.2.5033 (R Core Team, 2021; R Studio Team, 2021). We generated models from covariates derived from the publicly accessible imagery to simplify the analysis and make it easier to replicate the classification for continued future monitoring of *P. australis*. We used the equation,

$$
\begin{aligned}
Phrag(t) = {} & red(t) + blue(t) + green(t) \\
& + NIR(t) + Phrag\_Dist(t-1)
\end{aligned} \tag{1}
$$

where, Phrag(t) is the distribution of *P. australis* at time t, red(t), blue(t), green(t), and NIR(t) refer to color and infrared values extracted from NAIP imagery at time t, and Phrag_Dist(t − 1) is the distribution of *P. australis* in the previous classification iteration. We used random forest classifiers (Breiman, 2001; Cutler et al., 2007) built in R to compare the covariate values of *P. australis* points against those of non-Phragmites points. Random forest is a machine-learning model which generates a series of decision trees that each "cast a vote" for the most popular output class based on input vectors (Breiman, 2001; Pal, 2005). We conducted preliminary testing on a variety of other model types including Mahalanobis distance, Maximum Likelihood, and Spectral Angle Mapping (SAM) on the 2020 NAIP imagery; however, random forest produced the highest accuracy metrics and was selected for our analyzes (Supplementary Table S1).

Random forest classifiers were generated using the package "randomForest" (Liaw and Wiener, 2002), and we employed 500 decision trees. To examine the accuracy of our classifiers, we compared the classes predicted by the model against the observed classes for our validation points. This process allowed us to calculate a variety of accuracy metrics including user's accuracy, producer's accuracy, overall accuracy, and Kappa's statistic (Fielding and Bell, 1997; Kraemer, 2015) for all classifications. User's accuracy is calculated for each class separately and describes the proportion of validation points that were correctly classified by the model. Producer's accuracy is similarly calculated for each class separately and measures the proportion of points classified as a class that are truly that class. Overall accuracy describes the percentage of all validation points that were correctly classified by the model. User's, producer's, and overall accuracies are measured on a scale from 0.00 to 1.00 (0–100%). Lastly, Kappa's statistic yields a metric similar to overall accuracy, while accounting for random chance in classification. Kappa's statistic is measured from −1.00 to 1.00 with higher values indicating higher accuracies.

For each year, we ran five random forest models based on a different random selection of training and validation data and averaged the accuracy metrics. The singular random forest model which produced the best accuracy metrics was then used to create a map of predicted *P. australis* each year with the package "raster" in R (version 3.6–11; Hijmans and van Etten, 2012). This process produced

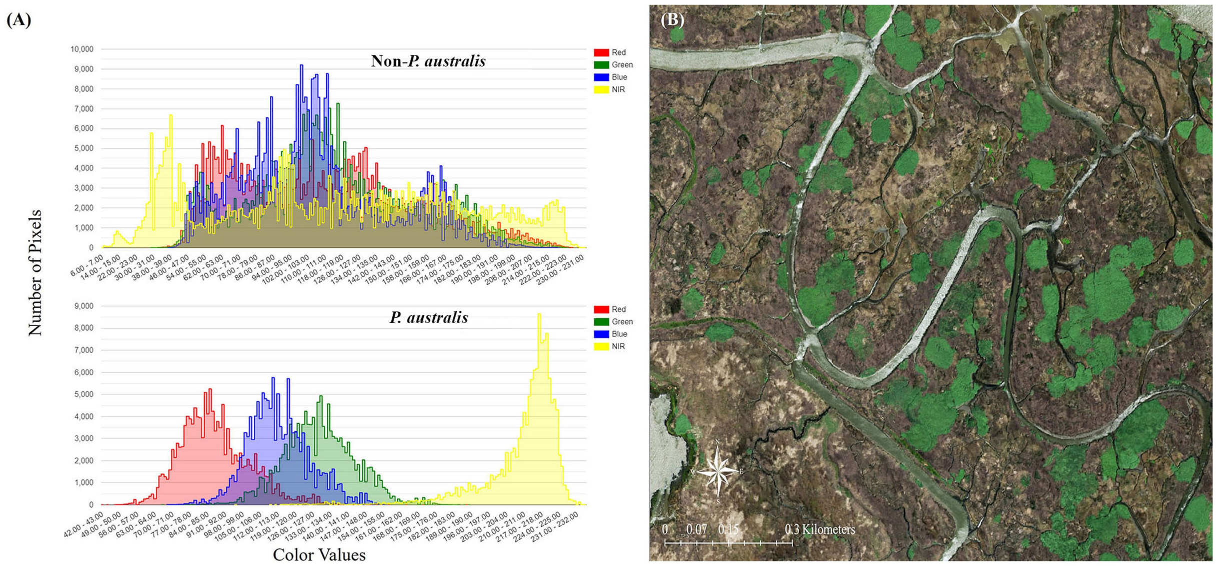

FIGURE 2
(A) Spectral signature of *Phragmites australis* subsp. *australis* and non-*P. australis* patches. Note that *P. australis* displays a unique signature and is visible in a narrow range of red, blue, green, and near-infrared values. **(B)** Distinct, green patches of *P. australis* in Suisun Marsh as they appear in the 2020 National Agriculture Imagery Program (NAIP) imagery.

a 2-meter (2003, 2006) or 1-meter (all other years) resolution raster with values of "1" to represent *P. australis* and "0" to represent non-*P. australis*.

2.3. Assessment of spread in Suisun Marsh

For each classification year, we examined a variety of metrics in ArcGIS Pro to better quantify the spread of *P. australis*. We calculated the hectares of classified *P. australis* for each year for all wetlands, managed wetlands and tidal wetlands, and the magnitude of change between each classification. We also quantified the amount of overlap between *P. australis* from one classification to the previous classification to determine the extent to which established patches persisted. This metric served to describe the spread of *P. australis* as expansion from existing patches compared to new emergent patches.

Since the rate of expansion is considered an important component of invasion (Kettenring et al., 2016), we calculated it on six representative patches distributed throughout the region that were present in both 2003 and 2020 (Figure 3). These patches needed to be spatially distinct from each other and unconfined by natural or anthropogenic barriers that could inhibit growth (i.e., roads or upland edges). We chose to measure perimeter expansion, rather than area expansion, following the methods described in Philipp and Field (2005). While generally ovular, *P. australis* patches can display irregular shapes, and we generated ellipses for each patch in each classification year to reconcile this issue. We found that the area and semi-major axis of these ellipses matched those of their respective patches as calculated in ArcGIS Pro, and a perimeter expansion rate (in meters/year) could be calculated from these ellipses by averaging the increase or decrease in both the semi-major and semi-minor axes and dividing by the number of years between classifications.

2.4. Comparison to VegCAMP manual classification

We examined the efficacy of our random forest models in classifying *P. australis* against a manual classification of the Suisun Marsh plant communities established in 1999 to detect change in habitats of the endangered salt marsh harvest mouse (CDFW, 2011; Askim et al., 2022). The Vegetation Classification and Mapping Program (VegCAMP) was established by the California Department of Fish and Wildlife to provide a vegetation mapping standard for the state (Askim et al., 2022). Observers manually identify plant associations or species from a mosaic of true-color images collected in the year of interest to create vegetation maps of key areas in California including Suisun Marsh (Askim et al., 2022).

VegCAMP maps have been generated from aerial images of Suisun Marsh taken every 3 years since 2000, and each report documents the vegetation composition that existed 3 years prior (the 2021 VegCAMP release describes the vegetation in 2018, for example). The 3-year or longer delay in providing the vegetation maps has been caused by the extensive manual processing and has been considered to be a shortcoming of VegCAMP, as the outdated information limits its value for ongoing annual vegetation management. Furthermore, VegCAMP plant associations are produced on a relatively coarse scale with the average polygon measuring 0.69 ha and the minimum measuring 0.10 ha (Askim et al., 2022) compared to 1-square meter pixels analyzed with NAIP imagery. Therefore, VegCAMP is unable to identify small, emergent vegetation patches, while remote sensing classifications with NAIP offer a quicker, cheaper, and more accurate method for examining specific vegetation types on a local scale and to guide invasive species management.

We extracted *P. australis* polygons from VegCAMP classifications in ArcGIS Pro by selecting classes labeled *Phragmites australis* from the "NVCSName" attribute. We compared the accuracy of VegCAMP

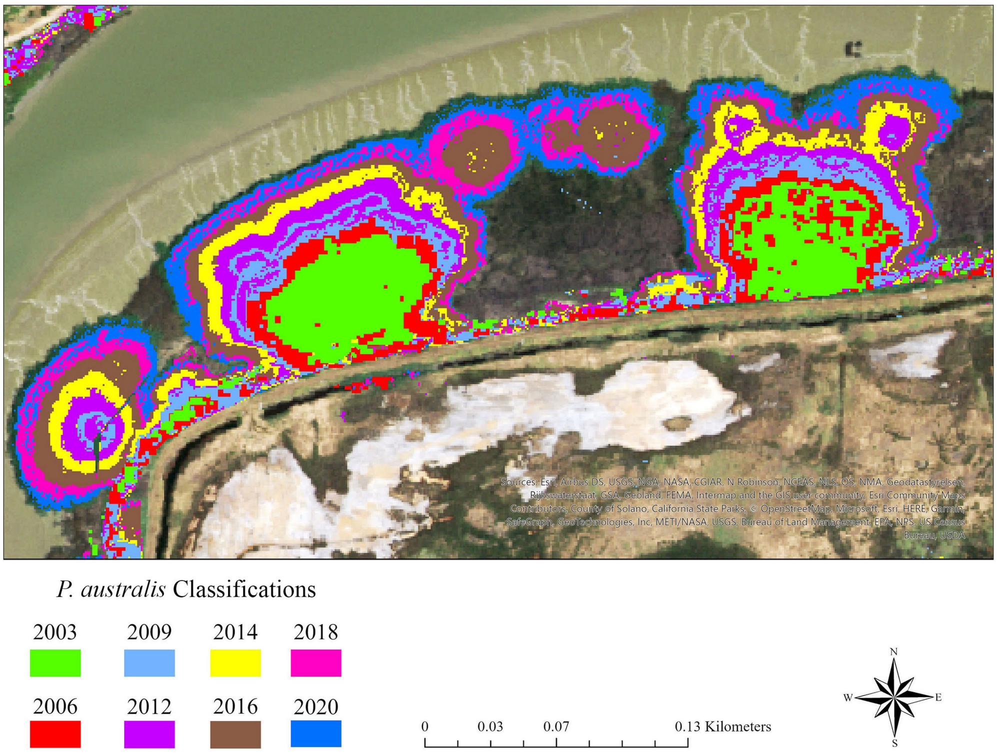

FIGURE 3
Expanding patches of *Phragmites australis* subsp. *australis* on Lower Joice Island, a parcel with both managed and tidal wetlands in Suisun Marsh, upper San Francisco estuary, northern California, United States. The patches are determined from random forest classifications where different colors are associated with different years. The growth in the size of existing patches is likely indicative of growth from spreading rhizomes.

relative to our NAIP classifications by (1) measuring the percent overlap between the two classifications for each year in ArcGIS Pro, and (2) calculating user's, producer's, and overall accuracies from the *P. australis* and non-*P. australis* polygons that we outlined to create our random forest models. Comparisons were made for the 5 years during which VegCAMP and NAIP overlapped in 2003, 2006, 2009, 2012, and 2018.

2.5. Generalized linear mixed models

Management of *P. australis* in Suisun Marsh has been ongoing since 2000 (S. Chappell, pers. comm.); however, the type of management practices allowed depends on the type of wetland (managed or tidal). The Suisun Resource Conservation District (SRCD) leads a *P. australis* control program in Suisun Marsh that was initiated in 2000 to encourage managed wetland landowners to control *P. australis* supported by funds from a foundation grant to subsidize the cost of herbicides for private landowners from 2000 to 2021 (S. Chappell, pers. comm.). Treatment on managed wetlands including herbicide applications is allowed when the marsh plains are drained for maintenance work during the mid-summer (July–September). However, treating *P. australis* with herbicides is not allowed on tidal wetlands to protect rapid dispersal into the estuarine waters, and most non-chemical methods are restricted in tidal wetlands to protect endangered species habitat. Therefore, land parcels that include areas open to tides often have source populations of *P. australis* that are essentially untreatable. In addition, Suisun Marsh is comprised of a mixture of both public and private landowners who make management decisions independently (Figure 4), and *P. australis* management may therefore differ greatly between neighboring land parcels.

To examine the effect of these management differences for managed and tidal wetlands, we generated generalized linear mixed models in R. We assessed the relationship between *P. australis* growth on wetland parcels with both managed and tidal areas or on wetland parcels with neighboring parcels with *P. australis*. The within-parcel models were excluded if they did not contain *P. australis* at any point between the first and last image. We used the change in area of *P. australis* on managed areas for each parcel between classification iterations as a response variable, the change in area of *P. australis* in tidal areas between classifications and parcel size as fixed effects, and year as a random effect.

For the neighboring parcel models, we included land parcels which directly shared a border with at least one other parcel that contained *P. australis* between the first and last image. Also, island parcels or those separated by sloughs or other sources of permanent water were not included. We used the change in the area of *P. australis* in managed areas for each parcel between classifications as a response variable. We included the change in area of *P. australis* in managed areas and tidal areas in neighboring parcels as fixed effects. The number of neighbors was also treated as a fixed effect, while year was considered a random effect. Neighbor statistics were calculated in ArcGIS Pro using the "Neighborhood Summary Statistics" tool.

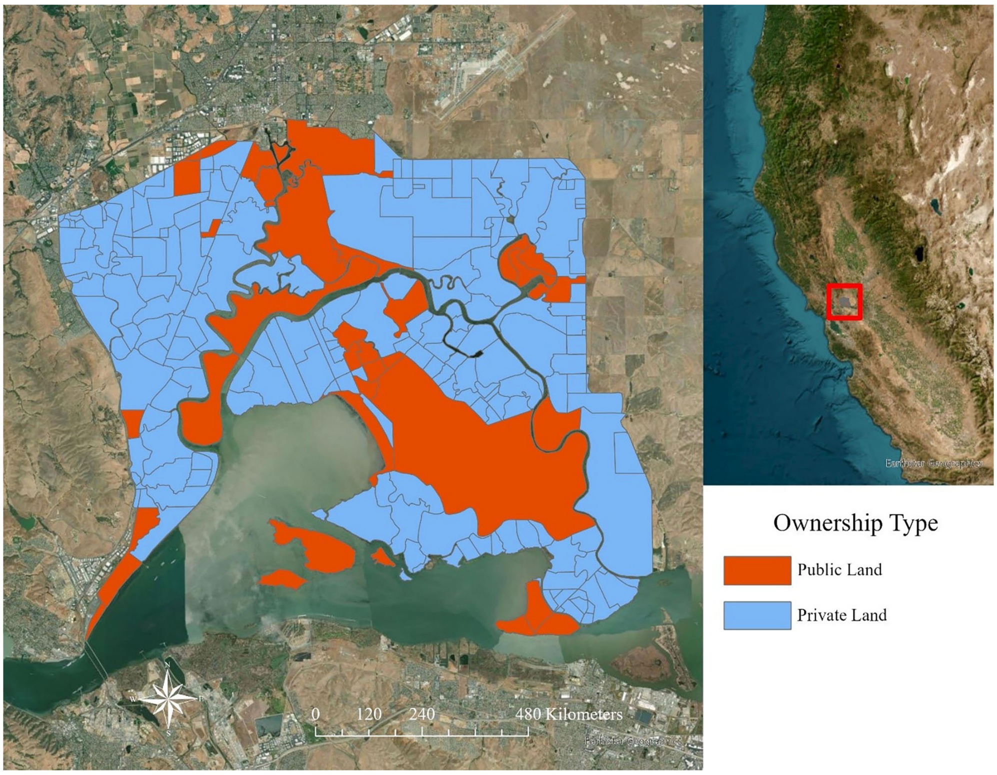

FIGURE 4
Ownership of land parcels in Suisun Marsh, upper San Francisco estuary in northern California, United States. Public lands are displayed in orange and private land parcels (including nonprofits) are shown in blue.

Before running any models, we tested for collinearity between covariates using Pearson's correlation test (Benesty et al., 2009; Sedgwick, 2012; Supplementary Table S2). After running our models, we employed a likelihood ratio test (package "lmtest"; Zeileis and Hothorn, 2002) to compare the full model with all covariates against a nested model from which each fixed effect was removed to identify the influence of individual covariates on *P. australis* expansion in managed areas. Models were processed using the "lme4" package (Bates et al., 2015).

3. Results

3.1. Random forest classifications

Random forest classifications of the yearly images included in the analysis yielded an average overall accuracy greater than 0.90 (Table 1). For *P. australis*, user's accuracy was >0.90 for all years except for 2006 (0.85); producer's accuracy was 0.90 for all years but 2003 (0.85) and 2006 (0.73). All classifications produced user's and producer's accuracies for non-Phragmites that was >0.90 and consistently >0.95 (Table 1).

3.2. Assessment of spread in Suisun Marsh

In 2003, 463 ha of Suisun Marsh were classified as *P. australis*, but by 2020, 980 ha were classified as *P. australis* (a 112% increase over 17 years; Figure 5). *Phragmites australis* peaked in 2018, with 1,547 ha classified as the invasive species (a 234% increase over 15 years; Figures 5, 6). The largest areal increase between classification years occurred between 2016 and 2018 (+392 ha); the largest percentage increase occurred between 2014 and 2016 (+35%). The areal extent of *P. australis* increased from the previous year except for in 2 cases: 2009 to 2012 (13% decrease) and 2018 to 2020 (37% decrease; Figure 5). With a total of about 20,560 ha of wetlands in Suisun Marsh, the 2020 classification indicated that 5% are covered by *P. australis* with a peak of 8% in 2018 compared with an initial estimate of 2% in 2003. We classified 271 ha of *P. australis* in managed wetlands and 191 ha in tidal wetlands in 2003 (Figure 6). At its peak in 2018, *P. australis* had expanded in managed wetlands by 721 ha (+266%), and by 364 ha in tidal wetlands (+190%).

The perimeter expansion of six representative *P. australis* patches averaged 1.32 m/year (± 0.53 SD) over 17 years. Expansion of patch perimeters ranged from a mean of 0.50 to 2.19 m/year Mean perimeter expansion was highest between 2012 and 2014 (2.19 ± 1.25 m/year) and lowest between 2018 and 2020 (0.61 ± 0.84 m/year; Figure 7). The largest expansion rate for a single *P. australis* patch between two classification years was 4.03 m/year (2012 to 2014); the lowest was −1.31 m/year (2010 to 2012; Figure 7).

3.3. Comparison to VegCAMP manual classification

VegCAMP manual classifications yielded accuracy metrics >0.90 for all years except 2003 (Table 2). The percent overlap between VegCAMP and random forest classifications presented here consistently increased from a low of 19% in 2003 to a maximum of 79% in 2018 (Table 2). In 2003, VegCAMP analyzes estimated 314 ha

TABLE 1 Accuracy metrics for random forest classifications of *Phragmites australis* subsp. *australis* in Suisun Marsh.

Metric	2003	2006	2009	2012	2014	2016	2018	2020
P. australis								
User's accuracy	0.96	0.85	0.96	0.88	0.94	0.98	1.00	1.00
Producer's accuracy	0.95	0.73	0.95	0.92	0.96	0.97	0.97	0.95
Non-*P. australis*								
User's accuracy	0.97	0.93	0.97	0.95	0.98	0.99	0.98	0.98
Producer's accuracy	0.99	0.96	0.98	0.94	0.97	0.99	1.00	1.00
Overall accuracy	0.97	0.92	0.97	0.93	0.97	0.99	0.99	0.98
Kappa statistic	0.90	0.73	0.93	0.84	0.92	0.97	0.97	0.96

Metrics are an average of five model iterations, each built and tested on a different random subset of data. User's, producer's, and overall accuracies are proportions ranging from 0.0–1.0 with higher values indicating a greater accuracy. The Kappa statistic controls for random chance in classifications and can range from −1.0 to 1.0 with higher values indicating a greater accuracy.

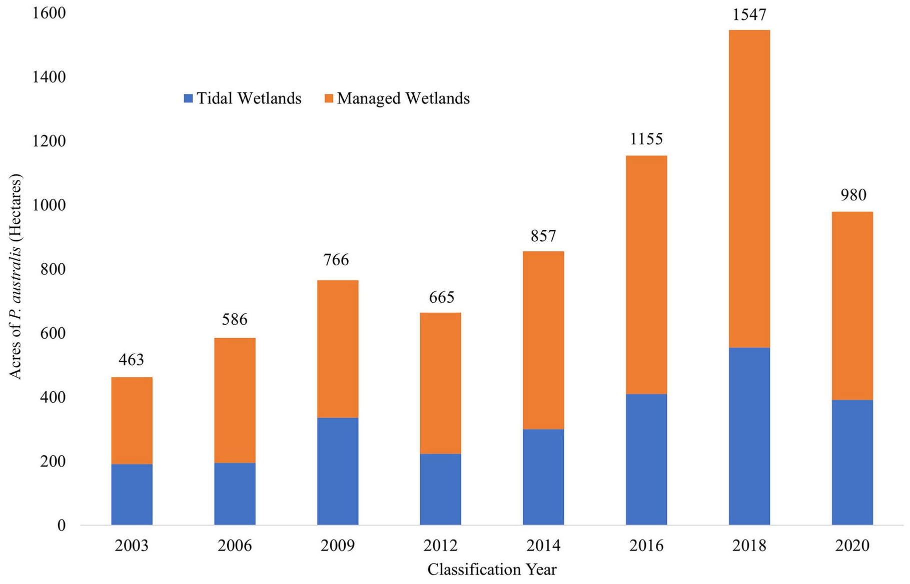

FIGURE 5
Estimated change in area of *Phragmites australis* subsp. *australis* between 2003 and 2020 as classified by random forest models. Columns are partitioned by wetland type: managed wetlands (orange) are surrounded by levees and have water control structures to regulate flooding and draining, while tidal wetlands (blue) are open to tidal waters which includes two mixed, daily semi-diurnal low and high tides. Managed wetlands are maintained during the summer (July–September) after wetlands are drained, while management of tidal wetlands are restricted and must be individually permitted to protect water quality and listed species. Labels above the bars indicate the total estimated area (in hectares) of *P. australis* in all wetlands for each classification year and show an increasing trend of *P. australis* over the past 2 decades.

of *P. australis* in Suisun Marsh while in 2018, VegCAMP analyzes estimated 1,739 ha (a 453% increase).

3.4. Generalized linear mixed models

We analyzed 227 land parcels of varying size (137 ha ± 274) in Suisun Marsh, and of those, 186 had *P. australis* at some point during the study period. During this time frame, one third of parcels (61, 33%) showed a decrease in *P. australis* on their managed areas. For the within-parcel analysis, we included 167 parcels that possessed both managed and tidal areas within their boundaries. The change in area of *P. australis* in tidal areas within a parcel had a statistically significant effect ($p < 0.01$) on the change in *P. australis* in the managed areas of the same parcel. Change in area of *P. australis* increased with increasing parcel size, but the effect was not significant ($p = 0.06$; Table 3).

Our adjacent neighbor models included 178 parcels that shared a border with at least one other parcel and that had *P. australis* between 2003 and 2020. The number of adjacent neighbors ranged from 1 to 16, with a mean of 4.3 (± 2.2). Increasing *P. australis* in both tidal and managed wetlands of adjacent neighboring parcels had a significant effect associated with the change in area of *P. australis* in managed areas as did the number of adjacent neighbors (Table 4).

4. Discussion

Understanding the historical expansion of *P. australis* as well as potential mechanisms that promote its growth may help landowners and conservation practitioners implement effective management plans to combat its continued spread (Meyerson et al., 2010a,b; Hazelton et al., 2014; Long et al., 2017b). We used publicly accessible NAIP

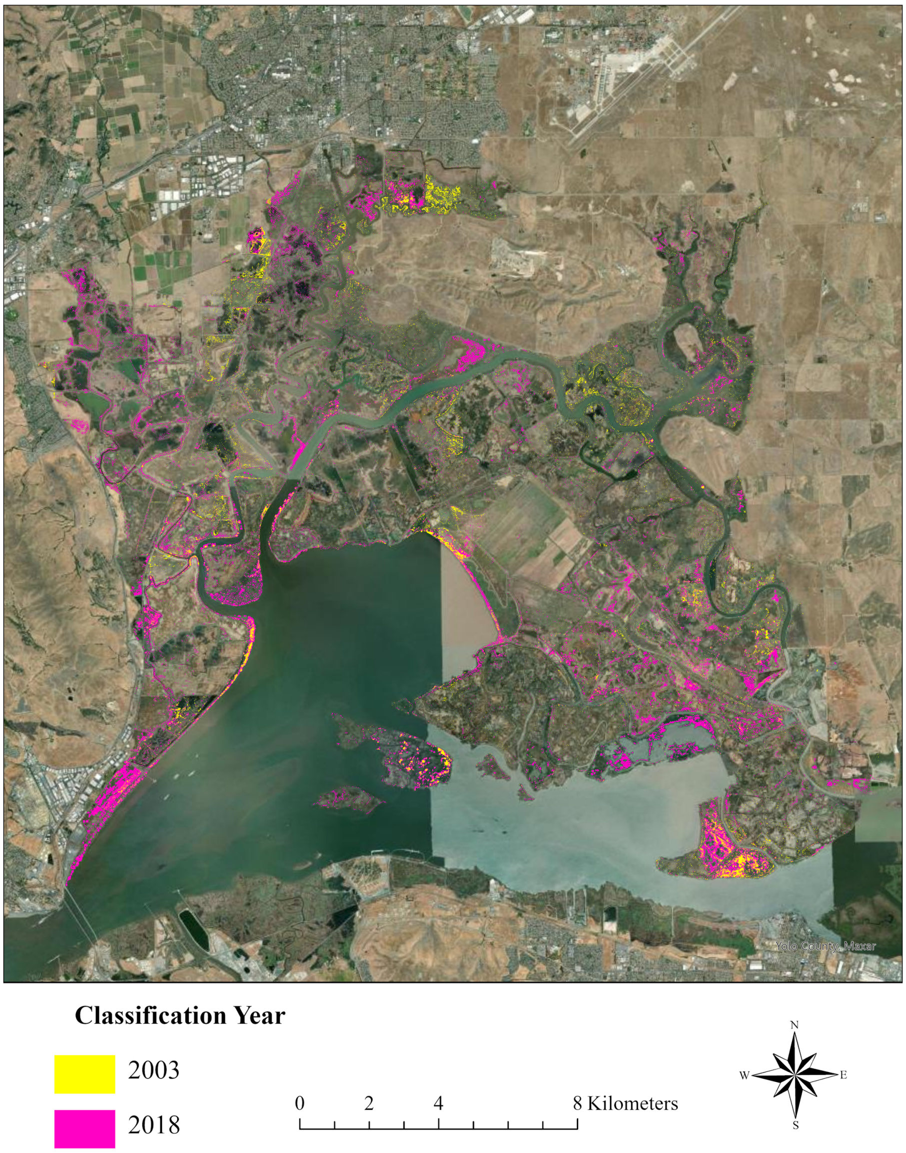

FIGURE 6
Expansion of *Phragmites australis* subsp. *australis* in Suisun Marsh, upper San Francisco estuary, northern California, United States from the first classification year (2003, lime green) to the most recent peak extent in 2018 (pink). We estimated 463 hectares of Phragmites in 2003, which expanded to a peak in 2018 (1,547 hectares; 234% increase).

imagery to create a simple, replicable, but highly accurate classification for *P. australis* to document the historical expansion of the invasion. Our results indicated that *P. australis* has expanded substantially in the region over the past two decades despite extensive management efforts to control it. We also found that *P. australis* expansion in managed wetland areas in Suisun Marsh may be related to the extent of invasion in tidal areas within the same parcel or in neighboring parcels of managed or tidal wetlands.

4.1. National Agriculture Imagery Program (NAIP) classifications and the expansion of *Phragmites australis* in Suisun Marsh

The results produced by our classification models highlighted the challenges of managing an invasive species over large temporal and geographic scales. *Phragmites australis* has increased substantially and consistently in Suisun Marsh over the past 2 decades, and the 234% increase in *P. australis* extent or 16%/year rate was greater or more rapid than results published from other ecosystems (Wilcox et al., 2003; Philipp and Field, 2005; Ji et al., 2009). In Lake Erie, a 152% increase in *P. australis* was reported between 1945 and 1999 (3%/year, Wilcox et al., 2003), and a 242% expansion was estimated in the Liahoe Delta of China between 1953 and 2006 (5%/year, Ji et al., 2009). Similarly, the perimeter expansion rate of *P. australis* in wetland ecosystems has varied considerably (Burdick et al., 2001; Philipp and Field, 2005; Fussell et al., 2015; Kettenring et al., 2016), but the mean perimeter expansion rate estimated here (1.32 m/year) was higher than most other estimates in the literature. For example, In the wetlands of Delaware and Maine, *P. australis* perimeter expansion was calculated at a mean of 0.91 and 0.70 m/yr (Philipp and Field, 2005; Fussell et al., 2015).

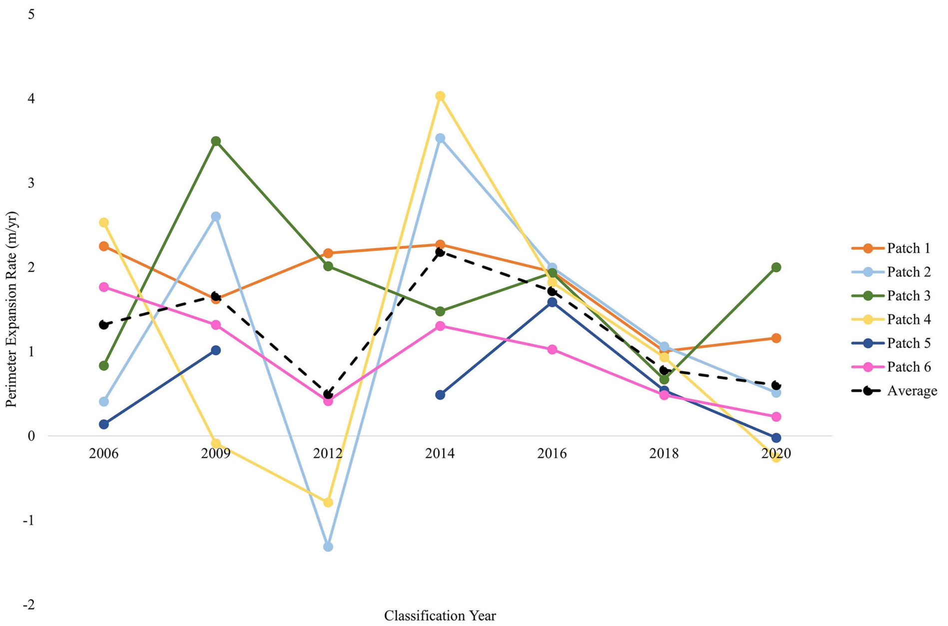

FIGURE 7
Perimeter expansion rates for six representative *Phragmites australis* subsp. *australis* patches distributed across Suisun Marsh shows consistent increases in the growth of patches. The perimeter expansion was calculated from 2006 to 2020 and indicated a consistent rate of linear increase that would result in an exponential increase in area. The average expansion rate of the six patches is displayed by a black dashed line. Data was unavailable for Patch 5 (dark blue) in 2012.

TABLE 2 Accuracy and comparison metrics for VegCAMP manual classifications of *Phragmites australis* subsp. *australis*.

Metric	2003	2006	2009	2012	2018
P. australis extent					
NAIP (hectares)	463	586	766	665	1,547
VegCAMP (hectares)	314	460	739	1,006	1738
Overlap (hectares)	89	119	253	373	1,226
Overlap (percent; relative to NAIP)	19	20	33	56	79
VegCAMP *P. australis*					
User's accuracy	0.79	0.77	0.94	0.97	0.99
Producer's accuracy	1.00	1.00	1.00	0.97	1.00
VegCAMP Non-*P. australis*					
User's accuracy	1.00	1.00	1.00	0.99	1.00
Producer's accuracy	0.96	0.94	0.97	0.99	1.00
VegCAMP overall accuracy	0.97	0.95	0.98	0.98	1.00

Metrics were calculated only for years in which VegCAMP and NAIP overlap. User's, producer's, and overall accuracies are proportions ranging from 0.0–1.0, with higher values indicating a greater accuracy. The Kappa statistic controls for random chance in classifications, and can range from −1.0 to 1.0, with higher values indicating a greater accuracy.

The patch expansion rate that we estimated combined with a larger and more rapid increase in *total* area suggests that our brackish study site may be particularly susceptible to the invasive *P. australis* growth and expansion. Previous studies have shown that the species is especially adept at invading disturbed areas, and its detrimental impact is aggravated by anthropogenic activities (Saltonstall, 2002; Mozdzer et al., 2013; Hazelton et al., 2014; Kettenring et al., 2015). Wide variation in annual precipitation in this Mediterranean climate region may likewise play a role in the *P. australis* expansion reported in this study. Average perimeter expansion of *P. australis* patches was highest in 2014 (2.19 m/yr) a drier period regionally, and lowest in 2012 (0.50 m/yr) during a comparatively wetter period (California Nevada River Forecast Center, National Ocean and Atmospheric Administration). *Phragmites australis* may therefore be able to withstand, if not thrive, in years of water deficit (Patger et al., 2005; Touchette et al., 2007), as it has been shown to rapidly expand in extreme low-water conditions elsewhere (Eller et al., 2017).

Other classification types, including object-based classification, texture analysis, and hyperspectral classification, have been used to model the distribution of *P. australis* (Arzandeh and Wang, 2003;

TABLE 3 Likelihood ratio tests indicated that increases in growth of *Phragmites australis* subsp. *australis* in managed areas were related to change in area of *P. australis* in tidal areas on the same land parcels between two subsequent iterations of our random forest classifications.

Model	DF	Chi-Sq	Value of *p*
Full (all covariates)	5	---	---
Change in tidal *P. australis*	4	52.0	<0.01
Parcel size	4	3.6	0.06
Null (no fixed effects)	3	56.5	<0.01

The response may have been related to parcel size, but the effect was not significant. Classification year was included as a random effect. All model comparisons were made relative to the full model.

TABLE 4 Results of likelihood ratio tests assessing the effect of change in area of *Phragmites australis* subsp. *australis* in managed and tidal areas of adjacent neighboring land parcels on the change in area of *P. australis* in managed areas on a given parcel between two subsequent iterations of our random forest classifications.

Model	DF	Chi-Sq	Value of *p*
Full (all covariates)	6	---	---
Change in neighbors' tidal *P. australis*	5	13.8	<0.01
Change in neighbors' managed *P. australis*	5	5.45	0.02
Number of neighbors	5	53.2	<0.01
Null (no fixed effects)	3	74.6	<0.01

Classification year was included as a random effect. All model comparisons were made relative to the full model.

Pengra et al., 2007; Samiappan et al., 2017; Abeysinghe et al., 2019). These previous efforts have consistently yielded accuracies over 0.80 but rely on more expensive methods of data collection (Abeysinghe et al., 2019). The accuracies produced from NAIP imagery were generally higher (> 0.90) and provide a more replicable and cost-effective option for wetland managers interested in monitoring *P. australis* distributions in the future (Walter and Mondal, 2023). Similarly, the use of publicly available imagery to create our classification will remove a barrier to continuous and long-term monitoring of the invasive species (Walter and Mondal, 2023). The ability to effectively monitor *P. australis* in the long term has shown to be critical in successfully managing the invasive species, but logistical and financial constraints are among the strongest deterrents to long-term monitoring (Hazelton et al., 2014; Long et al., 2017a; Quirion et al., 2018). Having a simple, replicable, and highly accurate classification model, is therefore valuable to ensuring future monitoring and successful control of *P. australis*. Managers interested in assessing the distribution or expansion of any invasive species should consider using publicly-available imagery like NAIP where applicable.

4.2. Remote sensing and manual classification accuracy: the potential for informing management

Our results on *P. australis* expansion generally agreed with results from the lengthy manual classification method conducted under VegCAMP. While VegCAMP may provide the accurate distribution of large *P. australis* patches, the size of the polygons analyzed limits its ability to identify small, emergent patches. This finding is further reinforced by the increased percent overlap between our random forest classifications and the VegCAMP analyzes. As *P. australis* patches become pervasive and more established, the overlap between the two classifications became larger (~80% in 2018).

In contrast to VegCAMP, our classifications built with remote sensing imagery can be generated in days, yield comparatively high accuracy metrics, and have the potential to effectively locate not only large patches but also emergent *P. australis* growth to support EDRR management (Huang and Asner, 2009; Bradley, 2014). The use of publicly available imagery also provides a much cheaper alternative to VegCAMP which costs 10 to over a hundred thousand dollars for each iteration (R. Klingonsmith, Department of Water Resources, pers. comm.). Finally, the rapid processing time of our classification allows better adaptive management to identify and target new invasions in real time (Huang and Asner, 2009; Bradley, 2014).

Despite the high accuracies produced by all of our classification iterations, certain shortcomings may be present. During its primary growth season, *P. australis* displays a distinct bright green signature and clusters of the invasive tend to form large, ovular patches (Kettenring et al., 2016). The classifications produced here were built upon these features; however, *P. australis* patches can demonstrate other visual characteristics. Before annual growth commences or toward the conclusion of its annual lifespan, *P. australis* patches may appear brown or beige (Figure 8). These brown marcescent patches can be difficult to distinguish and isolate given their visual similarity to a variety of other plants.

Similarly, annual precipitation varies considerably in this system, and in drier years *P. australis* biomass may be less visibly apparent despite its continued presence. *Phragmites australis* in Suisun Marsh increased steadily from 2003 to 2018 before dropping almost 50% between 2018 and 2020. This dramatic decrease could be attributed to precipitation in the rainy season preceding the 2 years which affected their color rather than an actual reduction in *P. australis*. October 2016–April 2018 yielded 145.8 cm of rain, while October 2018–April 2020 yielded just 114.6 cm (California Nevada River Forecast Center, National Ocean and Atmospheric Administration).

Also, other variation among years could have affected the results of our classification. The 2018 NAIP imagery was collected in July (all other years were collected in May or June), and biomass of *P. australis* is likely greatest later in the summer (Rice et al., 2000; Engloner, 2009). Ideally, classifications targeting *P. australis* or plants which grow through the summer would use aerial imagery taken at the end of the peak growing season. In addition, *P. australis* can be affected by the annual management of water in managed wetlands (Rohal et al., 2019a). Year-to-year changes occur when landowners flood or drain their land parcels with leach cycles to reduce soil salinities on different schedules depending on the availability and water quality (salinity) of applied water. It may affect when and how long the *P. australis* growth season occurs and when *P. australis* is most visible from the air. Recognizing the limitations in classifying *P. australis* from aerial imagery is crucial for interpreting the distribution maps presented here and for creating management plans based on the findings.

The unique spectral signature of healthy *P. australis* allowed for the development of a highly successful classification based primarily on color attributes. Unfortunately, the historical nature of this study limited our ability to include ground-truthing data for the NAIP data.

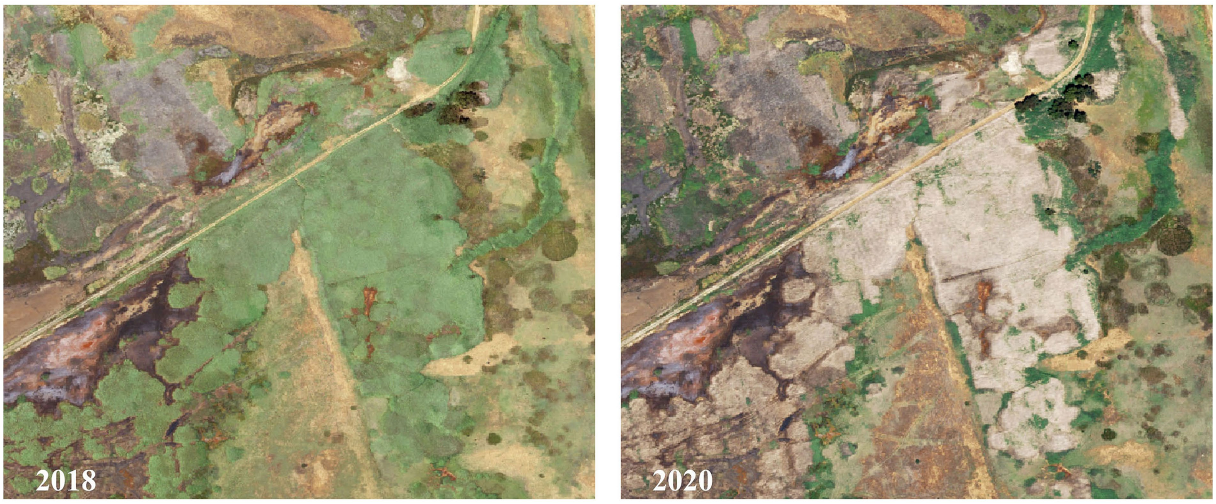

FIGURE 8
Effects of drought or seasonality on the visualization of *Phragmites australis* subsp. *australis* in Suisun Marsh, upper San Francisco estuary, northern California, United States. Vibrant, green patches of *P. australis* (2018) may appear as senesced and brown (2020) in drier years or earlier in the growing season. Our models were not trained to identify brown patches of *P. australis*.

We encourage scientists and wetland managers to employ ground-truth data to support the remote-sensing classifications when possible. The manual selection of training and validation *P. australis* polygons with aerial images can introduce human error and biases, and while we are confident that the polygons selected for our classifications were *P. australis*, ground-truth data would confirm our assessment. With adequate planning, the polygons used for classification could be outlined in the field to provide a more accurate training and validation data set for models. Ground-truth data also is valuable to better identify very small and emergent patches of *P. australis* ($<5\,m^2$) that would benefit remote-sensing classifications (Huang and Asner, 2009; Bradley, 2014) and allow implementation of EDRR management practices. Ground-truth data are best collected in the field concurrently with aerial imagery flights to ensure that temporal mismatches in phenology are avoided.

4.3. Drivers of *Phragmites australis* expansion and management implications

Control of *P. australis* in Suisun Marsh has included ground and aerial herbicide spraying, burning, mowing, and disking (S. Chappell pers. comm.). While *P. australis* has spread dramatically over the past two decades despite these efforts, it is important to note that *P. australis* management has not been completely ineffective. Although we lack a database to indicate which specific wetland areas were treated, 61 land parcels showed a decrease in *P. australis* between 2003 and 2020 despite the 111.6% increase in *P. australis* overall. It is likely that without management efforts, the current distribution of *P. australis* would be much more expansive. Instead, our findings reinforce the difficulty in managing a pervasive and highly successful invasive species at a large scale (Kettenring et al., 2011; Hazelton et al., 2014) and the importance of consistent, multi-year treatment programs (Rohal et al., 2019a,b). Innovative solutions may be needed to help reduce the pervasive spread of *P. australis*. For example, advancements in drone technology have produced an effective alternative for treating plant invasions (Shahbazi et al., 2014; Roslim et al., 2021; Takekawa et al., 2023). Small survey drones can shoot high-resolution imagery of small-to-medium geographic areas relatively quickly (Koh and Wich, 2012; Cruzan et al., 2016), after which spray-drones can precisely target invasive plants to treat with herbicides (Martinez-Guanter et al., 2019; Takekawa et al., 2023).

In addition, alternative factors to individual management efforts may influence *P. australis* expansion. Natural processes, such as wildfire, flooding, and drought, may also influence *P. australis* distributions (Thompson and Shay, 1985; Patger et al., 2005; Touchette et al., 2007; Eller et al., 2017) in addition to limiting herbicide effectiveness (i.e., *P. australis* response to herbicide is diminished under drought conditions, Rohal et al., 2019a,b). Also, *P. australis* in Suisun Marsh may be developing a resistance to herbicide, which could contribute to its unrelenting spread. Little is known about *P. australis* and herbicide resistance (Wang et al., 2017; Blossey et al., 2020), but resistance has been demonstrated on a variety of other wetland or aquatic plants, such as *Hydrilla verticillata* and *Agrostis stolonifera* (Bollman et al., 2012; Simberloff and Leppanen, 2019). Such resistance can severely hinder management efforts by failing to kill invasive plants and creating even stronger and more pervasive strains (Peterson et al., 2018).

Our within-parcel model showed that the change in *P. australis* in managed areas was significantly correlated with the change in *P. australis* in tidal areas within the same parcel. Most managed areas are bordered by tidal areas on the exterior side of the levee; *P. australis* in these tidal areas are likely the primary source that spread into the managed wetlands. *P. australis* has been shown to spread 0.5–10 kilometers via seed transmission, and rhizome fragments can spread clonally via water drift (Fér and Hroudova, 2009; McCormick et al., 2016). Continuous monitoring of *P. australis* will help ensure curtail its spread, but long-term monitoring has been expensive and time-consuming (Hazelton et al., 2014; Long et al., 2017a; Quirion et al., 2018). Our classification method that uses NAIP imagery may help to reconcile these issues and provide a simpler way to promote long-term monitoring.

Varying management efforts between adjacent neighboring parcels has also inhibited the overall eradication of *P. australis*. Our results show that the change in *P. australis* over time on managed areas of a parcel was associated with the change in *P. australis* on the tidal and managed areas of neighboring parcels. The number of neighbors bordering a parcel was also a significant factor influencing *P. australis* growth. Our results highlighted the complexity of *P. australis* management in a diverse landscape (Epanchin-Niell et al., 2010). Co-management of invasive species has shown to be a crucial aspect of successful eradication of detrimental plants (Graham, 2019; Graham et al., 2019; Clarke et al., 2021), including *P. australis* management in other regions (Young and Kettenring, 2020). The different ownerships that comprise Suisun Marsh create a landscape in which collaboration is essential to protecting health of the overall ecosystem. There is a clear need for more research on the social aspects of *P. australis* management, including decision-making processes, in order to establish an adaptive and cooperative treatment strategy where neighboring parcels, as well as private and public entities, work together more closely to halt the spread of this disruptive invasive species (Young and Kettenring, 2020; Conrad et al., 2023). Conservation practitioners in similarly complex social-ecological landscapes will need to consider these factors when managing their invasive plants.

Data availability statement

The datasets presented in this study can be found in online repositories. The names of the repository/repositories and accession number(s) can be found at: https://drive.google.com/drive/folders/1mgzlguW8TYEFjExTUrbHVnln9_-euW75?usp=sharing.

Author contributions

JH compiled the data, conducted the statistical and spatial analyzes, and wrote the initial draft of the manuscript. JT conceived of the project, advised the analyzes, and contributed to the writing. SC contributed to developing the project and provided input to the writing. RT contributed to developing the project and writing and review. AE provided support for writing and review. KK contributed to project development and writing and review comments. All authors contributed to the article and approved the submitted version.

Funding

This project was supported by the Suisun Resource Conservation District (SRCD) with funding under a grant (DSC-21005) from the Delta Stewardship Council.

Acknowledgments

The authors appreciate the data and analysis assistance of J. Collins and T. Edmunds (SRCD) and C. Potter (Casa 2100). E. Fintel (CSU Chico) provided 2018 VegCamp analysis results, and M. Levin (Columbia University) offered valuable suggestions for the modeling process. The authors received helpful comments on the draft from Z. Ma and V. Tripuraneni (Purdue University), and V. Matzek (Santa Clara University).

Conflict of interest

The authors declare that the research was conducted in the absence of any commercial or financial relationships that could be construed as a potential conflict of interest.

Publisher's note

Supplementary material

The Supplementary material for this article can be found online at: https://www.frontiersin.org/articles/10.3389/fevo.2023.1171245/full#supplementary-material

References

Abeysinghe, T., Simic Milas, A., Arend, K., Hohman, B., Reil, P., Gregory, A., et al. (2019). Mapping invasive *Phragmites australis* in the old Woman Creek estuary using UAV remote sensing and machine learning classifiers. *Remote Sens.* 11:1380. doi: 10.3390/rs11111380

Andrew, M. E., and Ustin, S. L. (2009). Habitat suitability modelling of an invasive plant with advanced remote sensing data. *Divers. Distrib.* 15, 627–640. doi: 10.1111/j.1472-4642.2009.00568.x

Arnold, T. (1996). *Suisun marsh history: Hunting and saving a wetland*. Monterey Pacific Publishers. Marina, CA. 257.

Arzandeh, S., and Wang, J. (2003). Monitoring the change of Phragmites distribution using satellite data. *Can. J. Remote. Sens.* 29, 24–35. doi: 10.5589/m02-077

Askim, L., Fintel, E., Kreb, B., and Quigley, K.. (2022). 2018 vegetation map update for Suisun marsh Solano County, California. A report to the California Department of Water Resources. *Prepared by Geographical Information Center California State University, Chico*, p, 75.

Bates, D., Mächler, M., Bolker, B., and Walker, S. (2015). Fitting linear mixed-effects models using lme4. *J. Stat. Softw.* 67, 1–48. doi: 10.18637/jss.v067.i01

Battisti, C., Grosso, G., Ioni, S., Zullo, F., and Cerfolli, F. (2020). Response of specialized birds to reed-bed aging in a Mediterranean wetland: significant changes in bird biomass after two decades. *Israel J. Ecol. Evol.* 67, 17–22. doi: 10.1163/22244662-bja10007

Benesty, J., Chen, J., Huang, Y., and Cohen, I. (2009). "Pearson correlation coefficient" in *Noise Reduction in Speech Processing* (Berlin: Springer), 1–4.

Benoit, L. K., and Askins, R. A. (1999). Impact of the spread of Phragmites on the distribution of birds in Connecticut tidal marshes. *Wetlands* 19, 194–208. doi: 10.1007/BF03161749

Blossey, B., Endriss, S. B., Casagrande, R., Häfliger, P., Hinz, H., Dávalos, A., et al. (2020). When misconceptions impede best practices: evidence supports biological control of invasive Phragmites. *Biol. Invasions* 22, 873–883. doi: 10.1007/s10530-019-02166-8

Bollman, M. A., Storm, M. J., King, G. A., and Watrud, L. S. (2012). Wetland and riparian plant communities at risk of invasion by transgenic herbicide-resistant *Agrostis* spp. in Central Oregon. *Plant Ecol.* 213, 355–370. doi: 10.1007/s11258-011-0015-z

Bradley, B. A. (2014). Remote detection of invasive plants: a review of spectral, textural and phenological approaches. *Biol. Invasions* 16, 1411–1425. doi: 10.1007/s10530-013-0578-9

Breiman, L. (2001). Random forests. *Mach. Learn.* 45, 5–32. doi: 10.1023/A:1010933404324

Burdick, D. M., Buchsbaum, R., and Holt, E. (2001). Variation in soil salinity associated with expansion of *Phragmites australis* in salt marshes. *Environ. Exp. Bot.* 46, 247–261. doi: 10.1016/S0098-8472(01)00099-5

CDFW. (2011). *Suisun marsh habitat management, preservation, and restoration plan: Final environmental impact statement/environmental impact report*. California Department of Fish and Wildlife, p. 176.

CDFW. (2023). *Suisun Marsh Atlas*. California Department of Fish and Wildlife. Available at: https://wildlife.ca.gov/Regions/3/Suisun-Marsh/Atlas. (Accessed January 26, 2023).

Chambers, R. M., Meyerson, L. A., and Saltonstall, K. (1999). Expansion of *Phragmites australis* into tidal wetlands of North America. *Aquat. Bot.* 64, 261–273. doi: 10.1016/S0304-3770(99)00055-8

Clarke, M., Ma, Z., Snyder, S. A., and Floress, K. (2021). Factors influencing family forest owners' interest in community-led collective invasive plant management. *Environ. Manag.* 67, 1088–1099. doi: 10.1007/s00267-021-01454-1

Conrad, L. J., Thomas, M., Jetter, K., Madsen, J., Pratt, P., Moran, P., et al. (2023) *Invasive aquatic vegetation in the Sacramento-san Joaquin Delta and Suisun marsh: The history and science of control efforts and recommendations for the path forward*. San Francisco. San Francisco Estuary and Watershed Science.

Cruzan, M. B., Weinstein, B. G., Grasty, M. R., Kohrn, B. F., Hendrickson, E. C., Arredondo, T. M., et al. (2016). Small unmanned aerial vehicles (micro-UAVs, drones) in plant ecology. *Appl Plant Sci* 4:160041. doi: 10.3732/apps.1600041

Cutler, D. R., Edwards Jr,, T. C., Beard, K. H., Cutler, A., Hess, K. T., Gibson, J., et al. (2007). Random forests for classification in ecology. *Ecol.* 88:2783–2792. doi: 10.1890/07-0539.1

Dibble, K. L., Pooler, P. S., and Meyerson, L. A. (2013). Impacts of plant invasions can be reversed through restoration: a regional meta-analysis of faunal communities. *Biol. Invasions* 15, 1725–1737. doi: 10.1007/s10530-012-0404-9

Eller, F., Skálová, H., Caplan, J. S., Bhattarai, G. P., Burger, M. K., Cronin, J. T., et al. (2017). Cosmopolitan species as models for ccophysiological responses to global change: the common reed *Phragmites australis*. *Front. Plant Sci.* 8:1833. doi: 10.3389/fpls.2017.01833

Engloner, A. I. (2009). Structure, growth dynamics and biomass of reed (*Phragmites australis*)–a review. *Flora* 204, 331–346. doi: 10.1016/j.flora.2008.05.001

Epanchin-Niell, R. S., Hufford, M. B., Aslan, C. E., Sexton, J. P., Port, J. D., and Waring, T. M. (2010). Controlling invasive species in complex social landscapes. *Front. Ecol. Environ.* 8, 210–216. doi: 10.1890/090029

ESRI. (2019). *ArcGIS Desktop: Release 10.7*. Redlands, CA: Environmental Systems Research Institute.

Fér, T., and Hroudova, Z. (2009). Genetic diversity and dispersal of *Phragmites australis* in a small river system. *Aquat. Bot.* 90, 165–171. doi: 10.1016/j.aquabot.2008.09.001

Fielding, A. H., and Bell, J. F. (1997). A review of methods for the assessment of prediction errors in conservation presence/absence models. *Environ. Conserv.* 24, 38–49. doi: 10.1017/S0376892997000088

Fussell, S. B., Dionne, M. L., and Theodose, T. A. (2015). Expansion rates of *Phragmites australis* patches in a partially restored Maine salt marsh. *Wetlands* 35, 557–565. doi: 10.1007/s13157-015-0645-3

Graham, S. (2019). Coordinating invasive plant management among conservation and rural stakeholders. *Land Use Policy* 81, 247–255. doi: 10.1016/j.landusepol.2018.10.043

Graham, S., Metcalf, A. L., Gill, N., Niemiec, R., Moreno, C., Bach, T., et al. (2019). Opportunities for better use of collective action theory in research and governance for invasive species management. *Conserv. Biol.* 33, 275–287. doi: 10.1111/cobi.13266

Hazelton, E. L. G., Mozdzer, T. J., Burdick, D. M., Kettenring, K. M., and Whigham, D. F. (2014). *Phragmites australis* management in the United States: 40 years of methods and outcomes. *AoB PLANTS* 6:plu001. doi: 10.1093/aobpla/plu001

Hijmans, R. J., and Van Etten, J. (2012). *Raster: Geographic Data Analysis and Modeling*. Available at: http://CRAN.R-project.org/package=raster (Accessed May 31, 2022).

Holdredge, C., and Bertness, M. D. (2011). Litter legacy increases the competitive advantage of invasive *Phragmites australis* in New England wetlands. *Biol. Invasions* 13, 423–433. doi: 10.1007/s10530-010-9836-2

Huang, C., and Asner, G. P. (2009). Applications of remote sensing to alien invasive plant studies. *Sensors* 9, 4869–4889. doi: 10.3390/s90604869

Ji, Y., Zhou, G., Lv, G., Zhao, X., and Jia, Q. (2009). Expansion of *Phragmites australis* in the Liaohe Delta, north-East China. *Weed Res.* 49, 613–620. doi: 10.1111/j.1365-3180.2009.00727.x

Kettenring, K. M., de Blois, S., and Hauber, D. P. (2012). Moving from a regional to a continental perspective of *Phragmites australis* invasion in North America. *AoB PLANTS* 2012:pls040. doi: 10.1093/aobpla/pls040

Kettenring, K. M., McCormick, M. K., Baron, H. M., and Whigham, D. F. (2011). Mechanisms of *Phragmites australis* invasion: feedbacks among genetic diversity, nutrients, and sexual reproduction. *J. Appl. Ecol.* 48, 1305–1313. doi: 10.1111/j.1365-2664.2011.02024.x

Kettenring, K. M., and Mock, K. E. (2012). Genetic diversity, reproductive mode, and dispersal differ between the cryptic invader, *Phragmites australis*, and its native conspecific. *Biol. Invasions* 14, 2489–2504. doi: 10.1007/s10530-012-0246-5

Kettenring, K. M., Mock, K. E., Zaman, B., and McKee, M. (2016). Life on the edge: reproductive mode and rate of invasive *Phragmites australis* patch expansion. *Biol. Invasions* 18, 2475–2495. doi: 10.1007/s10530-016-1125-2

Kettenring, K. M., Whigham, D. F., Hazelton, E. L. G., Gallagher, S. K., and Baron, H. M. (2015). Biotic resistance, disturbance, and mode of colonization impact the invasion of a widespread, introduced wetland grass. *Ecol. Appl.* 25, 466–480. doi: 10.1890/14-0434.1

Koh, L. P., and Wich, S. A. (2012). Dawn of drone ecology: low-cost autonomous aerial vehicles for conservation. *Trop. Conserv. Sci.* 5, 121–132. doi: 10.1177/194008291200500202

Kraemer, H. C. (2015). "Kappa coefficient" in *Wiley StatsRef: Statistics reference online* (Hoboken, NJ: Wiley), 1–4. doi: 10.1002/9781118445112.stat00365.pub2

Lambert, A. M., Dudley, T. L., and Saltonstall, K. (2010). Ecology and impacts of the large-statured invasive grasses *Arundo donax* and *Phragmites australis* in North America. *Invasive Plant Sci. Manage.* 3, 489–494. doi: 10.1614/ipsm-d-10-00031.1

Lathrop, R. G., Windham, L., and Montesano, P. (2003). Does Phragmites expansion alter the structure and function of marsh landscapes? Patterns and processes revisited. *Estuaries* 26, 423–435. doi: 10.1007/BF02823719

Liaw, A., and Wiener, M. (2002). Random forests. *R News* 2, 18–22. doi: 10.1023/A:1010933404324

Lombard, K. B., Tomassi, D., and Ebersole, J. (2012). Long-term management of an invasive plant: lessons from seven years of *Phragmites australis* control. *Northeast. Nat.* 19, 181–193. doi: 10.1656/045.019.s614

Long, A. L., Kettenring, K. M., Hawkins, C. P., and Neale, C. M. U. (2017b). Distribution and drivers of a widespread, invasive wetland grass, *Phragmites australis*, in wetlands of the great salt Lake, Utah, USA. *Wetlands* 37, 45–57. doi: 10.1007/s13157-016-0838-4

Long, A. L., Kettenring, K. M., and Toth, R. (2017a). Prioritizing management of the invasive grass common reed (*Phragmites australis*) in great salt Lake wetlands. *Invasive Plant Sci. Manage.* 10, 155–165. doi: 10.1017/inp.2017.20

Mack, R. N., Simberloff, D., Lonsdale, W. M., Evans, H., Clout, M., and Bazzaz, F. A. (2000). Biotic invasions: causes, epidemiology, global consequences, and control. *Ecol. Appl.* 10, 689–710. doi: 10.1890/1051-0761(2000)010[0689:BICEGC]2.0.CO;2

Martinez-Guanter, J., Agüera, P., Agüera, J., and Pérez-Ruiz, M. (2019). Spray and economics assessment of a UAV-based ultra-low-volume application in olive and citrus orchards. *Precis. Agric.* 21, 226–243. doi: 10.1007/s11119-019-09665-7

McCormick, M. K., Brooks, H. E., and Whigham, D. F. (2016). Microsatellite analysis to estimate realized dispersal distance in *Phragmites australis*. *Biol. Invasions* 18, 2497–2504. doi: 10.1007/s10530-016-1126-1

Meyerson, L. A., Lambert, A. M., and Saltonstall, K. (2010a). A tale of three lineages: expansion of common reed (*Phragmites australis*) in the U.S. southwest and Gulf Coast. *Invasive Plant Sci. Manage.* 3, 515–520. doi: 10.1614/ipsm-d-09-00052.1

Meyerson, L. A., Viola, D. V., and Brown, R. N. (2010b). Hybridization of invasive *Phragmites australis* with a native subspecies in North America. *Biol. Invasions* 12, 103–111. doi: 10.1007/s10530-009-9434-3

Minchinton, T., and Bertness, M. D. (2023). Disturbance-mediated competition and the spread of *Phragmites australis* in a coastal marsh. *Ecol. Appl.* 13, 1400–1416. doi: 10.1890/02-5136

Moyle, P. B., Manfree, A. D., and Fiedler, P. L. (2014). *Suisun marsh: Ecological history and possible futures*. Berkeley, CA: University of California Press.

Mozdzer, T. J., Brisson, J., and Hazelton, E. L. G. (2013). Physiological ecology and functional traits of north American native and Eurasian introduced *Phragmites australis* lineages. *AoB Plants* 5:plt048. doi: 10.1093/aobpla/plt048

Okoye, O. K., Li, H., and Gong, Z. (2020). Retraction of invasive *Spartina alterniflora* and its effect on the habitat loss of endangered migratory bird species and their decline in YNNR using remote sensing technology. *Ecol. Evol.* 10, 13810–13824. doi: 10.1002/ece3.6971

Orson, R. A. (1999). A paleoecological assessment of *Phragmites australis* in New England tidal marshes: changes in plant community structure during the last few millennia. *Biol. Invasions* 1, 149–158. doi: 10.1023/A:1010047731369

Pal, M. (2005). Random forest classifier for remote sensing classification. *Int. J. Remote Sens.* 26, 217–222. doi: 10.1080/01431160412331269698

Patger, M., Bragato, C., and Brix, H. (2005). Tolerance and physiological responses of *Phragmites australis* to water deficit. *Aquat. Biol.* 81, 285–299. doi: 10.1016/j.aquabot.2005.01.002

Paz-Kagan, T., Silver, M., Panov, N., and Karnieli, A. (2019). Multispectral approach for identifying invasive plant species based on flowering phenology characteristics. *Remote Sens.* 11:953. doi: 10.3390/rs11080953

Pengra, B. W., Johnston, C. A., and Loveland, T. R. (2007). Mapping an invasive plant, *Phragmites australis*, in coastal wetlands using the EO-1 Hyperion hyperspectral sensor. *Remote Sens. Environ.* 108, 74–81. doi: 10.1016/j.rse.2006.11.002

Peterson, M. A., Collavo, A., Ovejero, R., Shivrain, V., and Walsh, M. J. (2018). The challenge of herbicide resistance around the world: a current summary. *Pest Manag. Sci.* 74, 2246–2259. doi: 10.1002/ps.4821

Philipp, K. R., and Field, R. T. (2005). *Phragmites australis* expansion in Delaware Bay salt marshes. *Ecol. Eng.* 25, 275–291. doi: 10.1016/j.ecoleng.2005.04.008

Pimentel, D., Lach, L., Zuniga, R., and Morrison, D. (2000). Environmental and Economic Costs of Nonindigenous Species in the United States. *Bioscience* 50, 53–65. doi: 10.1641/0006-3568(2000)050[0053:EAECON]2.3.CO;2

Poulin, B., Lefebvre, G., and Mauchamp, A. (2002). Habitat requirements of passerines and reedbed management in southern France. *Biol. Conserv.* 107, 315–325. doi: 10.1016/S0006-3207(02)00070-8

Quirion, B., Simek, Z., Dávalos, A., and Blossey, B. (2018). Management of invasive Phragmites australis in the Adirondacks: a cautionary tale about prospects of eradication. *Biol. Invasions* 20, 59–73. doi: 10.1007/s10530-017-1513-2

R Core Team. (2021). *R: A language and environment for statistical computing.* R Foundation for Statistical Computing, Vienna, Austria. Available at: https://www.R-project.org/.

R Studio Team (2021). *RStudio: Integrated development for R.* RStudio, PBC, Boston, MA. Available at: http://www.rstudio.com/.

Reaser, J. K., Burgiel, S. W., Kirkey, J., Brantley, K. A., Veatch, S. D., and Burgos-Rodriguez, J. (2020). The early detection and rapid response (EDRR) to invasive species: a conceptual and federal capacities assessment. *Biol. Invasions* 22, 1–19. doi: 10.1007/s10530-019-02156-w

Rice, D., Rooth, J., and Stevenson, J. (2000). Colonization and expansion of *Phragmites australis* in upper Chesapeake Bay tidal marshes. *Wetlands* 20, 280–299. doi: 10.1672/0277-5212(2000)020[0280:CAEOPA]2.0.CO;2

Robichaud, C. D., and Rooney, R. C. (2017). Long-term effects of a *Phragmites australis* invasion on birds in a Lake Erie coastal marsh. *J. Great Lakes Res.* 43, 141–149. doi: 10.1016/j.jglr.2017.03.018

Rohal, C., Cranney, C., Hazelton, E., and Kettenring, K. M. (2019b). Invasive *Phragmites australis* management outcomes and native plant recovery are context dependent. *Ecol. Evol.* 9, 13835–13849. doi: 10.1002/ece3.5820

Rohal, C., Cranney, C., and Kettenring, K. M. (2019a). Abiotic and landscape factors constrain restoration outcomes across spatial scales of a widespread invasive plant. *Front. Plant Sci.* 10, 1–17. doi: 10.3389/fpls.2019.00481

Rohal, C. B., Hazelton, E. L. G., McFarland, E., Downard, R., McCormick, M., Whigham, D., et al. (2023). Landscape and site factors drive invasive Phragmites management and native plant recovery across Chesapeake Bay wetlands. *Ecosphere* 14:e4392. doi: 10.1002/ecs2.4392

Roslim, M. H. M., Juraimi, A. S., Che'Ya, N. N., Sulaiman, N., Manaf, M. N. H., Ramli, Z., et al. (2021). Using remote sensing and an unmanned aerial system for weed management in agricultural crops: a review. *Agronomy* 11, 1809–1824. doi: 10.3390/agronomy11091809

Royimani, L., Mutanga, O., Odindi, J., Dube, T., and Matongera, T. N. (2019). Advancements in satellite remote sensing for mapping and monitoring of alien invasive plant species (AIPs). *Phys. Chem. Earth Parts A/B/C* 112, 237–245. doi: 10.1016/j.pce.2018.12.004

Saltonstall, K.. (2002). *Cryptic invasion by a non-native genotype of the common reed, Phragmites australis, into North America*. Available at: https://www.pnas.org.

Samiappan, S., Turnage, G., Hathcock, L., Casagrande, L., Stinson, P., and Moorhead, R. (2017). Using unmanned aerial vehicles for high-resolution remote sensing to map invasive *Phragmites australis* in coastal wetlands. *Int. J. Remote Sens.* 38, 2199–2217. doi: 10.1080/01431161.2016.1239288

Sedgwick, P. (2012). Pearson's correlation coefficient. *BMJ* 345:e4483. doi: 10.1136/bmj.e4483

Shahbazi, M., Théau, J., and Ménard, P. (2014). Recent applications of unmanned aerial imagery in natural resource management. *GISci. Remote Sens.* 51, 339–365. doi: 10.1080/15481603.2014.926650

Simberloff, D., and Leppanen, C. (2019). Plant somatic mutations in nature conferring insect and herbicide resistance. *Pest Manag. Sci.* 75, 14–17. doi: 10.1002/ps.5157

Simpson, S., and Baruth, K. H.. (1966). *Suisun soil Conservation District final report phase I*. San Francisco, California.

Tadros, M. J., Al-Assaf, A., Othman, Y. A., Makhamreh, Z., and Taifour, H. (2020). Evaluating the effect of Prosopis juliflora, an alien invasive species, on land cover change using remote sensing approach. *Sustainability* 12:5887. doi: 10.3390/SU12155887

Takekawa, J. Y., Hagani, J. S., Edmunds, T. J., Collins, J. M., Chappell, S. C., Reynolds, W. H., et al. (2023). *The sky is not the limit: use of a spray drone to surgically apply herbicide and control an invasive plant in managed wetlands. In prep.*

Takekawa, J. Y., Woo, I., Spautz, H., Nur, N., Grenier, J. L., Malamud-Roam, K., et al. (2006). Environmental threats to tidal-marsh vertebrates of the San Francisco Bay estuary. *Stud. Avian Biol.* 32:176.

Tallamy, D. W. (2004). Do alien plants reduce insect biomass? *Conserv. Biol.* 18, 1689–1692. doi: 10.1111/j.1523-1739.2004.00512.x

Thompson, D. J., and Shay, J. M. (1985). The effects of fire on *Phragmites australis* in the Delta marsh, Manitoba. *Can. J. Bot.* 63, 1864–1869. doi: 10.1139/b85-261

Thorne, K., MacDonald, G., Guntenspergen, G., Ambrose, R., Buffington, K., Dugger, B., et al. (2018). US Pacific coastal wetland resilience and vulnerability to sea-level rise. *Sci. Adv.* 4:eaao3270. doi: 10.1126/sciadv.aao3270

Touchette, B. W., Iannacone, L. R., Turner, G. E., and Frank, A. R. (2007). Drought tolerance versus drought avoidance: a comparison of plant-water relations in herbaceous wetland plants subjected to water withdrawal and repletion. *Wetlands* 27, 656–667. doi: 10.1672/0277-5212(2007)27[656:DTVDAA]2.0.CO;2

Tozer, D. C., and Mackenzie, S. A. (2019). Control of invasive Phragmites increases marsh birds but not frogs. *Can. Wildl. Biol. Manage.* 8, 66–82.

Vitousek, P. M., D'antonio, C. M., Loope, L. L., Rejmánek, M., and Westbrooks, R. (1997). *Introduced species: a significant component of human-caused global change*. Available at: https://www.jstor.org/stable/24054520.

Volesky, J. D., Young, S. L., and Jenkins, K. H. (2017). Cattle grazing effects on *Phragmites australis* in Nebraska. *Invasive Plant Sci. Manage.* 9, 121–127. doi: 10.1614/IPSM-D-15-00056.1

Wails, C. N., Baker, K., Blackburn, R., Del Vallé, A., Heise, J., Herakovich, H., et al. (2021). Assessing changes to ecosystem structure and function following invasion by *Spartina alterniflora* and *Phragmites australis*: a meta-analysis. *Biol. Invasions* 23, 2695–2709. doi: 10.1007/s10530-021-02540-5

Walter, M., and Mondal, P. (2023). Mapping of Phragmites in estuarine wetlands using high-resolution aerial imagery. *Environ. Monit. Assess.* 195:478. doi: 10.1007/s10661-023-11071-6

Wang, Q., Li, C., Chen, C., Chen, J., Ma, X., and Que, X. (2017). Physiological responses of *Phragmites australis* to atrazine exposure and their relevance for tolerance. *J. Agroenviron. Sci.* 36, 1968–1977.

Wilcox, K. L., Petrie, S. A., Maynard, L. A., and Meyer, S. W. (2003). Historical distribution and abundance of *Phragmites australis* at long point, Lake Erie, Ontario. *J. Great Lakes Res.* 29, 664–680. doi: 10.1016/S0380-1330(03)70469-9

Young, S. L., and Kettenring, K. M. (2020). The social-ecological system driving effective invasive plant management: two case studies of non-native Phragmites. *J. Environ. Manag.* 267:110612. doi: 10.1016/j.jenvman.2020.110612

Zeileis, A., and Hothorn, T. (2002). Diagnostic checking in regression relationships. *R News* 2, 7–10.

frontiers | Frontiers in Ecology and Evolution

TYPE Brief Research Report
PUBLISHED 20 July 2023
DOI 10.3389/fevo.2023.1137111

OPEN ACCESS

EDITED BY
Zhouyuan Li,
Beijing Forestry University, China

REVIEWED BY
Maowei Liang,
University of Minnesota Twin Cities,
United States
Babar Zahoor,
Smithsonian Conservation Biology Institute
(SI), United States

*CORRESPONDENCE
Yu Peng
✉ yuupeng@163.com

RECEIVED 04 January 2023
ACCEPTED 28 June 2023
PUBLISHED 20 July 2023

CITATION
Peng Y, Xin J and Peng N (2023) Climate change alters the spatial pattern of plant spectral diversity across forest types.
Front. Ecol. Evol. 11:1137111.
doi: 10.3389/fevo.2023.1137111

Climate change alters the spatial pattern of plant spectral diversity across forest types

Yu Peng*, Jiaxun Xin and Nanyi Peng

College of Life and Environmental Sciences, Minzu University of China, Beijing, China

Species distribution, spatial distance, and neighboring interact6ions are among the most important drivers of global variation in plant species diversity. However, the effects of climate change on the relationship between spatial interactions and species diversity remain unknown. Here, we applied 12 machine learning models to assess the responses of spectral diversity (indicating species diversity) in forests in seven protected forest areas in China. Changes in 27 climatic variables during two time periods, 1990–2005 and 2005–2020, were analyzed. The results indicated that spectral diversity and intraspecific spatial distance have increased significantly with climate change. These results also provide insights into the variations in spectral diversity. Particularly, the contributions of neighboring interactions and plant–plant distances to the variation in species diversity between 1990 and 2000 were greater than the contribution of climate change in all forest types. Our analysis revealed that species diversity, plant–plant interactions, and spatial distance are closely associated with each other and sharply shifted under climate change. From this perspective, spatial interaction analysis—to a greater degree than analysis of community composition—can provide additional insights into the underlying mechanisms of changes in species diversity under current global-warming conditions.

KEYWORDS

spectral diversity, forests, spatial distance, macroecology, species diversity, climate change

1 Introduction

Global climate has been in a state of continuous warming for nearly a century. The current rate of temperature increase is approximately twice that of the previous century (Karl et al., 2015), and this increase is most pronounced at high elevations and latitudes (Peñuelas et al., 2013). Several studies have focused on the effects of climate change on plant diversity in different regions of the world (Boutin et al., 2017; Harrison et al., 2020). The species richness of vascular plants has also increased with the rise in temperature and nitrogen deposition, resulting in notable species-composition shifts (Boutin et al., 2017). In the Columbia River Gorge National Scenic Area, species richness, annual average temperature, and relative humidity were found to be significantly and positively related to each other (Matos et al., 2017). The higher the plant species diversity, the lower the impact of climate change (Li et al., 2018). Globally, regions with warm and wet climates support more species than those with cold or arid climates. This broad-scale climatic influence outweighs any other contributor to plant species diversity (Kreft & Jetz, 2007; Harrison et al., 2020). Reportedly, taxonomic diversity increases with increasing rainfall or varies with increasing productivity despite a slight decrease in temperature (Kreft & Jetz, 2007; Harrison et al., 2020). The relationship between woody species composition and climate is highly consistent across spatial scales and organizational levels (Kreft & Jetz, 2007; Harrison et al., 2020). Based on a very large dataset of six million trees in more than 180,000 field plots in central Africa, researchers have shown that sensitivity to climate change is the highest in endemic species-dominated forests and the driest forests (Réjou-Méchain et al., 2021). Further, recent studies in West Africa have shown that dry tropical forests exhibit larger functional changes compared with moist forests in response to long-term drought (Aguirre-Gutiérrez et al., 2019) and are likely to be more sensitive to global warming (Sullivan et al., 2020). In another study conducted in the Amazon, researchers found a peak in phylogenetic diversity at an intermediate level of precipitation (Neves et al., 2020). Conversely, forests dominated by widespread tree taxa adapted to anthropogenic pressures show relatively low sensitivity to climate change (Réjou-Méchain et al., 2021). Based on model predictions (Réjou-Méchain et al., 2021), undisturbed semi-deciduous and transitional forests appear phylogenetically more diverse than evergreen forests and demonstrate less sensitivity to climate change. However, these in-depth studies have mainly focused on the effects of climate change on plant species diversity in certain regions. Notably, an overall understanding of the spatial patterns of species diversity across vegetation types on a large scale remains lacking.

The measurement of species diversity on a large spatial scale is expected to be more time- and labor-intensive and expensive than on a small scale. With the use of remote sensing, it is now possible to monitor species diversity in large areas over a short period of time (Rocchini, 2007; Madonsela et al., 2017). Of the many different spectral vegetation indices that serve as proxy measures of species diversity, the coefficient of variation in the Normalized Difference Vegetation Index (CV-NDVI), which indicates the variation in spectral species within a plot, i.e., alpha diversity, is most widely used (Peng et al., 2019).

Forests are more appropriate for observing the effects of climate change than other ecosystems because trees have long growth stages and are less affected by occasional, short-term, or intravariable climatic fluctuations (Engler et al., 2009; Zwiener et al., 2018). Spectral diversity indices extracted from remote sensing imagery are particularly useful for predicting forest species diversity because the size of a tree crown usually matches well with the pixel size of satellite images. Furthermore, the use of protected areas (PAs) in this type of analysis can minimize non-climate anthropogenic impacts on plant diversity. An examination of the spatial distribution of plant species can help us to understand the mechanism of climate change impacting plant diversity and provide a reference for biodiversity conservation in world forests. In this study, we used spectral diversity (CV-NDVI) to evaluate plant species diversity. Based on the results of previous studies, we hypothesized the following: 1) species diversity could increase due to a rise in global temperature, associated with increased productivity; 2) increased plant diversity would produce strong neighboring effects, and plant–plant competition could become severe; 3) stronger neighboring interactions and plant–plant competition could lead to a longer spatial distance between plants, and the clustering community would become diffused; and 4) the changes in spatial distance and neighboring interactions could produce a feedback effect on species diversity (Figure 1). Using remote sensing techniques and spatial analysis, we tested our hypotheses based on the spectral diversity of vegetation in seven protected forests in China.

2 Study area and methods

2.1 Study area

For the present study, protected forest areas in China were selected as the data source based on the following criteria: 1) PAs established before 1980 to guarantee an undisturbed status of plant diversity in the area; 2) PAs having Landsat images in the growing seasons in 1990, 2005, and 2020, with a cloud cover of less than 10%; 3) PAs larger than 100 km^2, in which a core area with a buffer zone (larger than 2 km) can be created; and 4) PAs located entirely within one forest biome and not mixed with other forest types. These criteria were selected to ensure the quality of Landsat images, sufficient space for plot sampling, and the reliability of comparisons across different forest types. Out of all 474 national PAs, seven (with a median area of 100 km^2) (Figure 2), representing a geographically stratified and broad selection of evergreen broad-leaved, deciduous, and needle-leaved forests from low to high latitudes (Ricklefs & He, 2016), were selected for this study.

2.2 Plant diversity indices derived from Landsat images

Prior to calculating the spectral diversity indices, all the Landsat images were processed. Cloud-free Landsat satellite images (with a spatial resolution of 30 m) were obtained for the years 1990, 2005, and 2020 from the Global Land Cover Facility website (http://glcfapp.umiacs.umd.edu). All Landsat images were radiometrically and atmospherically corrected using Idrisi GIS (Levin et al., 2007). Thereafter, the images were validated for shading effects at 30-m resolution caused by topography using the ASTER global digital elevation model (http://gdem.ersdac.jspacesystems.or.jp). In order to differentiate the biological features of forests while minimizing the problems of image incompatibility due to seasonal or annual differences, images during the growing seasons were included. Radiance values were converted to surface reflectance, which helped identify the differences in exoatmospheric irradiance and solar zenith angles

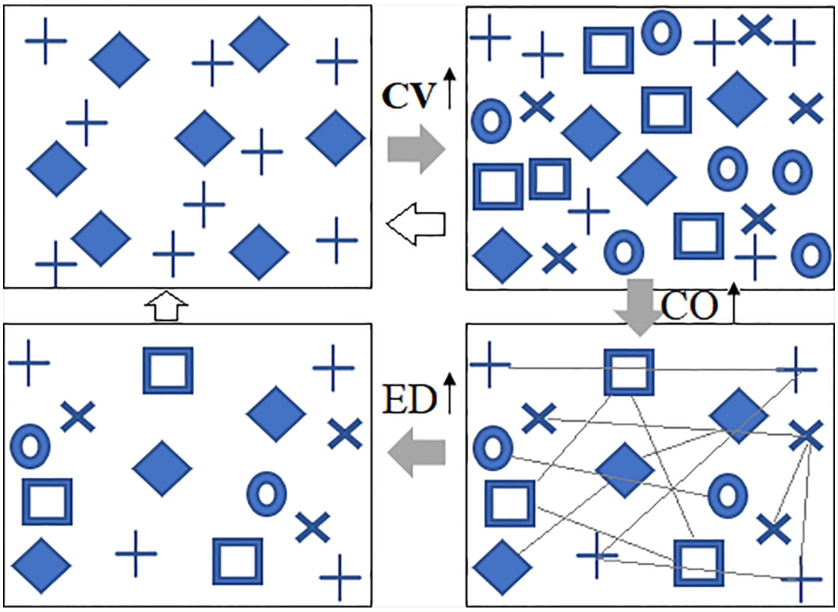

FIGURE 1
Conceptual illustrations of predicted changes in vegetation spectral diversity under climate warming. Under climate warming, species diversity (CV) could increase, the abundance of plants could increase, the neighboring interactions (CO) would become stronger, and, consequently, self-thinning effects will lead to a longer distance (ED) between two plants of the same species. The variation in ED and CO can also work on CV. Different symbols represent different spectral species; CV, spectral alpha diversity; CO, neighboring correlation; ED, spatial distance.

(Rocchini, 2007; Duro et al., 2014). All image processing was performed using ERDAS Imagine software.

After pre-processing, the CV of the NDVI (CVn) within a window of 3 × 3 pixels was calculated as the spectral alpha diversity index of the plot. A series of spectral biodiversity indices (CVn) was then generated at plot sizes of 3 × 3, 5 × 5, 9 × 9, 17 × 17, and 33 × 33 pixels. After investigating the effects of spatial autocorrelation, estimation accuracy, and environmental scale, we selected a window of 33 × 33 pixels as the most convenient size to calculate spectral diversity, which has also been used in similar studies on tropical mountain rainforests (Wallis et al., 2017) and savannah woodlands (Madonsela et al., 2017).

2.3 Spectral–spatial metrics

From the NDVI imagery, we derived three spectral–spatial measures, namely, spatial distance, spatial aggregation, and neighboring correlation, as species spatial pattern representatives. The Euclidean nearest-neighbor distance (ED) represents the distance (m) from spectral plant a to the nearest neighboring spectral plant b of the same species, computed from the shortest pixel–pixel distance. The aggregation index (AI) represents the number of similar adjacencies involving the corresponding spectral species divided by the maximum possible number of similar adjacencies involving the corresponding spectral species ($0 \leqq AI \leqq 100$). Given any pi, AI equals 0 when the focal cluster is maximally disaggregated (i.e., when there are no adjacencies), and AI equals 100 when the cluster is maximally aggregated into a single, compact cluster.

Neighboring interactions can be determined using the correlation coefficients (COs) of neighboring pixel–pixel pairs within a moving window (Hall-Beyer, 2017). Image texture metrics were derived from multiple-scale spectral values using a gray-level co-occurrence matrix (GLCM) in the ENVI 5.3 program. A detailed description of image texture measurements can be found in the ENVI software manual. A 33 × 33-pixel window size was used to detect the spectral–spatial variability (Kelsey and Neff, 2014), as this size was consistent with the spatial variability defined by the semi-variogram analysis in the present study area (Hernández-Stefanoni et al., 2012). We selected these metrics because they can successfully derive plant–plant spatial patterns across different extents (He et al., 2000). ED and AI values were calculated using Fragstats 4.3.

2.4 Climate data

Temperature and precipitation data for each PA between 1982 and 2020 were obtained from the China Meteorological Data Service Center. The data were developed using the spatial interpolation method in ArcGIS, based on more than 2,400 meteorological stations across the country. This method has been widely applied in the fields of meteorology, climate, ecology, and environment (Boutin et al., 2017; Harrison et al., 2020). Lastly, 27 groups of climatic data were developed at the annual level (e.g., annual maximum temperature (ATmax), annual minimum temperature (ATmin), and annual precipitation (AP)) and at the monthly level (e.g., mean monthly temperature (MMT), monthly maximum temperature (MTmax), and monthly minimum

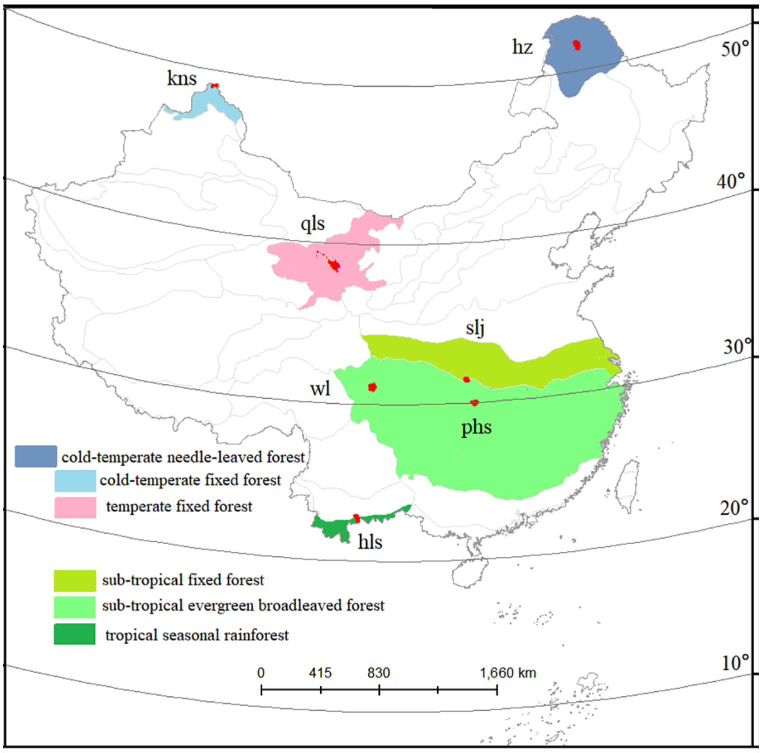

FIGURE 2
Study area. Seven protected forest areas across a latitudinal gradient. Forest types are indicated by colored areas.

temperature (MTmin)). Additionally, we collected data corresponding to cumulative temperatures ≥5°C and ≥10°C and precipitation seasonality.

2.5 Trends in plant diversity change

The spectral–spatial metric (CV, CO, ED, and AI) values for 1990, 2005, and 2020 were compared using Duncan's new multiple range test (DNMRT). This approach has been widely used to compare results across different measurements, environmental conditions, and sampling locations (Wang et al., 2010; He et al., 2017). The data were tested for normality and equality of variances and, if necessary, were converted to the square-root value or log-transformed prior to analysis. Change trends were classified based on six levels: decrease at $p < 0.01$, decrease at $p < 0.05$, insignificant decrease, insignificant increase, increase at $p < 0.05$, and increase at $p < 0.01$. DNMRT was conducted using the DPS software (http://www.chinadps.net, Zhejiang University, China).

2.6 Identification of key drivers

Twelve models were analyzed to identify the key influential factors of spectral–spatial patterns under climate change using the SPSS modeler (SPSS modeler 18, Statistical Package for the Social Sciences, Chicago, IL, USA). These 12 models were included with four regression models (linear regression, linear assignment (AS), general linear model, and partial least square regression), one classification model (k-nearest neighbors), and seven machine learning models (support vector machine (SVM), linear SVM, random tree, tree AS, classification and regression tree analysis, artificial neural network, and chi-squared automatic interaction detector). Model performance was assessed using three indicators: the coefficient of determination (R^2, calculated as the squared Pearson's correlation coefficient), root mean square error (RMSE), and significance level (p). The models with the highest R^2 and lowest RMSE ($p < 0.01$) were considered the best fit (Fassnacht et al., 2014). The climate variables in the best models with the most important values were regarded as key influencing variables and were further analyzed to determine their contributions to the variation in spectral–spatial matrices from 1990 to 2020. A total of 168 models were analyzed. The reliability and appropriateness of the 12 models for modeling and predicting spectral CV for climate change are described in the Supplementary Material.

To explore the relationships between the selected key climate variables, a redundancy analysis (RDA) was conducted using Canoco software 5.0. Partition analysis of the RDA-related variation was used to analyze the relative contributions of the three groups of explanatory variables (climate, spatial distance (ED), and neighboring interaction (CO)) to the variance of the response variable (CV). RDA-related ordination and variation partitioning analyses were conducted using Canoco 5.0 (Lepš and Šmilauer, 2003).

3 Results

3.1 Spectral CV variation

From 1990 to 2020, ED significantly ($p < 0.05$) increased as AI decreased (Figure 3). In contrast, CO did not vary significantly during the different periods. The regional spectral CVs in 2020 were higher than those in 1990 ($p < 0.05$). In addition, the CV values in cold-temperate climates increased more than the corresponding values in subtropical and tropical climates.

From low to high latitudinal gradient, CV values showed a significant v-curve ($r^2 = 0.22$), ED significantly ($r^2 = 0.33$) decreased, and AI ($r^2 = 0.90$) significantly increased (Figure 4). In turn, CO exhibited the least change. When annual precipitation increased from 900 to 1,900 mm, the values of CV increased significantly ($r^2 = 0.33$), and AI decreased significantly ($r^2 = 0.23$),

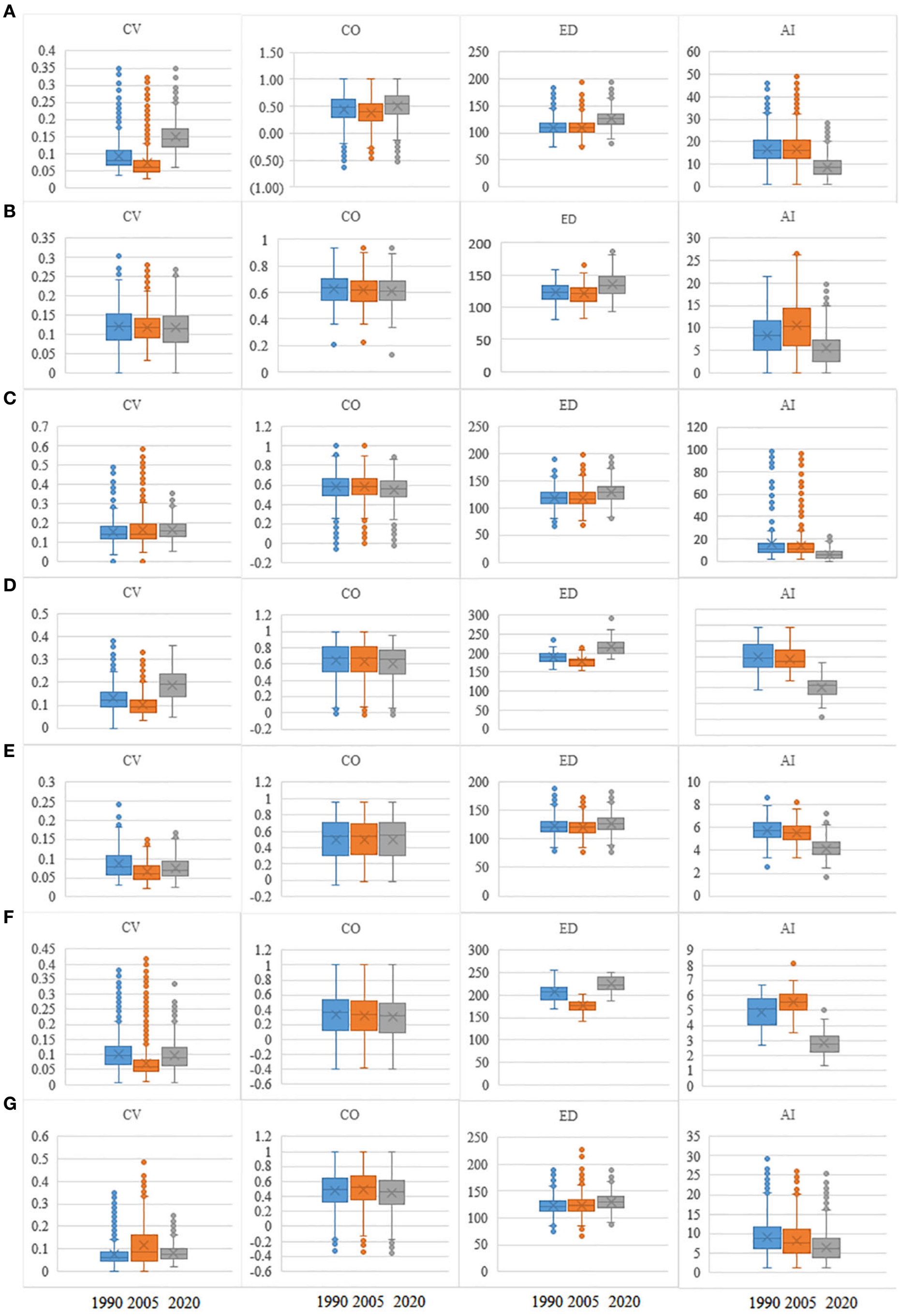

FIGURE 3
Values of CV, CO, ED, and AI in 1990, 2005, and 2020 for seven forest PAs. Lines in boxes represent medians, and box ends represent quartiles; whiskers mark the 95th percentiles, and circles represent outliers. Box width is proportional to the square root of the number of data points in each category. CV, spectral alpha diversity; CO, neighboring correlation; ED, spatial distance; AI, aggregation index; PAs, protected areas. **(A)** hz; **(B)** kns; **(C)** qls; **(D)** wl; **(E)** slj; **(F)** phs; **(G)** hls.

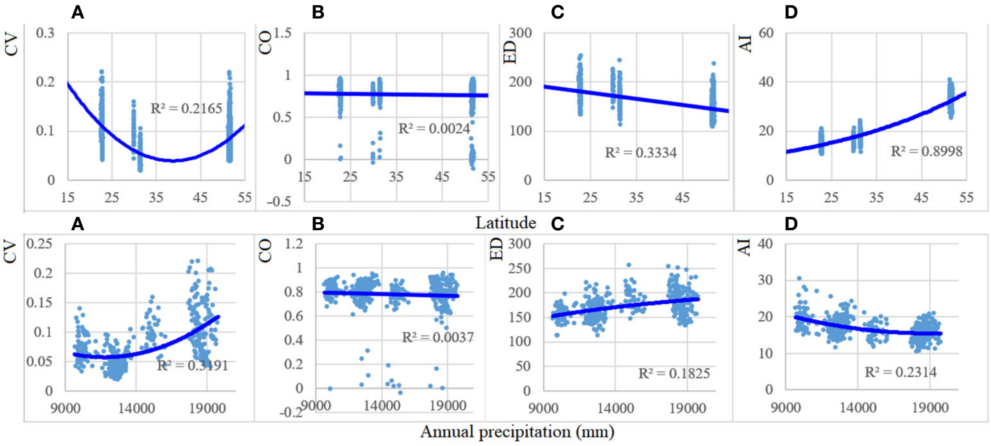

FIGURE 4
Patterns of CV, CO, ED, and AI with latitude and annual precipitation (×0.1 mm) gradients in 1990, 2005, and 2020. Forest spectral parameters and the environmental variables demonstrated a significant ($p < 0.001$) association, except those of CO. CV, spectral alpha diversity; CO, neighboring correlation; ED, spatial distance; AI, aggregation index. **(A)** CV; **(B)** CO; **(C)** ED; **(D)** AI.

whereas no significant ($r^2 = 0.18$) increase in ED ($r^2 = 0.18$) was observed.

3.2 Identification of key influential factors

Among the 12 models, the chi-squared automatic interaction detector (CHAID) model yielded the most accurate predictions for all response variables across the seven PAs under study (average $R^2 = 0.66$), generalized linear modeling (GLM) (average $R^2 = 0.61$), and artificial neural network (ANN) (average $R^2 = 0.56$) (Figure 5). CHAID is based on multi-way splits and adjusted significance testing (Bonferroni testing, $p < 0.05$). In every step, the predictor variable with the strongest interaction with the dependent variable was selected for the split. Default values of 100 iterations were used, with a minimum change of 0.05 in the expected cell frequencies. Our CHAID model yielded an out-of-sample predictive accuracy of 78%–98%. Therefore, five key influential climate variables were extracted based on the best model for each PA.

Nearly 10 climate variables (Figure 5) emerged as important in the overall models, explaining 89.82% of the variation in the response matrix of spectral CV between 1990 and 2005 and 87.22% of the variation between 2005 and 2020. Both cumulative temperature values of ≥5°C and ≥10°C were important in these models, particularly in April, June, September, and October (T_{10}-6, T_5-04, T_{10}-04, T_{10}-09, and T_5-10), as was the average temperature in March and November (m03 and m11). Of all 140 selected climate variables in the 168 models, 27.86% were accounted for.

The most influential climatic factors also varied from low to high latitudinal gradients (Figure 6). For boreal forests (hz), the highest temperature in December contributed the most to the

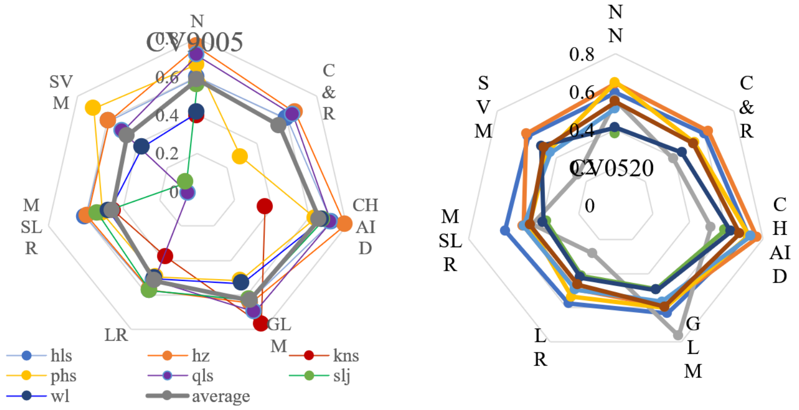

FIGURE 5
Model selection for regional vegetation spectral variation responses under climate change for core zones in seven protected forest areas. Vegetation spectral responses include differences between 1990–2005 (CV9005) (Left) and 2005–2020 (CV0520) (Right). Seven predictive models are shown and ranked by R2 and RMSE. ANN, artificial neural network; C&R, classification and regression tree analysis; CHAID, chi-squared automatic interaction detector; GLM, generalized linear model; LR, linear regression; MSLR, multiple stepwise linear regression; SVM, support vector machine.

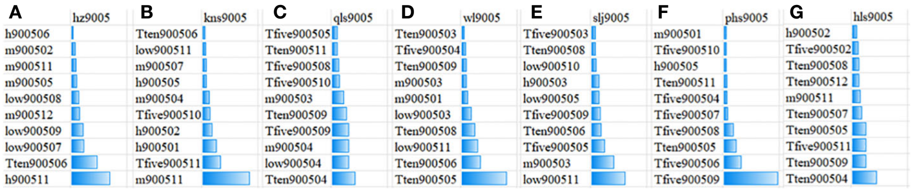

FIGURE 6
The 10 key climate variables that contributed the most to the variation in regional spectral CV from 1990 to 2005. m, mean temperature; h, highest temperature; low, lowest temperature; 01–12 indicate January to December; Tfive, cumulative temperature of ≥5°C; Tten, cumulative temperature of ≥10°C; 900502 indicates the difference in February between 1990s (1980–1990) and 2005s (1995–2005). **(A)** hz; **(B)** kns; **(C)** qls; **(D)** wl; **(E)** slj; **(F)** phs; **(G)** hls.

variation in the value of spectral CV (IV > 0.29). Cumulative and lowest temperatures in April (spring) were among the top predictors (IVs > 0.14) of changes in spectral CV in temperate forests (qls). The lowest temperature in winter was the key factor for changes in the spectral CV in subtropical forests (slj and phs). In the case of rainforests (hls), the key climatic factors were the highest and lowest temperatures in winter and cumulative temperatures in the spring and autumn (Figure 6).

3.3 RDA ordination: relationships among key climate variables

As per RDA ordination, the two axes explained 14.0% of the vegetation variation in the PA of hz, 18.55% of qls, 31.11% of wl, 13.49% of slj, 64.48% of phs, and 25.39% of hls (Figure 7). In PAs with cold temperate conditions, CV values were negatively related to AI, low08 (the lowest temperature in August, the following is

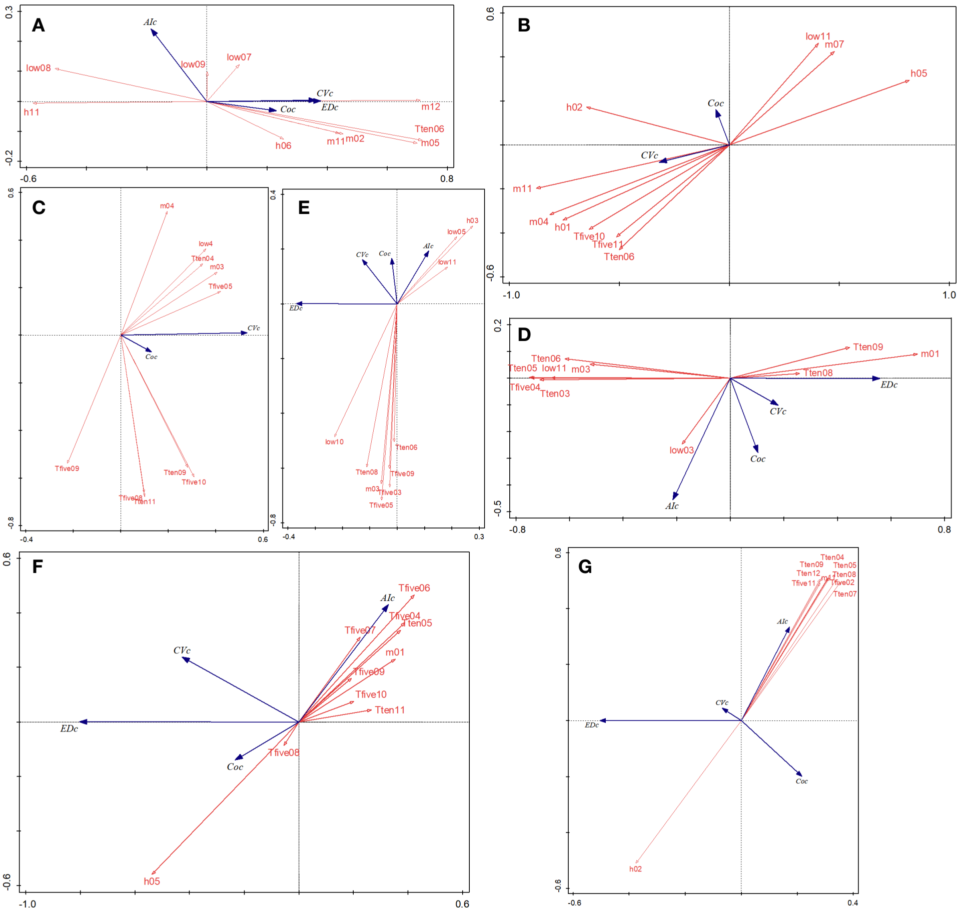

FIGURE 7
RDA ordinations between the regional spectral CV, ED, AI, CO, and environmental variables in seven forest PAs **(A–G)**. EDc, Euclidean distance (m); Coc, neighboring correlation; m, average temperature during a period (×0.1°C; low, lowest temperature during a period; h, highest temperature during a period; T5, cumulative temperature ≥ 5°C during a period; T10, cumulative temperature ≥10°C during a period). RDA, redundancy analysis; CV, spectral alpha diversity; ED, spatial distance; AI, aggregation index; CO, neighboring correlation; PAs, protected areas.

same), and h11 and positively related to m05 and m012. The performances of kns and qls were similar in that CV and CO values were positively associated. With respect to wl, T_{10}-5 and T_{10}-6 were negatively correlated with the CV. In sjl, low11 was positively and negatively correlated with CV and m03, respectively. Lastly, in the case of tropical and subtropical climate PAs (phs and hls), AI was negatively related to CV and differed from the values obtained in the other PAs.

3.4 Variation partitioning

Interestingly, spatial distance metrics (b; ED and AI) explained most (>10%) of the regional spectral variation of CV values in all seven PAs (Figure 8), and climate variables (a) explained a negligible proportion of CV variation (major in 0%–5%). Moreover, a greater proportion of the CV variation was explained by distance metrics (23.8%) in cold climate areas than in other areas. On average, the portion of neighbor correlation (c; Cor, 3.7%) was larger than that of climate variables (a; 2.3%). In tropical areas (hls), the interaction between climatic conditions and neighboring correlations (f) showed 10.8% of the spectral CV variation, whereas in cold areas (hz), this interaction accounted for only 0.6%.

4 Discussion

This study is the first attempt to link climate change, neighboring interactions, and spatial distance to species richness and evenness. Using high-accuracy modern machine learning models, we identified the key influencing factors that contributed to the variation in spectral diversity on a large scale using 27 climatic variables. Furthermore, we evaluated the contribution of climate, neighboring interactions, and spatial distance to the variation in spectral CV across forest types.

Consistent with previous studies (Zhang et al., 2017), our results indicated that spectral diversity has increased with climate warming. A recent study found that species richness increased on mountain summits in boreal-temperate forests in Europe (Pauli et al., 2012). Over 30 years of succession, species richness and phylogenetic diversity of plantation trees have increased monotonically (Yu et al., 2019). An increase in spectral species richness is closely associated with an increase in the NDVI, effective cumulative temperature, and seasonal variation in moisture availability (Harrison et al., 2015). In heterogeneous grasslands in California (USA), livestock grazing, fire, succession, nitrogen deposition, and exotic species did not contribute to fluctuations in plant diversity (Harrison et al., 2015). In this study, monthly cumulative temperature, rather than annual average temperature, contributed the most to the increase in spectral CV from 1990 to 2020.

We found that neighboring interactions and plant–plant spatial distance increased with increasing species diversity, presumably due to an increase in tree productivity and tree abundance resulting from ecological complementarity. A previously published global meta-analysis demonstrated that diversity effects are prevalent in the most productive environments, whereas abundance effects became dominant under the most limiting conditions (Madrigal-González et al., 2020). Therefore, a higher abundance will definitely affect plant–plant interactions (i.e., neighboring interactions), and the consequences of this may be either positive or negative, depending on species traits, economics, and environmental conditions (Madrigal-González et al., 2020). A meta-analysis showed that larger positive effects favored sapling emergence and survival, whereas smaller negative effects act on plant growth and density (Gómez-Aparicio, 2009). The life form of the interacting species largely influences the outcome of the interaction; for example, herbaceous plants have strong negative effects, especially on other herbaceous species, whereas shrubs have strong supportive effects, especially on trees (Gómez-Aparicio, 2009). Semiarid and

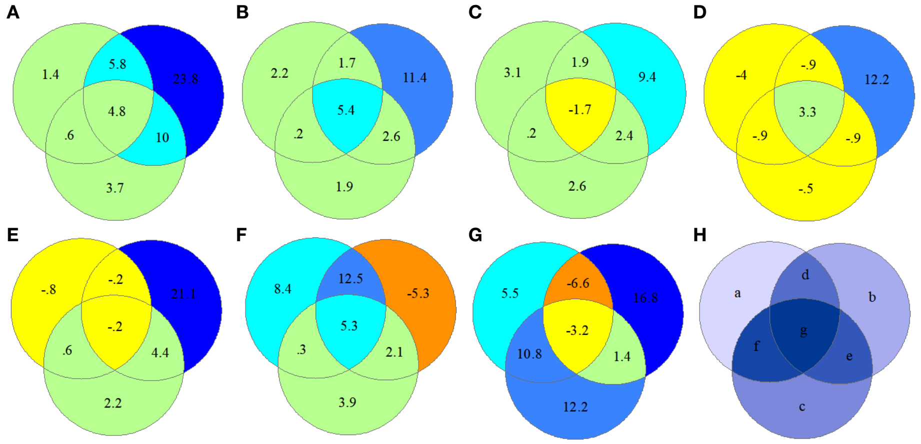

FIGURE 8
RDA ordination-based regional spectral CV variation partitioning in seven protected forest areas by selecting "Var-part-3groups-conditional-effects-tested." a, climate (ten climate variables selected); b, spatial distance (ED and AI); c, neighbor interaction (CO); d = a + b, e = b + c, f = a + c, and g = d + e + f. **(A)** hz; **(B)** kns; **(C)** qls; **(D)** wl; **(E)** slj; **(F)** phs; **(G)** hls; **(H)** components of variation partitioning. RDA, redundancy analysis; CV, spectral alpha diversity; ED, spatial distance; AI, aggregation index; CO, neighboring correlation.

tropical ecosystems, but particularly temperate ecosystems, show more positive neighbor effects than wetlands (Gómez-Aparicio, 2009). Biotic interactions are thought to be relatively more important in shaping biodiversity at tropical than at temperate latitudes (Roslin et al., 2017). Ignoring biotic interactions affects the estimate of climatic niche limits that determine the responses of plant diversity to climate change in models (Newbold et al., 2020). The results of the current study underscore the need to include biotic interactions in climate change modeling.

Neighboring species may demonstrate strong positive or negative correlations. However, when both types of correlation exist, the total neighboring interaction in the region may become null or weak, given that positive and negative values counteract each other (Dray et al., 2012). Weak or null values of neighboring interactions may result when both positive and negative correlations shape species spatial distributions (Wagner, 2013; Biswas et al., 2016). In the present study, warming on a regional scale increased plant species richness (spectral CV), creating a stronger spatial correlation between neighboring species, whereas competition on a plant–plant scale created a negative spatial correlation (Biswas et al., 2017). Although neighboring interactions were weak, they still highly contributed to variation in plant species diversity (spectral CV) in our study.

Considering these results, it is reasonable to expect that stronger neighboring interactions will enhance plant–plant competition, thereby producing a negative effect on intraspecific associations. Conclusively, only species distributed over large distances will survive. Therefore, climate warming leads to a large plant–plant distance. Hypotheses 2 and 3 were confirmed by our data. Specifically, we found that the spatial distance between the same spectral species increased with increasing spectral CV under climate change. The spatial patterns of communities are shaped by environmental filtering and biological competition. Environmental filtering produces a spatially aggregated pattern, whereas competition produces a spatially segregated pattern (He & Biswas, 2019). Possibly, intraspecies competition played a stronger role than environmental filtering in structuring the communities studied from 1990 to 2020, likely because the soil properties, landforms, and slope remained unchanged during this period, whereas plant diversity (spectral CV) increased. To a certain extent, higher plant abundance and species numbers might have confounded the positive effects of climate warming at a local scale. Moreover, our results confirmed that the contribution of plant–plant distance to species diversity was higher than that of climate variables for all forest types (hypothesis 1). Consistent with these findings, a previously published field experiment has shown that biotic interactions have a strong effect on plant fitness and eventually override the effects of climate (Tomiolo et al., 2015).

The patterns of spectral metrics in response to climate change were the same as those in the field survey. Consequently, we determined that spectral metrics are reliable proxy measures of plant species parameters. Several dissimilarity measurements have been introduced to quantify the overall heterogeneity in plant species composition on a few or multiple sites. However, pairwise dissimilarities do not account for patterns of co-occurrence at more than two sites (Baselga, 2013). Consequently, the average of the pairwise dissimilarities may not accurately reflect the overall compositional heterogeneity at multiple sites (Baselga, 2013). Within a highly diverse plant community, many plant species lived together or were associated with higher stem abundance. In remote sensing images, the former demonstrates a cluster with high heterogeneity, while the latter demonstrates similar neighboring pixels. A dataset based on remote sensing is reliable for analyzing both the spectral diversity and spatial patterns of plant species in forests.

In the current study, we found that geophysical factors including soil pH and clay content tended to have higher effects on tree species diversity. Although climate is changing rapidly, geophysical factors are relatively fixed and are not likely to change significantly over the timescales considered in this analysis. Consequently, geophysical variables were not included in the models. In addition, evolutionary and biogeographic histories, including past diversification processes and environmental changes, influence the distribution of tree diversity, and such factors should be considered in future studies on the spatial patterns of plant diversity.

5 Conclusions

Our results indicated that climate warming has increased species diversity, which in turn has increased neighboring interactions, ultimately leading to a longer plant–plant distance. However, we found that climate change contributed less to species diversity than neighboring interactions and spatial distance. Conclusively, we did not detect a significant change in the overall neighboring correlation on a regional scale under climate warming, although we did observe an increase in the spatial distance across spectral species. In future studies, the relevant biotic and abiotic factors should be quantified, and an assessment of the relative contribution of abiotic factors to the spatial pattern of species diversity should be performed. The general effects of neighboring interactions on plant diversity should be considered at the global scale, considering all vegetation types under the conditions of ongoing climate change.

Data availability statement

The original contributions presented in the study are included in the article/Supplementary Material. Further inquiries can be directed to the corresponding author.

Author contributions

YP devised the project and developed the research questions and study design. NP and JX processed and analyzed data. All authors contributed to the manuscript writing and editing. All authors contributed to the article and approved the submitted version.

Funding

This research was funded by the General Program of the National Natural Science Foundation of China (32271555), the Top Discipline and First-class University Construction Project (ydzxxk201618) of Minzu University of China, and Special Project of Strategic Leading Science and Technology of Chinese Academy of Sciences (No: XDA 19030104).

Conflict of interest

Publisher's note

Supplementary material

The Supplementary Material for this article can be found online at: https://www.frontiersin.org/articles/10.3389/fevo.2023.1137111/full#supplementary-material

References

Aguirre-Gutiérrez, J., Oliveras, I., Rifai, S., Fauset, S., Adu-Bredu, S., Affum-Baffoe, K., et al. (2019). Drier tropical forests are susceptible to functional changes in response to a long-term drought. *Ecol. Lett.* 22, 855–865. doi: 10.1111/ele.13243

Baselga, A. (2013). Multiple site dissimilarity quantifies compositional heterogeneity among several sites, while average pairwise dissimilarity may be misleading. *Ecography* 36 (2), 124–128. doi: 10.1111/j.1600-0587.2012.00124.x

Biswas, S. R., Macdonald, R. L., and Chen, H. (2017). Disturbance increases negative spatial autocorrelation in species diversity. *Landscape Ecol.* 32 (4), 823–834. doi: 10.1007/s10980-017-0488-9

Biswas, S. R., Mallik, A. U., Braithwaite, N. T., and Wagner, H. H. (2016). A conceptual framework for the spatial analysis of functional trait diversity. *Oikos* 125 (2), 192–200. doi: 10.1111/oik.02277

Boutin, M., Corcket, M., Alard, D., Villar, L., Jiménez, J. J., Blaix, C., et al. (2017). Nitrogen deposition and climate change have increased vascular plant species richness and altered the composition of grazed subalpine grasslands. *J. Ecol.* 105 (5), 1199–1209. doi: 10.1111/1365-2745.12743

Dray, S., Pelissier, R., Couteron, P., Fortin, M. J., Legendre, P., Peres-Neto, P.R., et al. (2012). Community ecology in the age of multivariate multiscale spatial analysis. *Ecol. Monogr.* 82 (3), 257–275. doi: 10.1890/11-1183.1

Duro, D. C., Girard, J., King, D. J., Fahrig, L., Mitchell, S., Lindsay, K., et al. (2014). Predicting species diversity in agricultural environments using Landsat TM imagery. *Remote Sens. Environ.* 144, 214–225.

Engler, R., Randin, C. F., Vittoz, P., Czáka, T., Beniston, M., Zimmermann, N. E., et al. (2009). Predicting future distributions of mountain plants under climate change: does dispersal capacity matter? *Ecography* 32, 34–45. doi: 10.1111/j.1600-0587.2009.05789.x

Fassnacht, F., Hartig, F., Latifi, H., Berger, C., Hernández, J., Corvalán, P., et al (2014). Importance of sample size, data type and prediction method for remote sensing-based estimations of aboveground forest biomass. *Remote Sens. Environ.* 154, 102–114. doi: 10.1016/j.rse.2014.07.028

Gómez-Aparicio, L. (2009). The role of plant interactions in the restoration of degraded ecosystems: a meta-analysis across life-forms and ecosystems. *J. Ecol.* 97, 1202–1214. doi: 10.1111/j.1365-2745.2009.01573.x

Hall-Beyer, M. (2017). Practical guidelines for choosing GLCM textures to use in landscape classification tasks over a range of moderate spatial scales. *Int. J. Remote Sens.* 38, 1312–1338.

Harrison, S. P., Gornish, S. E., and Copeland, S. (2015). Climate-driven diversity loss in a grassland. *Proc. Natl. Acad. Sci.* 112 (28), 8672–8677. doi: 10.1073/pnas.1502074112

Harrison, S., Spasojevic, M. J., and Li, D. (2020). Climate and plant community diversity in space and time. *Proc. Natl. Acad. Sci. U.S.A.* 117 (9), 4464–4470. doi: 10.1073/pnas.1921724117

He, D., and Biswas, S. R. (2019). Negative relationship between interspecies spatial association and trait dissimilarity. *Oikos* 128, 659–667. doi: 10.1111/oik.05876

He, H. S., DeZonia, B. E., and Mladenoff, D. J. (2000). An aggregation index (AI) to quantify spatial patterns of landscapes. *Landscape Ecol.* 15, 591–601. doi: 10.1023/A:1008102521322

He, N., Wen, D., Zhu, J., Tang, X., Xu, L., Zhang, L., et al. (2017). Vegetation carbon sequestration in Chinese forests from 2010 to 2050. *Global Change Biol.* 23, 1575–1584. doi: 10.1111/gcb.13479

Hernández-Stefanoni, J. L., Gallardo-Cruz, J. A., Meave, J. A., Rocchini, D., Bello-Pineda, J., and López-Martínez, J. O. (2012). Modeling α-and β-diversity in a tropical forest from remotely sensed and spatial data. *Int. J. Appl. Earth Observ. Geoinf.* 19, 359–368. doi: 10.1016/j.jag.2012.04.002

Karl, T. R., Arguez, A., Huang, B., Lawrimore, J. H., McMahon, J. R., Menne, M. J., et al. (2015). CLIMATE CHANGE. possible artifacts of data biases in the recent global surface warming hiatus. *Science* 348 (6242), 1469–1472. doi: 10.1126/science.aaa5632

Kelsey, K. C., and Neff, J. C. (2014). Estimates of aboveground biomass from texture analysis of Landsat imagery. *Remote Sens.* 6 (7), 6407–6422. doi: 10.3390/rs6076407

Kreft, H., and Jetz, W. (2007). Global patterns and determinants of vascular plant diversity. *Proc. Natl. Acad. Sci. U.S.A.* 104, 5925–5930. doi: 10.1073/pnas.0608361104

Lepš, J., and Šmilauer, P. (2003). *Multivariate analysis of ecological data using CANOCO* (Cambridge, UK: Cambridge University Press).

Levin, N., Shmida, A., Levanoni, O., Tamari, H., and Kark, S. (2007). Predicting mountain plant richness and rarity from space using satellite-derived vegetation indices: predicting mountain biodiversity from space. *Divers. Distrib.* 13 (6), 692–703. doi: 10.1111/j.1472-4642.2007.00372.x

Li, X. R., Jia, R. L., Zhang, Z. S., Zhang, P, and Hui, R. (2018). Hydrological response of biological soil crusts to global warming: a ten-year simulative study. *Global Change Biol.* 24 (10), 4960–4971. doi: 10.1111/gcb.14378

Madonsela, S., Cho, M. A., Ramoelo, A., and Mutanga, O. (2017). Remote sensing of species diversity using Landsat 8 spectral variables. *ISPRS J. Photogram. Remote Sens.* 133, 116–127. doi: 10.1016/j.isprsjprs.2017.10.008

Madrigal-González, J., Calatayud, J., Ballesteros-Canovas, J. A., Escudero, A., and Stoffel, M. (2020). Climate reverses directionality in the richness-abundance relationship across the world's main forest biomes. *Nat. Commun.* 11 (1), 5635. doi: 10.1038/s41467-020-19460-y

Matos, P., Geiser, L., Hardman, A., Glavich, D., Pinho, P., Nunes, A., et al. (2017). Tracking global change using lichen diversity: towards a global-scale ecological indicator. *Methods Ecol. Evol.* 8, 788–798. doi: 10.1111/2041-210X.12712

Neves, D. M., Dexter, K.G., Baker, T. R., de Souza, F. C., Oliveira-Filho, A.T., Queiroz, L.P., et al. (2020). Evolutionary diversity in tropical tree communities peaks at intermediate precipitation. *Sci. Rep.* 10, 1188. doi: 10.1038/s41598-019-55621-w

Newbold, T., Oppenheimer, P., Etard, A., and Williams, J. J. (2020). Tropical and mediterranean biodiversity is disproportionately sensitive to land-use and climate change. *Nat. Ecol. Evol.* 4, 1630–1638. doi: 10.1038/s41559-020-01303-0

Pauli, H., Gottfried, M., Dullinger, S., Abdaladze, O., Akhalkatsi, M., Alonso, J. L. B., et al. (2012). Recent plant diversity changes on Europe's mountain summits. *Science* 336 (6079), 353–355. doi: 10.1126/science.1219033

Peng, Y., Fan, M., Bai, L., Sang, W., Feng, J., Zhao, Z., et al. (2019). Identification of the best hyperspectral indices in estimating plant species richness in sandy grasslands. *Remote Sens.* 11, 588. doi: 10.3390/rs11050588

Peñuelas, J., Sardans, J., Estiarte, M., Ogaya, R., Carnicer, J., Coll, M., et al. (2013). Evidence of current impact of climate change on life: a walk from genes to the biosphere. *Glob. Change Biol.* 19, 2303–2338. doi: 10.1111/gcb.12143

Réjou-Méchain, M., Mortier, F., Bastin, J. F., Cornu, G., Barbier, N., Bayol, N., et al. (2021). Unveiling African rainforest composition and vulnerability to global change. *Nature* 593 (7857), 90–94. doi: 10.1038/s41586-021-03483-6

Ricklefs, R. E., and He, F. (2016). Region effects influence local tree species diversity. *Proc. Natl. Acad. Sci. United States America* 113, 674–679.

Rocchini, D. (2007). Effects of spatial and spectral resolution in estimating ecosystem α-diversity by satellite imagery. *Remote Sens. Environ.* 111, 423–434. doi: 10.1016/j.rse.2007.03.018

Roslin, T., Hardwick, B, Novotny, V, Petry, WK, Andrew, NR, Asmus, A, et al. (2017). Higher predation risk for insect prey at low latitudes and elevations. *Science* 356, 742–744. doi: 10.1126/science.aaj1631

Sullivan, M. J. P., Lewis, S. L., Affum-Baffoe, K., Castilho, C., Costa, F., Sanchez, A. C., et al. (2020). Long-term thermal sensitivity of Earth's tropical forests. *Science* 368, 869–874. doi: 10.1126/science.aaw7578

Tomiolo, S., van der Putten, W. H., and Tielbörger, K. (2015). Separating the role of biotic interactions and climate in determining adaptive response of plants to climate change. *Ecology* 96, 1298–1308. doi: 10.1890/14-1445.1

Wagner, H. H. (2013). Rethinking the linear regression model for spatial ecological data. *Ecology* 94 (11), 2381–2391. doi: 10.1890/12-1899.1

Wallis, C. I. B., Brehm, G., Donoso, D. A., Fiedler, K., Homeier, J., Paulsch, D., et al (2017). Remote sensing improves prediction of tropical montane species diversity but performance differs among taxa. *Ecol. Indicators* 83, 538–549.

Wang, C., Yang, J., and Zhang, Q. (2010). Soil respiration in six temperate forests in China. *Global Change Biol.* 12 (11), 2103–2114. doi: 10.1111/j.1365-2486.2006.01234.x

Yu, Q., Rao, X., Ouyang, S., Xu, Y., Hanif, A., Ni, Z., et al. (2019). Changes in taxonomic and phylogenetic dissimilarity among four subtropical forest communities during 30 years of restoration. *For. Ecol. Manage.* 432, 983–1001. doi: 10.1016/j.foreco.2018.10.033

Zhang, J., Nielsen, S. E., Chen, Y., Georges, D., Qin, Y., Wang, S., et al. (2017). Extinction risk of North American seed plants elevated by climate and land-use change. *J. Appl. Ecol.* 54, 303–312. doi: 10.1111/1365-2664.12701

Zwiener, V. P., Lira-Noriega, A., Grady, C. J., Padial, A. A., and Vitule, J. R. S. (2018). Climate change as a driver of biotic homogenization of woody plants in the Atlantic Forest. *Global Ecol. Biogeogr.* 27, 298–309. doi: 10.1111/geb.12695

frontiers | Frontiers in Ecology and Evolution

TYPE Original Research
PUBLISHED 27 July 2023
DOI 10.3389/fevo.2023.1153448

Projected effects of climate change and urban expansion on species-level biodiversity of plants in main city clusters of Northern China

Tianxiao Ma[1], Yu Liang[1,2]*, Zhouyuan Li[3]*, Bo Liu[1], Mia M. Wu[1], Matthew K. Lau[4] and Yue Feng[1]*

[1]CAS Key Laboratory of Forest Ecology and Management, Institute of Applied Ecology, Chinese Academy of Sciences, Shenyang, China, [2]Key Laboratory of Terrestrial Ecosystem Carbon Neutrality, Liaoning, Shenyang, China, [3]China Grassland Research Center, School of Grassland Science, Beijing Forestry University, Beijing, China, [4]Department of Applied Sciences, University of Hawai'i, Kapolei, HI, United States

OPEN ACCESS

EDITED BY
Juergen Pilz,
University of Klagenfurt, Austria

REVIEWED BY
Lesley Lovett-Doust,
Nipissing University, Canada
Haimeng Liu,
Chinese Academy of Sciences (CAS), China

*CORRESPONDENCE
Yu Liang
liangyu@iae.ac.cn
Zhouyuan Li
lizhouyuan@bjfu.edu.cn
Yue Feng
lunamoon77@163.com

RECEIVED 29 January 2023
ACCEPTED 06 July 2023
PUBLISHED 27 July 2023

CITATION
Ma T, Liang Y, Li Z, Liu B, Wu MM, Lau MK and Feng Y (2023) Projected effects of climate change and urban expansion on species-level biodiversity of plants in main city clusters of Northern China.
Front. Ecol. Evol. 11:1153448.
doi: 10.3389/fevo.2023.1153448

Introduction: Northern China is considered a global hotspot of biodiversity loss due to dramatic climate and land use change characterized by rapid urban expansion. However, little is known that the impacts of these two drivers in shaping the future availability of habitat for plants in urban areas of Northern China, especially at a high spatial resolution.

Methods: Here, we modelled the habitat suitability of 2,587 plant species from the flora of Northern China and estimated how future climate and urban expansion may affect species-level plant biodiversity across three shared socioeconomic pathway (SSP) scenarios for the year 2050 in main city clusters.

Results: The results suggested that climate and urban expansion combined could cause a decline of up to 6.5% in plant biodiversity of Northern China, while urban expansion alone may cause 4.7–6.2% and climate change cause 0.0–0.3% by 2050. The contribution of urban expansion was higher in urban areas, while the contribution of climate change was higher in natural areas. Species may lose an average of 8.2–10.0% of their original environmentally suitable area. Our results verified that the process of urban expansion would necessarily result in large-scale biodiversity loss.

Discussion: The plant biodiversity loss in city clusters of Northern China was mainly determined by urban expansion rather than climatic change. The impact of climate change should not be ignored, since climate change will likely cause a higher reduction of area for some species. Based on these findings, we proposed that plant biodiversity loss in Northern China will accelerate in the future unless both urban expansion change and climate change are minimized.

KEYWORDS

climate change, urban expansion, plant biodiversity, species distribution modelling, Northern China

1 Introduction

Biodiversity loss has been reported as one of the most serious menaces to sustainable development, threatening the contribution and regulation of ecosystem services on which humanity relies (Steffen et al., 2015; Diaz et al., 2018; Roberts et al., 2021). A growing body of evidence indicates that the current rate of biodiversity loss is higher than that documented in historic times (Dirzo et al., 2014; Ceballos et al., 2020) and is predicted to further accelerate in future (Di Marco et al., 2019; Seebens et al., 2021). This is associated with significant natural and anthropogenic threats such as climate change (Scheffers et al., 2016) and the intensification of urban expansion (Simkin et al., 2022; Zhou et al., 2023), resulting in substantial reductions in habitat suitability and species' range size (Velazco et al., 2019). As two major drivers of terrestrial biodiversity loss (IPCC, 2021; Li et al., 2022; Newbold, 2018), impacts of climate change and urban expansion are usually estimated separately because of the differences in time scales and patterns of biodiversity loss (Gomes et al., 2019). A realistic scenario that guides ecological conservation policies should take the combined effects of climate change and urban expansion, which may be the greatest threat to future biodiversity, especially for plants (McDonald et al., 2020; Fang et al., 2021).

Climate-driven changes with the most pervasive impact on species redistribution, such as habitat loss and elevational range shifts (Powers & Jetz, 2019; Scheffers and Pecl, 2019), will affect global biodiversity patterns and shape new hotspots. This may be more profound in the future when climate change intensifies (Visconti et al., 2016). For example, recent climate change has likely exacerbated habitat loss and fragmentation in 18.5% of ecoregions, while 43.5% of ecoregions with loss is projected under future climate change scenarios (Segan et al., 2016). However, the responses of plant species to climate change are complex and hard to predict (Corlett, 2016). Projected changes in climate differ among regions and across emissions scenarios, potentially leading to distinct ecological responses of plants across the world (Di Marco et al., 2019). Furthermore, biodiversity decline is substantially underestimated when indirect interactions between climate change and other stressors (e.g. urban expansion, pollution) are neglected (Arneth et al., 2020). Thus, it will be important to know how climate change will affect plant species and how it combines with other major threats.

Urban expansion occurs alongside threats to biodiversity driven by climate change, contributing to global biodiversity declines. Here, "urban expansion" was defined as the increase in the area of cities or towns, which is different from the term "urbanization" that usually was used to refer to the change in the proportion of a population living in an urban area (McDonald et al., 2020). The urban area tends to alter the type of habitats available (Geschke et al., 2018), support more invasive species (McKinney, 2006), and produce rapid eco-evolutionary change (Alberti et al., 2017). In addition, urban expansion can accelerate urban microclimate change, increase warming in urban and the intensity of precipitation in the local area (Krayenhoff et al., 2018). These impacts generally rise with urban area expansion and intensity in changing climate, resulting in significant changes in the abundance and composition of species when urban area replaces natural habitat (McDonald et al., 2020). Existing researches demonstrate that future global urban expansion will lead to 11–33 million hectares of natural habitat loss and a 34% reduction in species richness by 2100 (Li et al., 2022). Despite the apparent importance of urban expansion as a driver of habitat loss, three main shortcomings in present forecasts for urban impacts on biodiversity. The first concerns driving factors, which until recently have not considered climate change and urban expansion together (Li et al., 2022; Simkin et al., 2022). The second shortcoming is that most studies are conducted on a single climate change scenario and coarse spatial resolution (Seto et al., 2012; McDonald et al., 2020). The third shortcoming is that existing studies only focus on vertebrates without containing plant species (Li et al., 2022; Simkin et al., 2022), which are more sensitive to climate change and urban expansion (Burley et al., 2019). Therefore, such forecasts become less useful and an updated set of forecasts to overcome these limitations is required.

Northern China is considered a global hotspot of biodiversity loss due to dramatic climate and land use change characterized by rapid urban expansion in the past few decades and projected future (McDonald et al., 2018; McDonald et al., 2020). From 1978, the Chinese government implemented large-scale ecological restoration programs (Fu et al., 2018) to prevent further ecological problems in Northern China. Thus, the combined effects of natural and anthropogenic factors have been, still are, and will be shaping biodiversity patterns in Northern China (Mi et al., 2021). However, few studies examined the impacts of climate change and urban expansion on the biodiversity of plants simultaneously, as shortcomings existed in present studies. This inadequacy limits our understanding of the spatiotemporal heterogeneity in biodiversity and the underlying mechanisms behind the effects of climate change and urban expansion. Realistic forecasting of plant biodiversity changes in the urban area of Northern China is urgently needed to explore the underlying mechanisms of species distribution, quantify threats to endangered species and evaluate the interaction between biodiversity and socioeconomic development.

Here, we aim to quantify (i) changes in species-level biodiversity of plants due to climate change and urban expansion, (ii) the relationship between changes in species-level biodiversity and climate change/urban expansion, and (iii) the relative importance of these two drivers to the future species range and richness in five main city clusters of Northern China. Specifically, we hypothesized that: (a) combined effects of projected climate change and urban expansion will cause substantially larger losses of habitat suitability; (b) species with smaller increased temperature and greater increased precipitation are more negatively affected by climate change and urban expansion; and (c) urban expansion has the higher relative contribution than climate change for change in species-level diversity under all climate change scenarios. To test these hypotheses, we estimated the area of occupancy (AOO) for 2,587 plant species based on a species distribution model (SDM) in

Northern China. We then quantified the species richness and its changes produced by historical urban expansion, three scenarios of urban expansion for 2050, three scenarios of climate change for 2050 and their interactions. Specifically, we investigated how projected changes in climate and urban area affect the AOO and species richness in five main city clusters of Northern China, which is a relatively rapid urban expansion and highly threatened region. The results would highlight important implications of our study for biodiversity conservation of plant and help form better planning for ecological restoration project in Northern China.

2 Method and materials

2.1 Study area

Northern China has a large area, which consists of 236.14 million km^2 with 8 Provinces and Municipalities (Figure 1). The average annual precipitation of this area varies between 300 and 1000 mm, and the annual average temperature ranges from −3 to 10°C. To quantify the impacts of climate change and urban expansion on species-level biodiversity, five main city clusters (79% of urban area in Northern China) were focused (Table 1 and Figure S1) in analysis. The five main city clusters include Beijing-Tianjin-Hebei (BTH), Central-South Liaoning (CSR), Harbin-Changchun (HC), Hohhot-Baotou-Ordos (HBO), and Middle Shanxi (MS). Detailed information of city clusters was also given in Table 1.

2.2 Data source and processing

2.2.1 Species occurrence data

20,892,510 raw occurrences of plants were obtained from Global Biodiversity Information Facility (GBIF, www.gbif.org) and iPLANT platform (www.iplant.cn). To avoid problems in SDM related to modelling with partial geographic ranges, the occurrences in Northern China and also all occurrences in Eurasia were obtained for each species (Raes, 2012). To improve the quality of these records, we used the R package "CoordinateCleaner" (Zizka et al., 2019) to flag and remove records that satisfied any of the following criteria: 0,0 coordinates, coordinates in an ocean, coordinates within 5 km of country centroids and capitals, records within 1 km of biodiversity institutions, and records with reversed latitude and longitude values. After removing these geographical errors, we cleaned the species names by removing unusual characters and uncertain identifications, and assigned all single occurrence at the species level. Then, we checked synonyms and used accepted names, and kept only species occurring in the eight provinces of Northern China according to Flora of China (FOC) from iPLANT. Our database was composed of 325,027 unique records, representing 3,214 total species (92% of the 3,503 species of Northern China).

All species with a small number of collections were tested with all datasets to identify poorly collected species (Ter Steege et al., 2015). Only species occurring in 5 or more unique locations had their habitat suitability modelled. This procedure ensured that each species had robust range size (Rivers et al., 2011) and an

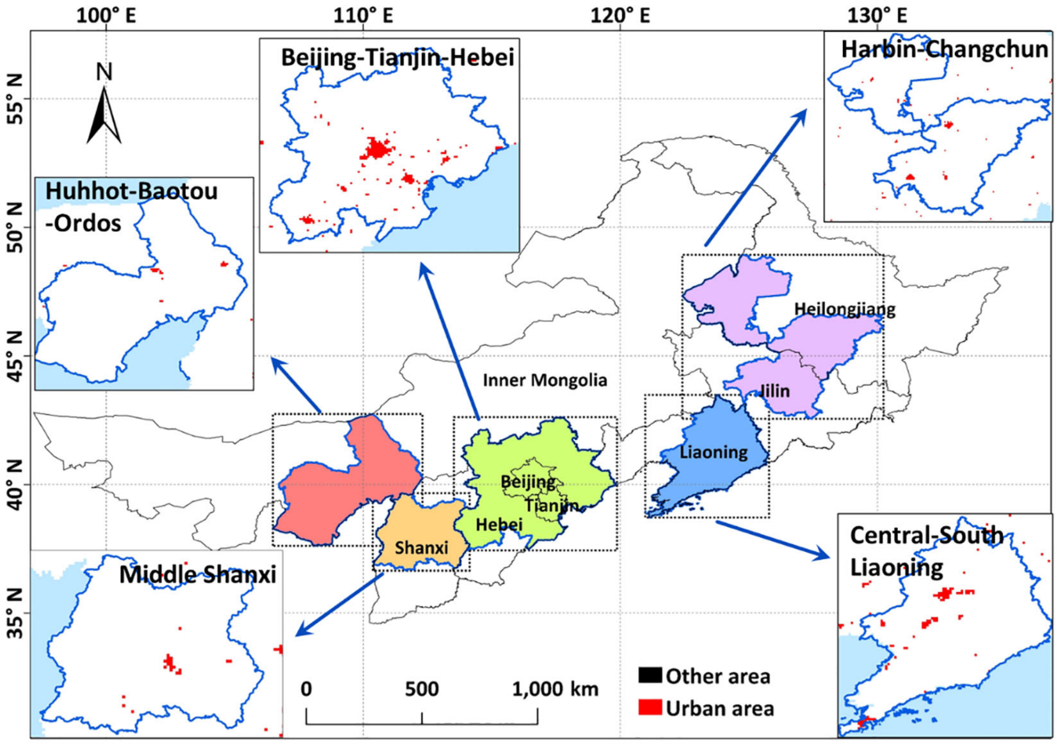

FIGURE 1
Spatial pattern of main city clusters in Northern China.

TABLE 1 The detailed information of five main city clusters in Northern China.

Urban cluster	Abbreviation	Area (km^2)	Annual average precipitation (mm)	Annual average temperature (°C)	Population density (people per km^2)
Beijing-Tianjin-Hebei	BTH	311,210	1,076.8	12.9	1,370
Central-South Liaoning	CSL	171,631	796.1	9.9	294
Harbin-Changchun	HC	346,253	751.8	5.5	111
Middle Shanxi	MS	119,380	593.6	10.4	238
Huhhot-Baotou-Ordos	HBO	223,923	390.7	7.3	21

environmental suitability model significantly different from a bias-corrected null models (Gomes et al., 2019), which is important to fit reliable habitat suitability models (Thibaud et al., 2014). Species with a small number of collections (<5) and not present in the final dataset based on a restricted number of locations (Gomes et al., 2019). Consequently, further modelling and analyses were conducted for 2,587 plant species (74% of the total species).

2.2.2 Current and future climate data

To estimate the area of occupancy (AOO) for each species based on environmental suitability, we initially obtained 19 bioclimatic variables derived from the current climate at 30 seconds spatial resolution (approximately 1 km at the equator) from WorldClim (Hijmans et al., 2005, https://www.worldclim.org/), which were produced using monthly interpolated climate data. For future climate data, we used multi-model ensemble estimates of 19 bioclimatic variables from seven global climate model (GCM) projections (including ACCESS-ESM, BCC-CSM2, FIO-ESM2, GFDL-ESM4, INM-CM5, IPSL-CM6A-LR, and MIROC6) for the IPCC Sixth Assessment Report (AR6). These selected future climate datasets were also downloaded from the WorldClim Database. The derived bioclimatic variables were used to assess the effects of climate change in the year 2050 (average for 2041–2060) under the three shared socioeconomic pathways (SSP126, SSP245, and SSP585), which represent taking the sustainability, middle of the road, and the fossil-fueled development, respectively (You et al., 2021; Li et al., 2022). SSP126, SSP245, and SSP585 typically lead to 421 ppm, 538 ppm, and 936 ppm of CO_2 concentrations by the year 2100, which represent low, moderate, and high emission scenario separately (Tian and Zhang, 2020).

Due to spatially correlated bioclimatic variables, we selected the less correlated predictor variables based on their biological relevance and on their scores using Spearman's rank correlation coefficient threshold $|\rho| > 0.7$ (Dormann et al., 2013). Those variables that presented correlation values over 0.7 were removed from the analysis (Supplementary materials Figure S1). For the final modelling stage, we selected six less correlated predictor variables: mean diurnal range (BIO2), Isothermality (BIO3), temperature annual range (BIO7), mean temperature of warmest quarter (BIO10), annual precipitation (BIO12), precipitation seasonality (BIO15). These climatic parameters were preprocessed to a general spatial resolution of 5 km as it represents a fine scale to avoid undesired distortions and recognize spatial patterns (Leao et al., 2020).

2.2.3 Data of urban expansion

Current (2015) and projected future (2050) patterns of urban expansion with three selected SSP scenarios in Northern China were obtained from the global projection of urban expansion dataset (Chen et al., 2020; https://doi.org/10.1594/PANGAEA.905890), which describes the grid cells of 1km resolution occupied by current and future urban land demand (Supplementary materials Figure S2). This dataset used panel data regression to estimate future urban land areas based on the factors of population, urbanization rate (percentage of urban population to total population) and gross domestic product (GDP). In this study, we selected three climate change scenarios (SSP126, SSP245, and SSP585) which represent sustainability, middle of the road, and fossil-fueled development routes, respectively (Jiang and O'Neill, 2017). Specifically, SSP126 ("sustainability" scenario) envisions a development path of rapid urban expansion with high income growth for all country groups. SSP245 ("middle of the road" scenario) envisions a development path of moderate urban expansion and moderate income growth for all country groups. SSP585 ("fossil-fueled development" scenario) envisions that all country groups will experience rapid urban expansion. Under SSP126, SSP245, and SSP585, urban area corresponds to predictions of 65%, 55% and 70% expansion for 2050 in five main city clusters of Northern China, respectively.

To further estimate the spatial distribution of biodiversity change due to urban expansion under three SSP scenarios in each 5 km grid cell, we calculated the fraction of area that will be occupied by urban expansion between 2015 and 2050. We then multiplied this value by the number of species in each grid cell to estimate the potential number of species change due to urban expansion (Li et al., 2022). Generally, the species with lower habitat suitability are more vulnerable to urban expansion. To determine which species are affected by urban expansion, we estimated the habitat suitability using Maxent models for each species and all species were sorted by their habitat suitability in each grid cell. Species with lower habitat suitability for the potential number of species loss were regarded as the species affected by urban expansion. Corresponding grid cells were eliminated from the AOO of affected species.

2.3 Estimating the area of occupancy for each species in Northern China

In this study, we used the maximum entropy model (Phillips et al., 2006; Maxent version 3.4.1) to estimate the area of occupancy (AOO) in Northern China. For each species, 75% of the occurrence data were used as a training model and the remaining 25% for validating the Maxent model. Climate values from 10,000 randomly sampled points records as background data to account for sampling intensity and reduce spatial sampling bias (Thornhill et al., 2017). The algorithm runs either 1000 iterations of these processes or continues until convergence (threshold 0.00001). The modelling extent was restricted to the complete area of Eurasia, which was used for all species models. MaxEnt models were generated using 10 cross-validated replicate runs with the aforementioned parameters. Outputs were transformed into binary maps with a 10% training presence threshold and restricted to Northern China by clipping.

To calibrate and validate the performance of the Maxent model, threshold-independent receiver-operating characteristic (ROC) analyses were used (Phillips et al., 2006). An area under the ROC curve (AUC) was examined for additional precision analyses. The AUC values between 0 and 0.5 indicate predictions are no better than random and the highest value of 1 gives the best prediction (Elith et al., 2011). The average AUC training value was 0.949, indicating both models performed well and generated excellent evaluations. We also used a Jackknife test and the percent variable contribution to identify the relative importance of each variable. In MaxEnt, the jack-knife test systematically drops one variable each time and compares the predictions using the model with all variables except the dropped one and a model based on that variable only (Phillips et al., 2006).

To estimate the impacts of urban expansion and climate change on plants in Northern China, we produced eleven different scenarios (Table 2). First, we modelled the species' current AOO

TABLE 2 Results for all scenarios showing estimation of change in AOO and mean species richness.

Scenario	City clusters		BTH		CSL		HC		HBO		MS	
	Average change in AOO (%)	Mean species richness	Average change in AOO (%)	Mean species richness	Average change in AOO (%)	Mean species richness	Average change in AOO (%)	Range of species richness	Average change in AOO (%)	Mean species richness	Average change in AOO (%)	Mean species richness
Current	0.0	1,280	0.0	1,621	0.0	1,667	0.0	1,203	0.0	668	0.0	1,218
Current and 2015 urban area	−3.8	1,227	−4.8	1,498	−2.9	1,598	−1.7	1,178	−1.2	663	−1.0	1,196
SSP126	1.0	1,304	0.5	1,645	3.2	1,676	0.1	1,206	6.5	706	0.0	1,286
SSP245	0.0	1,274	0	1,610	0.2	1,666	0.0	1,178	2.5	675	0.0	1,241
SSP585	−0.3	1,265	0.2	1,647	0.0	1,623	0.0	1,169	0.0	627	0.0	1,232
SSP126 and 2015 urban area	−2.7	1,249	−2.5	1,522	−1.7	1,606	−0.8	1,180	4.0	701	−0.2	1,261
SSP126 and 2050 urban area	−3.7	1,237	−4.0	1,493	−2.4	1,590	−1.2	1,176	3.6	700	−0.5	1,255
SSP245 and 2015 urban area	−3.8	1,220	−4.0	1,488	−1.8	1,597	−1.3	1,154	0.5	670	−0.3	1,219
SSP245 and 2050 urban area	−4.7	1,210	−5.2	1,463	−2.4	1,584	−1.7	1,150	0.3	669	−0.5	1,214
SSP585 and 2015 urban area	−5.3	1,212	−3.2	1,526	−2.9	1,555	−1.7	1,145	−0.6	623	−0.3	1,209
SSP585 and 2050 urban area	−6.5	1,198	−4.9	1,492	−3.8	1,537	−2.1	1,140	−0.9	622	−0.6	1,202

For change in AOO, positive values represent expand of AOO, whereas negative values represent loss of AOO.

with and without considering urban area. Then, we estimated the impacts of climate change by modelling the species' AOO of 2050 (SSP126, SSP245, and SSP585) without considering urban area. Furthermore, we calculated the impacts of six combined scenarios of urban expansion and climate change: 1) no urban expansion: SSP126, SSP245, and SSP585 with 2015 urban area; 2) urban expansion: SSP126, SSP245 and SSP585 with their corresponding 2050 urban area. Considering these eleven scenarios, we produced species distribution model (SDM) maps for all species, and species richness maps (defined as the number of species per grid cell) by adding the predicted species in each grid cell for each scenario to assess species richness.

2.4 Data analysis for main city clusters in Northern China

To reflect the potential impact of urban expansion and climate change, the range of analyses presented here was restricted to five main city clusters based on projected results of Northern China under eleven scenarios. We first calculated the change in species richness and AOO of each scenario to evaluate future changes in species distribution. The change in species richness and AOO was calculated as the difference between the projected results under scenarios for the years 2050 and scenarios without considering urban area in 2015. For analyzing the individual and combined effects of urban expansion and climate, we separated the change of urban area and climate when designing the scenarios (see the names of these scenarios in Table 2). For example, we could estimate the individual effect of climate change under SSP585 by comparing the "current" and "SSP585" scenario; we could estimate the individual of urban expansion by comparing the "SSP585 and 2015 urban area" and "SSP585 and 2050 urban area" scenario. For combined effects, we could compare scenarios which has different conditions of climate and urban area. In addition, we fitted simple ordinary least-squares regression models to understand how changes in species richness and AOO change relate to increased temperature, precipitation, and urban expansion to examine the roles of urban expansion and climate influences on vegetation dynamics. Finally, we used the metrics proposed by Lindeman, Merenda, and Gold (LMG) (Grömping, 2006) to quantify the relative contributions of climate change and urban expansion to the variation of the species richness dynamics in each 25 km^2 grid cell of five main city clusters under three climate change scenarios.

3 Results

3.1 Changes in species-level biodiversity of plants due to climate change/urban expansion

Urban expansion is the major cause of species that may lose sufficient AOO to become threatened, while the losses of species richness produced by combined effects of climate change and urban expansion are expected to be higher (Table 2). The mean current species richness in the urban area of Northern China was 1,280. The 2015 urban area was responsible for a mean decline of 3.8% in the estimated AOO of plant species. Current species richness was higher in CSL and BTH, while loss by urban area mainly occurred in the same region. The average change in AOO by 2050 was 1.0%, 0.0%, and −0.3% in the SSP126, SSP245, and SSP585 scenario without considering urban expansion, whereas mean species richness is expected to slightly decrease under SSP245. Compared to the current scenario, climate change scenarios have a lower average change in AOO. Under the SSP126 scenario, the species richness will increase in most city clusters. Under the SSP245 climate scenario, the AOO stayed the same as current scenario. Under the SSP585 climate scenario, the species richness will have a great loss, and the change in AOO will shift from gain to loss.

The combined effect of urban expansion and climate change is a greater threat to plant biodiversity in Northern China under SSP585. The projected urban expansion for 2050 (with urban growth of 65% in SSP126, 55% in SSP245, and 70% in SSP585) is expected to produce an average loss of AOO of 3.7%, 4.7%, and 6.5% for SSP126, SSP245, and SSP585, respectively. The patterns of change in losses of species richness by urban expansion are consistent with the projections of urban area. As the projected urban expansion is high in BTH, species richness was predicted to suffer higher impacts of urban expansion in BTH.

Species richness is more negatively affected by the combined effects of climate change and urban expansion, and by the independent effects of urban expansion (Figure 2). When

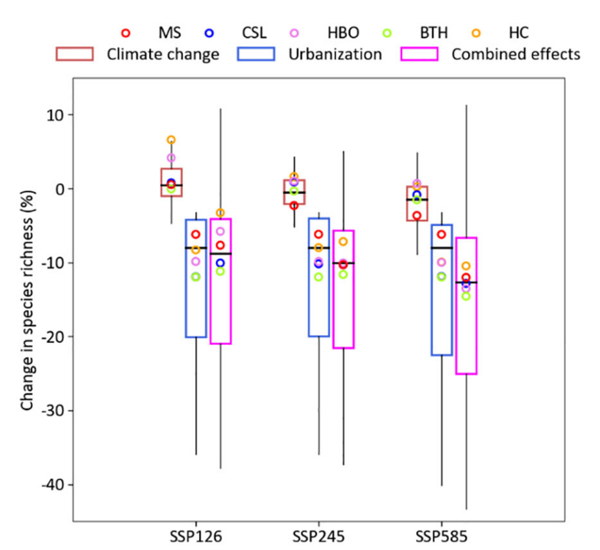

FIGURE 2
Box plot of the predicted effects of climate change and urban expansion for change in species richness given the three scenarios in the year 2050 at the urban area.

simulating the effects of climate change alone and keeping urban area constant, the mean species richness of each grid cell increased by 0.5% under SSP126 (min. = −6.6%, max. = 8.3%), decreased by 0.5% under SSP245 (min. = −6.8%, max. = 5.9%) and by 1.4% under SSP585 (min. = −11.2%, max. = 7.1%). Simulating the effects of urban expansion alone, keeping the climate constant, reduced the mean species richness of each grid cell by around 8% for all three climate change scenarios (min. = −40.0%, max. = −3.2%). The combined effect of climate change and urban expansion reduced the mean species richness of each grid cell by 8.7% under SSP126 (min. = −36.3%, max. = 11.3%) by 10.1% under SSP245 (min. = −35.3%, max. = 8.2%) and by 12.7% under SSP585 (min. = −42.5%, max. = 10.9%). In addition, our prediction showed that the negative effects of urban expansion to the urban area in the high latitude (e.g. HC) would become more significant.

Few species gained AOO due to projected combined change in climate and urban area, while the majority of the species lost substantial amounts of AOO (Figure 3). The mean change in AOO by climate change was 1.4% in the SSP 126 scenario, 0.3% in the SSP245 and −0.7% in the SSP585 (Figure 3A). Mean AOO is expected to decrease by urban expansion between 5.1% in SSP245 and 5.4% in SSP585. The best-case combined scenario for 2050 resulted in a mean loss of estimated AOO of 3.9% (SSP126), followed by SSP245 with 4.9%, and the worst-case combined scenario (SSP585) with 6.7%. Another striking aspect of the predicted combined impacts is the right-skewed distribution of changes in AOO (Figures 3B–D). Future AOO was at least 10% smaller for 31% of the species under SSP126, 36% of the species under SSP245, and 38% of the species under SSP585. In contrast, future habitat suitability was at least 10% larger for only 10% of the species under SSP126, and 7% of the species under SSP245 and SSP585.

3.2 Relationship between changes in species-level biodiversity and climate change/urban expansion

Under effects of climate changes and urban expansion, the correlation between change in species richness and climatic driving factors were converse (Figure 4). Due to the effect of climate change, grid cells with larger increased precipitation and smaller increased temperature lost larger species richness, especially for city clusters with lower urban expansion (e.g. HBO and HC). In contrast, grid cells lost larger species richness with smaller increased precipitation and larger increased temperature due to urban expansion and combined effects. Across SSP scenarios, this pattern of correlation is more obvious under scenario SSP585 than under other scenarios. It is consistent for all scenarios that projected urban expansion is expected to reduce species richness.

Changes in AOO were negatively associated with increased annual precipitation, temperature, and urban expansion, especially for SSP585 due to urban expansion and combined effects (Figure 5). Linear regressions between the factors and changes in AOO were significant at a 99% confidence level. The slopes of linear regression indicate that there is more loss in estimated AOO with much larger increased annual precipitation, temperature, and urban expansion, particularly true in temperate regions with high urban expansion (e.g. BTH and CSL).

3.3 Relative contribution of climate change and urban expansion

The contribution of urban expansion and climate change suggested that urban expansion (> 50%) is the key driving factor for

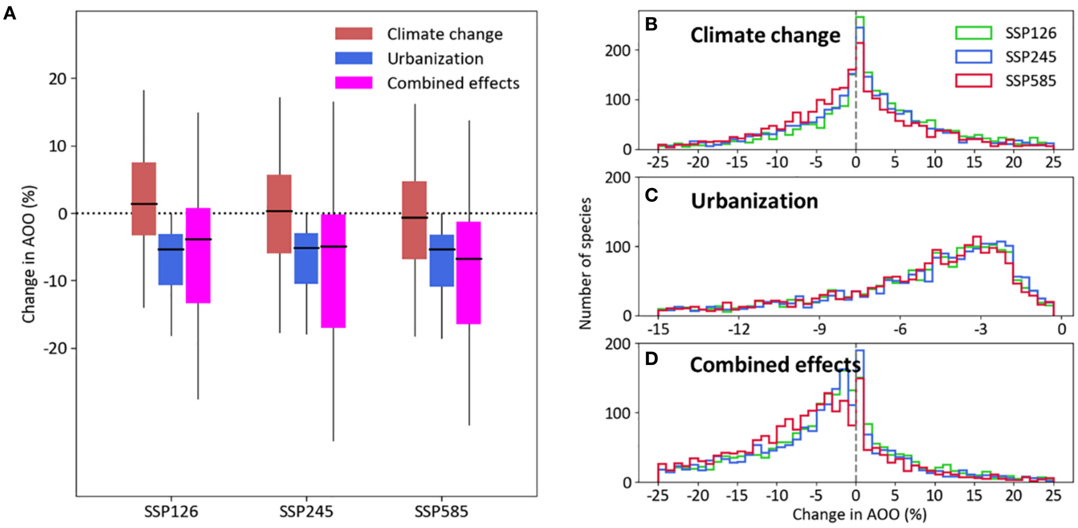

FIGURE 3
(A) Box plot of the predicted effects and **(B–D)** frequency distribution of climate change and urban expansion in AOO change given the three scenarios for climate change and urban expansion in the year 2050. In **(A)**, lines inside the boxes show median effects, the lower and upper limits of the boxes show first and third quantiles respectively, and whiskers show range from minimum to maximum values excluding outliers (not shown).

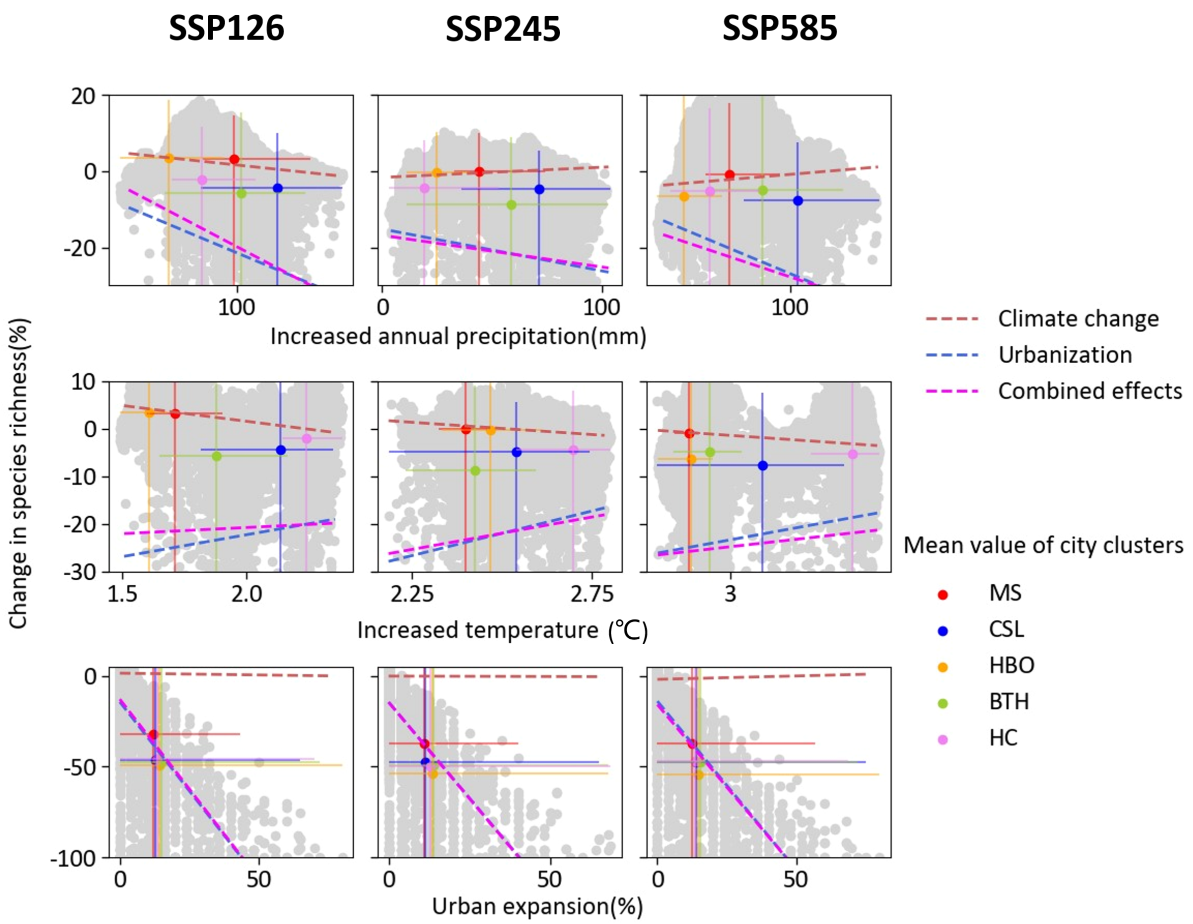

FIGURE 4
Relationship between the magnitude of species richness of change and driving factors (increased annual precipitation, increased temperature and urban expansion) in each climate change scenarios. Grey points represent change in species richness and corresponding driving factors in each grid. Colorful points indicate mean values of city clusters. Error bars shows the range of x- and y-axis values of corresponding city clusters. Lines are the fitted lines based on the generalized least squares model in natural and urban area. Significance levels $p < 0.01$ for all fitting.

the change in species richness under all climate change scenarios in the urban area (Figure 6). Around 89%, 92%, and 82% area of change in species richness could be mainly explained by urban expansion for SSP126, SSP245, and SSP585, respectively (Figure 6A). The contribution ratio of urban expansion exceeded 60% in all city clusters (Figure 6B). The responses of species richness to climate change and urban expansion exhibited strong discrepancies among city clusters. More developed city clusters with more precipitation (i.e. BTH and CSL) would be more sensible to the effect of urban expansion (Figure 6B). It showed that species richness of southern BTH was more sensitive to the effect of climate change across scenarios. The species richness of CSL displayed higher sensitivity to the effect of urban expansion. The species richness of MS was sensitive to climate change under SSP126, whereas the species richness of MS was mainly affected by urban expansion under the other two scenarios. In addition, the contribution ratio of MS had a greater variation than other city clusters among climate change scenarios. The species richness of HC demonstrated strong sensitivity to climate change under SSP585.

At different city clusters, the relative contributions of climate change and urban expansion to changes in AOO strongly vary depending on the climatic characteristic and level of urban expansion for different future scenarios (Figure 7). The changes in AOO were mainly explained by urban expansion, while the contribution of climate change was less than 20%. In contrast, the relative contribution of urban expansion exceeded 80% in all city clusters. Generally, the higher relative contribution of urban expansion were found in CSL, BTH, and HC, and the lowest one was in HBO (less than 88%). Compared to other city clusters, the variation of relative contribution was higher in arid region, such as MS and HBO with 9–11% and 13–15% for relative contribution of climate, respectively.

4 Discussion

Our results demonstrated that biodiversity loss will accelerate in the future unless both urban expansion and climate change are minimized. In particular, if the sustainable pathway (i.e., scenario SSP126) is properly implemented, humans will be able to maintain a relatively low natural habitat loss and a high level of species conservation. On the other hand, SSP585 and 2050 urban area was the most extensive biodiversity loss among the three climate scenarios. This finding is in accordance with the results of Li et al. (2021), which claimed that greater declines in habitat quality would be observed under SSP585. However, it is different that urban expansion *per se* was the predominant driver of biodiversity loss rather than climate change due to the different methods used to assess their impacts. In addition, we noticed that species' sensitivity to climate change and urban expansion varies among scenarios and regions (Table 2). The existence of such geographical and climatic variation implies that attempts to extrapolate the impact of climate change and urban expansion may be misleading (Newbold et al., 2020). This suggests that further work on the impacts of climate change and urban expansion (based on multi-source datasets) at different regions and scenarios is needed to achieve precise conservation of plant biodiversity. Avoiding the SSP585 scenario should be largely beneficial to the conservation of plant species in Northern China.

Our results suggested that losses of habitat area will be much larger from the impacts of urban expansion than climate change (Table 2; Figures 2, 3), which is consistent with the findings from other studies at the national scale (Li et al., 2020). Our results showed the urban expansion may cause 4.7–6.2% of loss in plant biodiversity. This is consistent with other literature, which showed the loss caused by urban expansion ranged from 3.3% to 10.4% (He et al., 2014; Tang et al., 2021). Although the influences of temperature and precipitation among different climate change scenarios were very similar, the response of species richness and mean geographic range (AOO) to temperature and precipitation exhibited strong differences (Figures 4, 5). Our results are in agreement with previous studies that temperature tended to negatively affect species' geographic range in Northern China, whereas the temperature positively affects the species richness (Li et al., 2020; Figures 4, 5). The spatial shift of species' geographic range (i.e. AOO changes) reflects the ability of tracking suitable climatic conditions at the regional scale, while species richness reflects the ability of adapting to the new climatic conditions in the local range (Bellard et al., 2012). The opposite response of AOO and species richness to climate change with the positive effect of temperature on AOO changes indicate that plant species of Northern China tend to adapt to the new conditions rather than shift to a different habitat.

Urban expansion explained above 85% of the variations in plant species richness of urban areas under all scenarios (Figure 6), which indicated that the effects generated by urban expansion should not be ignored. Specifically, the future urban expansion will disproportionately affect the natural habitat around the urban area. The biodiversity loss becomes higher in as urban areas get closer to the patch edges of natural habitat. In addition, the key biodiversity hotspots and ecologically vulnerable ecoregions that have higher plant species richness will suffer the highest percentage

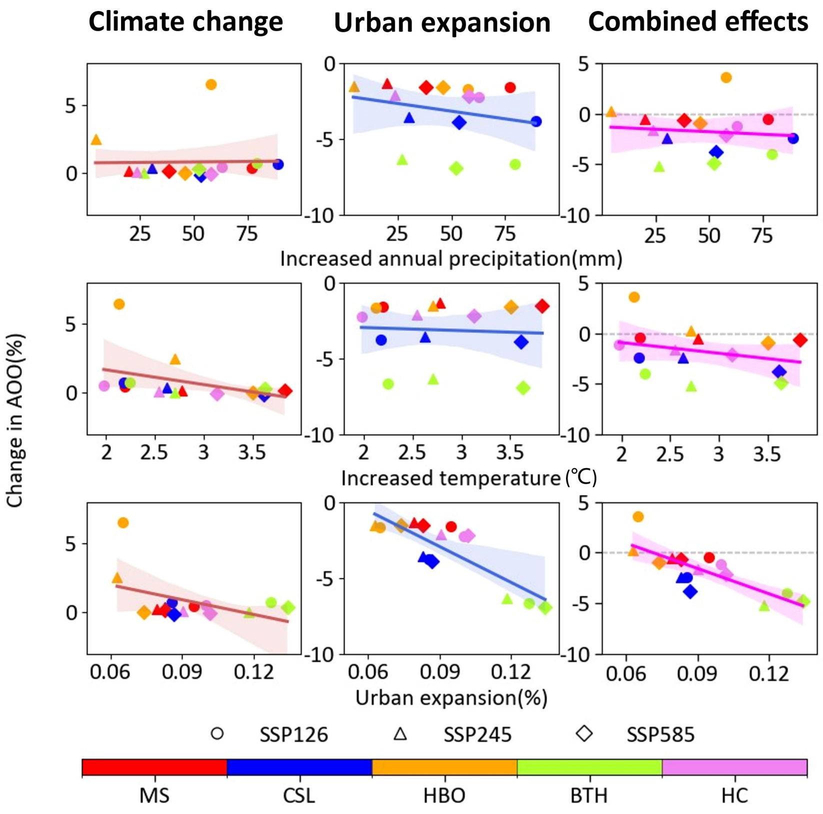

FIGURE 5
Relationships between projected change in species' AOO and increased annual precipitation, increased temperature and urban expansion in different city clusters under SSP126, SSP245 and SSP585 due to climate change, urban expansion and their combined effects. The linear fits are also shown each subplot.

of urban expansion such as BTH, CSL, and MS (Figure 6). These city clusters usually have a population density higher than 200 people/km^2 (Zhou et al., 2021), indicating explicit shifts and depletion of plants occurs when exceeding 200 people/km^2. For these city clusters with high population density and located in biodiversity-vulnerable regions, choosing an appropriate urban development pathway may be the most considered requirement for balancing urban expansion and biodiversity conservation of plant (Peng et al., 2016).

The combined effects of urban expansion and climate change are the greatest threat to plant biodiversity in Northern China. In regions with lower increased temperature, high urban expansion, and higher increased precipitation, species richness was more sensitive to the combined impacts of urban expansion and climate change (Figures 4, 5). *Leersia* spp. and *Amaranthus* spp. suffered more than other species. This pattern may be related to species in numerous human-dominated land uses (e.g. Northern China), which have been found to have higher proportions of individuals affiliated with higher temperatures and lower precipitation levels than that within natural habitats (Williams and Newbold, 2020). When the increased temperature is lower and increased precipitation is higher, species in Northern China with higher temperatures and lower precipitation levels are more susceptible and often suffer from projected changes in climate. More attention should be given to such relatively susceptible regions and species, which is important for biodiversity conservation under future climate change.

In our study, we quantified biodiversity loss by using species richness and AOO, which represent two aspects of species-level biodiversity dynamics. Change in AOO, which can include changes in range size or location of species, can be driven by changes in local habitat suitability (Molinos et al., 2015). Changes in species richness are driven by individual species shifting their ranges (i.e. AOO) into or out of a region (Batt et al., 2017). Therefore, the selection of indicators substantially determines whether the climate change or urban expansion are important for biodiversity loss. Our results indicated that plant species richness is more sensitive to the combined changes in climate and urban area (Figures 2, 3). However, changes in plant species richness are more commonly driven by the loss due to the impact of urban expansion for multiple species to shift their geographic ranges (Figures 2, 3) and become more common as urban expands for future developed scenarios (Li et al., 2022). Currently, less clear is how species-level range size affects plant species richness at regional scales. Future work should consider whether climate change or urban expansion played a role in affecting range sizes and richness of plant species, and how the timing of changes in these two drivers affect.

Applying broad-scale models to analyze the response of biodiversity to both urban expansion and climate change has several important known limitations. First, we only examined how future urban expansion will directly affect plant biodiversity without considering its indirect effects. Indirect impacts include the impacts of resources (e.g. Energy and food) and wastes (including solid, liquid and gaseous wastes) from urban areas (McDonald et al., 2020). Although it is currently difficult to accurately quantify such indirect effects which are not simply additive, high-resolution data may facilitate us to analyze the embodied biodiversity loss from such indirect effects. Second, due to a lack of available future land

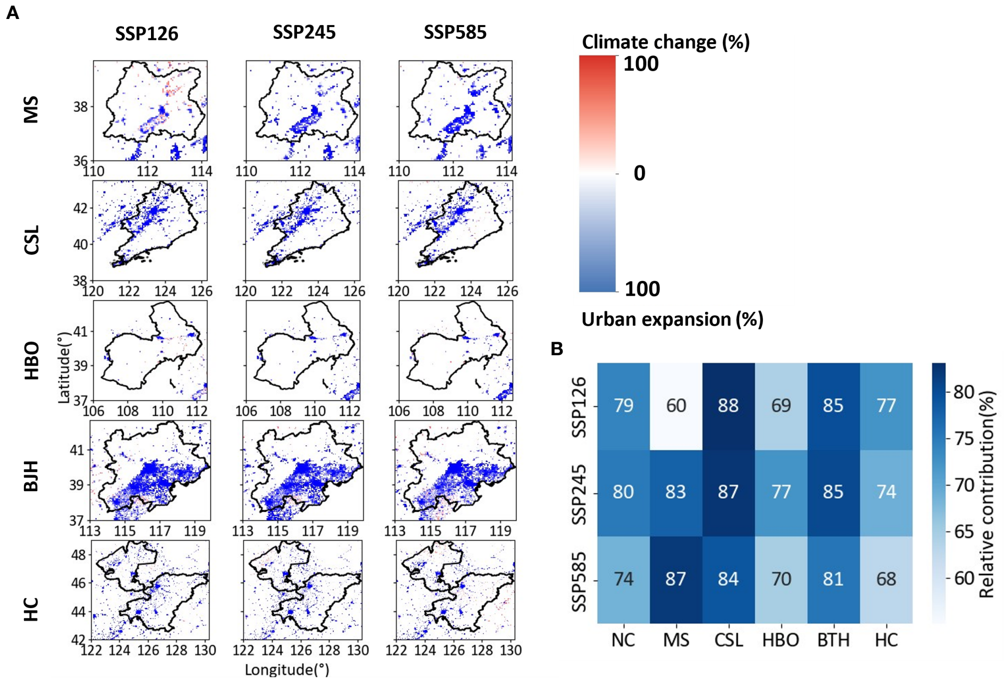

FIGURE 6
(A) Spatial distributions and **(B)** mean value of the relative importance of climate change and urban expansion for the projected change in species richness in different city clusters of Northern China under SSP126, SSP245 and SSP585.

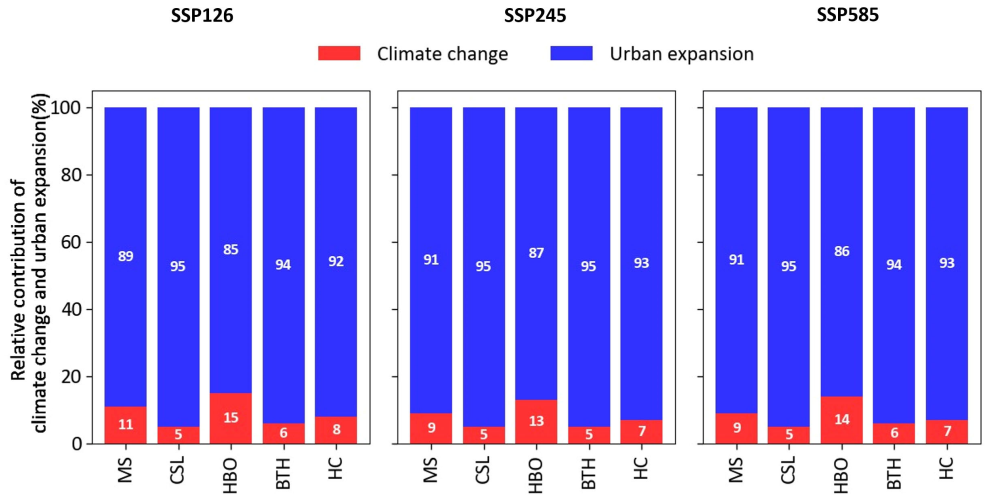

FIGURE 7
Relative importance of climate change and urban expansion for the projected change in AOO for species of different city clusters under three scenarios in Northern China.

cover and dynamic biodiversity data, we could not accurately estimate the dynamic changes in habitat fragmentation and biodiversity losses due to climate change and urban expansion. Third, we used SDM based on presence-only data for estimating species habitat suitability to reflect biodiversity patterns. However, the time lag between the reduction in habitat suitability and the loss of biodiversity may be large enough to hinder our perception of climate change and urban expansion, particularly for plants (Leao et al., 2021). In addition, rare species and species with few records are also probably over-predicted (Gomes et al., 2019). Finally, though our results suggest that plants in urban areas of Northern China may lose lower proportions of their habitat from climate change, this should not be taken as evidence that climate change is not a major threat in urban areas. Current CMIP6 climate data forecast more extreme changes in climate, and therefore greater losses in biodiversity, which should be particularly concerning in future research because previous estimates were based on climate data that typically project smaller climate changes.

5 Conclusion

In this study, we quantified the effects of climate change and urban expansion on plant biodiversity by mapping the variations of species' habitat range and richness of Northern China for the current and the year 2050. Firstly, urban expansion rather than climate change will likely cause more losses to the species richness of plants during the next several decades in city clusters of Northern China. The contribution of urban expansion was higher in urban areas which have higher plant species richness and population density. Secondly, the combined effects of projected urban expansion and climate change are the greatest threat to plants in Northern China, especially under the SSP585 scenario. It should be noted that the SSP585 scenario should be avoided to benefit the conservation of plant species. Thirdly, the results indicate that species with smaller increased temperature and greater increased precipitation are more negatively affected by climate change and urban expansion. These findings will be beneficial in future urban built-up strategies and policy decisions to enable both the satisfaction of human needs and biodiversity maintenance. For future research, other impacts of urban expansion (e.g. road expansion, afforestation, or agricultural activities) and climate (e.g. fire, solar radiation, nitrogen deposition, or rising CO_2) need to be further investigated to improve our understanding the dynamics of plant biodiversity. Also, policy-related issues of urban expansion in regard to the intensity of settlement (high density high-rise apartment buildings, or larger single-family properties with gardens, etc.) and transportation system (public transit, personal vehicles etc.) could be useful areas to explore in future.

Data availability statement

The original contributions presented in the study are included in the article/Supplementary Material. Further inquiries can be directed to the corresponding authors.

Author contributions

TM: Methodology, Software, Writing – Original Draft, Visualization. YL: Supervision, Funding acquisition. ML: Writing – Review and Editing, Project administration. BL: Writing – Review and Editing, Investigation. MW: Validation, Formal analysis. YF: Writing – Review and Editing, Conceptualization, Supervision. All authors contributed to the article and submitted and approved the submitted section.

Funding

This research was supported by the National Natural Science Foundation of China (Grant No. 31961133027, 31971486, 42050410324, 32171562, 32101324), Major Program of Institute of Applied Ecology, Chinese Academy of Sciences (Grant No. IAEMP202201), the Natural Science Foundation of Liaoning Province (Grant No. 2021-BS-013) and the Fundamental Research Funds for the Central Universities (Grant No. WK2080000161, 2021ZY85) and the Open Research Fund of State Key Laboratory of Simulation and Regulation of Water Cycle in River Basin, China Institute of Water Resources and Hydropower Research (Grant NO. IWHR-SKL-KF202303).

Conflict of interest

The authors declare that the research was conducted in the absence of any commercial or financial relationships that could be construed as a potential conflict of interest.

Publisher's note

Supplementary material

The Supplementary Material for this article can be found online at: https://www.frontiersin.org/articles/10.3389/fevo.2023.1153448/full#supplementary-material

References

Alberti, M., Correa, C., Marzluff, J. M., Hendry, A. P., Palkovacs, E. P., Gotanda, K. M., et al. (2017). Global urban signatures of phenotypic change in animal and plant populations. *Proceedings of the National Academy of Sciences* 114 (34), 8951–8956.

Arneth, A., Shin, Y. J., Leadley, P., Rondinini, C., Bukvareva, E., Kolb, M., et al. (2020). Post-2020 biodiversity targets need to embrace climate change. *Proc. Natl. Acad. Sci. U. S. A.* 117 (49), 30882–30891. doi: 10.1073/pnas.2009584117

Batt, R. D., Morley, J. W., Selden, R. L., Tingley, M. W., and Pinsky, M. L. (2017). Gradual changes in range size accompany long-term trends in species richness. *Ecol. Lett.* 20 (9), 1148–1157. doi: 10.1111/ele.12812

Bellard, C., Bertelsmeier, C., Leadley, P., Thuiller, W., and Courchamp, F. (2012). Impacts of climate change on the future of biodiversity. *Ecol. Lett.* 15 (4), 365–377. doi: 10.1111/j.1461-0248.2011.01736.x

Burley, H., Beaumont, L. J., Ossola, A., Baumgartner, J. B., Gallagher, R., Laffan, S., et al. (2019). Substantial declines in urban tree habitat predicted under climate change. *Sci. Total. Environ.* 685, 451–462. doi: 10.1016/j.scitotenv.2019.05.287

Ceballos, G., Ehrlich, P. R., and Raven, P. H. (2020). Vertebrates on the brink as indicators of biological annihilation and the sixth mass extinction. *Proc. Natl. Acad. Sci. U. S. A.* 117 (24), 13596–13602. doi: 10.1073/pnas.1922686117

Chen, G., Li, X., Liu, X., Chen, Y., Liang, X., Leng, J., et al. (2020). Global projections of future urban land expansion under shared socioeconomic pathways. *Nat. Commun.* 11, 537. doi: 10.1038/s41467-020-14386-x

Corlett, R. T. (2016). Plant diversity in a changing world: Status, trends, and conservation needs. *Plant Divers.* 38, 10–16. doi: 10.1016/j.pld.2016.01.001

Diaz, S., Pascual, U., Stenseke, M., Martin-Lopez, B., Watson, R. T., Molnar, Z., et al. (2018). Assessing nature's contributions to people. *Science* 359 (6373), 270–272. doi: 10.1126/science.aap8826

Di Marco, M., Harwood, T. D., Hoskins, A. J., Ware, C., Hill, S. L., and Ferrier, S. (2019). Projecting impacts of global climate and land-use scenarios on plant biodiversity using compositional-turnover modelling. *Global Change Biol.* 25 (8), 2763–2778. doi: 10.1111/gcb.14663

Dirzo, R., Young, H. S., Galetti, M., Ceballos, G., Isaac, N. J., et al. (2014). Defaunation in the anthropocene. *Science* 345 (6195), 401–406. doi: 10.1126/science.1251817

Dormann, C. F., Elith, J., Bacher, S., Buchmann, C., Carl, G., Carre, G., et al. (2013). Collinearity: a review of methods to deal with it and a simulation study evaluating their performance. *ECOGRAPHY* 36, 27–46. doi: 10.1038/s41558-019-0500-2

Elith, J., Phillips, S. J., Hastie, T., Dudik, M., Chee, Y. E., and Yates, C. J. (2011). A statistical explanation of MaxEnt for ecologists. *Divers. Distrib.* 17, 43–57. doi: 10.1111/j.1472-4642.2010.00725.x

Fang, C., Liu, H., and Wang, S. (2021). The coupling curve between urbanization and the eco-environment: China's urban agglomeration as a case study. *Ecol. Indic.* 130, 108107. doi: 10.1016/j.ecolind.2021.108107

Fu, W., Lv, Y., Harris, P., Comber, A., and Wu, L. (2018). Peri-urbanization may vary with vegetation restoration: a large scale regional analysis. *Urban. For. Urban. Greening.* 29, 77–87. doi: 10.1016/j.ufug.2017.11.006

Geschke, A., James, S., Bennett, A. F., and Nimmo, D. G. (2018). Compact cities or sprawling suburbs? Optimising the distribution of people in cities to maximise species diversity. *J. Appl. Ecol.* 55 (5), 2320–2331. doi: 10.1111/1365-2664.13183

Gomes, V. H., Vieira, I. C., Salomao, R. P., and Ter Steege, H. (2019). Amazonian tree species threatened by deforestation and climate change. *Nat. Clim. Change* 9 (7), 547–553. doi: 10.1038/s41558-019-0500-2

Grömping, U. (2006). Relative importance for linear regression in R: the package relaimpo. *J. Stat. Softw.* 17 (1), 1–27. doi: 10.1080/10629360600569147

He, C., Liu, Z., Tian, J., and Ma, Q. (2014). Urban expansion dynamics and natural habitat loss in China: A multiscale landscape perspective. *Global Change Biol.* 20 (9), 2886–2902. doi: 10.1111/gcb.12553

Hijmans, R. J., Cameron, S. E., Parra, J. L., Jones, P. G., and Jarvis, A. (2005). Very high resolution interpolated climate surfaces for global land areas. *Int. J. Climatol.* 25, 1965–1978. doi: 10.1002/joc.1276

IPCC. (2021). *Climate change 2021: The physical science basis. Contribution of working group I to the sixth assessment report of the Intergovernmental Panel on Climate Change.* (Cambridge: Cambridge University Press).

Jiang, L., and O'Neill, B. C. (2017). Global urbanization projections for the Shared Socioeconomic Pathways. *Glob. Environ. Change* 42, 193–199. doi: 10.1016/j.gloenvcha.2015.03.008

Krayenhoff, E. S., Moustaoui, M., Broadbent, A. M., Gupta, V., and Georgescu, M. (2018). Diurnal interaction between urban expansion, climate change and adaptation in US cities. *Nat. Clim. Change* 8 (12), 1097–1103. doi: 10.1038/s41558-018-0320-9

Leao, T. C., Lughadha, E. N., and Reich, P. B. (2020). Evolutionary patterns in the geographic range size of Atlantic Forest plants. *Ecography* 43, 1510–1520. doi: 10.1111/ecog.05160

Leao, T. C., Reinhardt, J. R., Nic Lughadha, E., and Reich, P. (2021). Projected impacts of climate and land use changes on the habitat of Atlantic forest plants in Brazil. *B. Glob. Ecol. Biogeogr.* 30 (10), 2016–2028. doi: 10.1111/geb.13365

Li, J., Chen, X., Kurban, A., Van de Voorde, T., De Maeyer, P., and Zhang, C. (2021). Coupled SSPs-RCPs scenarios to project the future dynamic variations of water-soil-carbon-biodiversity services in Central Asia. *Ecol. Indic.* 129, 107936. doi: 10.1016/j.ecolind.2021.107936

Li, G., Fang, C., Li, Y., Wang, Z., Sun, S., He, S., et al. (2022). Global impacts of future urban expansion on terrestrial vertebrate diversity. *Nat. Commun.* 13 (1), 1–12. doi: 10.1038/s41467-022-29324-2

Li, D., Wu, S., Liang, Z., and Li, S. (2020). The impacts of urbanization and climate change on urban vegetation dynamics in China. *Urban. For. Urban. Greening.* 54, 126764. doi: 10.1016/j.ufug.2020.126764

MacDonald, D. W., Bothwell, H. M., Hearn, A. J., Cheyne, S. M., Haidir, I., Hunter, L. T., et al. (2018). Multi-scale habitat selection modeling identifies threats and conservation opportunities for the sunda clouded leopard (Neofelis diardi). *Biol. Conserv.* 227, 92–103. doi: 10.1016/j.biocon.2018.08.027

McDonald, R. I., Mansur, A. V., Ascensao, F., Crossman, K., Elmqvist, T., Gonzalez, A., et al. (2020). Research gaps in knowledge of the impact of urban growth on biodiversity. *Nat. Sustainabil.* 3 (1), 16–24. doi: 10.1073/pnas.2117297119

McKinney, M. L. (2006). Urbanization as a major cause of biotic homogenization. *Biol. Conserv.* 127 (3), 247–260. doi: 10.1016/j.biocon.2005.09.005

Mi, X., Feng, G., Hu, Y., Zhang, J., Chen, L., Corlett, R. T., et al. (2021). The global significance of biodiversity science in China: an overview. *Natl. Sci. Rev.* 8 (7), nwab032. doi: 10.1093/nsr/nwab032

Molinos, J. G., Halpern, B. S., Schoeman, D. S., Brown, C. J., Kiessling, W., Moore, P. J., et al. (2015). Climate velocity and the future global redistribution of marine biodiversity. *Nat. Clim. Change* 6, 83–88. doi: 10.1038/nclimate2769

Newbold, T. (2018). Future effects of climate and land-use change on terrestrial vertebrate community diversity under different scenarios. *Proc. R. Soc B.* 285 (1881), 20180792. doi: 10.1098/rspb.2018.0792

Newbold, T., Oppenheimer, P., Etard, A., and Williams, J. J. (2020). Tropical and Mediterranean biodiversity is disproportionately sensitive to land-use and climate change. *Nat. Ecol. Evol.* 4 (12), 1630–1638. doi: 10.1038/s41559-020-01303-0

Peng, J., Du, Y., Liu, Y., and Hu, X. (2016). How to assess urban development potential in mountain areas? An approach of ecological carrying capacity in the view of coupled human and natural systems. *Ecol. Indic.* 60, 1017–1030. doi: 10.1016/j.ecolind.2015.09.008

Phillips, S. J., Anderson, R. P., and Schapire, R. E. (2006). Maximum entropy modeling of species geographic distributions. *Ecol. Model.* 190, 231–259. doi: 10.1016/j.ecolmodel.2005.03.026

Powers, R. P., and Jetz, W. (2019). Global habitat loss and extinction risk of terrestrial vertebrates under future land-use-change scenarios. *Nat. Clim. Change* 9 (4), 323–329. doi: 10.1038/s41558-019-0406-z

Raes, N. (2012). Partial versus full species distribution models. *Nat. Conserv.* 10, 127–138. doi: 10.4322/natcon.2012.020

Rivers, M. C., Taylor, L., Brummitt, N. A., Meagher, T. R., Roberts, D. L., and Lughadha, E. N. (2011). How many herbarium specimens are needed to detect threatened species? *Biol. Conserv.* 144 (10), 2541–2547. doi: 10.1016/j.biocon.2011.07.014

Roberts, L., Hassan, A., Elamer, A., and Nandy, M. (2021). Biodiversity and extinction accounting for sustainable development: A systematic literature review and future research directions. *Bus. Strateg. Environ.* 30 (1), 705–720. doi: 10.1002/bse.2649

Scheffers, B. R., De Meester, L., Bridge, T. C. L., Hoffmann, A. A., Pandolfi, J. M., Corlett, R. T., et al. (2016). The broad footprint of climate change from genes to biomes to people. *Science* 354 (6313), aaf7671. doi: 10.1126/science.aaf7671

Scheffers, B. R., and Pecl, G. (2019). Persecuting, protecting or ignoring biodiversity under climate change. *Nat. Clim. Change* 9, 581–586. doi: 10.1038/s41558-019-0526-5

Seebens, H., Bacher, S., Blackburn, T. M., Capinha, C., Dawson, W., Dullinger, S., et al. (2021). Projecting the continental accumulation of alien species through to 2050. *Global Change Biol.* 27 (5), 970–982. doi: 10.1111/gcb.15333

Segan, D. B., Murray, K. A., and Watson, J. E. (2016). A global assessment of current and future biodiversity vulnerability to habitat loss–climate change interactions. *Global Ecol. Conserv.* 5, 12–21. doi: 10.1016/j.gecco.2015.11.002

Seto, K. C., Güneralp, B., and Hutyra, L. R. (2012). Global forecasts of urban expansion to 2030 and direct impacts on biodiversity and carbon pools. *Proc. Natl. Acad. Sci.* 109 (40), 16083–16088. doi: 10.1073/pnas.1211658109

Simkin, R. D., Seto, K. C., McDonald, R. I., and Jetz, W. (2022). Biodiversity impacts and conservation implications of urban land expansion projected to 2050. *Proc. Natl. Acad. Sci. U. S. A.* 119 (12), e2117297119. doi: 10.1073/pnas.2117297119

Steffen, W., Richardson, K., Rockstrom, J., Cornell, S. E., Fetzer, I., Bennett, E. M., et al. (2015). Planetary boundaries: Guiding human development on a changing planet. *Science* 347 (6223), 1259855. doi: 10.1126/science.1259855

Tang, L., Ke, X., Chen, Y., Wang, L., Zhou, Q., Zheng, W., et al. (2021). Which impacts more seriously on natural habitat loss and degradation? Cropland expansion or urban expansion? *Land. Degradation. Dev.* 32 (2), 946–964. doi: 10.1002/ldr.3768

Ter Steege, H., Pitman, N. C., Killeen, T. J., Laurance, W. F., Peres, C. A., Guevara, J. E., et al. (2015). Estimating the global conservation status of over 15,000 Amazonian tree species. *Sci. Adv.* 1 (10), e1500936. doi: 10.1126/sciadv.1500936

Thibaud, E., Petitpierre, B., Broennimann, O., Davison, A. C., and Guisan, A. (2014). Measuring the relative effect of factors affecting species distribution model predictions. *Methods Ecol. Evol.* 5, 947–955. doi: 10.1111/2041-210X.12203

Thornhill, A. H., Baldwin, B. G., Freyman, W. A., Nosratinia, S., Kling, M. M., Morueta-Holme, N., et al. (2017). Spatial phylogenetics of the native California flora. *BMC Biol.* 15 (1), 96. doi: 10.1186/s12915-017-0435-x

Tian, J., and Zhang, Y. (2020). Detecting changes in irrigation water requirement in Central Asia under CO2 fertilization and land use changes. *J. Hydrol.* 583, 124315. doi: 10.1016/j.jhydrol.2019.124315

Velazco, S. J. E., Villalobos, F., Galvao, F., and De Marco Júnior, P. (2019). A dark scenario for Cerrado plant species: Effects of future climate, land use and protected areas ineffectiveness. *Divers. Distrib.* 25 (4), 660–673. doi: 10.1111/ddi.12886

Visconti, P., Bakkenes, M., Baisero, D., Brooks, T., Butchart, S. H., Joppa, L., et al. (2016). Projecting global biodiversity indicators under future development scenarios. *Conserv. Lett.* 9 (1), 5–13. doi: 10.1111/conl.12159

Williams, J. J., and Newbold, T. (2020). Local climatic changes affect biodiversity responses to land use: A review. *Divers. Distrib.* 26 (1), 76–92. doi: 10.1111/ddi.12999

You, Q., Cai, Z., Wu, F., Jiang, Z., Pepin, N., and Shen, S. S. (2021). Temperature dataset of CMIP6 models over China: evaluation, trend and uncertainty. *Clim. Dyn.* 57 (1), 17–35. doi: 10.1007/s00382-021-05691-2

Zhou, C., Li, M., Zhang, G., Chen, J., Zhang, R., and Cao, Y. (2021). Spatiotemporal characteristics and determinants of internal migrant population distribution in China from the perspective of urban agglomerations. *PloS One* 16 (2), e0246960. doi: 10.1371/journal.pone.0246960

Zhou, T., Liu, H., Gou, P., and Xu, N. (2023). Conflict or Coordination? measuring the relationships between urbanization and vegetation cover in China. *Ecol. Indic.* 147, 109993. doi: 10.1016/j.ecolind.2023.109993

Zizka, A., Silvestro, D., Andermann, T., Azevedo, J., Ritter, C. D., Edler, D., et al. (2019). CoordinateCleaner: Standardized cleaning of occurrence records from biological collection databases. *Methods Ecol. Evol.* 10 (5), 744–751. doi: 10.1111/2041-210X.13152

Frontiers in Ecology and Evolution

TYPE Original Research
PUBLISHED 24 October 2023
DOI 10.3389/fevo.2023.1176131

OPEN ACCESS

EDITED BY
Jixi Gao,
Ministry of Ecology and Environment (China), China

REVIEWED BY
Yahui Guo,
Central China Normal University, China
Hao Zhou,
Chinese Academy of Sciences (CAS), China

*CORRESPONDENCE
Qiong Liu
liuq@mail.cgs.gov.cn
Yali Liu
liuyali@bjfu.edu.cn

RECEIVED 28 February 2023
ACCEPTED 05 October 2023
PUBLISHED 24 October 2023

CITATION
Gao M, Liu Q, Liu Y, Yang N, Wang Y and Li X (2023) Spatial and temporal variations of vegetation water use efficiency and its response to climate change and human activities in the West Liao River Plain, China.
Front. Ecol. Evol. 11:1176131.
doi: 10.3389/fevo.2023.1176131

Spatial and temporal variations of vegetation water use efficiency and its response to climate change and human activities in the West Liao River Plain, China

Mengmeng Gao[1], Qiong Liu[1*], Yali Liu[2*], Nan Yang[1,3], Yi Wang[1] and Xiaolei Li[1]

[1]China Institute of Geological Environmental Monitoring, Beijing, China, [2]School of Grassland Science, Beijing Forestry University, Beijing, China, [3]Institute of Geophysical and Geochemical Exploration, Chinese Academy of Geological Sciences, Langfang, China

Water use efficiency [WUE = gross primary production (GPP)/evapotranspiration (ET)] is an important indicator of the degree of coupling between carbon and water cycles in ecosystems. However, the response of the carbon and water cycles to climate change and human activities,as well as the underlying driving mechanisms in the West Liao River Plain (WLRP), a typical farming–pasturing ecotone in northern China, remain unclear. This study examined the temporal and spatial variation characteristics of WUE in the WLRP from 2000 to 2020 using linear regression and the coefficient of variation (CV) method based on MODIS GPP and ET datasets. The relationships between WUE, meteorological factors, and human activities as well as the mechanism driving WUE changes were revealed through correlation analyses, residual analysis, and the grey correlation model. The interannual change of WUE from 2000 to 2020 showed a fluctuating but weakly upward trend. The intra-annual change in WUE followed an M-type bimodal trend, with two peaks from May to June and August to September. Areas with increased WUE accounted for 50.82% of the study area, and 11.11% of these showed a significant increasing trend. WUE was mainly positively correlated with temperature and solar radiation and negatively correlated with precipitation and VPD and presented obvious regional differences. Solar radiation had the most significant impact on WUE. WUE change is not entirely driven by climate change, and human activities have also played an important role. In areas where WUE increased, The average contribution rate of climate change was 72.4%, and that of human activities was 27.6%. This study reveals the temporal and spatial dynamics of WUE in the WLRP and highlights the influence of human activities on WUE changes.

KEYWORDS

water use efficiency (WUE), climate change, human activities, residual analysis, grey correlation model, West Liao River Plain (WLRP)

1 Introduction

Water use efficiency (WUE) is defined as the amount of biomass produced per unit of water used by a plant. This concept was introduced 100 years ago by Briggs and Shantz (1913), who demonstrated the relationship between plant productivity and water use. As a key measurement of the coupled carbon and water cycle function of terrestrial ecosystems, WUE not only reflects the interrelationship between these two factors but also explains the response of terrestrial ecosystems to climate change (Gang et al., 2016; Hatfield and Dold, 2019).

WUE can be estimated in different ways, depending on the temporal and spatial scales or the scientific question of interest (Bhattacharya, 2019). Based on its definition, agricultural scientists usually determine WUE as the relationship between either biomass or crop yield and either transpiration or the total water provided to the crop, which includes the amount of water provided by precipitation and irrigation (Gadanakis et al., 2015; Bhattacharya, 2019). In ecology, when WUE is calculated on a regional scale, the mass of CO_2 assimilation may be measured as the gross primary productivity (GPP), net primary productivity (NPP), or net ecosystem carbon production (NEP), and the water use may be measured as evapotranspiration (ET) or annual rainfall (Tian et al., 2020). Among these, one common way of calculating WUE is to use the ratio of GPP to ET. This method is typically used to analyze the carbon and water coupling characteristics of ecosystems and their responses to environmental changes over long timescales, such as months or years (Jassal et al., 2009; Zhen et al., 2017; Ai et al., 2020).

In addition to being regulated by the vegetation system, WUE is closely related to external environmental conditions. Temperature, precipitation, humidity, solar radiation, and CO_2 concentration are key climatic factors affecting vegetation WUE (Hatfield and Dold, 2019). In the context of global climate change, the warming rate is remarkable, precipitation on land has increased, the carbon dioxide concentration is at its highest level in the past two million years, and extreme climate events are occurring frequently (IPCC, 2021). Therefore, temporal and spatial variations in ecosystem WUE under climate change and the response of WUE to climate change have attracted considerable attention (Niu et al., 2011; Klein et al., 2013; Hao et al., 2019; Jia et al., 2023).

The West Liao River Plain (WLRP), located between the eastern plain of Inner Mongolia and the southwestern part of Northeast China, is one of the important birthplaces of agricultural civilization in northern China. As this region is located in the monsoon fringe area, the transition zone between arid, semi-arid, and semi-humid regions, and at the edge of the Horqin Sandy Land, plant growth is particularly sensitive to climate change, environmental transition, and human activities. Currently, studies on the vegetation ecology and related climatic factors in this region focus mostly on the vegetation community and coverage, NPP, crop yields, biomass, and NEP (Huang et al., 2013; Feng et al., 2014; Gao et al., 2017; Zhao, 2017; Yan et al., 2018; Aruna, 2020; Gao W. D. et al., 2022; Zhu et al., 2022). Few studies have examined WUE and its response to meteorological factors and human activities.

Through an analysis of the spatiotemporal change trend of WUE and the relationship between WUE, climate change, and human activities from 2000 to 2020, this study identified the driving mechanism of WUE change in the WLRP. This study has considerable significance for promoting the protection of ecosystems, utilizing and managing water resources, and achieving sustainable development of agriculture in the region.

2 Materials and methods

2.1 Study area

The WLRP is located in a farming–pasturing ecotone in Northeast China (42°21'–45°20' N, 119°01'–123°43' E), which is within a semiarid region including the Horqin Sandy Land, where the ecological environment is extremely fragile. It covers an area of 57,600 km^2 (Gao M. M. et al., 2022), has an altitude range of 6–748 m, and slopes gradually from southwest to northeast (Figure 1A). The main geomorphic units are river impact plains and eolian dunes. The land-use types are mainly grassland and cropland, which account for more than 89% of the total area (Figure 1B). The grassland pastoral area is distributed in the north, agricultural areas are distributed in the center and at the southern edge, and sandy land is mainly distributed in the southwest. The average annual precipitation in this area is 385 mm, which occurs mainly in the form of rainstorms from June to September. The average annual temperature of the WLRP is 6.9°C.

The WLRP includes the Xiliao and Xinkai Rivers, which have run dry since 1999. Exploitation of groundwater since the 1960s has reduced groundwater levels in the surrounding sandy land and aggravated desertification. However, in recent years, the ecological environment has improved as a result of comprehensive actions to control desertification.

2.2 Data sources and processing

2.2.1 Modis data

GPP data and ET data were obtained from MOD17A2 and MOD16A2 during the time period from 2000 to 2020 (https://earthdata.nasa.gov/). The spatial resolution of GPP (Zhao et al., 2005; Fu et al., 2017) and ET (Mu et al., 2011; Stavroula and Konstantinos, 2021) is 500 m, and the temporal resolution is 8 days. MODIS Reprojection Tool (MRT) software was used to process the GPP and ET datasets, including mosaic, projection, and format conversion.

WUE was expressed as the ratio of the GPP to ET of vegetation based on previous research (Hu et al., 2008; Zhu et al., 2014; Adams et al., 2016; An, 2022). It was formulated as follows:

$$WUE = \frac{GPP}{ET} \tag{1}$$

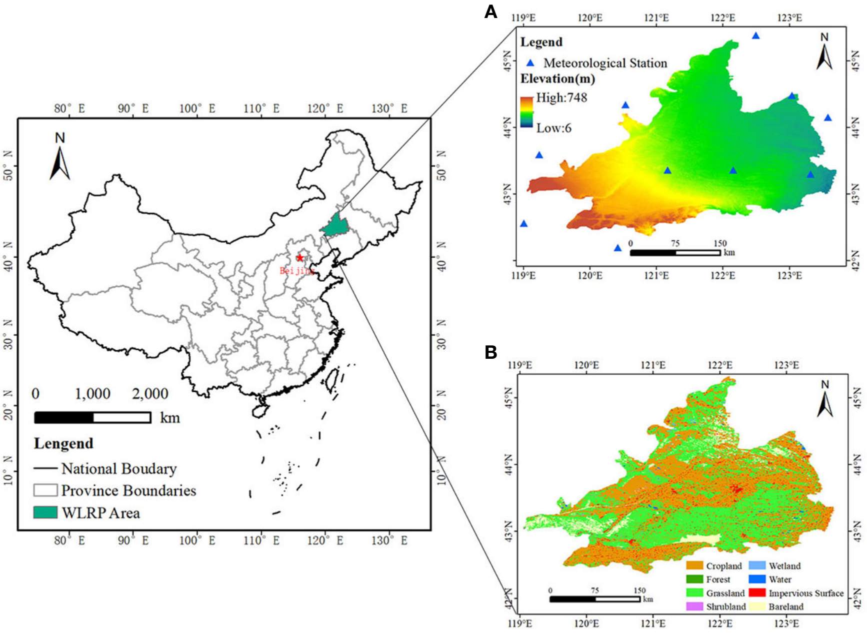

FIGURE 1
Location of the West Liao River Plain (WLRP). Meteorological station distribution and elevation **(A)** and land use in 2020 **(B)**.

where *WUE* is the water use efficiency ($gC{\cdot}mm^{-1}{\cdot}m^{-2}$), *GPP* is the gross primary productivity of the terrestrial ecosystem ($g\,C{\cdot}m^{-2}$), and *ET* is the evapotranspiration of the ecosystem (mm).

2.2.2 Meteorological data

Precipitation, temperature, solar radiation, and vapor pressure deficit (VPD) data were used in this study. Monthly precipitation and temperature data of 11 meteorological observation stations in the WLRP and surrounding areas were obtained from China Meteorological Data Sharing Service System (http://cdc.cma.gov.cn). Monthly solar radiation data with a spatial resolution of 0.1° × 0.1° were obtained from European Centre for Medium-Range Weather Forecasts (ERA5) Reanalysis Datasets (https://cds.climate.copernicus.eu/). All these monthly data were processed to annual data using kriging interpolation with a resolution of 500 m.

The vapor pressure deficit (VPD) indicates the dryness of air, which is often used to study the impact of climate change on WUE (Riha and Melkonian, 2023). This factor was calculated using the mean monthly maximum temperature, minimum temperature, and relative humidity and the following formula (Li et al., 2014). The above data used in Eqs. 3 and 4 were also obtained from China Meteorological Data Sharing Service System. The monthly VPDs were calculated first, and then, the average annual VPD was calculated using the monthly VPD.

$$VPD = e_s - e_a \tag{2}$$

$$e_s = \frac{e^0(T_{\max}) + e^0(T_{\min})}{2} \tag{3}$$

$$e_a = e_s \frac{\lambda_{mean}}{100} \tag{4}$$

where e_s is saturated vapor pressure (*kPa*), e_a is the actual vapor pressure (*kPa*),λ_{mean} is the mean relative humidity (%), and $e^0(T_{max})$ and $e^0(T_{min})$ are the saturated vapor pressure at the mean monthly maximum temperature and minimum temperature, respectively, which can be calculated by *Tetens'* empirical formula (Allen et al., 1998) as follows:

$$e^0(T) = 0.6108 \exp\left[\frac{17.27T}{T + 237.3}\right] \tag{5}$$

where T is the temperature (°C), and $e^0(T)$ is the saturated vapor pressure at the temperature T (*kPa*). The spatial distribution of the multi-year mean precipitation (A), temperature (B), solar radiation (C), VPD (D) from 2000 to 2020 in the WLRP were shown in Supplementary Figure 1.

2.2.3 Human activities data

Land use data were obtained from Landsat-derived annual land cover product of China (CLCD) developed by Yang and Huang (2021), with a spatial resolution of 30 m. The land cover was classified into eight types: cropland, forest, grassland, wetland, shrubland, water, bareland, and impervious surface (Figure 1B). Population density datasets were obtained from Worldpop hub (https://hub.worldpop.org/) with a 1 km resolution from 2000 to 2020. Global NPP-VIIRS-Like Nighttime Light data (NTL) were obtained from National Earth System Science Data Center with 500 resolution from 2000 to 2020.

2.3 Methods

2.3.1 Linear regression

The mean annual WUE trends from 2000 to 2020 were analyzed using linear regression analysis, which was calculated using the following formula (Mafi-Gholami et al., 2019; Yan et al., 2022):

$$slope = \frac{n\sum_{i=1}^{n} iWUE_i - \sum_{i=1}^{n} i \sum_{i=1}^{n} WUE_i}{n\sum_{i=1}^{n} i^2 - (\sum_{i=1}^{n} i)^2} \tag{6}$$

where n is the number of samples, i is the serial year number (i = 1,2,3……, 21), WUE_i is the WUE value in year i, and *slope* represents the change trend. If *slope* > 0, *WUE* has an increasing trend; if *slope* = 0, *WUE* does not change; if *slope*< 0, *WUE* has a decreasing trend.

The *F*-test was used to analyze the significance of the results. By combining the *slope* value and the F test, the results were divided into five grades: extremely significant decrease area (slope< 0, $p< 0.01$), significant decrease area (slope< 0, $0.01< p< 0.05$), stable area ($p > 0.05$), significant increase area (slope > 0, $0.01< p< 0.05$), and extremely significant increase area (slope > 0, $p< 0.01$).

The calculation formula for the *F*-test was based on the study of Chen et al. (2017).

2.3.2 Coefficient of variation

The coefficient of variation (CV), a statistic describing the degree of dispersion of random variables, was used to analyze the dispersion of WUE (Tucker et al., 1991; Milich and Weiss, 2000). The formula was

$$CV_{WUE} = \frac{\sigma_{WUE}}{\overline{WUE}} \tag{7}$$

where CV_{WUE} is the coefficient of variation of WUE, σ_{WUE} is the standard deviation of WUE, and $\overline{WUE}$ is the mean annual WUE. When the CV is larger, the change of *WUE* is more unstable; when CV is smaller, it is more stable.

2.3.3 Correlation analysis

The correlation between WUE and the meteorological factors was analyzed. The correlation coefficient was calculated as follows:

$$r_{xy} = \frac{\sum_{i=1}^{n}(x_i - \bar{x})(y_i - \bar{y})}{\sqrt{\sum_{i=1}^{n}(x_i - \bar{x})^2}\sqrt{\sum_{i=1}^{n}(y_i - \bar{y})^2}} \tag{8}$$

where r_{xy} is the correlation coefficient of factor x and y, x_i and y_j are the values of factor x and y in year i, $\bar{x}$ *and* $\bar{y}$ are the mean values of x_i and y_j, respectively. The value range of r_{xy} is [−1,1]. If $r_{xy}>0$, the correlation between x and y is positive. The greater the absolute value of r_{xy}, the stronger the correlation between x and y.

The *t*-test was used to test the significance of the correlation coefficient. The calculation formula for *t*-test refers to the paper Miao et al. (2023).

2.3.4 Residual analysis

The sampling multiple linear regression residual analysis method was used to analyze the effects and contributions of human activities and climate change on WUE (Evans and Geerken, 2004). The predicted and residual WUE was calculated using the following formula:

$$WUE_{pre} = a \times PRE + b \times TEM + c \times VPD + d \times RAD + e \tag{9}$$

$$WUE_{res} = WUE_{obs} - WUE_{pre} \tag{10}$$

where a, b, c, d, and e are regression coefficients, *PRE* is the annual precipitation, *TEM* is the average annual temperature, *VPD* is the average annual vapor pressure deficit, *RAD* is the annual solar radiation. WUE_{res}, WUE_{obs}, and WUE_{pre} are the residual, observed, and predicted values of *WUE*, respectively. The value of WUE_{res} reflects the influence of human activities on WUE, while the value of WUE_{pre} reflects the influence of climate change on WUE.

The contribution of climate change and human activities to the changes in WUE can be analyzed by grading the residual results. The criteria for determining the drivers of WUE changes (Supplementary Table 1) were defined by referring to previous studies (Gao W. D. et al., 2022; Yu et al., 2022).

2.3.5 Grey correlation model

To quantify the impact of climate change and human activity on WUE in the study area, the grey correlation model was introduced to calculate the correlation degree of each evaluation index (Liu et al., 2017). The higher the correlation degree, the higher the influence of this index on WUE.

3 Results

3.1 Spatial distribution of the multi-year mean WUE

The spatial distribution of WUE differed significantly across the WLRP (Figure 2). The multi-year mean WUE of the WLRP ranged from 0.458 to 2.027 gC·mm^{-1}·m^{-2}. The areas with the highest WUE were predominantly located in the southern and central regions of the study area. The areas with the lowest WUE were mainly in the western Horqin Sandy Land. The average WUE values of different vegetation types were ranked as follows: forest (1.38 gC·mm^{-1}·m^{-2}), cropland (1.34 gC·mm^{-1}·m^{-2}), grassland (1.31 gC·mm^{-1}·m^{-2}), wetland (1.23 gC·mm^{-1}·m^{-2}), shrubland (1.22 gC·mm^{-1}·m^{-2}) and bareland (1.04 gC·mm^{-1}·m^{-2}), respectively.

3.2 Temporal change of WUE

3.2.1 Interannual change of WUE

Figure 3 shows the interannual variations of WUE from 2000 to 2020, revealing the temporal changes of WUE in the WLRP. The interannual change of WUE showed a fluctuating but weakly upward

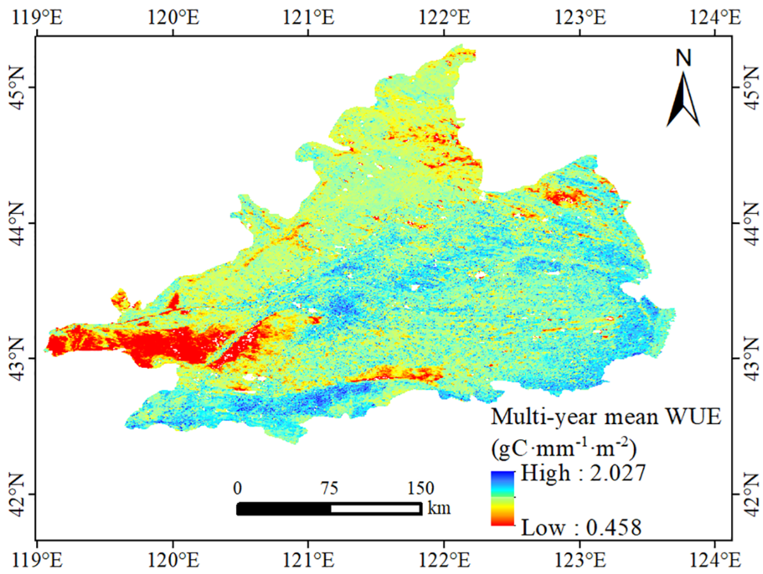

FIGURE 2
Spatial distribution of the multi-year mean water use efficiency (WUE) from 2000 to 2020 in the WLRP.

trend, with the highest and lowest values being observed in 2019 and 2010, respectively. The interannual change trend was divided into two stages. The first stage, from 2000 to 2010, showed a downward trend with a rate of decrease of 0.00449 gC·mm^{-1}·m^{-2}·a^{-1}. The second stage, from 2010 to 2020, showed an upward trend with a rate of increase of 0.00766 gC·mm^{-1}·m^{-2}·a^{-1}.

3.2.2 Intra-annual change of WUE

Figure 4 shows the monthly WUE change from 2000 to 2020, revealing the intra-annual change of WUE in the WLRP. The intra-annual change of WUE showed an M-type bimodal mode, with two peaks occurring from May to June and August to September, respectively. The average seasonal WUE decreased in the following order: summer (2.00 gC·mm^{-1}·m^{-2}) > spring (1.64 gC·mm^{-1}·m^{-2}) > autumn (1.23 gC·mm^{-1}·m^{-2}) > winter (0.01 gC·mm^{-1}·m^{-2}).

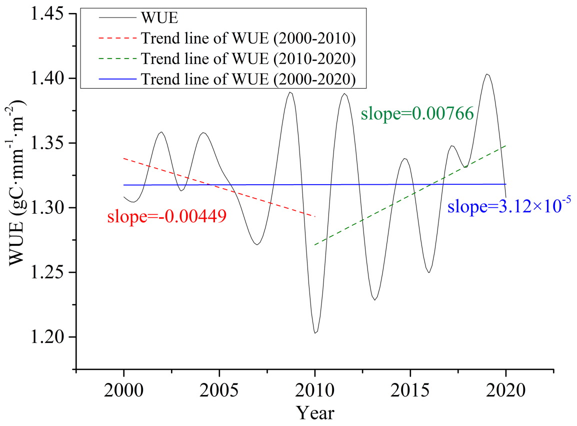

FIGURE 3
Interannual variations of WUE from 2000 to 2020 in the WLRP.

3.3 The spatial distributions of trend in WUE

Figure 5 shows the slope of the annual WUE for each pixel from 2000 to 2020, revealing the spatial change of WUE in the WLRP. The change trend of WUE in the study area showed obvious spatial differentiation, with slope values ranging from −0.05 to 0.05 gC·mm^{-1}·m^{-2}·a^{-1}. The areas of increasing and decreasing trends of WUE accounted for 50.82% and 49.18% of the total, respectively (Figure 5A). However, the significance test of the WUE change trend showed that more than half of the total area (77.13%) showed no significant change. The extremely significant decrease and significant decrease areas accounted for 6.57% and 5.20% of the total, respectively, and were mainly distributed in the western region. The extremely significant increase and significant increase areas accounted for 5.85% and 5.26%, respectively, and were mainly distributed in the southern and central regions (Figure 5B).

Figure 6 shows the proportions of different types of WUE change trends for the different land-use types. Areas where WUE showed no trend accounted for the largest proportion of the total area in all land-use types: forest (84.39%), grassland (81.23%), wetland (78.37%), shrubland (74.86%), cropland (74.24%), and bareland (70.35%). The proportions of areas that showed decreasing trends (including both extremely significant decrease and significant decrease) were in the following order: bareland (18.96%) > cropland (16.01%) > forest (11.13%) > shrubland (8.69%) > grassland (6.75%) > wetland (3.85%). The proportions of areas that showed an increasing trend (extremely significant increase and significant increase) were in the following order:

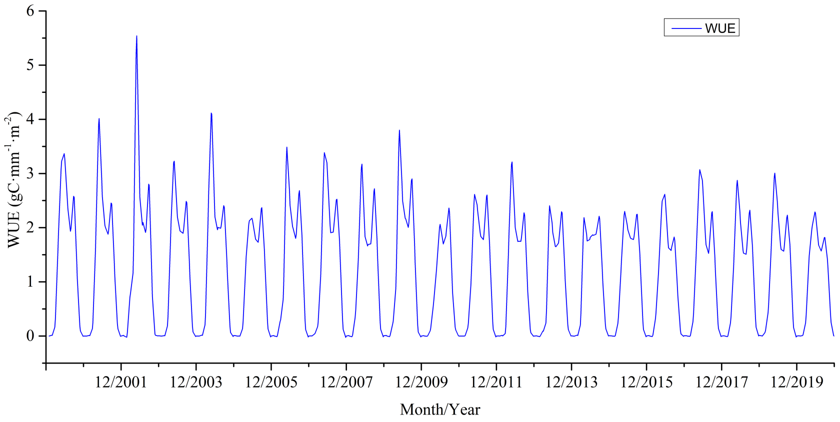

FIGURE 4
Monthly change of WUE from 2000 to 2020 in the WLRP.

wetland (17.77%) > shrubland (16.45%) > grassland (12.80%) > bareland (10.69%) > cropland (9.75%) > forest (4.48%).

Figure 7 shows the degree of dispersion of WUE. The CV of the annual WUE ranged from 0.02 to 0.68. As there was low dispersion of WUE in most of the study area, the WUE in most areas was likely relatively stable. Areas with high CV values, exhibiting unstable WUE changes, were mainly located in the west, south, and northeast portions of the study area. The CV values of the different vegetation types were in the following order: bareland (0.120), shrubland (0.080), wetland (0.077), grassland (0.064), cropland (0.051), and forest (0.050), respectively.

3.4 Correlation analysis between WUE and meteorological factors

The correlations between meteorological factors and WUE were examined to determine the causes of the WUE trends. To analyze the impact of each meteorological factor on WUE, the coefficient of correlation was calculated between WUE and each meteorological factor. There were obvious regional differences in the correlation between WUE and precipitation, temperature, solar radiation, and VPD and their average correlation coefficients were −0.015, 0.124, 0.222, and −0.044, respectively (Figures 8A, C, E, G). Areas with positive and negative correlations between WUE and precipitation accounted for 46.20% and 53.80% of the WLRP. The areas with a positive correlation in the western region were larger than those in the eastern region. Areas with a positive correlation between WUE and temperature accounted for 71.60% of the WLRP which were mainly distributed in the northern and southern parts of the study area, whereas areas with a negative correlation accounted for 28.40% of the WLRP which were mainly distributed in the southwestern and central portions of the study area. Areas with a positive correlation between WUE and solar radiation accounted for 84.55% of the WLRP which were mainly distributed in the southeastern parts of the study area, whereas areas with a negative correlation accounted for 15.45% of the WLRP which were mainly distributed in the central and western regions of the study area. The areas with positive and negative correlations between WUE and VPD accounted for 45.65% and 54.35%, respectively. The regions with positive correlation were mainly distributed in the eastern and northern regions, while that with negative correlation were mainly distributed in the central and southwestern regions.

Overall, WUE in the WLRP was positively correlated with temperature and solar radiation, while it was negatively correlated with precipitation and VPD. However, the areas that passed the

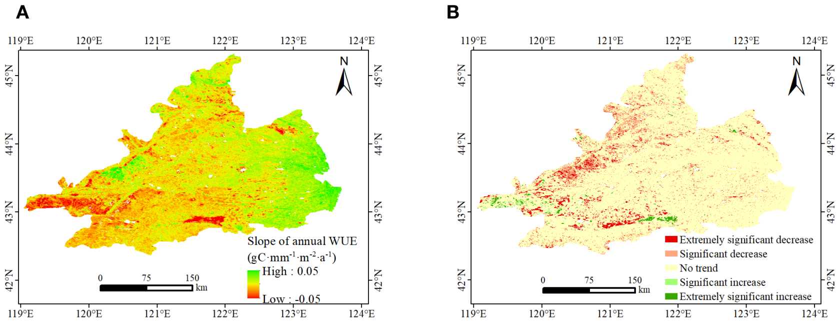

FIGURE 5
The spatial distributions of trend in WUE from 2000 to 2020 in the WLRP. Slope of annual WUE **(A)**, and significant changes in WUE **(B)**.

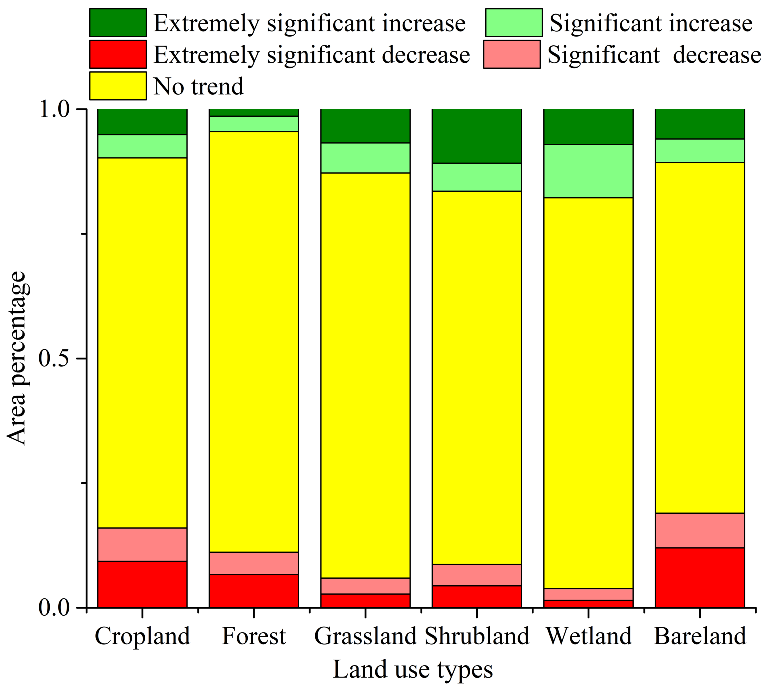

FIGURE 6
Proportions of different types of WUE change in different land-use types from 2000 to 2020 in the WLRP.

significance test ($P<0.05$) only accounted for 4.70%, 7.33%, 16.12%, and 0.64% (Figures 8B, D, F, H), which indicated that the change in WUE in the WLRP was not determined by a single indicator and was influenced by multiple indicators. In addition to meteorological factors, human activities need to be considered.

3.5 Trends of climate change on WUE change

The value of the predicted WUE could reflect the influence of climate change on WUE. The slope of the predicted WUE ranged from -0.03 and 0.03 $gC \cdot mm^{-1} \cdot m^{-2} \cdot a^{-1}$, with a regional average of 0.0008 $gC \cdot mm^{-1} \cdot m^{-2} \cdot a^{-1}$ (Figure 9A). The proportion of areas where meteorological factors have a positive impact on WUE was 60.27%, and these areas were mainly distributed in the western regions, indicating that climate change had a positive impact on WUE in this region. The proportion of areas where meteorological factors have a negative impact on WUE was 39.73%, and these areas were mainly distributed in the central and southern regions, indicating that climate change had a negative impact on WUE in this region. Among them, the regions with significant positive ($P<0.05$) and significant negative effects ($P<0.05$) accounted for 22.82% and 11.76%, respectively (Figure 9B).

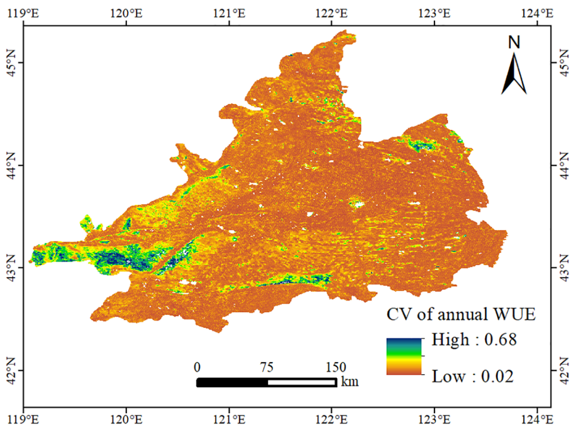

FIGURE 7
Spatial distribution of the CV of annual WUE from 2000 to 2020 in the WLRP.

3.6 Trend of human activities on WUE change

The value of residual WUE could reflect the influence of human activities on WUE. The slope of the predicted WUE ranged from –0.02 and 0.02 $gC \cdot mm^{-1} \cdot m^{-2} \cdot a^{-1}$, with a regional average of –0.0007$gC \cdot mm^{-1} \cdot m^{-2} \cdot a^{-1}$ (Figure 10A). The proportion of areas where human activities have a positive impact on WUE was 38.07%, and these areas were mainly distributed in the southeastern and northwestern regions, indicating that human activities had a positive impact on WUE in this region. The proportion of areas where human activities have a negative impact on WUE was 61.93%, and these areas were mainly distributed in the central and southern regions, indicating that human activities had a negative impact on WUE in this region. Among them, the regions with significant positive ($P<0.05$) and

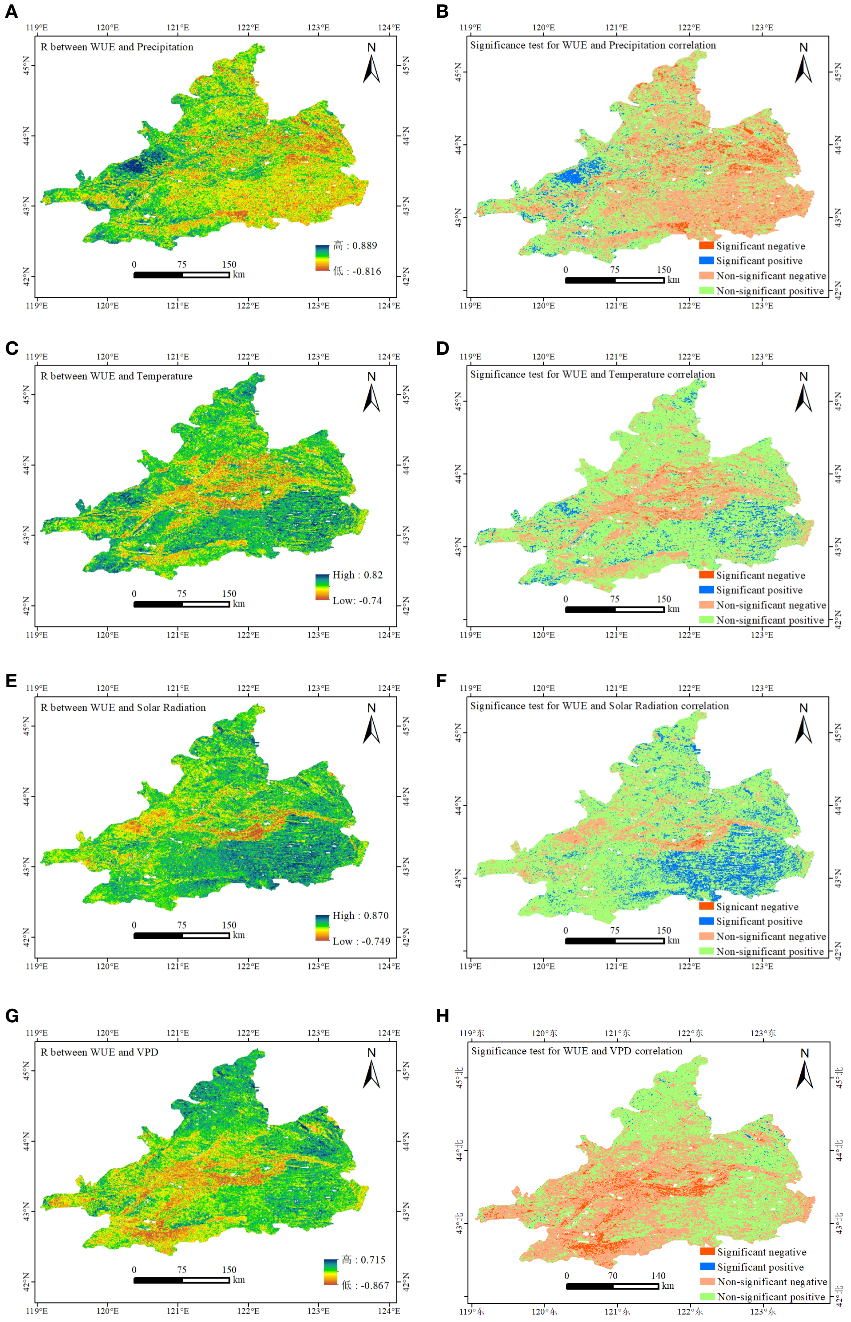

FIGURE 8
Spatial distributions of the correlation coefficients between WUE and **(A)** precipitation, **(C)** temperature, **(E)** solar radiation, and **(G)** VPD in the WLRP from 2000 to 2020; Significant test of correlation between WUE and **(B)** precipitation, **(D)** temperature, **(F)** solar radiation, and **(H)** VPD in the WLRP from 2000 to 2020.

significant negative effects ($P<0.05$) accounted for 0.83% and 2.58%, respectively (Figure 10B).

3.7 Comprehensive analysis of WUE change

The contribution rate of climate change and human activities to regional WUE from 2000 to 2020 in the WLRP could be obtained by determining the criteria for driving factors and calculating the contribution rate (Supplementary Table 1). Overall, driven by both human activities and climate change, the area where the WUE has improved accounted for 50.82%, with an average contribution rate of 72.4% for climate change and 27.6% for human activities (Figures 11A, B). The combined effect of human activities and climate change could also have a negative impact on WUE. The area where WUE decreased driven by both factors accounted for approximately 49.18% of the total area of the region, with an average contribution of 39.9% for climate

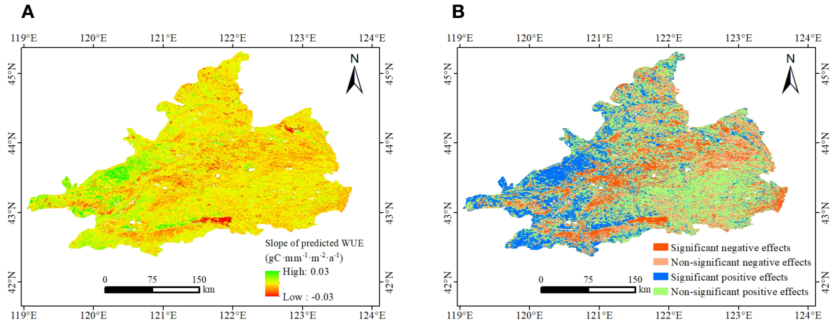

FIGURE 9
The spatial distributions of trend in predicted WUE from 2000 to 2020 in the WLRP. Slope of predicted WUE **(A)**, and significance test in predicated WUE **(B)**.

change and 60.1% for human activities (Figures 11C, D). Overall, the main contribution of WUE improvement was climate change, while the decrease in WUE was mainly due to human activities.

To further explore the driving factors affecting WUE, human activity indicators such as population density (PD), the proportion of impervious surface area (IS), and nighttime light (NTL) were selected and were combined with meteorological factors such as precipitation (PRE), temperature (TEM), vapor pressure deficit (VPD), and solar radiation(RAD), the grey correlation model was used to identify the main control factors on WUE changes (Table 1). The results showed that for the seven evaluation factors in this study, the top three factors in terms of correlation degree were RAD, PD, and VPD, in which RAD had the highest correlation degree (0.939), indicating that WUE changes were considerably affected by RAD. The impact of human activities on WUE cannot be ignored, especially that of PD, which had a correlation degree of 0.93.

4 Discussion

4.1 Spatial and temporal distribution of WUE

From 2000–2020, the annual mean WUE of the WLRP ranged from 0.458 to 2.027 gC·mm^{-1}·m^{-2}, and the regional average was 1.31. This result is consistent with the result of Luo et al. (2022), who reported an annual mean WUE in Inner Mongolia of 1.39 gC·mm^{-1}·m^{-2}, with a range of 0–3.03 gC·mm^{-1}·m^{-2} and an increasing trend. There were different trends of regional WUE during 2001-2010 and 2010-2020 in WLRP, which is directly related to the sharp decrease in WUE in 2010. In 2010, the decrease in solar radiation led to a decrease in vegetation photosynthesis and carbon sequestration capacity, resulting in lower levels of GPP, while an increase in precipitation resulted in higher levels of ET, resulting in a drastic decrease in WUE values. In previous studies, although some regions also showed a downward trend in WUE from 2000 to 2010 (Zhang et al., 2016), most regions showed an overall upward trend in WUE during the study period and did not show a significant segmented trend (Zhao et al., 2019; Luo et al., 2022). This is related to the differences in geographical location, meteorological conditions, and human activity interference in the study area.

WUE reflects the trade-off between GPP and ET in an ecosystem, that is, the relationship between organic carbon and water consumption (Shao et al., 2020). There was no significant change trend in most areas of the WLRP from 2000 to 2020. The main reason for this result is that the change trends of GPP and ET in the study area were consistent (Figures 12A, B), and the linear correlation coefficient of these variables was as high as 0.94 (Figure 12C), indicating that the carbon-fixing ability in this area

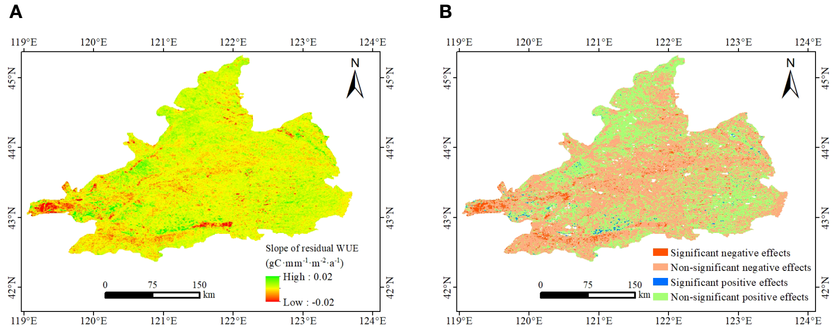

FIGURE 10
The spatial distributions of trend in residual WUE from 2000 to 2020 in the WLRP. Slope of residual WUE **(A)**, and significance test in residual WUE **(B)**.

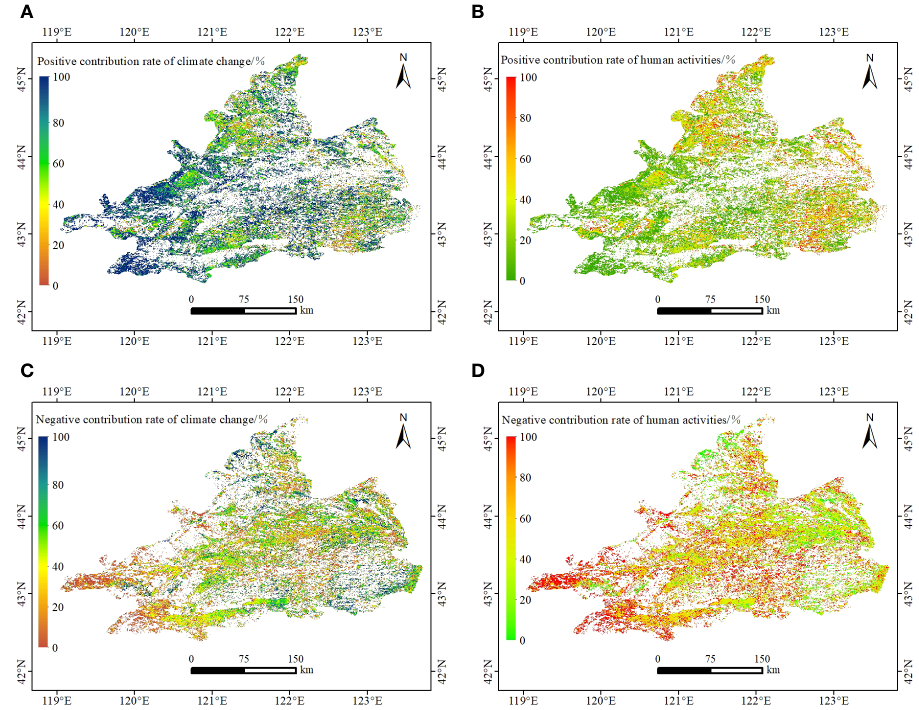

FIGURE 11
Spatial distribution of positive **(A, B)** and negative **(C, D)** contributions of climate change and human activities to WUE in the WLRP from 2000 to 2020.

is directly proportional to water consumption and leads to the insignificant change trend of WUE.

The average WUE values of the different vegetation types ranked in the order of forest, cropland, grassland, wetland, shrubland, and bareland, respectively, were in general agreement with the results of previous studies (Feng et al., 2018; Chang et al., 2021). Although the WUE values followed the same order rule, the same land-use type showed different WUE values in different regions, which is consistent with the conclusions of other researchers (Liu et al., 2015; Muhammad et al., 2018). This is probably attributable to physiological, zonal, and climatic differences (Tang et al., 2014; Yao et al., 2014; Zhang et al., 2022). Wang et al. (2020) also reported water and heat conditions and their uneven distribution as the main reasons for zonal differences in WUE, which are not solely determined by the physiological characteristics of plants.

TABLE 1 The grey correlation result.

Evaluation factors	Correlation degree	Ranking
RAD	0.939	1
PD	0.93	2
VPD	0.884	3
TEM	0.858	4
IM	0.775	5
PRE	0.725	6
NLI	0.576	7

Forest vegetation can obtain deep soil water and nutrients through developed roots to support plant growth (Chang et al., 2021), and croplands often receive sufficient irrigation water for plant growth(Zheng et al., 2019). Both forest and cropland have relatively high vegetation coverage, which can reduce soil water evaporation and increase the efficiency with which water is converted into organic matter, which is produced more abundantly by forests than cropland (Xia et al., 2015). Therefore, the WUE values of cropland and forest were high, and those of forest were the highest. The GPP values of bareland and shrubland, with little vegetation, are low, and evapotranspiration depends mainly on soil water evaporation. Therefore, bareland and shrubland had the smallest values of WUE. The GPP of shrubland may also be underestimated (Zhang et al., 2012; Zhang et al., 2015; Chang et al., 2021). In grassland, the root system is short, plants depend primarily on precipitation and shallow soil water, and evaporation of soil water is high, making full use of the available water difficult.

In areas with a significant downward trend in WUE, the proportion of bareland, cropland, and forest land is relatively large. This is because better hydrothermal conditions can lead to an increase in ET, resulting in a significant decrease of WUE in bareland. Cropland and forest in the area mainly depend irrigation, resulting in a more stable interannual variation in GPP (Tian et al., 2011). However, unreasonable irrigation may promote higher ET, which may lead to a decreasing trend of WUE in cropland and forest.

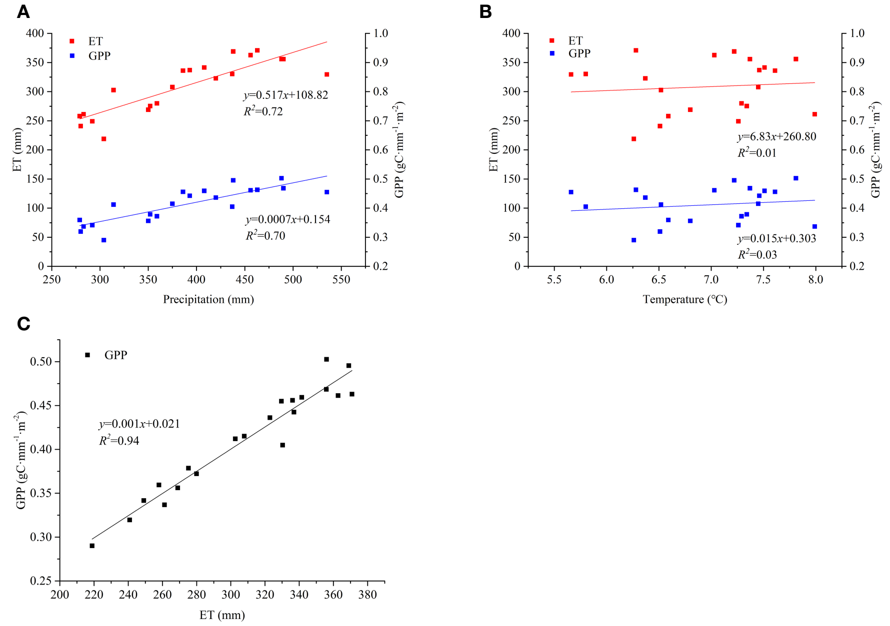

FIGURE 12
Change trends of ET and GPP with precipitation **(A)**, change trends of ET and GPP with temperature **(B)**, and correlation between ET and GPP **(C)** on an annual scale.

4.2 Effects of climate change and human activities on WUE change

In addition to being regulated by the internal vegetation of the system, WUE is also affected by external environmental conditions. Previous studies have shown that precipitation and temperature have either promotional or inhibitory effects on WUE (Zhang et al., 2012; Qiu et al., 2015; Xue et al., 2015; Sun et al., 2016; Wei et al., 2016). Generally, a moderate increase in precipitation is favorable for WUE, but excessive precipitation is unfavorable (Tian et al., 2010; Qiu et al., 2015; Wei et al., 2016; Li et al., 2017). Qiu et al. (2015) and Xue et al. (2015) found a nonlinear relationship between WUE and precipitation and other researchers have reported similar findings (Hu et al., 2010; Mu et al., 2014; Li et al., 2015). Yin et al. (2022) and Shao et al. (2020) found that WUE was negatively correlated with temperature. However, some studies also found that there was a critical value for the impact of temperature on WUE: temperatures that are too high or too low are unfavorable for vegetation WUE (Xiao, 2001; Zhou et al., 2014; Qiu et al., 2015; Xue et al., 2015; Wei et al., 2016). Solar radiation is one of the important factors in plant photosynthesis and also has a significant impact on plant WUE. Previous studies have found a high correlation between solar radiation and WUE (Xu, 2008). In areas with solar radiation below 242.2 W/m^2, WUE showed an increasing trend with an increase in solar radiation, and after exceeding the critical value, WUE showed a decreasing trend (Xue et al., 2015). In addition, most studies have found that the increase in VPD has a negative impact on WUE (Wang et al., 2022; Zheng and Zhang, 2022; Li F. et al., 2023).

WUE was positively correlated with temperature and solar radiation in most of the study area. The increase in temperature and solar radiation promoted photosynthesis, resulting in higher production of dry matter and an increase in the GPP (Li et al., 2002). Although the increase in temperature and solar radiation can also lead to an increase in ET, previous studies have found that the impact on GPP is more significant than that on ET (Wang et al., 2020). WUE was negatively correlated with precipitation and vapor pressure deficit in most of the study area.

In arid and semi-arid areas, available water is the most important factor in controlling vegetation function, and its reduction can increase the physiological stress and vulnerability of plants. In arid areas, vegetation chooses more conservative water use methods when the precipitation decreases and adapts to drought stress by increasing WUE (Chen et al., 2003). The main reason for the negative correlation between VPD and WUE was the interannual variation of VPD, which has a limiting effect on the terrestrial primary productivity (GPP) (He B. et al., 2022). This is because an increase in VPD may cause stomatal closure to avoid excessive water loss in plants due to high air evaporation demand. However, this can also lead to a negative carbon balance, causing plants to consume a large amount of carbohydrate reserves and cause carbohydrate starvation (Yuan et al., 2019). This is consistent with the conclusion of Li F. et al. (2023), who showed that an increase in VPD leads to WUE stagnation.

In addition, the impact of human activities on WUE cannot be ignored, and population density has the highest correlation with WUE. The main reason was that in the past two decades, with the increase in population and the implementation of a series of ecological engineering practices, the area of cropland and forest in the region has increased. Due to their high WUE, the overall WUE has increased. Although the WUE values of forest and cropland were high, this result does not mean that a large amount of land can be reclaimed for artificial tree planting or expansion of cultivated land area. The high WUE was largely attributable to the relatively abundant water resource conditions caused by artificial irrigation, and the local irrigation water is mainly sourced from groundwater; thus, excessive exploitation of this water will lead to the deterioration of the ecological environment.

4.3 Limitations and uncertainties

4.3.1 Data accuracy

This study analyzed the impact of meteorological factors on WUE based on remote sensing data. The Kriging interpolation method was used for the meteorological data. However, the volume and accuracy of the data were limited, and the difference in interpolation methods may have affected the results. Previous studies have shown that ET and GPP data from MODIS play a good performance (Turner et al., 2006; Velpuri et al., 2013), which were widely used in WUE calculations (Huang et al., 2017; Li X. Y. et al., 2023). But the use of remote sensing data, especially that from the same sensor inevitably introduces some potential uncertainties such as data self-correlated problem. Besides MODIS data, more and more remote sensing data products were used in WUE calculated such as GLASS data (Luo et al., 2023), Sentinel-2 data (Elfarkh et al., 2023) and PML-V2 product (He S. Y. et al., 2022; Ji et al., 2023). Different data sources may result in differences in evaluation results due to differences in resolution and model. Therefore, further analysis is needed to obtain more reliable conclusions regarding the consistency and uncertainty generated by different data sources, combining multi-source data.

4.3.2 Analytical methods

Only linear methods such as linear regression analysis and residual analysis were used to analyze the relationship between WUE and factors such as temperature, precipitation, VPD, and solar radiation, without considering the nonlinear relationship between meteorological factors and WUE. In addition, this paper demonstrated the impact of human activities on WUE, but its driving mechanism needs to be further analyzed. For example, human activities affect biological characteristics such as Leaf area index (LAI) and NDVI by modifying surface features such as afforestation, urban expansion, cropland reclamation, or changing irrigation methods, thereby affecting WUE.

5 Conclusions

This study explored the changes in WUE in the WLRP from 2001 to 2020 using linear regression and the CV method based on the MODIS GPP and ET datasets. The relationships between WUE and climate change and human activities and the driving mechanism of WUE changes were revealed through correlation analyses, residual analysis, and the grey correlation model. From 2001 to 2020, most areas of the WLRP (77.13%) were in a stable state without significant changes, whereas a small part of the WLRP (22.87%) changed significantly. WUE change is not entirely driven by climate change, and human activities have also played an important role. In areas where WUE increased, the average contribution rate of climate change was 72.4%, and that of human activities was 27.6%.

Data availability statement

Publicly available datasets were analyzed in this study. This data can be found here: http://cdc.cma.gov.cn, https://cds.climate.copernicus.eu/, https://hub.worldpop.org/, https://earthdata.nasa.gov/.

Author contributions

QL and YL conceptualized the study. MG and QL drafted the manuscript and were responsible for data preparation and analysis. NY, YW, and XL were responsible for verifying the results and reviewing the article. All authors reviewed the manuscript.

Funding

This research was supported by the National Natural Science Foundation of China (41702386) and Geological Survey Project of the China Geological Survey (DD20190506 and DD20221726).

Conflict of interest

The authors declare that this study was conducted in the absence of any commercial or financial relationships that could be considered potential conflicts of interest.

Publisher’s note

Supplementary material

The Supplementary Material for this article can be found online at: https://www.frontiersin.org/articles/10.3389/fevo.2023.1176131/full#supplementary-material

References

Adams, M. A., Turnbull, T. L., Sprent, J. I., and Buchmann, N. (2016). Legumes are different:leaf nitrogen,photosynthesis, and water use efficiency. *J.Proc.Natl.Acad.Sci* 113 (15), 4098–4103. doi: 10.1073/pnas.1523936113

Ai, Z. P., Wang, Q. X., Yang, Y. H., Manevski, K., Yi, S., and Zhao, X. (2020). Variation of gross primary production, evapotranspiration and water use efficiency for global croplands. *J. Agric. For. Meteorology*. 287, 107935. doi: 10.1016/j.agrformet.2020.107935

Allen, R. G., Pereira, L. S., Raes, D., and Smith, M. (1998). *Crop evapotranspiration—guidelines for computing crop water requirements* (Rome, Italy: FAO).

An, X. (2022). Responses of Water Use Efficiency to climate change in evapotranspiration and transpiration ecosystems. *J. Ecol. Indic.* 141, 109157. doi: 10.1016/j.ecolind.2022.109157

Aruna (2020). *Trade-off and synergy analyses and sustainable management of ecosystem services in West Liao River Plain* (Xi'an: Northwest University).

Bhattacharya, A. (2019). *Changing Climate and Resource Use Efficiency in Plants* (London: Academic Press), 15. doi: 10.1016/B978-0-12-816209-5.00001-5

Briggs, L. J., and Shantz, H. L. (1913). "The water requirement of plants," in *Bureau of Plant Industry Bulletin* (Washington, DC: US Department of Agriculture), 282–285.

Chang, X. G., Wang, Z. H., Wei, F. ,. Y., Xiao, P. Q., Shen, Z. Z., Lv, X. Z., et al. (2021). Determining the contributions of vegetation and climate change to ecosystem WUE variation over the last two decades on the Loess Plateau. *J. Forests* 12 (11), 1442. doi: 10.3390/f12111442

Chen, L., Chen, S. J., Cai, X. B., and Liu, H. (2017). Analysis on spatial-temporal variation characteristics of vegetation cover in the Three Gorges Reservoir Area based on time series NDVI data. *J. J. Cent. China Normal Univ. (Natural Sciences)*. 51 (3), 407–415. doi: 10.19603/j.cnki.1000-1190.2017.03.021

Chen, T., Yang, M. X., and Feng, H. Y. (2003). Spatial distribution of stable carbon isotope compositions of plant leaves in the north of the Tibetan Plateau. *J.Journal Glaciology Geocryology* 25 (1), 83–87. doi: 10.1023/A:1022289509702

Elfarkh, J., Johansen, K., Hajj, M. E., Almashharawi, S. K., and McCabe, M. F. (2023). Evapotranspiration, gross primary productivity and water use efficiency over a high-density olive orchard using ground and satellite based data. *J.Agricultural Water Manage.* 287, 108423. doi: 10.1016/j.agwat.2023.108423

Evans, J., and Geerken, R. (2004). Discrimination between climate and human induced dryland degradation. *J.Journal Arid Environments.* 57 (4), 535–554. doi: 10.1016/S0140-1963(03)00121-6

Feng, C. Y., Wang, H. S., and Sun, J. X. (2018). Temporal changes of vegetation water use efficiency and its influencing factors in Northern China. *J. Chin. J. Plant Ecol.* 42 (04), 453–465. doi: 10.17521/cjpe.2017.0214

Feng, Z. M., Yang, L., and Yang, Y. Z. (2014). Temporal and spatial distribution patterns of grain crops in the west liaohe river basin. *J. J. Resour. Ecol.* 5 (3), 244–252.

Fu, G., Zhang, J., Shen, Z., Shi, P. L., He, Y. T., and Zhang, X. Z. (2017). Validation of collection of 6 MODIS/Terra and MODIS/Aqua gross primary production in an alpine meadow of the Northern Tibetan Plateau. *Int.J.Rem.Sens* 38 (16), 4517–4534. doi: 10.1080/01431161.2017.1323283

Gadanakis, Y., Bennett, R., Park, J., and Areal, F. J. (2015). Improving productivity and water use efficiency: A case study of farms in England. *J.Agricultural Water Manage.* 160, 22–32. doi: 10.1016/j.agwat.2015.06.020

Gang, C. C., Wang, Z. Q., Chen, Y. Z., Yang, Y., Li, J. L., Cheng, J. M., et al. (2016). Drought-induced dynamics of carbon and water use efficiency of global grasslands from 2000 to 2011. *J. Ecol. Indic.* 67, 788–797. doi: 10.1016/j.ecolind.2016.03.049

Gao, Z. D., He, J. S., Dong, K. B., and Li, X. (2017). Trends in reference evapotranspiration and their causative factors in the West Liao River basin, China. *J. Agric. For. Meteorology* 232, 106–117. doi: 10.1016/j.agrformet.2016.08.006

Gao, M. M., Liu, Q., Wang, Y., Li, X. L., and Shi, P. (2022). Spatial and temporal variations in vegetation index and its impact factors in the West Liaohe Plain in Inner Mongolia. *J. Hydrogeology Eng. Geology*. 49 (1), 175–182. doi: 10.16030/j.cnki.issn.1000-3665.202108051

Gao, W. D., Zheng, C., Liu, X. H., Lu, Y. D., Chen, Y. F., Wei, Y., et al. (2022). NDVI-based vegetation dynamics and their responses to climate change and human activities from 1982 to 2020: A case study in the Mu Us Sandy Land, China. *J. Ecol. Indic.* 137, 108745. doi: 10.1016/j.ecolind.2022.108745

Hao, X. M., Ma, H. Y., Hua, D., Qin, J. X., and Zhang, Y. (2019). Response of ecosystem water use efficiency to climate change in the Tianshan Mountains, Central Asia. *J.Environmental Monit. Assess.* 191 (9). doi: 10.1007/s10661-019-7673-z

Hatfield, J. L., and Dold, C. (2019). Water-use efficiency: advances and challenges in a changing climate.J. *Front. Plant Science.* 10, 1–14. doi: 10.3389/fpls.2019.00103

He, B., Chen, C., and Lin, S. (2022). Worldwide impacts of atmospheric vapor pressure deficit on the interannual variability of terrestrial carbon sinks. *J. Natl. Sci. Review.* 9 (04), 33–40. doi: 10.1093/nsr/nwab150

He, S. Y., Zhang, Y. Q., Ma, N., Tian, J., Kong, D. D., Liu, C. M., et al. (2022). A daily and 500m coupled evapotranspiration and gross primary production across China during 2000-2020. *J.Earth Syst.Sci.Data* 14, 5463–5488. doi: 10.5194/essd-14-5463-2022

Hu, Z. M., Yu, G. R., Fan, J. W., Zhong, H. P., Wang, S. Q., and Li, S. G. (2010). Precipitation-use efficiency along a 4500-km grassland transect. *J. Global Ecol. Biogeography* 19 (6), 842–851. doi: 10.1111/j.1466-8238.2010.00564.x

Hu, Z. M., Yu, G. R., Fu, Y. L., Sun, X. M., L, Y. N., Shi, P. L., et al. (2008). Effects of vegetation control on ecosystem water use efficiency within and among four grassland ecosystems in China. *J. Global Change Biol.* 14 (7), 1609–1619. doi: 10.1111/j.1365-2486.2008.01582.x

Huang, L., He, B., Han, L., Liu, J. J., Wang, H. Y., and Chen, Z. Y. (2017). A global examination of the response of ecosystem water-use efficiency to drought based on MODIS data. *J.Science Total Environ.* 601–602, 1097–1107. doi: 10.1016/j.scitotenv.2017.05.084

Huang, F., Zhang, H. J., and Wang, P. (2013). Assessment of vegetation change and its causes in the West Liaohe River Basin of China using SPOT-VGT image. *J.Earth Resour. Environ. Remote sensing/GIS applications.*, 889312, 1–11. doi: 10.1117/12.2028227

IPCC (2021). *Climate change 2021: The Physical Science Basis* (Cambridge: Cambridge University Press).

Jassal, R. S., Black, T. A., Spittlehouse, D. L., Brümmer, C., and Nesic, Z. (2009). Evapotranspiration and water use efficiency in different-aged Pacific Northwest Douglas-fir stands. *J.Agric For Meteorol* .149, 1168–1178. doi: 10.1016/j.agrformet.2009.02.004

Ji, Y. Y., Zeng, S. D., Tang, Q. Q., Yan, L. Y., Wu, S. J., Fan, Y. C., et al. (2023). Spatiotemporal variations and driving factors of China's ecosystem water use efficiency. *J.Ecological Indic.* 148, 110077. doi: 10.1016/j.ecolind.2023.110077

Jia, B. H., Luo, X., Wang, L. H., and Lai, X. (2023). Changes in water use efficiency caused by climate change, CO2 fertilization, and land use changes on the tibetan plateau. *J. Adv. Atmospheric Sci.* 40 (01), 144–154. doi: 10.1007/s00376-022-2172-5

Klein, T., Shpringer, I., Fikler, B., Elbaz, G., Cohen, S., and Yakir, D. (2013). Relationships between stomatal regulation, wateruse, and water-use efficiency of two coexisting key Mediterranean tree species. *J.Forest Ecol. Manage.* 302, 34–42. doi: 10.1016/j.foreco.2013.03.044

Li, Z. X., Feng, Q., Liu, W., Wang, T. T., Gao, Y., Wang, Y. M., et al. (2014). Spatial and temporal trend of potential evapotranspiration and related driving forces in Southwestern China, during 1961–2009. *J.Quaternary Int.* 336 (26), 127–144. doi: 10.1016/j.quaint.2013.12.045

Li, H. D., Guan, D. X., Yuan, F. H., Wang, A. Z., Jin, C. J., Wu, J. B., et al. (2015). Water use efficiency and its influential factor over Horqin Meadow. *J.Acta Ecologica Sinica.* 35 (02), 478–488. doi: 10.5846/stxb201303310566

Li, F. S., Kang, S. Z., and Zhang, F. C. (2002). Effects of elevated atmospheric CO$_2$ concentration and temperature on crop physiology and ecology. *J. J. Appl. Ecology.* 09, 1169–1173.

Li, F., Xiao, J. F., Chen, J. Q., Ballantyne, A., and Jin, K. (2023). Global water use efficiency saturation due to increased vapor pressure deficit. *J. Sci. (New York N.Y.).* 381 (6658), 672–677. doi: 10.1126/science.adf5041

Li, X. J., Zhang, F. P., Wang, H. W., Lei, S. J., and Gao, Z. (2017). Analysis of the spatio-temporal characteristics of water use efficiency of vegetation and its relationship with climate in the Heihe River Basin. *J. J. Desert Res.* 37 (4), 733–741.

Li, X. Y., Zou, L., Xia, J., Wang, F. Y., and Li, H. W. (2023). Identifying the Responses of Vegetation Gross Primary Productivity and Water Use Efficiency to Climate Change under Different Aridity Gradients across China. *J. Remote Sens.* 15 (6). doi: 10.3390/rs15061563

Liu, S. F., Dang, Y. G., and Fang, Z. G. (2017). *Gray system theory and its application* (Beijing: Science Press).

Liu, Y., Xiao, J., Ju, W., Zhou, Y., Wang, S., and Wu, X. (2015). Water use efficiency of China's terrestrial ecosystems and responses to drought. *Sci. Rep.* 5, 13799. doi: 10.1038/srep13799

Luo, H., Bie, X. J., Yi, G. H., Zhou, X. B., Zhang, T. B., Li, J. J., et al. (2022). Dominant impacting factors on water-use efficiency variation in inner Mongolia from 2001 to 2018: vegetation or climate? *J. Remote Sens.* 14 (18), 4541. doi: 10.3390/rs14184541

Luo, X., Wang, Y. F., and Li, Y. G. (2023). Responses of ecosystem water use efficiency to drought in the Lancang-Mekong River Basin. *J.Fron.Ecol.Evol* 11. doi: 10.3389/fevo.2023.1203725

Mafi-Gholami, D., Zenner, E. K., Jaafari, A., and Ward, R. D. (2019). Modeling multi-decadal mangrove leaf area index in response to drought along the semi-arid southern coasts of Iran. *J. Total Environ.* 656, 1326–1336. doi: 10.1016/j.scitotenv.2018.11.462

Miao, L., Lu, Q., and Liu, G. L. (2023). Spatiotemporal evolution characteristics of NDVI of different vegetation types and its response to climate factors on the Qinghai-Tibet Plateau from 1999 to 2019. *J. Res. Soil Water Conserv.* 30 (1), 97–105. doi: 10.13869/j.cnki.rswc.2023.01.027

Milich, L., and Weiss, E. (2000). GAC NDVI interannual coefficient of variation (CoV) images: ground truth sampling of the Sahel along north-south transects. *J. Remote Sens.* 21 (2), 235–260. doi: 10.1080/014311600210812

Mu, Q., Zhao, M., and Running, S. W. (2011). Improvements to a MODIS global terrestrial evapotranspiration algorithm. *J. Remote Sens. Environ.* 115, 1781–1800. doi: 10.1016/j.rse.2011.02.019

Mu, S. J., Zhou, K. X., Qi, Y., Chen, Y. Z., Fang, Y., and Zhu, C. (2014). Spatio-temporal patterns of precipitation-use efficiency of vegetation and their controlling factors in Inner Mongolia. *J. Chin. J. Plant Ecology.* 38 (01), 1–16. doi: 10.3724/SP.J.1258.2014.00001

Muhammad, K., Ahmed, E. N., Lars, R., and Karl, S. (2018). Spatio-temporal variations in climate, primary productivity and efficiency of water and carbon use of the land cover types in Sudan and Ethiopia. *Sci. Total Environ.* 624, 790–806. doi: 10.1016/j.scitotenv.2017.12.090

Niu, S. L., Xing, X. R., Zhang, Z., Xia, J. Y., Zhou, X. H., Song, B., et al. (2011). Water-use efficiency in response to climate change: from leaf to ecosystem in a temperate steppe. *J. Global Change Biol.* 17 (2), 1073–1082. doi: 10.1111/j.1365-2486.2010.02280.x

Qiu, K. B., Cheng, J. F., and B.Q, J. (2015). Spatio-temporal distribution of cropland water use efficiency and influential factors in middle and east of China. *J. Trans. Chin. Soc. Agric. Engineering.* 31 (11), 103–109. doi: 10.11975/j.issn.1002-6819.2015.11.015

Riha, S. J., and Melkonian, J. (2023). Limited impact of vapor pressure deficit on rainfed maize evapotranspiration, CO_2 flux, and canopy temperature. *J. Agron. J.* 115 (2), 844–858. doi: 10.1002/agj2.21254

Shao, H., Zhang, Y. D., Gu, F. X., Miao, N., and Liu, S. R. (2020). Changes of water use efficiency in the Yangtze River Economic Zone and its relationship with temperature and precipitation. *J. Acta Ecologica Sinica.* 40 (16), 5579–5590. doi: 10.5846/stxb201901020010

Stavroula, D., and Konstantinos, G. ,. N. (2021). Annual actual evapotranspiration estimation via GIS models of three empirical methods employing remotely sensed data for the peloponnese, Greece, and comparison with annual MODIS ET and pan evaporation measurements. *J.ISPRS Int. J. Geo-Information* 7 (8), 522. doi: 10.3390/ijgi10080522

Sun, Y., Piao, S. L., Huang, M. T., Ciais, P., Zeng, Z. Z., Cheng, L., et al. (2016). Global patterns and climate drivers of water-use efficiency in terrestrial ecosystems deduced from satellite-based datasets and carbon cycle models. *J.Global Ecol. Biogeography* 25 (3), 311–323. doi: 10.1111/geb.12411

Tang, X., Li, H., Desai, A. R., Nagy, Z., Luo, J., Kolb, T. E., et al. (2014). How is water-use efficiency of terrestrial ecosystems distributed and changing on Earth? *J.Sci.Rep.* 4, 7483. doi: 10.1038/srep07483

Tian, H. Q., Chen, G. S., Liu, M. L., Zhang, C., Sun, G., Lu, C. Q., et al. (2010). Model estimates of net primary productivity, evapotranspiration, and water use efficiency in the terrestrial ecosystems of the southern United States during 1895–2007. *J. For. Ecol. Manage.* 259 (7), 1311–1327. doi: 10.1016/j.foreco.2009.10.009

Tian, H., Lu, C., Chen, G., Xu, X., Liu, M., Ren, W., et al. (2011). Climate and land use controls over terrestrial water use efficiency in monsoon Asia. *J. Ecohydrology* 4, 322–340. doi: 10.1002/eco.216

Tian, F., Zhang, Y., and Lu, S. H. (2020). Spatial-temporal dynamics of cropland ecosystem water-use efficiency and the responses to agricultural water management in the Shiyang River Basin, northwestern China. *J.Agricultural Water Management.* 237, 106176. doi: 10.1016/j.agwat.2020.106176

Tucker, C. J., Newcomb, W. W., Los, S. O., and Prince, S. D. (1991). Mean and inter-year variation of growing-season normalized difference vegetation index for the Sahel 1981-1989. *J.Remote Sens.* 12 (6), 1133–1135. doi: 10.1080/01431169108929717

Turner, D. P., Ritts, W. D., Cohen, W. B., Gower, S. T., Running, S. W., Zhao, M., et al. (2006). Evaluation of MODIS NPP and GPP products across multiple biomes.J. *Remote Sens. Env.* 102 (3–4), 282–292. doi: 10.1016/j.rse.2006.02.017

Velpuri, N. M., Senay, G. B., Singh, R. K., Bohms, S., and Verdin, J. P. (2013). A comprehensive evaluation of two MODIS evapotranspiration products over the conterminous United States: using point and gridded FLUXNET and water balance ET. *J.Remote Sens. Env.* 139, 35–49. doi: 10.1016/j.rse.2013.07.013

Wang, C. Y., Li, S. E., Wu, M. S., Zhang, W. X., He, H. X., Yang, D. N., et al. (2022). Water use efficiency control for a maize field under mulched drip irrigation. *J. Sci. total Environ.* 857 (3), 159457. doi: 10.1016/j.scitotenv.2022.159457

Wang, J. Y., Qin, S. G., and Zhang, Y. Q. (2020). Spatial-temporal patterns of vegetation water use efficiency in the Mu Us Desert. *J.Journal Desert Res.* 40 (05), 120–129.

Wei, H. J., Zhang, Y. F., Dong, X. B., Lu, N. C., and Wang, X. C. (2016). Estimating the spatio-temporal characteristic of vegetation water use efficiency over Weihe River Basin. *J. J. Natural Resources.* 31 (08), 1275–1288. doi: 10.11849/zrzyxb.20151064

Xia, L., Wang, F., Mu, X., Jin, K., Sun, W., Gao, P., et al. (2015). Water use efficiency of net primary production in global terrestrial cosystems. *J. Earth Syst. Sci.* 124, 921–931. doi: 10.1007/s12040-015-0587-4

Xiao, C. W. (2001). Potential effect of simulated precipitation change on the evapotranspiration of salix psammophylla seedlings in maowusu sandland. *J. J. grassland.* 9 (2), 121–127. doi: 10.11733/j.issn.1007-0435.2001.02.009

Xu, X. T. (2008). *Analysis of spatiotemporal characteristics of NPP and vegetation water use efficiency in the source area of the Yellow River* (Lanzhou: Lanzhou University).

Xue, B. L., Guo, Q. H., Otto, A., Xiao, J. F., Tao, S. L., and Li, L. (2015). Global patterns, trends, and drivers of water use efficiency from 2000 to 2013. *J. Ecosphere* 6 (10), 1–18. doi: 10.1890/ES14-00416.1

Yan, L., Chen, M. J., and Ma, J. (2018). A study of the ecological patterns of farming-pastoral zones in semi-arid regions: using the west liaohe river plain of China as an example. *J. Appl. Ecol. Environ. Res.* 16 (03), 3229–3244. doi: 10.15666/aeer/1603_32293244

Yan, X., Wang, R., and Niu, Z. G. (2022). Response of China's wetland NDVI to climate changes. *J.Wetlands.* 42 (6). doi: 10.1007/s13157-022-01568-0

Yang, J., and Huang, X. (2021). The 30 m annual land cover dataset and its dynamics in China from 1990 to 2019. *J. Earth System Sci. Data* 13 (8), 3907–3925. doi: 10.5194/essd-13-3907-2021

Yao, Y., Liang, S., Li, X., Hong, Y., Fisher, J. B., Zhang, N., et al. (2014). Bayesian multimodel esrimation of global terrestrial latent heat flux from eddy covariance, meteorological, and satellite observations. *J.Geophys.Res.Atmos.* 119, 4521–4545. doi: 10.1002/2013JD020864

Yin, C. H., Luo, M., Meng, F. H., Sa, C. L., and Bao, Y. H. (2022). The spatiotemporal variation and influencing factors of vegetation carbon and water use efficiency in the Mongolian Plateau. *J. Chin. J. Ecology.* 41 (06), 1079–1089. doi: 10.13292/j.1000-4890.202205.008

Yu, Y. Y., Song, F. Y., and Zhang, S. J. (2022). Quantitative analysis of temporal and spatial changes of NDVI and Its driving factors in Henan province from 2000 to 2020. *J.Ecology Environ. Sci.* 31 (10), 1939–1950. doi: 10.16258/j.cnki.1674-5906.2022.10.002

Yuan, W. P., Zheng, Y., Piao, S. L., Ciais, P., Lombardozzi, D., Wang, Y. P., et al. (2019). Increased atmospheric vapor pressure deficit reduces global vegetation growth. *J. Sci. Advances.* 2019, 5(8). doi: 10.1126/sciadv.aax1396

Zhang, Z., Jiang, H., Liu, J. X., Zhou, G. M., Liu, S. R., and Zhang, X. Y. (2012). Assessment on water use efficiency under climate change and heterogeneous carbon dioxide in China terrestrial ecosystems. *J.Procedia Environ. Sci.* 13, 2031–2044. doi: 10.1016/j.proenv.2012.01.194

Zhang, Y. D., Pang, R., Gu, F. X., and Liu, S. R. (2016). Temporal-spatial variations of WUE and its response to climate change in alpine area of southwestern China. *J. Acta Ecologica Sinica.* 36 (6), 1515–1525. doi: 10.5846/stxb201408121602

Zhang, L., Tian, J., He, H., Ren, X., Sun, X., Yu, G., et al. (2015). Evaluation of water use efficiency derived from MODIS products against eddy variance measurements in China. *J.Remote. Sens.* 7, 11183–11201. doi: 10.3390/rs70911183

Zhang, H., Zhan, C., Xia, J., Yeh, P. J. F., Ning, L., Hu, S., et al. (2022). The role of groundwater in the spatio-temporal variations of vegetation water use efficiency in the Ordos Plateau,China. *J.Hydrol.* 605, 127332. doi: 10.1016/j.jhydrol.2021.127332

Zhao, Z. Z. (2017). *Study on ecological environment change of Horqin Sandy Land based on multi-source data* (Wuhan: Wuhan University).

Zhao, M., Heinsch, F. A., Nemani, R. R., and Running, S. W. (2005). Improvements of the MODIS terrestrial gross and net primary production global data set. *J.Remote Sens. Environ.* 95, 164–176. doi: 10.1016/j.rse.2004.12.011

Zhao, A. Z., Zhang, A. B., Feng, L. L., Wang, D. L., and Cheng, D. Y. (2019). Spatio-temporal characteristics of water-use efficiency and its relationship with climatic factors in the Haihe River basin. *J. Acta Ecologica Sinica.* 39 (4), 1452–1462.

Zhen, Y., Wang, J. X., Liu, S. R., Rentch, J. S., Sun, P. S., and Lu, C. Q. (2017). Global gross primary productivity and water use efficiency changes under drought stress. *J.Envirinmental Res. Lett.* 12 (1), 014016. doi: 10.1088/1748-9326/aa5258

Zheng, H., Lin, H., Zhou, W. J., Bao, H., Zhu, X. J., Jin, Z., et al. (2019). Revegetation has increased ecosystem water-use efficiency during 2000–2014 in the Chinese Loess Plateau: Evidence from satellite data. *J.Ecological Indic.* 102, 507–518. doi: 10.1016/j.ecolind.2019.02.049

Zheng, Z. T., and Zhang, Y. J. (2022). Variation in ecosystem water use efficiency and its attribution analysis during 1982-2018 in Qingzang Plateau. *J. Chin. J. Plant Ecology.* 46 (12), 1486–1496. doi: 10.17521/cjpe.2021.0187

Zhou, M., Zhou, S. S., Wang, J. X., Zhang, Z. W., and Yang, J. H. (2014). Research advance on influencing factors of crop water use efficiency. *J.Agricultural Sci. Technol.* 15 (11), 1967–1976. doi: 10.16175/j.cnki.1009-4229.2014.11.031

Zhu, Y. H., Xi, X. K., Ma, P. F., Yun, T., and Zhang, J. (2022). Spatiotemporal variation of vegetation net primary productivity and its influencing factors. *J. J. Inner Mongolia Agric. University(Natural Sci. Edition).* 43 (01), 21–26. doi: 10.16853/j.cnki.1009-3575.2022.01.005

Zhu, X. J., Yu, G. R., Wang, Q. F., Hu, Z. M., Han, S. J., Yan, J. H., et al. (2014). Seasonal dynamics of water use efficiency of typical forest and grassland ecosystems in China. *J. J. For. Res.* 19 (1), 1609–1619. doi: 10.1007/s10310-013-0390-5

Frontiers in
Ecology and Evolution

Ecological and evolutionary research into our natural and anthropogenic world

This multidisciplinary journal covers the spectrum of ecological and evolutionary inquiry. It provides insights into our natural and anthropogenic world, and how it can best be managed.

Discover the latest Research Topics

See more →

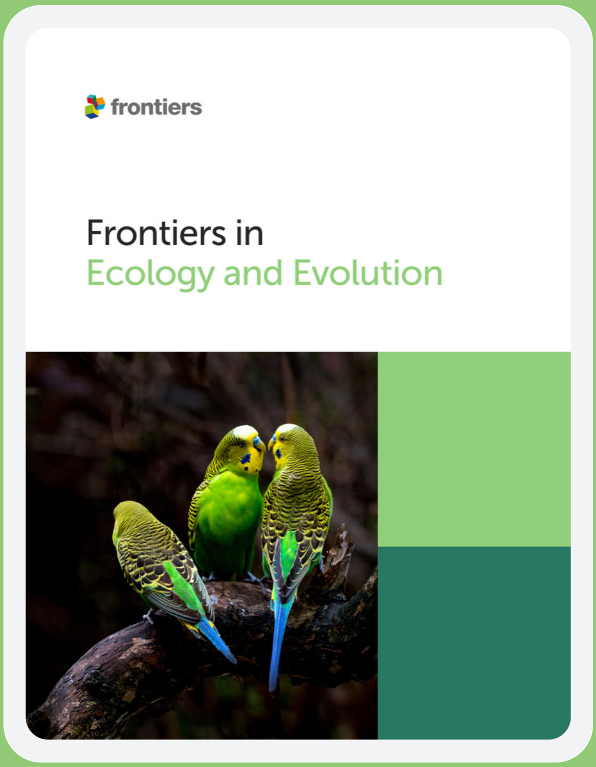
frontiers

Frontiers in
Ecology and Evolution

Frontiers

Avenue du Tribunal-Fédéral 34
1005 Lausanne, Switzerland
frontiersin.org

Contact us

+41 (0)21 510 17 00
frontiersin.org/about/contact